RADIOLOGY
AND
ONCOLOGY

Publisher

Association of Radiology and Oncology

Affiliated with

Slovenian Medical Association – Slovenian Association of Radiology, Nuclear Medicine Society,
Slovenian Society for Radiotherapy and Oncology, and Slovenian Cancer Society

Croatian Medical Association – Croatian Society of Radiology

Societas Radiologorum Hungarorum

Friuli-Venezia Giulia regional groups of S.I.R.M.

Italian Society of Medical Radiology

Aims and scope

Radiology and Oncology is a journal devoted to publication of original contributions in diagnostic and interventional radiology, computerized tomography, ultrasound, magnetic resonance, nuclear medicine, radiotherapy, clinical and experimental oncology, radiobiology, radiophysics and radiation protection.

Indexed and abstracted by:

- *Celdes*
- *Chemical Abstracts Service (CAS)*
- *Chemical Abstracts Service (CAS) - SciFinder*
- *CNKI Scholar (China National Knowledge Infrastructure)*
- *CNPIEC*
- *DOAJ*
- *EBSCO - Biomedical Reference Collection*
- *EBSCO - Cinahl*
- *EBSCO - TOC Premier*
- *EBSCO Discovery Service*
- *Elsevier - EMBASE*
- *Elsevier - SCOPUS*
- *Google Scholar*
- *J-Gate*
- *JournalTOCs*
- *Naviga (Softweco)*
- *Primo Central (ExLibris)*
- *ProQuest - Advanced Technologies Database with Aerospace*
- *ProQuest - Health & Medical Complete*
- *ProQuest - Illustrata: Health Sciences*
- *ProQuest - Illustrata: Technology*
- *ProQuest - Medical Library*
- *ProQuest - Nursing & Allied Health Source*
- *ProQuest - Pharma Collection*
- *ProQuest - Public Health*
- *ProQuest - Science Journals*
- *ProQuest - SciTech Journals*
- *ProQuest - Technology Journals*
- *PubMed*
- *PubsHub*
- *ReadCube*
- *SCImago (SJR)*
- *Summon (Serials Solutions/ProQuest)*
- *TDOne (TDNet)*
- *Thomson Reuters - Journal Citation Reports/Science Edition*
- *Thomson Reuters - Science Citation Index Expanded*
- *Ulrich's Periodicals Directory/ulrichsweb*
- *WorldCat (OCLC)*

This journal is printed on acid- free paper

contents

radiophysics

research article

The concept of radiation-enhanced stem cell differentiation

Adam A. Mieloch and Wiktoria M. Suchorska

Radiobiology Laboratory, Department of Medical Physics, The Greater Poland Cancer Centre

Correspondence to: Dr. Wiktoria M. Suchorska, Radiobiology Laboratory, Department of Medical Physics, The Greater Poland Cancer Centre, 15th Garbary Street, 61-866 Poznan, Poland. Phone: +48 618 850 477; wiktoria.suchorska@wco.pl

Disclosure: No potential conflicts of interest were disclosed.

Background. Efficient stem cell differentiation is considered to be the holy grail of regenerative medicine. Pursuing the most productive method of directed differentiation has been the subject of numerous studies, resulting in the development of many effective protocols. However, the necessity for further improvement in differentiation efficiency remains. This review contains a description of molecular processes underlying the response of stem cells to ionizing radiation, indicating its potential application in differentiation procedures. In the first part, the radiation-induced damage response in various types of stem cells is described. Second, the role of the p53 protein in embryonic and adult stem cells is highlighted. Last, the hypothesis on the mitochondrial involvement in stem cell development including its response to ionizing radiation is presented.

Conclusions. In summary, despite the many threats of ionizing radiation concerning genomic instability, subjecting cells to the appropriate dosage of ionizing radiation may become a useful method for enhancing directed differentiation in certain stem cell types.

Key words: stem cells; ionizing radiation; differentiation; regenerative medicine; tissue engineering

Introduction

Stem cells (SCs) possess a set of unique advantages, including the ability to replicate and the ability to differentiate into many different types of cells, called "pluripotency". Due to the pluripotent characteristic of these cells, they play a pivotal role in tissue development and maintenance by replenishing the depletion of cells caused by damaging factors or that occurs physiologically during tissue turn-over.[1] The majority of recent studies have mainly focused on two types of stem cells: Embryonic stem cells (ESCs) and adult stem cells (ASCs), also known as somatic tissue or mesenchymal stem cells.[2] ESCs are derived from the inner cell mass of the blastocyst and are capable of differentiating into the three embryonic germ layers: ectoderm, mesoderm and endoderm, thus contributing to the formation of almost every cell type. ASCs reside in tissue-specific niches in a quiescent state. Upon activation, they undergo asymmetric division, which simultaneously increases the number of cells in the niche and the number differentiating into tissue specific lineages, providing cells required for tissue regeneration.[3,4]

Stem cells have had a significant impact on the progress of many fields of biotechnology, including cell-based regenerative therapies, drug testing and screening, disease modeling, side effects in radiotherapy and many more. In 2006, Yamanaka *et al*. announced a breakthrough finding in regenerative medicine, describing the reprogramming of mouse adult fibroblasts into induced pluripotent stem cells (iPSs) by introducing four factors: Oct3/4, Sox2, c-Myc, and Klf4. iPSs in many aspects resemble ESCs.[5] This discovery solved many of the ethical disputes concerning the procurement of ESCs from human embryos and began a new era in regenerative medicine.

Since then, many attempts to harness the pluripotency of stem cells into directed differentiation have been successful.[6,7] Some of developed pro-

tocols require the formation of embryoid bodies (EBs) prior to further differentiation. EBs are three-dimensional cellular aggregates obtained by spontaneous differentiation of ESCs or IPSs. EBs consist of ESCs that are mostly differentiated into the embryonic germ layers: ectoderm, endoderm and mesoderm.[8] The differentiation process in many aspects mimics early mammalian embryogenesis, including cell to cell interactions. Moreover, the most essential method of EBs formation is based on suspension culture deprived of antidifferentiation factors. Due to simple methodology and similarity to embryogenesis, EBs are widely utilized as an intermediate stage during *in vitro* differentiation of both human and murine ESCs. [9]

Currently, many stem cell-based therapies are undergoing clinical trials, for example, "Intravenous Stem Cells After Ischemic Stroke", "Human Neural Stem Cell Transplantation in Amyotrophic Lateral Sclerosis (ALS)" and "Treatment of Knee Osteoarthritis by Intra-articular Injection of Bone Marrow Mesenchymal Stem Cells".[10–12] These trials are just a few from a still enlarging group of studies investigating the potential applications of stem cells in regenerative medicine, which indicates a growing need for reliable methods of directed differentiation of SCs.

Ionizing radiation (IR) has been used for many years as a basic tool in cancer treatment.[13] The response of non-stem cells to irradiation has been extensively investigated by a number of studies, and to date, many molecular mechanisms of this phenomena have been thoroughly elucidated.[14–16] However, based on the current understanding concerning non-SCs, the radio-response of SCs cannot be anticipated and it could result in unexpected outcomes.

Radiation-induced differentiation has already been reported in multiple studies[17,18]; however, it has not been investigated as a potential tool in stem cell differentiation protocols. The main goal of this review is to present research based indications that radiation-enhanced differentiation is a promising technology for further development of stem cell engineering.

Radiation-induced DNA damage response in stem cells

Radiation-induced damage to genomic DNA triggers a cascade of biochemical reactions known as the DNA damage response (DDR), which includes cell cycle arrest, DNA repair and, in the case of unmanageable lesions, senescence or apoptosis. The functional mechanism of DNA damage repair is crucial for the maintenance of genomic stability.

The most dangerous type of DNA lesions are double strand breaks (DSBs), which are usually caused by IR or free radical exposure. Repair of DSBs is driven by two major pathways: homologous recombination (HR) and non-homologous end joining (NHEJ).[19] In the process of HR, sister chromatids serve as a template; thus, the repair is considered error-free. NHEJ does not utilize sister chromatids as a template and is therefore significantly more prone to error introduction. Depending on the phase of the cell cycle, one of the pathways is used predominantly. The requirement for sister chromatids in HR restrains its activity to the S and G2 phases. The NHEJ response dominates through the rest of the cell cycle.[20] There are also other types of DNA damage repair mechanisms: nucleotide excision repair (NER), base excision repair (BER) and mismatch repair (MMR). However, their contribution to radiation-enhanced differentiation seems to be negligible and will not be considered in this study.

DNA damage repair in embryonic stem cells (ESCs)

It has been proven that the mechanisms of DNA damage repair in ESCs are more efficient compared to other cell types.[21] ESCs display a unique cell cycle structure. The G1 phase is significantly shortened and the G1 to S transition is facilitated in order to promote rapid self-renewal. Consequently, the majority of the ESC population is in the phases of cell cycle where sister chromatids are available for use as a template. Due to this phenomena, ESCs predominantly utilize high-fidelity HR.[22]

ESCs serve as a pool of cells for the development of the whole organism. Therefore, DNA repair in these cells requires high efficiency and accuracy in order to provide genomic stability. In the case of insults in the genomic DNA that cannot be repaired, the cell undergoes apoptosis, which is significantly facilitated by a mechanism known as mitochondrial priming in ESCs.[23] Mitochondrial priming is determined by the equilibrium between levels of anti-apoptotic and pro-apoptotic proteins of the B-cell lymphoma 2 (Bcl-2) protein family. ESCs display elevated levels of pro-apoptotic proteins within the mitochondria. Consequently, the initiation of apoptosis requires a considerably weaker stimuli in order to cross the apoptotic threshold. This phenomenon ensures elimination of genetically unstable cells and prevents further transmission of mutations.

A previous study by Sokolov and Naumann revealed that human embryonic stem cells (hESCs) undergo apoptosis after relatively low-dose irradiation. In the study, a 1.0 Gy dose of X-ray radiation triggered robust apoptosis. Conversely, doses of 0.5 Gy and 0.2 Gy did not increase the apoptotic response.[24] A study by Lan *et al.* reported that a 2.0 Gy dose of X-ray radiation resulted in an almost 60% decrease in the survival rate of hESCs 5 days post-irradiation. The same study found that X-ray irradiation elevated metabolic activity (XTT assay) 1.5-fold after a 2.0 Gy dose and 2.5-fold after a 5.0 Gy dose. The same dosage of 2.0 Gy and 5.0 Gy resulted in elevated levels of reactive oxygen species (ROS) and nitrogen (RNS) species for 1 week following exposure.[25]

DNA damage repair in adult stem cells (ASCs)

ASC sensitivity to irradiation varies greatly, depending on their type and developmental stage. However, it is postulated that the DNA repair mechanism becomes less efficient upon differentiation in general. Therefore, ASCs display reduced DNA damage repair (DDR) capabilities in comparison to ESCs, which has been shown previously.[26] It is important to note that the mechanism of DDR in ASCs is distinctly different than the one observed in ESCs.[27] ASCs reside in a quiescent state in the G0 phase of the cell cycle. Slower cell cycle progression corresponds to a higher radioresistance.[28,29] Therefore, despite a lower efficacy of DDR, ASCs exhibit a lower sensitivity to IR compared to the rapidly dividing ESCs. It has been shown that upon DNA damage, ASCs can exit quiescence and progress into the G1 phase, in which error-prone NHEJ repair is performed.[30] Consequently, ASCs are more susceptible to DNA damage accumulation, which can be passed onto progeny.

In 1996, Schwenke *et al.* [17] found that γ-irradiation of murine erythroid progenitor cells resulted in enhanced differentiation. This observed enhancement was determined to be due to the omission of mitotic cell cycling, which is necessary for progenitor cells to undergo terminal differentiation. Moreover, Zheng *et al.* [31] found that DSB suppresses the self-renewal and promotes the further differentiation of neuronal stem cells (NSCs) in a p53-dependent manner.

Role of p53 in stem cells

The p53 protein has been widely studied for many years, and a number of its properties have been elucidated.[32] However, the complexity of its interactions and associations with various molecular processes has left many novel functions of this protein remaining to be discovered.

p53 is a tumor suppressor protein responsible for the induction of reversible cell cycle arrest, which enables DNA repairs to be conducted, and the initiation of apoptosis in the case of irreversible DNA damage. p53 is a transcription factor that, upon activation, binds to the promoters of target genes, either inducing or repressing their transcription depending on the gene.[33] p53 can trigger apoptosis via two pathways: the transcriptional (intrinsic) pathway, as described above, or the *non*-transcriptional (mitochondrial) pathway by direct interactions with *pro-* and *anti*-apoptotic proteins. The main target genes for its proapoptotic activity include p53 upregulated modulator of apoptosis (Puma) and Bcl-2-associated X (Bax) proteins, which belong to the Bcl-2 family.[34] DNA damage results in ataxia telangiectasia mutated (ATM) protein activation, which drives mouse double minute 2 homolog (Mdm2) polyubiquitination and further degradation. Mdm2 is an oncoprotein that mediates p53 polyubiquitination and further degradation by the 26S proteasome. Therefore, Mdm2 degradation contributes to the increased stability of p53. It is worth noting that other mechanisms of p53 regulation also exist. Furthermore, p53 performs a regulatory function over cell proliferation by controlling the expression of the p21 protein, known as cyclin-dependent kinase inhibitor.[35] Silencing of p53 expression has also been shown to increase the efficiency of reprogramming in iPSs generation, indicating its contribution to the maintenance of a differentiated state.[36] Nonetheless, p53 activity during reprogramming ensures elimination of cells bearing genomic aberrations. Therefore, disruption of p53 pathway increases the efficacy of reprogramming and the risk of mutations concomitantly.[37,38] Down regulation of p53 activity has been shown to induce normal SCs transformation towards neoplastic, tumor cells.[39] This may in turn result in cancer stem cells (CSs) formation. CSs share the fundamental properties of SCs, but their activity contributes to the cancer grow and maintenance instead of replenishing normal cell pool.[40] Moreover, teratomas generated from p53 knockout iPSs showed the presence of double-strand DNA breaks and DDR activation, leading to the conclusion that p53 inhibition decreases genomic stability.[41] Due to the high risk of tumor generation after transplantation, methods utilizing p53 inhibition in iPSs generation seem to be unsuitable for therapeutic use.

TABLE 1. The examples of adult stem cell (ASC) types and their corresponding tissue of origin, progenitors and fully differentiated cells

Organ	Stem cell type	Progenitors and fully differentiated cells
Bone marrow	Hematopoietic stem cells	Myeloid progenitor cells, Lymphoid progenitor cells
Intestine	Intestinal stem cells	Enterocytes, Goblet cells, Entero-endocrine cells, Paneth cells
Brain	Neural stem cells	Neurons, Astrocytes, Oligodendrocytes
Mammary gland	Mammary stem cells	Luminal cells, Myoepithelial cells
Muscle	Myosatellite cells	Mioblasts

p53 in embryonic stem cells (ESCs)

It has been shown that p53 accumulates at low levels in the nucleus of hESCs, although in a deacetylated, inactive state. Apart from its canonical activity, p53 also performs a regulatory function over cell proliferation by controlling the expression of p21, known as cyclin-dependent kinase inhibitor. p21 inhibits the activity of cyclin/cdk2 complexes and restrains cell cycle progression. Dolezalova *et al.* revealed that after UVC-irradiation of hESCs, p21 mRNA is present, although its translation is inhibited by various microRNAs.[42] However, a study by Maimets *et al.* contradicts these findings, revealing that the small molecule Nutlin, functioning as a p53 activator, elevates p21 protein levels in hESCs.[43] Therefore, the role of p21 in the p53 pathway remains elusive.

p53 plays an important role in ESC differentiation. It has been shown that spontaneous differentiation occurs at significantly lower rates when the p53 level is reduced.[44] However, one of the most crucial mechanisms supporting the theory of radiation-enhanced differentiation is the reduced expression of pluripotency factors driven by p53 activity. p53 binds directly to the promoters of NANOG and octamer-binding transcription factor 3/4 (Oct3/4), inhibiting their transcription. Moreover, elevated levels of p53 induce expression of differentiation markers GATA4 and GATA6.[43] Furthermore, upon stabilization, in addition to its canonical function, p53 triggers the expression of miR-34a and miR-145, which subsequently repress the pluripotency factors Oct3/4, Kruppel-like factor 4 (Klf4), protein lin-28 homolog A (Lin-28A) and sex determining region Y-box 2 (Sox2), which supports differentiation.[45]

Retinoic acid (RA) is a commonly used differentiation factor utilized in various differentiation protocols, including those inducing the generation of neural cells, cardiomyocytes or chondrocytes.[46–48] RA treatment results in the suppression of NANOG expression. However, this effect was not observed after p53 gene deletion, suggesting that p53 is required for RA-mediated NANOG suppression.[49] Therefore, synergistic cooperation between these two proteins may be hypothesized.

It is important to mention that p53 also performs anti-differentiation stimulation through the Wnt canonical signaling pathway, which is responsible for the maintenance and self-renewal of human and murine ESCs.[50,51]

p53 in adult stem cells (ASCs)

Adult stem cells comprise endothelial progenitors cells (ESC) and hematopoietic stem cells (HSC) and tissue cells, called mesenchymal stem cells (MSC), found in many different organs of the human body and the one discussed in this review are listed in Table 1. Every ASC type contributes to a different cell lineage; therefore, any indications concerning radiation-enhanced differentiation may be true for some ASC types and completely false for others. To clarify the reasoning behind this statement, the properties of p53 activity in three different types of ASCs will be described: neural stem cells (NSCs), hematopoietic stem cells (HSCs) and mammary stem cells (MaSCs).

Neural stem cells (NSCs)

Neural stem cells have the potential to differentiate into neurons, astrocytes and oligodendrocytes. In adults, neurogenesis of the central nervous system begins within the subventricular zone (SVZ) and the subgranular zone of the dentate gyrus of the hippocampus, which serves as a niche for NSCs. The SVZ is a narrow zone of tissue in the wall of the lateral ventricle in the forebrain and is the most active neurogenic region in the adult brain.[52] Neurons generated within SVZ migrate through a path called rostral migratory stream and reach their final destination within the olfactory bulb. A complete turn-over of resident cells within SVZ occurs every 2 to 4 weeks. Nearly 30 000 neuronal precursors are produced daily.[53]

It has been demonstrated that the neuronal progenitors of p53$^{-/-}$ mice display a significantly higher

proliferation rate compared to wild-type mice. NSCs can be maintained in culture as aggregates or neurospheres. p53^{-/-}-derived NSCs formed substantially larger neurospheres than wild type cells, which was due to an increased number of cells per sphere, rather than larger cells. This finding indicates that one of the functions of p53 in NSCs is to restrain excessive proliferation.[54]

Monje *et al.* found that gamma irradiation of neural progenitor cells resulted in a higher efficiency of differentiation. Cultures irradiated with a 10.0 Gy dose showed increased differentiation compared to cells irradiated with a 2.0 Gy dose and control cells. However, the ratio between neurons and astrocytes/oligodendrocytes remained undisturbed, which is an important factor to consider in the context of radioenhancement.[55]

As previously mentioned, p53 also stimulates the Wnt signaling pathway. Data obtained by Wei *et al.* indicated that the Wnt/β-catenin signaling pathway plays a crucial role in the proliferation and differentiation of NSCs in the hippocampus. In this study, a low dose of ionizing radiation (0.3 Gy) was shown to activate the Wnt/β-catenin pathway. As a result, NSCs subjected to irradiation showed increased proliferation and differentiation with a concomitant decrease in apoptosis. Moreover, a water-maze test performed on mice indicated an improvement in the behavioral learning of these mice after low-dose irradiation compared to non-irradiated mice.[56]

Mammary stem cells (MaSCs)

Mammary stem cells are located in the mammary glands. They can differentiate into all lineages of mammary epithelial cells. MaSCs are also responsible for mammary gland development during puberty and pregnancy.[57] MaSCs can be cultured *in vitro* as floating aggregates called mammospheres. A mammosphere is a spherical colony derived from a single MaSC by clonal proliferation.[58] However, the division of MaSCs occurs predominantly by asymmetric division. Therefore, mammospheres usually contain a single stem cell surrounded by more differentiated progeny.[59] Despite their self-renewal capabilities, they were shown to have a limited life span in culture conditions.

MaSCs derived from p53^{-/-} mice displayed an increased self-renewing potential, resulting in an increased number of MaSCs per mammosphere and an unlimited life span in culture conditions. This finding suggests that p53 is involved in the prevention of pathological proliferation by promoting asymmetric division, thus contributing to increased differentiation.[60] It is also consistent with many scientific data regarding the role of p53 mutation in breast cancer development.[61] Interestingly, MaSCs subjected to 4.0 Gy irradiation showed 2.7 fold increase in mammosphere reconstitution capacity, confirming that X-ray increases MaSCs proliferation.[62]

Hematopoietic stem cells (HSCs)

Hematopoietic stem cells (HSCs) are one of the best characterized human stem cells. For many years, they have been used in clinical applications, including leukemia treatment. HSCs differentiate into all of the blood cell lineages. They can be found in the red bone marrow. HSCs differentiate into myeloid and lymphoid progenitors, which may differentiate further giving rise to monocytes, erythrocytes, neutrophils and macrophages (myeloid progenitors) or T-lymphocytes, B-lymphocytes and NK-cells (lymphoid progenitors). The majority of HSCs reside in a quiescent state, while only a small fraction remains active and replenishes the blood cell pool.[63]

During steady-state hematopoiesis, p53 regulates HSC self-renewal and quiescence. It is also responsible for cell competition in the HSC niche. Cells expressing higher than average level of p53 undergo cell cycle arrest and senescence. This mechanism contributes to the maintenance of tissue homeostasis by the eradication of less functional cells.

Milyavsky *et al.* found that HSCs subjected to a 3.0 Gy irradiation dose exhibited a delayed DSB repair and an increased apoptotic response via the p53/antiphagocytic protein 1 (APP1) pathway compared to progenitor cells, which indicated a high sensitivity of HSCs to ionizing radiation.[64] This finding is in agreement with the common notion that HSCs are one of the cell types most vulnerable to ionizing radiation (IR). However, despite its deteriorating effects, X-ray radiation has induced almost twofold increase in absolute number of murine HSCs. Increased number of murine HSCs in bone marrow was still detectable 2 months after irradiation. This effect was not observable in p21^{-/-} mice, suggesting p21 as a key factor of X-ray induced proliferation.[62]

Mitochondria in the context of enhanced differentiation

Mitochondria are double-layered organelles that conduct the metabolic activities associated with energy production through oxidative phosphorylation. Their morphology varies between tissues

TABLE 2. Examples of differences between human and murine cells affecting IR response

Differences between human and murine DNA repair mechanisms	References
Murine cells are deficient in p53 global genomic repair	72
Human ESC rejoin X-ray induced DSB faster than murine ESC	71
Murine cells repair DNA base damage more efficiently	73
Murine cells are more sensitive to oxidative stress	74,75
Murine cells are more prone to oncogenic transformation	76,77

DSB = double strand breaks; ESC = embryonic stem cells

and is strictly connected to the metabolic state of a given cell. In addition to tissue specific differences, mitochondria may undergo fusion or fission, giving rise to tubular or fragmented mitochondria, respectively. The fusion/fission mechanism is strictly connected with proliferation and differentiation.[65] However, the outcome of tubular or fragmented mitochondria generation differs between cell types. In ESCs, the mitochondria reside in a fragmented state, and an increase in mitochondrial fusion precedes differentiation.

Ionizing radiation affects mitochondria in various ways. Mitochondrial DNA (mtDNA) is significantly more susceptible to IR compared to genomic DNA because it does not possess repair mechanisms as efficient as those found in the nucleus. Furthermore, mtDNA does not contain histones, which results in decreased resistance to various in-

sults and a higher mutation rate.[66] IR has also been found to induce both intracellular and mitochondrial oxidative stress.[67] However, IR-induced mitochondrial production of reactive oxygen species (ROS) has been proven to be the most influential in mediating cellular damage compared to ROS generated in other compartments.[68]

Damage to mitochondria may trigger apoptosis, autophagy or, in the case of less severe lesions, fusion. This mechanism provides cross-complementation between impaired mitochondria, supporting their functionality by alleviation of IR-induced deficiencies.[69] A 0.005 to 5.0 Gy dose of X-ray radiation has been shown to prompt a 1.5- to 3.8- fold increase in mitochondrial mass, which supports a theory of increased mitochondrial fusion after IR exposure.[70]

Lan *et al*. have shown that ESCs subjected to IR display a significantly increased level of ROS generation and metabolic activity.[25] Both of these phenomena contribute to the induction of mitochondrial fusion, which in turn is a stimulus for differentiation. Therefore, it may be speculated that the radio-enhancement of differentiation could also involve changes in the mitochondrial fission/fusion machinery.

Summary

A growing amount of evidence indicates that radiation-enhanced stem cell differentiation may become a potent tool for use in stem cell engineering
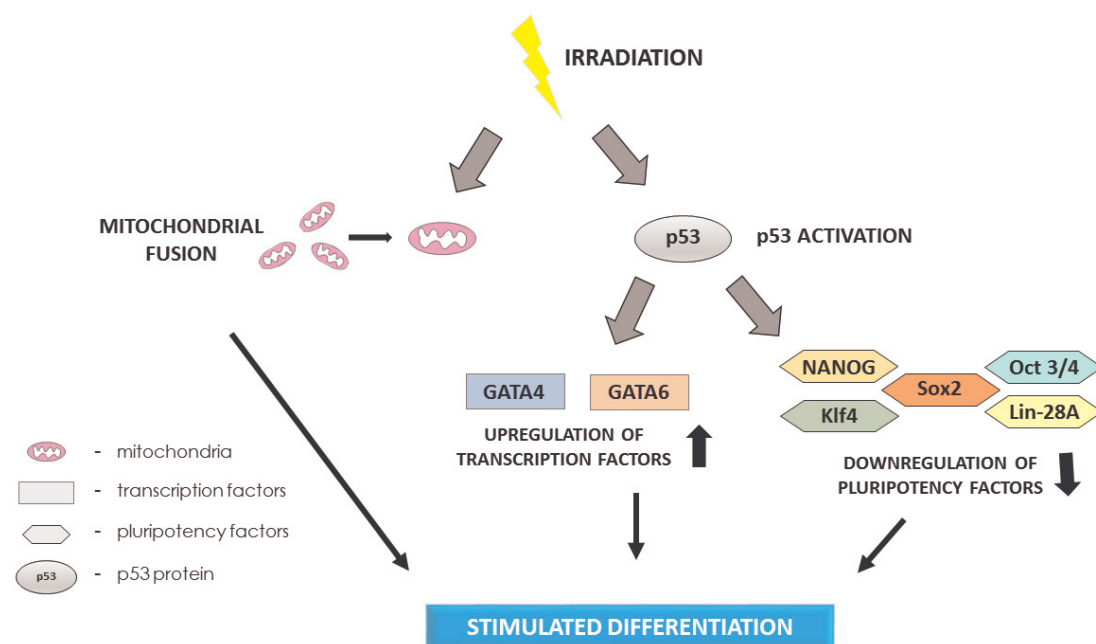
FIGURE 1. The pathway of radiation-enhanced differentiation.

(Figure 1). Ionizing radiation triggers an excessive amount of side effects and does not enable the use of directed differentiation as a sole method in stem cell applications. However, a proper dosage may increase its efficacy while concomitantly reducing its disadvantages. It is important to highlight that despite very efficient mechanisms of DDR in the majority of stem cells, IR bears the risk of introducing genomic instability. Therefore, it is of great importance to define the radiation dose that maximizes the stimulation of differentiation and minimizes the genotoxic effects. The response to irradiation varies between different stem cell types; thus, each type of stem cell requires an independent evaluation of dosage. The deteriorating effects of irradiation could also be partially overcome by the formation of embryoid bodies, which display a significant increase in radioresistance compared to human embryonic stem cells (hESCs). It is also important to note that there are significant discrepancies between murine and human cell models in response to IR (Table 2.); thus, any assumptions based on murine models should be confirmed in human cells.[71] Nonetheless, despite the presence of molecular evidence indicating the probable application to stem cell differentiation methodologies, the concept of radiation-enhanced stem cell differentiation remains to be scientifically proven.

Acknowledgement

References

1. Jones DL, Wagers AJ. No place like home: anatomy and function of the stem cell niche. *Nat Rev Mol Cell Biol* 2008; **9:** 11-21.

2. Tropepe V, Turksen K. The ontogeny of somatic stem cells. *Stem Cell Rev* 2012; **8:** 548-50.

3. Moore K A, Lemischka IR. Stem cells and their niches. *Science* 2006; **311:** 1880-5.

4. Turksen K. Adult stem cells and cardiac regeneration. *Stem Cell Rev* 2013; **9:** 537-40.

5. Takahashi K, Yamanaka S. Induction of pluripotent stem cells from mouse embryonic and adult fibroblast cultures by defined factors. *Cell* 2006; **126:** 663-76.

6. Shi Y, Kirwan P, Livesey FJ. Directed differentiation of human pluripotent stem cells to cerebral cortex neurons and neural networks. *Nat Protoc* 2012; **7:** 1836-46.

7. Lian X, Zhang J, Azarin SM, Zhu K, Hazeltine LB, Bao X, et al. Directed cardiomyocyte differentiation from human pluripotent stem cells by modulating Wnt/β-catenin signaling under fully defined conditions. *Nat Protoc* 2013; **8:** 162-75.

8. Bratt-Leal AM, Carpenedo RL, McDevitt TC. Engineering the embryoid body microenvironment to direct embryonic stem cell differentiation. *Biotechnol Prog* 2009; **25:** 43-51.

9. Kurosawa H. Methods for inducing embryoid body formation: in vitro differentiation system of embryonic stem cells. *J Biosci Bioeng* 2007; **103:** 389-98.

10. Detante O. Intravenous stem cells after ischemic stroke (ISIS). 2014. Available from: http://clinicaltrials.gov/ct2/show/NCT00875654. Accessed 8 March 2015.

11. Vescovi AL. Human neural stem cell transplantation in amyotrophic lateral sclerosis (ALS) (hNSCALS). 2014. Available from: https://clinicaltrials.gov/ct2/show/NCT01640067. Accessed 8 March 2015.

12. Lamo-Espinosa J, Prosper F, Blanco J. Treatment of knee osteoarthritis by intra-articular injection of bone marrow mesenchymal stem cells. 2014. Available from: https://clinicaltrials.gov/ct2/show/NCT02123368. Accessed 8 March 2015.

13. Isa N. Evidence based radiation oncology with existing technology. *Reports Pract Oncol Radiother* 2014; **19:** 259-66.

14. Valerie K, Yacoub A, Hagan MP, Curiel DT, Fisher PB, Grant S, et al. Radiation-induced cell signaling: inside-out and outside-in. *Mol Cancer Ther* 2007; **6:** 789-801.

15. Rodemann HP, Blaese MA. Responses of normal cells to ionizing radiation. *Semin Radiat Oncol* 2007; **17:** 81-8.

16. Paulino AC, Constine LS, Rubin P, Williams JP. Normal tissue development, homeostasis, senescence, and the sensitivity to radiation injury across the age spectrum. *Semin Radiat Oncol* 2010; **20:** 12-20.

17. Schwenke K, Peterson HP, von Wangenheim KH, Feinendegen LE. Radiation-enhanced differentiation of erythroid progenitor cells and its relation to reproductive cell death. *Int J Radiat Biol* 1996; **69:** 309-17.

18. Von Wangenheim KH, Peterson HP, Schwenke K. Review: a major component of radiation action: interference with intracellular control of differentiation. *Int J Radiat Biol* 1995; **68:** 369-88.

19. Fortini P, Ferretti C, Dogliotti E. The response to DNA damage during differentiation: pathways and consequences. *Mutat Res* 2013; **743-744:** 160-8.

20. Nagaria P, Robert C, Rassool F V. DNA double-strand break response in stem cells: mechanisms to maintain genomic integrity. *Biochim Biophys Acta* 2013; **1830:** 2345-53.

21. Rocha CRR, Lerner LK, Okamoto OK, Marchetto MC, Menck CFM. The role of DNA repair in the pluripotency and differentiation of human stem cells. *Mutat Res* 2013; **752:** 25-35.

22. Tichy ED, Pillai R, Deng L, Liang L, Tischfield J, Schwemberger SJ, et al. Mouse embryonic stem cells, but not somatic cells, predominantly use homologous recombination to repair double-strand DNA breaks. *Stem Cells Dev* 2010; **19:** 1699-711.

23. Liu JC, Guan X, Ryan JA, Rivera AG, Mock C, Agrawal V, et al. High mitochondrial priming sensitizes hESCs to DNA-damage-induced apoptosis. *Cell Stem Cell* 2013; **13:** 483-91.

24. Sokolov M V, Neumann RD. Radiation-induced bystander effects in cultured human stem cells. *PLoS One* 2010; **5:** e14195.

25. Lan ML, Acharya MM, Tran KK, Bahari-Kashani J, Patel NH, Strnadel J, et al. Characterizing the radioresponse of pluripotent and multipotent human stem cells. *PLoS One* 2012; **7:** e50048.

26. Adams BR, Golding SE, Rao RR, Valerie K. Dynamic dependence on ATR and ATM for double-strand break repair in human embryonic stem cells and neural descendants. *PLoS One* 2010; **5:** e10001.

27. Blanpain C, Mohrin M, Sotiropoulou PA, Passegué E. DNA-damage response in tissue-specific and cancer stem cells. *Cell Stem Cell* 2011; **8:** 16-29.

28. Mandal PK, Blanpain C, Rossi DJ. DNA damage response in adult stem cells: pathways and consequences. *Nat Rev Mol Cell Biol* 2011; **12:** 198-202.

29. Latella L, Lukas J, Simone C, Puri PL, Bartek J. Differentiation-induced radioresistance in muscle cells. *Mol Cell Biol* 2004; **24:** 6350-61.

30. Mohrin M, Bourke E, Alexander D, Warr MR, Barry-Holson K, Le Beau MM, et al. Hematopoietic stem cell quiescence promotes error-prone DNA repair and mutagenesis. *Cell Stem Cell* 2010; **7:** 174-85.

31. Zheng H, Ying H, Yan H, Kimmelman AC, Hiller DJ, Chen AJ, et al. p53 and Pten control neural and glioma stem/progenitor cell renewal and differentiation. *Nature* 2008; **455**: 1129-33.

32. Bonizzi G, Cicalese A, Insinga A, Pelicci PG. The emerging role of p53 in stem cells. *Trends Mol Med* 2014; **18**: 6-12.

33. Solozobova V, Blattner C. P53 in stem cells. *World J Biol Chem* 2011; **2**: 202-14.

34. Haupt S, Berger M, Goldberg Z, Haupt Y. Apoptosis - the p53 network. *J Cell Sci* 2003; **116**: 4077-85.

35. Yu J, Zhang L. The transcriptional targets of p53 in apoptosis control. *Biochem Biophys Res Commun* 2005; **331**: 851-8.

36. Hong H, Takahashi K, Ichisaka T, Aoi T, Kanagawa O, Nakagawa M, et al. Suppression of induced pluripotent stem cell generation by the p53–p21 pathway. *Nature* 2009; **460**: 1132-5.

37. Menendez S, Camus S, Belmonte JCI. p53: Guardian of reprogramming. *Cell Cycle* 2010; **9**: 3887-91.

38. Tapia N, Schöler HR. P53 connects tumorigenesis and reprogramming to pluripotency. *J Exp Med* 2010; **207**: 2045-8.

39. Zheng H, Ying H, Yan H, Kimmelman AC, Hiller DJ, Chen AJ, et al. p53 and Pten control neural and glioma stem/progenitor cell renewal and differentiation. *Nature* 2008; **455**: 1129-33.

40. Dosch J, Lee CJ, Simeone DM. Cancer stem cells: pancreatic cancer. *Stem Cells Cancer* 2009; **414**: 105-11.

41. Marión RM, Strati K, Li H, Murga M, Blanco R, Ortega S, et al. A p53-mediated DNA damage response limits reprogramming to ensure iPS cell genomic integrity. *Nature* 2009; **460**: 1149-53.

42. Dolezalova D, Mraz M, Barta T, Plevova K, Vinarsky V, Holubcova Z, et al. MicroRNAs regulate p21(Waf1/Cip1) protein expression and the DNA damage response in human embryonic stem cells. *Stem Cells* 2012; **30**: 1362-72.

43. Maimets T, Neganova I, Armstrong L, Lako M. Activation of p53 by nutlin leads to rapid differentiation of human embryonic stem cells. *Oncogene* 2008; **27**: 5277-87.

44. Sabapathy K, Klemm M, Jaenisch R, Wagner EF. Regulation of ES cell differentiation by functional and conformational modulation of p53. *EMBO J* 1997; **16**: 6217-29.

45. Jain AK, Allton K, Iacovino M, Mahen E, Milczarek RJ, Zwaka TP, et al. p53 regulates cell cycle and microRNAs to promote differentiation of human embryonic stem cells. *PLoS Biol* 2012; **10**: e1001268.

46. Okada Y, Shimazaki T, Sobue G, Okano H. Retinoic-acid-concentration-dependent acquisition of neural cell identity during in vitro differentiation of mouse embryonic stem cells. *Dev Biol* 2004; **275**: 124-42.

47. Burridge PW, Keller G, Gold JD, Wu JC. Production of de novo cardiomyocytes: human pluripotent stem cell differentiation and direct reprogramming. *Cell Stem Cell* 2012; **10**: 16-28.

48. Kawaguchi J, Mee PJ, Smith AG. Osteogenic and chondrogenic differentiation of embryonic stem cells in response to specific growth factors. *Bone* 2005; **36**: 758-69.

49. Lin T, Chao C, Saito S, Mazur SJ, Murphy ME, Appella E, et al. p53 induces differentiation of mouse embryonic stem cells by suppressing Nanog expression. *Nat Cell Biol* 2005; **7**: 165-71.

50. Dravid G, Ye Z, Hammond H, Chen G, Pyle A, Donovan P, et al. Defining the role of Wnt/β-catenin signaling in the survival, proliferation, and self-renewal of human embryonic stem cells. *Stem Cells* 2005; **23**: 1489-501.

51. Sato N, Meijer L, Skaltsounis L, Greengard P, Brivanlou AH. Maintenance of pluripotency in human and mouse embryonic stem cells through activation of Wnt signaling by a pharmacological GSK-3-specific inhibitor. *Nat Med* 2004; **10**: 55-63.

52. Taupin P, Gage FH. Adult neurogenesis and neural stem cells of the central nervous system in mammals. *J Neurosci Res* 2002; **69**: 745-9.

53. Galli R, Gritti A, Bonfanti L, Vescovi AL. Neural stem cells: an overview. *Circ Res* 2003; **92**: 598-608.

54. Armesilla-Diaz A, Bragado P, Del Valle I, Cuevas E, Lazaro I, Martin C, et al. p53 regulates the self-renewal and differentiation of neural precursors. *Neuroscience* 2009; **158**: 1378-89.

55. Monje ML, Mizumatsu S, Fike JR, Palmer TD. Irradiation induces neural precursor-cell dysfunction. *Nat Med* 2002; **8**: 955-62.

56. Wei L-C, Ding Y-X, Liu Y-H, Duan L, Bai Y, Shi M, et al. Low-dose radiation stimulates Wnt/β-catenin signaling, neural stem cell proliferation and neurogenesis of the mouse hippocampus in vitro and in vivo. *Curr Alzheimer Res* 2012; **9**: 278-89.

57. Visvader JE, Stingl J, Genes D. Mammary stem cells and the differentiation hierarchy: current status and perspectives. *Genes Dev* 2014; **28**: 1143-58.

58. Shackleton M, Vaillant F, Simpson KJ, Stingl J, Smyth GK, Asselin-Labat ML, et al. Generation of a functional mammary gland from a single stem cell. *Nature* 2006; **439**: 84-8.

59. Dontu G, Abdallah WM, Foley JM, Jackson KW, Clarke MF, Kawamura MJ, et al. In vitro propagation and transcriptional profiling of human mammary stem/progenitor cells. *Genes Dev* 2003; **17**: 1253-70.

60. Cicalese A, Bonizzi G, Pasi CE, Faretta M, Ronzoni S, Giulini B, et al. The tumor suppressor p53 regulates polarity of self-renewing divisions in mammary stem cells. *Cell* 2014; **138**: 1083-95.

61. Ziyaie D, Hupp TR, Thompson AM. P53 and breast cancer. *Breast* 2000; **9**: 239-46.

62. Insinga a, Cicalese a, Faretta M, Gallo B, Albano L, Ronzoni S, et al. DNA damage in stem cells activates p21, inhibits p53, and induces symmetric self-renewing divisions. *Proc Natl Acad Sci U S A* 2013; **110**: 3931-6.

63. Kondo M, Wagers AJ, Manz MG, Prohaska SS, Scherer DC, Beilhack GF, et al. Biology of hematopoietic stem cells and progenitors: implications for clinical application. *Annu Rev Immunol* 2003; **21**: 759-806.

64. Milyavsky M, Gan OI, Trottier M, Komosa M, Tabach O, Notta F, et al. A distinctive DNA damage response in human hematopoietic stem cells reveals an apoptosis-independent role for p53 in self-renewal. *Cell Stem Cell* 2014; **7**: 186-97.

65. Mitra K. Mitochondrial fission-fusion as an emerging key regulator of cell proliferation and differentiation. *Bioessays* 2013; **35**: 955-64.

66. Yakes FM, Van Houten B. Mitochondrial DNA damage is more extensive and persists longer than nuclear DNA damage in human cells following oxidative stress. *Proc Natl Acad Sci* 1997; **94**: 514-9.

67. Kam WW-Y, Banati RB. Effects of ionizing radiation on mitochondria. *Free Radic Biol Med* 2013; **65**: 607-19.

68. Azzam EI, Jay-Gerin JP, Pain D. Ionizing radiation-induced metabolic oxidative stress and prolonged cell injury. *Cancer Lett* 2012; **327**: 48-60.

69. Youle RJ, van der Bliek AM. Mitochondrial fission, fusion, and stress. *Science* 2012; **337**: 1062-5.

70. Nugent SME, Mothersill CE, Seymour C, McClean B, Lyng FM, Murphy JEJ. Increased mitochondrial mass in cells with functionally compromised mitochondria after exposure to both direct γ radiation and bystander factors. *Radiat Res* 2007; **168**: 134-42.

71. Bañuelos CA, Banáth JP, MacPhail SH, Zhao J, Eaves CA, O'Connor MD, et al. Mouse but not human embryonic stem cells are deficient in rejoining of ionizing radiation-induced DNA double-strand breaks. *DNA Repair (Amst)* 2008; **7**: 1471-83.

72. Hanawalt P. Functional characterization of global genomic DNA repair and its implications for cancer. *Mutat Res Mutat Res* 2003; **544**: 107-14.

73. Purschke M, Kasten-Pisula U, Brammer I, Dikomey E. Human and rodent cell lines showing no differences in the induction but differing in the repair kinetics of radiation-induced DNA base damage. *Int J Radiat Biol* 2004; **80**: 29-38.

74. Parrinello S, Samper E, Krtolica A, Goldstein J, Melov S, Campisi J. Oxygen sensitivity severely limits the replicative lifespan of murine fibroblasts. *Nat Cell Biol* 2003; **5**: 741-7.

75. Hornsby PJ. Mouse and human cells versus oxygen. *Sci Aging Knowl Environ* 2003; **2003**: PE21.

76. Wright WE, Shay JW. Telomere dynamics in cancer progression and prevention: fundamental differences in human and mouse telomere biology. *Nat Med* 2000; **6**: 849-51.

77. Hornsby PJ. Replicative senescence of human and mouse cells in culture: significance for aging research. *Mech Ageing Dev* 2003; **124**: 853-5.

review

Gamma-enolase: a well-known tumour marker, with a less-known role in cancer

Tjasa Vizin, Janko Kos

Faculty of Pharmacy, University of Ljubljana, Ljubljana, Slovenia

Background. Gamma-enolase, known also as neuron-specific enolase (NSE), is an enzyme of the glycolytic pathway, which is expressed predominantly in neurons and cells of the neuroendocrine system. As a tumour marker it is used in diagnosis and prognosis of cancer; however, the mechanisms enrolling it in malignant progression remain elusive. As a cytoplasmic enzyme gamma-enolase is involved in increased aerobic glycolysis, the main source of energy in cancer cells, supporting cell proliferation. However, different cellular localisation at pathophysiological conditions, proposes other cellular engagements.

Conclusions. The C-terminal part of the molecule, which is not related to glycolytic pathway, was shown to promote survival of neuronal cells by regulating neuronal growth factor receptor dependent signalling pathways, resulting also in extensive actin cytoskeleton remodelling. This additional function could be important also in cancer cells either to protect cells from stressful conditions and therapeutic agents or to promote tumour cell migration and invasion. Gamma-enolase might therefore have a multifunctional role in cancer progression: it supports increased tumour cell metabolic demands, protects tumour cells from stressful conditions and promotes their invasion and migration.

Key words: gamma-enolase; cancer; glycolysis; cell survival; tumour marker

Introduction

Enolases (EC 4.2.1.11) are intracellular enzymes that catalyse the dehydration of 2-phospho-D-glycerate to phosphoenolpyruvate in the catabolic direction of the glycolytic pathway, a process converting glucose into pyruvate, which enables the formation of high-energy compounds of ATP and NADH. In the anabolic direction during gluconeogenesis, they catalyse the reverse reaction of hydration of phosphoenolpyruvate to 2-phospho-D-glycerate. The glycolytic pathway and its enzymes are one of the most conserved and important metabolic networks in living organisms and therefore, enolases are among the most ubiquitously and abundantly expressed proteins.[1-4] Despite being expressed in most cells, the gene that encodes for enolase is not a housekeeping gene since its expression varies during several developmental, metabolic or pathophysiological conditions.[5] In addition to their innate glycolytic function, many enzymes of the glycolytic pathway, including enolase, were shown to possess various specific regulatory functions and to play a pleiotropic role in physiological and pathological processes, including cancer.[1,2,6,7] In this paper we review the properties, distribution and function of gamma-enolase and its role in enhanced glycolysis and proliferation of tumour cells. Additionally, we expose new mechanisms through which gamma-enolase may promote cancer progression: aiding adaptation of tumour cells to stressful conditions by activating survival promoting signalling pathways and promoting migration of tumour cells. Finally, we discuss the role of gamma-enolase as a marker of exposure to carcinogenic pollutants and review the diagnostic and prognostic utility of gamma-enolase in cancer patients.

Properties and distribution of enolase

Enolases are functionally active as dimers, composed of non-covalently linked subunits alpha- (α), beta- (β) and gamma- (γ), facing each other in an antiparallel fashion, which may form five homodimeric or heterodimeric isoenzymes, expressed in a development and tissue-specific manner. The isoenzyme $\alpha\alpha$ (alpha-enolase) is localized in all foetal and in the majority of adult mammal tissues. During tissue development, it is replaced by other isoforms: in skeletal and heart muscles by αβ and ββ (beta-enolase), and in neuronal cells and cells of the diffuse neuroendocrine system by isoenzymes $\alpha\gamma$ and $\gamma\gamma$ (gamma-enolase). In mammals, each of the three isoenzymes is encoded by an independent loci.[8,9] All enolase isoforms have a molecular range between 82 and 100 kDa and share high sequence identity and kinetic properties.[1,6,10-12] However, each isoform possesses characteristic short variable regions, which are situated predominantly on the surface of the molecule and might be the sites of contact with different cytoskeleton elements or other cell components.[13]

Besides the peptide molecule, enolase requires a divalent metal ion for its stabilisation and catalytic activity. Six divalent metals have been demonstrated to activate enolase: Mg^{2+}, Zn^{2+}, Cd^{2+}, Co^{2+}, Mn^{2+} and Ni^{2+}. The most abundant is Mg^{2+}, which provides the highest activation strength.[1,14,15] The metal ion is not firmly bound into the protein part of the molecule; therefore enolase is not a typical metalloenzyme, but defined as a "metal-ion-activated enzyme complex".[16] Enolase has two binding sites for Mg^{2+}, both contributing to catalysis: binding to the first site, Mg^{2+} induces conformational changes of the active site enabling the binding of the substrates, whereas the binding of a second Mg^{2+} is an essential part of the catalytic apparatus.[1,17-19]

Enolase localizes predominantly in the cytosol however, variations in cellular localisation were observed for all three enolase isoforms. Alpha-enolase was observed in the nucleus, on the cell surface and in extracellular space. It may interact with different cytoplasmic, nuclear and membrane molecules and exhibits several other functions besides catalysis.[1,20] The nuclear form of alpha-enolase was recognized as Myc promoter-binding protein-1 (MBP-1), an alternative splicing form involved in regulation of transcription by repressing the function of Myc and acting as a tumour suppressor.[6,21-23] Alpha-enolase localizes also on cell surface of neuronal, endothelial and hematopoietic cells as well on pancreatic, breast and lung cancer cells. Its surface expression was shown to depend on the pathophysiological conditions of the cells and its C-terminal lysine residue acts as a plasminogen-binding receptor modulating pericellular fibrinolytic activity and promoting migration and metastasis of cancer cells. The cell surface alpha-enolase is catalytically active, maintaining its active dimeric form. Alpha-enolase was shown also to be secreted from cells by exosomes, cell derived vesicles, proposed to play an important role in intercellular communication.[23-25] However, the mechanisms of surface translocation, membrane attachment, cell surface expression or secretion remain unknown.[6,26-32] The properties and function of alpha-enolase in malignant disease have been extensively studied and reviewed.[1,2,6,20,23]

Different subcellular localisation and interactions with other proteins were observed also for beta-enolase during maturation, normal function and regeneration of muscles. Specific interactions with macromolecules may address beta-enolase to the subcellular site where ATP, produced through glycolysis, is most needed for muscular contraction or regeneration.[33-35] Increased expression of beta-enolase was detected in rhabdomyosarcoma tissue, which is, to our knowledge, the only evidence that this isoform might be involved in cancer.[36,37]

Gamma-enolase

Gamma-enolase, is a 433 amino acid long acidic dimeric protein, which includes two enolase isoenzymes, $\gamma\gamma$ and $\alpha\gamma$, and is also referred as neuron-specific enolase (NSE). The subunit molecular mass is approximately 39 kDa, whereas Mr of the native form is 78 kDa which might vary on the subunit combination. Gamma-enolase localizes predominantly in neuronal cells and in neuroendocrine cells, particularly in those of the amine precursor uptake and decarboxylation (APUD) lineage, for example in the intestine, lung, thyroid and pituary gland and pancreas.[8,38] It is found in lower amounts also in non-neuronal and non-neuroendocrine tissues or cells, such as erythrocytes, platelets, breast tissue, prostate and uterus.[39-41] The $\gamma\gamma$ isoform is found predominantly in mature neurons and is also used as marker of neuronal maturation and differentiation, while the $\alpha\gamma$ isoenzyme localizes in higher amounts in non-neuronal cells.[8,9]

The C-terminal end of gamma-enolase contains a PDZ-binding motif (431S-433L: SVL) (Figure 1), which might enable an interaction with several

proteins that contain a PDZ-domain and are involved in intracellular redistribution of molecules and signalling pathway events. Different gamma-enolase cellular localisation, which depends on the pathophysiological conditions of the cells, propose other cellular engagement besides glycolysis. In neuronal, glial and astrocytic cells, gamma-enolase was shown to associate with the plasma membrane, or even appear on the surface of cells[42-45], which might occur through its hydrophobic domain in the N-terminal region (32A-43Y: AAVPSGASTGIY). Also, on the cell surface alpha-enolase may bind to plasminogen by C-terminal lysine.[46] In contrast to alpha-enolase, gamma-enolase has no C-terminal lysine and does not bind plasminogen; therefore it might exert other functions on cell surface.[43,46-48] Gamma-enolase was detected also in the nucleus of malignantly transformed urothelial and epithelial breast cells and in glioblastoma cells; however its role remains unknown.[40,49-51] Significantly higher increase of gamma-enolase antigen levels than its catalytic activity was observed during exponential growth of small-cell lung cancer cells, proposing that cellular gamma-enolase exists also as an enzymatically inactive compound, that might possess other functions.[52]

FIGURE 1. Position of gamma-enolase catalytical active site and the PDZ-binding motif containing C-terminal end. Subunits of the γγ-dimer are represented by separate colours (wheat and violet). The orange part represents the catalytical active site, yellow balls represent Mg^{2+} ions and the magenta part represents the C-terminal end of the molecule (the last 6 amino acids). For better representation, active site and C-terminal end are shown only in one subunit. The image was created using PyMOL (DeLano LLC Scientific). Gamma-enolase crystal structure (1TE6) was obtained from Protein Data Bank (PDB). The image was prepared by authors and has not been published elsewhere.

The function of gamma-enolase in increased glycolysis in cancer

It is generally known that glycolysis is drastically enhanced in tumour cells and is a hallmark of cancer progression.[53,54] In tumours that outgrow its feeding circulation, cells are exposed to an environment with poor oxygen and nutrients supply[50], which leads to a prevalence of aerobic glycolysis over mitochondrial oxidative phosphorylation.[55-57] This metabolic switch referred also to as the Warburg effect, enables tumour cells to produce energy to survive and eventually proliferate regardless the presence of oxygen. Glycolysis alone, however, is energetically less efficient than oxidative phosphorylation. Therefore, reactions of the glycolytic pathway have to be drastically accelerated to satisfy the higher metabolic needs of proliferating tumour cells, which is evident from a net increase in glucose consumption and higher expression of glycolytic enzymes.[55,58-60]

Gamma-enolase is overly-expressed in tumours[39] and its major contribution to tumour progression is, no doubt, the participation to accelerated glycolysis of cancer cells. For instance, malignant transformation of astrocytic[61], breast[40] and urothelial cells[49]

led to occurrence of gamma-enolase in originally gamma-enolase-negative cells and to colony formation and proliferation, which strongly suggests that transformed cells might obtain the ability to express gamma-enolase in order to adapt to increased metabolic needs of a neoplastic state.[61,62] Further, malignantly transformed urothelial cells, which were able to proliferate and form tumours when inoculated into immune compromised mice, were shown to express higher levels of gamma-enolase, compared to less active and differentiated cells. Authors proposed that cells, which express gamma-enolase at higher rates, might have an advantage in tumour initiation and subsequent growth.[49] Gamma-enolase was significantly up-regulated also in glioblastoma cells exposed to hypoxia and serum starvation, and additionally, its knock-down significantly diminished cell growth[50], supporting the findings that the dependence of tumour cell growth on glycolysis is even more emphasized in stressful conditions.[55,60,63] Finally, in non-small cell lung cancer cells, an alternative splicing form of c-H-ras, p19[ras], was shown to specifically bind gamma-enolase and inhibit its enzymatic activity, resulting in diminished cell proliferation.[58] The glycolytic function of gamma-enolase and its impact on promoting tumour cell growth represents a promising target for cancer therapy.[64]

The pro-survival function of gamma-enolase in cancer

Gamma-enolase was shown to act as a neurotropic factor in neuronal cells.[7,65,66] This function is manifested through an additional active site, which is not a part of the catalytical apparatus involved in glycolysis, but localized at the C-terminal end of the molecule. For instance, a 30 amino acid long peptide, mimicking the C-terminal part of gamma-enolase, was shown to promote survival, differentiation and regeneration of neurons by activating signal transduction pathways which are normally triggered by the activation of Trk receptor: phosphatidylinositol 3-kinase (PI3K) and mitogen-activated protein kinase (MAPK) pathways. Additionally, the C-terminal peptide of gamma-enolase was demonstrated to impair apoptosis and to interact with p75 neurotrophin receptor (p75[NTR]) and suppress the activation of its downstream effectors in apoptotic signalling. Despite having similar amino acid sequence in the C-terminal part, other enolase isoforms do not show a neurotropic function.[7,43,46,67-69] Gamma-enolase neurotrophic effect is regulated by cathepsin X, a cysteine carboxymonopeptidase, which is frequently expressed in neuronal and glial cells.[70,71] Cathepsin X was shown to sequentially cleave the final two amino acids (433L and 432V) at the C-terminal end of gamma-enolase and to disrupt the PDZ motif, through which gamma-enolase binds to the scaffold protein gamma-1-syntrophin. The latter mediates the translocation of gamma-enolase and its association with plasma membrane, which is a prerequisite for neurotrophic activity.[43,46] Therefore, only C-terminally uncleaved gamma-enolase has a pro-survival activity. The protective function of gamma-enolase was observed also in brains of a mouse model of Alzheimer disease (Tg2576): C-terminally truncated gamma-enolase localized in immediate plaque vicinity and strongly colocalized with cathepsin X, while uncleaved gamma-enolase exhibiting neuroprotective activity, localized in microglia cells in close proximity of senile plaques. Additionally, using a mouse microglial cell model, gamma-enolase was shown to protect neuronal cells from amyloid-β peptide toxicity and cathepsin X reversed its function.[66]

Gamma-enolase has been proposed to act as a pro-survival factor also in cancer cells. It was shown to support glioblastoma cell adaptation to cellular stress, such as serum starvation, hypoxia, chemotherapy and radiotherapy; however, no specific mechanism has yet been proposed.[50] Both, starvation and hypoxia have been linked to progression of
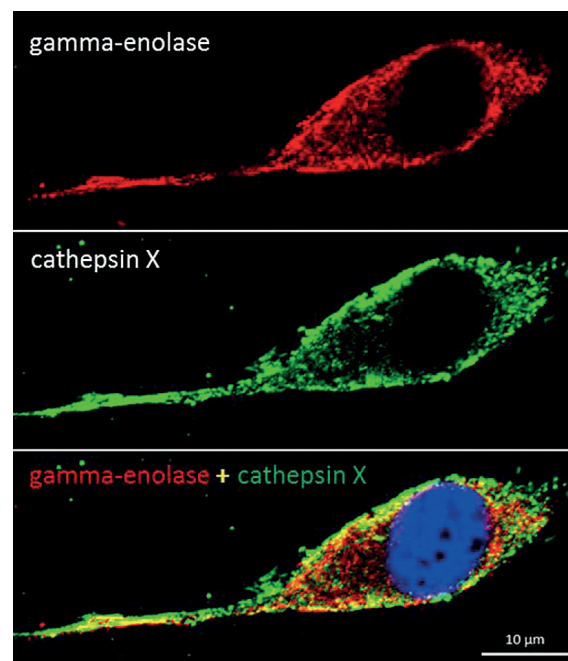
FIGURE 2. Co-localization of gamma-enolase and cathepsin X in human glioblastoma cells U87-MG grown in serum-free medium for 72 h. U87-MG cells were grown in Eagle´s Minimum Essential Medium (EMEM, Sigma), supplemented with 10% (v/v) foetal bovine serum (HyClone), 1% L-glutamine (Sigma) and 1% penicillin/streptomycin (Sigma) at 37°C and humidified atmosphere with 5% CO_2. For protein visualization, cells were seeded on glass coverslips at a concentration of 1 x 10⁴ cells/ml in 24 well plates. After 24 h, complete growth medium was replaced with serum-free medium and cells were left to grow for additional 72 h. After treatment cells were fixed with 10% formalin for 30 min at room temperature and then permeabilized by 0.5% Tween®20 in phosphate buffered saline (PBS), pH 7.4 for 10 min. Non-specific binding was blocked with 3% bovine serum albumin (BSA) in PBS, pH 7.4 for 1.5 h at room temperature. Cells were then incubated with primary antibody against N-terminal end of gamma-enolase (10 μg/ml, goat polyclonal, Santa Cruz Biotechnology) and active cathepsin X (10 μg/ml, mouse monoclonal, 2F12) in 3% BSA in PBS pH 7.4 for 2 h at room temperature. After three washes with PBS, pH 7.4, cells were incubated with Alexa Fluor 555 donkey anti-goat (Molecular Probes™) and Alexa Fluor 488 donkey anti-mouse (Molecular Probes™) secondary antibody in 3% BSA in PBS, pH 7.4. After washing with PBS, ProLong® Gold Antifade Mountant with 4',6-diamidino-2-phenylindole, dilactate (DAPI, Molecular Probes™) was used to mount coverslips on glass slides. Fluorescence microscopy was performed by Carl Zeiss LSM 710 confocal microscope (Carl Zeiss Oberkochen) with ZEN 2012 image software. Gamma-enolase (red) and cathepsin X (green) staining showed co-localisation in the perimembrane region. The blue staining with DAPI represents the nucleus. The image was prepared by authors and has not been published elsewhere.

cancer and resistance to treatment by inducing biological changes in tumour cells, one of them being increased glycolysis.[55,60,72] However, C-terminally uncleaved gamma-enolase might additionally support tumour cell adaptation to stressful conditions

by activating survival promoting signalling pathways as it does in neuronal cells, and cathepsin X, which is present also in tumour cells[71], might regulate its function (Figure 2). For instance, in glioblastoma cell lines, exposed to serum starvation or hypoxia, gamma-enolase expression was significantly increased[50]; moreover, significant increases in protein and phosphoprotein levels were observed also in PI3K/Akt and MAPK/ERK and anti-apoptotic signalling pathways[73,74], which are triggered by gamma-enolase in neuronal cells. Separate analysis of expression and role of C-terminally uncleaved and truncated gamma-enolase in cancer cells and tumour tissue might provide new information on its involvement in tumour progression.

The role of gamma-enolase in migration of tumour cells

Recently, a study on glioma cells showed that gamma-enolase knockdown significantly reduced migration of cells; however, no specific mechanism has been proposed.[75] An important prerequisite for cell migration is a dynamic remodelling of actin cytoskeleton. Remodelling is stimulated by several molecules that link migratory signals to the actin filaments and are upregulated in invasive and metastatic cancer cells.[76] In neuroblastoma cells, gamma-enolase was shown to co-localize with actin filaments, an interaction that depends on the presence of gamma-1-syntrophin.[43] Additionally, gamma-enolase C-terminal peptide was shown to regulate RhoA kinase, a regulator of actin cytoskeleton organization. Consequently, gamma-enolase induced actin polymerisation and its redistribution to growth cones of neurites.[68] Similarly, alpha-enolase was shown to bind to actin and tubulin[77] and to mediate invasiveness of tumour cells[78] and sensitivity to microtubule targeted drugs.[79] These results provide evidence, that gamma-enolase might be involved in migration of tumour cells through interactions with actin filaments and regulation of RhoA kinase function.

Gamma-enolase as a marker of exposure to environmental carcinogenic pollutants arsenic and cadmium

Arsenic and cadmium exposure is linked to breast and bladder cancer occurrence. Exposure of breast epithelial and urothelial cells to As^{3+} or Cd^{2+} was shown to induce malignant transformation of cells and an increase of mRNA and protein levels of gamma-enolase in the cytoplasm and nucleus of cells, while expression of alpha-enolase did not change. Authors proposed that gamma-enolase might be translated as a possible biomarker for chronic environmental exposure to As^{3+} or Cd^{2+}. Its expression in non-malignant cells was influenced also by methylation and histone modifications, induced by a histone deacetylase inhibitor (MS-275) and a methylation inhibitor (5-AZC), which proposed that gamma-enolase gene expression is controlled by methylation and histone modifications. The later provides evidence that environmental carcinogenic pollutants, such as cadmium and arsenic, might cause changes in epigenetic regulation of genes, which specifically affect the expression and function of gamma-enolase in breast epithelial cells and urothelial cells.[40,49]

Gamma-enolase in tumour tissues

Gamma-enolase is typically overexpressed in tumours of neurogenic and neuroendocrine origin and has been used as a marker for detection of neuroendocrine differentiation of tumour cells. It is considered the most important tumour marker for poorly differentiated neuroendocrine tumours, since a tumour is classified as a neuroendocrine tumour only when it expresses at least two neuroendocrine markers of which one is gamma-enolase.[80,81] Immunohistochemistry of gamma-enolase is regularly used for differential diagnosis of small-cell lung cancer (SCLC) from other lung cancer histological subtypes (Table 1).[82,83] Gamma-enolase increased expression was observed also in other tumours, including breast cancer, with increased staining in lymph node metastases compared to primary breast tumours[84] or in glioblastomas, with higher levels in advanced stage tumours, which were related to shorter patient survival.[50] Nevertheless, immunostaining of gamma-enolase in tumour tissue has limited diagnostic or prognostic utility, since many clinical studies provided contradictory results.[80,85-87]

Gamma-enolase in extracellular fluids of cancer patients

In general, gamma-enolase serum levels are better indicators than its tissue expression (Table 1).[80]

TABLE 1. Use of gamma-enolase as a tumour marker

	Neuroendocrine cancer	Proposed use	Use in clinical practice	Recommendations	Reference
Tumour tissues	SCLC	Differential diagnosis from other lung cancer subtypes	Yes	EGTM, NACB	[82, 83]
	Other neuroendocrine tumours (neuroblastoma, endocrine pancreatic tumours, seminoma, medullary thyroid carcinoma, phaeochromocytoma, ect.)	Diagnosis or detection of neuroendocrine differentiation of tumour	Yes		[80, 81, 95, 96]
Serum	SCLC	Differential diagnosis from other lung cancer subtypes when biopsy is not possible	Yes	EGTM, NACB	[82, 83]
		Prognosis	Unknown		[82, 83, 97]
		Post-operative surveillance	Yes	EGTM, NACB	[82, 83]
		Monitoring efficacy of therapy	Yes	EGTM, NACB	[82, 83]
		Detection of recurrent disease after primary surgery	Yes	NACB	[82, 83]
	NSCLC	Monitoring therapy in advanced disease	No		[83]
		Prognosis	Unknown		[83]
	Testicular cancer (seminoma)	Diagnosis	Experimental	EGTM	[98]
	Carcinoids	Diagnosis	Unknown		[96, 99]
		Monitoring efficacy of therapy	Yes	EGTM	[8, 39]
		Detection of early relapse	Yes		[8, 39, 96]
	Medullary thyroid carcinomas	Monitoring efficacy of therapy	Yes	EGTM	[8, 39]
		Detection of early relapse	Yes		[8, 39]
	Phaeochromocytoma	Monitoring efficacy of therapy	Yes	EGTM	[8, 39]
		Detection of early relapse	Yes		[8, 39]
	Endocrine pancreatic tumours	Diagnosis	Yes		[95, 96]
		Monitoring efficacy of therapy	Yes	EGTM	[8, 39]
		Detection of early relapse	Unknown		[8, 39, 99]
	Paraganglioma	Diagnosis	Unknown		[99]
	Neuroblastoma	Differential diagnosis	Unknown		[8]
		Prognosis	Yes	ACS	[100]
		Monitoring efficacy of therapy	Yes	EGTM	[8, 100]
		Detection of recurrent disease	Yes		[97]

ACS = American Cancer Society; EGTM = European Group for Tumour Markers; NACB = National Academy of Clinical Biochemistry; NSCLC = non-small-cell lung cancer; SCLC = small-cell lung cancer

Levels of gamma-enolase are elevated in sera from patients with various cancers, however, its appearance in extracellular fluids without any apparent cellular damage is not clear.[1,88] After stroke, brain injury or cardiac arrest, gamma-enolase is released into the cerebrospinal fluid and eventually into the bloodstream due to damage or death of neuronal cells or impairment of the blood-brain barrier in-

tegrity. For instance, levels of gamma-enolase in cerebrospinal fluid and serum have been used as a biomarker of cerebral injury and for the assessment of neurological disorders.[38,89,90] Gamma-enolase is the only neuroendocrine tumour marker, which is used as a serum marker for follow up and monitoring of therapy effectiveness. Increased gamma-enolase levels in extracellular fluids are related to cancer progression and are typical for cancer in advances stages with distant metastases.[8,39,80,84-87] The levels of gamma-enolase in non-treated cancer increase proportionally to the tumour mass, stage and number of metastases and are related to worse prognosis, however, the levels are not related to the location of metastases.[39]

Gamma-enolase is used in clinical practice in patients with SCLC and neuroblastoma. Its levels are significantly elevated compared to healthy subjects; however, specificity and sensitivity are too low to be used in screening.[39,91] According to the recommendations of expert groups for the use of markers in lung cancer, gamma-enolase is recommended as an auxiliary marker in SCLC for differential diagnosis when biopsy is not possible and when other neuroendocrine tumours are excluded. Further, it is recommended for SCLC postoperative surveillance, for monitoring of therapy in advanced disease and for detection of recurrent disease.[83,91] During chemotherapy, a transient rise of gamma-enolase serum levels occurs due to cytolysis of tumour cells, which disappears in case of successful treatment. However, persistently elevated levels show unsuccessful therapy. Gamma-enolase is not a recommended tumour marker in neuroblastoma; however, it is frequently used for differential diagnosis of neuroblastoma from nefroblastoma and for disease monitoring.[8,91]

Gamma-enolase is used as an auxiliary serum marker for follow-up and monitoring of therapy effectiveness in patients with carcinoids, melanoma, seminoma, feocromocitoma, medullary thyroid carcinoma, and endocrine pancreatic tumours. In patients with brain tumours, the levels of gamma-enolase in sera are not elevated, however, increased levels were reported in cerebrospinal fluid.[39,91]

Increased serum levels of gamma-enolase were reported also in patients with cancers of non-neuroendocrine origin, such as T-cell leukaemia[92], B-cell lymphoma[93] and malignant melanoma.[94] In general, higher serum levels of gamma-enolase are related to worse prognosis and are the highest in patients with advanced metastatic stage.[39]

Gamma-enolase is usually measured in serum samples and less frequently in cerebrospinal fluid, pleural exudate or ascites. Its half-life in serum is estimated to be approximately 30 h.[101] The $\alpha\gamma$ isoform is expressed in large amounts also in erythrocytes and in platelets, therefore it is important to separate blood cells from plasma or serum within 60 minutes from sample collection to prevent haemolysis of blood samples, which could lead to falsely elevated levels of gamma-enolase.[80,102,103] Falsely elevated serum levels of gamma-enolase might be also due to various noncancerous pathological causes[104], such as benign pulmonary diseases[105], renal failure[106], brain injuries, seizures, stroke[38,107], severe hypoglycaemia[108], benign liver diseases[109] or systemic sclerosis.[110]

Concluding remarks

Glycolytic enzymes were shown to exert various specific regulatory functions and to play a pleiotropic role in physiological and pathological processes. Therefore, their participation to accelerated glycolysis could not be the only contribution to tumour progression.[2] Alpha-enolase, the most exhaustively studied enolase isoform, was found to be one of the most frequently altered proteins in human pathologies and suggested as a universal cellular sensor that responds to multiple stimuli and reacts through multiple mechanisms.[6,111] Gamma-enolase, sharing high-sequence identity with alpha-enolase, is also emerging as a multifunctional molecule. Different cellular localisation and interactions with other molecules strongly suggest its multiple cellular engagements.

Gamma-enolase primary role in cancer is the participation to the accelerated glycolysis, which supports increased tumour cell metabolic demands and enables their proliferation. Its C-terminal end might protect tumour cells from stressful conditions and action of therapeutic agents by activating survival-promoting signalling pathways and regulating apoptosis. An additional role of gamma-enolase in cancer progression is its involvement in actin remodelling and consequently in promotion of migration and invasion of tumour cells. These findings suggest that the role of this well-known tumour marker, whose expression is altered during development and progression of a variety of cancers, is pleiotropic and still has to be defined. Future work should be focused on elucidation of gamma-enolase cellular redistribution, interactions with other molecules and involvement in cell signalling. Understanding these processes, together with the tools enabling effective inhibition of

gamma-enolase glycolytic activity, might provide new opportunities for cancer treatment.

Acknowledgements

References

1. Pancholi V. Multifunctional alpha-enolase: its role in diseases. *Cell Mol Life Sci* 2001; **58:** 902-20.

2. Kim JW, Dang CV. Multifaceted roles of glycolytic enzymes. *Trends Biochem Sci* 2005; **30:** 142-50.

3. Masoudi-Nejad A, Asgari Y. Metabolic cancer biology: Structural-based analysis of cancer as a metabolic disease, new sights and opportunities for disease treatment. *Semin Cancer Biol* 2015; **30:** 21-9.

4. Dang CV, Semenza GL. Oncogenic alterations of metabolism. *Trends Biochem Sci* 1999; **24:** 68-72.

5. McAlister L, Holland MJ. Targeted deletion of a yeast enolase structural gene. Identification and isolation of yeast enolase isozymes. *J Biol Chem* 1982; **257:** 7181-8.

6. Diaz-Ramos A, Roig-Borrellas A, Garcia-Melero A, Lopez-Alemany R. Alpha-enolase, a multifunctional protein: its role on pathophysiological situations. *J Biomed Biotechnol* 2012; **2012:** 156795.

7. Hattori T, Takei N, Mizuno Y, Kato K, Kohsaka S. Neurotrophic and neuro-protective effects of neuron-specific enolase on cultured neurons from embryonic rat brain. *Neurosci Res* 1995; **21:** 191-8.

8. Suresh MR. Cancer Markers. In: Wild D, editor. *The immunoassay handbook*. Third edition. Oxford, UK: Elsevier; 2005. p. 664-94.

9. Marangos PJ, Parma AM, Goodwin FK. Functional properties of neuronal and glial isoenzymes of brain enolase. *J Neurochem* 1978; **31:** 727-32.

10. Fletcher L, Rider CC, Taylor CB. Enolase isoenzymes: III. Chromatographic and immunological characteristics of rat brain enolase. *Biochim Biophys Acta* 1976; **452:** 245-52.

11. Giallongo A, Feo S, Moore R, Croce CM, Showe LC. Molecular cloning and nucleotide sequence of a full-length cDNA for human alpha enolase. *Proc Natl Acad Sci U S A* 1986; **83:** 6741-5.

12. Feo S, Oliva D, Barbieri G, Xu WM, Fried M, Giallongo A. The gene for the muscle-specific enolase is on the short arm of human chromosome 17. *Genomics* 1990; **6:** 192-4.

13. Lebioda L, Stec B. Mapping of isozymic differences in enolase. *Int J Biol Macromol* 1991; **13:** 97-100.

14. Faller LD, Johnson AM. Calorimetric studies of the role of magnesium ions in yeast enolase catalysis. *Proc Natl Acad Sci U S A* 1974; **71:** 1083-7.

15. Brewer JM. Specificity and mechanism of action of metal ions in yeast enolase. *FEBS Letters* 1985; **182:** 8-14.

16. Vallee BL. Zinc and metalloenzymes. *Adv Protein Chem* 1955; **10:** 317-84.

17. Faller LD, Baroudy BM, Johnson AM, Ewall RX. Magnesium ion require-ments for yeast enolase activity. *Biochemistry* 1977; **16:** 3864-9.

18. Brewer JM. Yeast enolase: mechanism of activation by metal ions. *CRC Crit Rev Biochem* 1981; **11:** 209-54.

19. Brewer JM, Ellis PD. 31P-nmr studies of the effect of various metals on substrate binding to yeast enolase. *J Inorg Biochem* 1983; **18:** 71-82.

20. Ko-Jiunn L, Neng-Yao S. The role of enolase in tissue invasion and metasta-sis of pathogens and tumor cells. *J Cancer Mol* 2007; **3:** 45-8.

21. Ghosh AK, Steele R, Ray RB. Functional domains of c-myc promoter binding protein 1 involved in transcriptional repression and cell growth regulation. *Mol Cell Biol* 1999; **19:** 2880-6.

22. Feo S, Arcuri D, Piddini E, Passantino R, Giallongo A. ENO1 gene product binds to the c-myc promoter and acts as a transcriptional repressor: re-lationship with Myc promoter-binding protein 1 (MBP-1). *FEBS Lett* 2000; **473:** 47-52.

23. Capello M, Ferri-Borgogno S, Cappello P, Novelli F. Alpha-Enolase: a promis-ing therapeutic and diagnostic tumor target. *FEBS J* 2011; **278:** 1064-74.

24. Mears R, Craven RA, Hanrahan S, Totty N, Upton C, Young SL, et al. Proteomic analysis of melanoma-derived exosomes by two-dimensional polyacrylamide gel electrophoresis and mass spectrometry. *Proteomics* 2004; **4:** 4019-31.

25. Yu X, Harris SL, Levine AJ. The regulation of exosome secretion: a novel function of the p53 protein. *Cancer Res* 2006; **66:** 4795-801.

26. Cappello P, Tomaino B, Chiarle R, Ceruti P, Novarino A, Castagnoli C, et al. An integrated humoral and cellular response is elicited in pancreatic cancer by alpha-enolase, a novel pancreatic ductal adenocarcinoma-associated antigen. *Int J Cancer* 2009; **125:** 639-48.

27. He P, Naka T, Serada S, Fujimoto M, Tanaka T, Hashimoto S, et al. Proteomics-based identification of alpha-enolase as a tumor antigen in non-small lung cancer. *Cancer Sci* 2007; **98:** 1234-40.

28. Seweryn E, Pietkiewicz J, Bednarz-Misa IS, Ceremuga I, Saczko J, Kulbacka J, et al. Localization of enolase in the subfractions of a breast cancer cell line. *Z Naturforsch C* 2009; **64:** 754-8.

29. Nakajima K, Hamanoue M, Takemoto N, Hattori T, Kato K, Kohsaka S. Plasminogen binds specifically to alpha-enolase on rat neuronal plasma membrane. *J Neurochem* 1994; **63:** 2048-57.

30. Miles LA, Dahlberg CM, Plescia J, Felez J, Kato K, Plow EF. Role of cell-sur-face lysines in plasminogen binding to cells: identification of .alpha.-eno-lase as a candidate plasminogen receptor. *Biochemistry* 1991; **30:** 1682-91.

31. Dudani AK, Cummings C, Hashemi S, Ganz PR. Isolation of a novel 45 kDa plasminogen receptor from human endothelial cells. *Thromb Res* 1993; **69:** 185-96.

32. Redlitz A, Fowler BJ, Plow EF, Miles LA. The role of an enolase-related molecule in plasminogen binding to cells. *Eur J Biochem* 1995; **227:** 407-15.

33. Merkulova T, Lucas M, Jabet C, Lamandé N, Rouzeau JD, Gros F, et al. Biochemical characterization of the mouse muscle-specific enolase: de-velopmental changes in electrophoretic variants and selective binding to other proteins. *Biochem J* 1997; **323:** 791-800.

34. Keller A, Demeurie J, Merkulova T, Geraud G, Cywiner-Golenzer C, Lucas M, et al. Fibre-type distribution and subcellular localisation of alpha and beta enolase in mouse striated muscle. *Biol Cell* 2000; **92:** 527-35.

35. Merkulova T, Dehaupas M, Nevers MC, Créminon C, Alameddine H, Keller A. Differential modulation of alpha, beta and gamma enolase isoforms in regenerating mouse skeletal muscle. *Eur J Biochem* 2000; **267:** 3735-43.

36. Royds JA, Variend S, Timperley WR, Taylor CB. An investigation of beta enolase as a histological marker of rhabdomyosarcoma. *J Clin Pathol* 1984; **37:** 905-10.

37. Royds JA, Variend S, Timperley WR, Taylor CB. Comparison of beta enolase and myoglobin as histological markers of rhabdomyosarcoma. *J Clin Pathol* 1985; **38:** 1258-60.

38. Tiainen M, Roine RO, Pettila V, Takkunen O. Serum neuron-specific enolase and S-100B protein in cardiac arrest patients treated with hypothermia. *Stroke* 2003; **34:** 2881-6.

39. Lamerz R. NSE (neuron-specific enolase) γ-enolase. In: Thomas L, editor. *Clinical laboratory diagnostics: use and assessment of clinical laboratory re-sults.* 1st. edition. Frankfurt/Main, Germany: TH-Books Verlagsgesellschaft; 1998. p. 979-81.

40. Soh MA, Garrett SH, Somji S, Dunlevy JR, Zhou XD, Sens MA, et al. Arsenic, cadmium and neuron specific enolase (ENO2, γ-enolase) expression in breast cancer. *Cancer Cell Int* 2011; **11:** 41.

41. Haimoto H, Takahashi Y, Koshikawa T, Nagura H, Kato K. Immunohistochemical localization of gamma-enolase in normal human tissues other than nervous and neuroendocrine tissues. *Lab Invest* 1985; **52:** 257-63.

42. Vinores SA, Herman MM, Rubinstein LJ. Electron-immunocytochemical localization of neuron-specific enolase in cytoplasm and on membranes of primary and metastatic cerebral tumours and on glial filaments of glioma cells. *Histopathology* 1986; **10:** 891-908.

43. Hafner A, Obermajer N, Kos J. gamma-1-syntrophin mediates trafficking of gamma-enolase towards the plasma membrane and enhances its neurotrophic activity. *Neurosignals* 2010; **18:** 246-58.

44. Burack WR, Shaw AS. Signal transduction: hanging on a scaffold. *Curr Opin Cell Biol* 2000; **12:** 211-6.

45. Ponting CP, Phillips C, Davies KE, Blake DJ. PDZ domains: targeting signalling molecules to sub-membranous sites. *Bioessays* 1997; **19:** 469-79.

46. Obermajer N, Doljak B, Jamnik P, Fonovic UP, Kos J. Cathepsin X cleaves the C-terminal dipeptide of alpha- and gamma-enolase and impairs survival and neuritogenesis of neuronal cells. *Int J Biochem Cell Biol* 2009; **41:** 1685-96.

47. McAleese SM, Dunbar B, Fothergill JE, Hinks LJ, Day IN. Complete amino acid sequence of the neurone-specific gamma isozyme of enolase (NSE) from human brain and comparison with the non-neuronal alpha form (NNE). *Eur J Biochem* 1988; **178:** 413-7.

48. Butterfield DA, Lange ML. Multifunctional roles of enolase in Alzheimer's disease brain: beyond altered glucose metabolism. *J Neurochem* 2009; **111:** 915-33.

49. Soh M, Dunlevy JR, Garrett SH, Allen C, Sens DA, Zhou XD, et al. Increased neuron specific enolase expression by urothelial cells exposed to or malignantly transformed by exposure to Cd^{2+} or As^{3+}. *Toxicol Lett* 2012; **212:** 66-74.

50. Yan T, Skaftnesmo KO, Leiss L, Sleire L, Wang J, Li X, et al. Neuronal markers are expressed in human gliomas and NSE knockdown sensitizes glioblastoma cells to radiotherapy and temozolomide. *BMC Cancer* 2011; **11:** 524.

51. Loja T, Chlapek P, Kuglik P, Pesakova M, Oltova A, Cejpek P, et al. Characterization of a GM7 glioblastoma cell line showing CD133 positivity and both cytoplasmic and nuclear localization of nestin. *Oncol Rep* 2009; **21:** 119-27.

52. Splinter TA, Verkoelen CF, Vlastuin M, Kok TC, Rijksen G, Haglid KG, et al. Distinction of two different classes of small-cell lung cancer cell lines by enzymatically inactive neuron-specific enolase. *Br J Cancer* 1992; **66:** 1065-9.

53. Kroemer G, Pouyssegur J. Tumor cell metabolism: cancer's Achilles' heel. *Cancer Cell* 2008; **13:** 472-82.

54. Vesselle H, Schmidt RA, Pugsley JM, Li M, Kohlmyer SG, Vallires E, et al. Lung cancer proliferation correlates with [F-18]fluorodeoxyglucose uptake by positron emission tomography. *Clin Cancer Res* 2000; **6:** 3837-44.

55. Porporato PE, Dhup S, Dadhich RK, Copetti T, Sonveaux P. Anticancer targets in the glycolytic metabolism of tumors: a comprehensive review. *Front Pharmacol* 2011; **2:** 49.

56. Golpour M, Akhavan Niaki H, Khorasani HR, Hajian A, Mehrasa R, Mostafazadeh A. Human fibroblast switches to anaerobic metabolic pathway in response to serum starvation: a mimic of warburg effect. *Int J Mol Cell Med* 2014; **3:** 74-80.

57. Wu C-A, Chao Y, Shiah S-G, Lin W-W. Nutrient deprivation induces the Warburg effect through ROS/AMPK-dependent activation of pyruvate dehydrogenase kinase. *Biochim Biophys Acta* 2013; **1833:** 1147-56.

58. Jang SM, Kim JW, Kim CH, Kim D, Rhee S, Choi KH. p19(ras) Represses proliferation of non-small cell lung cancer possibly through interaction with Neuron-Specific Enolase (NSE). *Cancer Lett* 2010; **289:** 91-8..

59. Amoêdo Ní D, Valencia J P, Rodrigues M F, Galina A, Rumjanek F D. How does the metabolism of tumour cells differ from that of normal cells. *Biosci Rep*. 2013; **33:** e00080.

60. Sedoris KC, Thomas SD, Miller DM. Hypoxia induces differential translation of enolase/MBP-1. *BMC Cancer* 2010; **10:** 157.

61. Vinores SA, Bonnin JM, Rubinstein LJ, Marangos PJ. Immunohistochemical demonstration of neuron-specific enolase in neoplasms of the CNS and other tissues. *Arch Pathol Lab Med* 1984; **108:** 536-40.

62. Vinores SA, Marangos PJ, Bonnin JM, Rubinstein LJ. Immunoradiometric and immunohistochemical demonstration of neuron-specific enolase in experimental rat gliomas. *Cancer Res* 1984; **44:** 2595-9.

63. Kondoh H, Lleonart ME, Bernard D, Gil J. Protection from oxidative stress by enhanced glycolysis; a possible mechanism of cellular immortalization. *Histol Histopathol* 2007; **22:** 85-90.

64. Pelicano H, Martin DS, Xu RH, Huang P. Glycolysis inhibition for anticancer treatment. *Oncogene* 2006; **25:** 4633-46.

65. Takei N, Kondo J, Nagaike K, Ohsawa K, Kato K, Kohsaka S. Neuronal survival factor from bovine brain is identical to neuron-specific enolase. *J Neurochem* 1991; **57:** 1178-84.

66. Hafner A, Glavan G, Obermajer N, Zivin M, Schliebs R, Kos J. Neuroprotective role of gamma-enolase in microglia in a mouse model of Alzheimer's disease is regulated by cathepsin X. *Aging Cell* 2013; **12:** 604-14.

67. Hattori T, Ohsawa K, Mizuno Y, Kato K, Kohsaka S. Synthetic peptide corresponding to 30 amino acids of the C-terminal of neuron-specific enolase promotes survival of neocortical neurons in culture. *Biochem Biophys Res Commun* 1994; **202:** 25-30.

68. Hafner A, Obermajer N, Kos J. gamma-Enolase C-terminal peptide promotes cell survival and neurite outgrowth by activation of the PI3K/Akt and MAPK/ERK signalling pathways. *Biochem J* 2012; **443:** 439-50.

69. Pišlar AH, Kos J. C-terminal peptide of gamma-enolase impairs amyloid-beta-induced apoptosis through p75(NTR) signaling. *Neuromolecular Med* 2013; **15:** 623-35.

70. Wendt W, Zhu X-R, Lübbert H, Stichel CC. Differential expression of cathepsin X in aging and pathological central nervous system of mice. *Expl Neurol* 2007; **204:** 525-40.

71. Kos J, Vižin T, Fonović UP, Pišlar A. Intracellular signaling by cathepsin X: Molecular mechanisms and diagnostic and therapeutic opportunities in cancer. *Semin Cancer Biol* 2015; **31**: 76-83.

72. Amberger-Murphy V. Hypoxia helps glioma to fight therapy. *Curr Cancer Drug Targets* 2009; **9:** 381-90.

73. Levin VA, Panchabhai SC, Shen L, Kornblau SM, Qiu Y, Baggerly KA. Different changes in protein and phosphoprotein levels result from serum starvation of high-grade glioma and adenocarcinoma cell lines. *J Proteome Res* 2010; **9:** 179-91.

74. Levin VA, Panchabhai S, Shen L, Baggerly KA. Protein and phosphoprotein levels in glioma and adenocarcinoma cell lines grown in normoxia and hypoxia in monolayer and three-dimensional cultures. *Proteome Sci* 2012; **10:** 5.

75. Yan T, Skaftnesmo KO, Leiss L, Sleire L, Wang J, Li X, et al. Neuronal markers are expressed in human gliomas and NSE knockdown sensitizes. *BMC Cancer* 2011; **11:** 524.

76. Yamaguchi H, Condeelis J. Regulation of the actin cytoskeleton in cancer cell migration and invasion. *Biochim Biophys Acta* 2007; **1773:** 642-52.

77. Walsh JL, Keith TJ, Knull HR. Glycolytic enzyme interactions with tubulin and microtubules. *Biochim Biophys Acta* 1989; **999:** 64-70.

78. Trojanowicz B, Winkler A, Hammje K, Chen Z, Sekulla C, Glanz D, et al. Retinoic acid-mediated down-regulation of ENO1/MBP-1 gene products caused decreased invasiveness of the follicular thyroid carcinoma cell lines. *J Mol Endocrinol* 2009; **42:** 249-60.

79. Georges E, Bonneau AM, Prinos P. RNAi-mediated knockdown of alpha-enolase increases the sensitivity of tumor cells to antitubulin chemotherapeutics. *Int J Biochem Mol Biol* 2011; **2:** 303-8.

80. Kasprzak A, Zabel M, Biczysko W. Selected markers (chromogranin A, neuron-specific enolase, synaptophysin, protein gene product 9.5) in diagnosis and prognosis of neuroendocrine pulmonary tumours. *Pol J Pathol* 2007; **58:** 23-33.

81. Tapia FJ, Polak JM, Barbosa AJ, Bloom SR, Marangos PJ, Dermody C, et al. Neuron-specific enolase is produced by neuroendocrine tumours. *Lancet* 1981; **1:** 808-11.

82. Lopez J. Carl A. Burtis, Edward R. In: Ashwood and David E. Bruns, editors. *Tietz textbook of clinical chemistry and molecular diagnosis.* 5th edition. St. Louis, USA: Elsevier; 2012.

83. Stieber P, Hatz R, Holdenrieder S, Molina R, Nap M, von Pawel J, et al. National Academy of Clinical Biochemistry Guidelines for the use of tumor markers in lung cancer. Section 3P. AACC press; 2006. [cited 2015 Jan 25]. Available at http://www.nacb.org.

84. Hao X, Sun B, Hu L, Lahdesmaki H, Dunmire V, Feng Y, et al. Differential gene and protein expression in primary breast malignancies and their lymph node metastases as revealed by combined cDNA microarray and tissue microarray analysis. *Cancer* 2004; **100:** 1110-22.

85. Miremadi A, Pinder SE, Lee AH, Bell JA, Paish EC, Wencyk P, et al. Neuroendocrine differentiation and prognosis in breast adenocarcinoma. *Histopathology* 2002; **40:** 215-22.

86. Sawaki M, Yokoi K, Nagasaka T, Watanabe R, Kagawa C, Takada H, et al. Prognostic importance of neuroendocrine differentiation in Japanese breast cancer patients. *Surg Today* 2010; **40:** 831-5.

87. Allen FJ, Van Velden DJ, Heyns CF. Are neuroendocrine cells of practical value as an independent prognostic parameter in prostate cancer? *Br J Urol* 1995; **75:** 751-4.

88. Marangos PJ, Schmechel DE. Neuron specific enolase, a clinically useful marker for neurons and neuroendocrine cells. *Annu Rev Neurosci* 1987; **10:** 269-95.

89. Rundgren M, Cronberg T, Friberg H, Isaksson A. Serum neuron specific enolase - impact of storage and measuring method. *BMC Res Notes* 2014; **7:** 726.

90. Yuan SM. Biomarkers of cerebral injury in cardiac surgery. *Anadolu Kardiyol Derg* 2014; **14:** 638-45.

91. Sturgeon C. Practice guidelines for tumor marker use in the clinic. *Clin Chem* 2002; **48:** 1151-9.

92. Fujiwara H, Arima N, Ohtsubo H, Matsumoto T, Kukita T, Kawada H, et al. Clinical significance of serum neuron-specific enolase in patients with adult T-cell leukemia. *Am J Hematol* 2002; **71:** 80-4.

93. Wang L, Liu P, Chen X, Geng Q, Lu Y. Serum neuron-specific enolase is correlated with clinical outcome of patients with non-germinal center B cell-like subtype of diffuse large B-cell lymphoma treated with rituximab-based immunochemotherapy. *Med Oncol* 2012; **29:** 2153-8.

94. Lorenz J, Dippold W. Neuron-specific enolase-a serum marker for malignant melanoma. *J Natl Cancer Inst* 1989; **81:** 1754-5.

95. Ro C, Chai W, Yu VE, Yu R. Pancreatic neuroendocrine tumors: biology, diagnosis, and treatment. *Chin J Cancer* 2013; **32:** 312-24.

96. Massironi S, Sciola V, Peracchi M, Ciafardini C, Spampatti MP, Conte D. Neuroendocrine tumors of the gastro-entero-pancreatic system. *World J Gastroenterol* 2008; **14:** 5377-84.

97. DeYoung C, Edelman M. Prognostic Factors for Small-Cell Lung Cancer. In: Syrigos K, Nutting C, Roussos C, editors. *Tumors of the chest.* Berlin, Heidelberg: Springer; 2006. p. 189-97.

98. Sturgeon CM, Duffy MJ, Stenman UH, Lilja H, Brunner N, Chan DW, et al. National Academy of Clinical Biochemistry laboratory medicine practice guidelines for use of tumor markers in testicular, prostate, colorectal, breast, and ovarian cancers. *Clin Chem* 2008; **54:** e11-79.

99. Lamberts SWJ, Hofland LJ, Nobels FRE. Neuroendocrine tumor markers. *Front Neuroendocrinol* 2001; **22:** 309-39.

100. Riley RD, Heney D, Jones DR, Sutton AJ, Lambert PC, Abrams KR, et al. A systematic review of molecular and biological tumor markers in neuroblastoma. *Clin Cancer Res* 2004; **10:** 4-12.

101. Johnsson P, Blomquist S, Lührs C, Malmkvist G, Alling C, Solem J-O, et al. Neuron-specific enolase increases in plasma during and immediately after extracorporeal circulation. *Ann Thorac Surg* 2000; **69:** 750-4.

102. Ramont L, Thoannes H, Volondat A, Chastang F, Millet MC, Maquart FX. Effects of hemolysis and storage condition on neuron-specific enolase (NSE) in cerebrospinal fluid and serum: implications in clinical practice. *Clin Chem Lab Med* 2005; **43:** 1215-7.

103. Marangos PJ, Campbell IC, Schmechel DE, Murphy DL, Goodwin FK. Blood platelets contain a neuron-specific enolase subunit. *J Neurochem* 1980; **34:** 1254-8.

104. Trape J, Filella X, Alsina-Donadeu M, Juan-Pereira L, Bosch-Ferrer A, Rigo-Bonnin R. Increased plasma concentrations of tumour markers in the absence of neoplasia. *Clin Chem Lab Med* 2011; **49:** 1605-20.

105. Collazos J, Esteban C, Fernandez A, Genolla J. Measurement of the serum tumor marker neuron-specific enolase in patients with benign pulmonary diseases. *Am J Respir Crit Care Med* 1994; **150:** 143-5.

106. Filella X, Cases A, Molina R, Jo J, Bedini JL, Revert L, et al. Tumor markers in patients with chronic renal failure. *Int J Biol Markers* 1990; **5:** 85-8.

107. DeGiorgio CM, Gott PS, Rabinowicz AL, Heck CN, Smith TD, Correale JD. Neuron-specific enolase, a marker of acute neuronal injury, is increased in complex partial status epilepticus. *Epilepsia* 1996; **37:** 606-9.

108. Strachan MW, Abraha HD, Sherwood RA, Lammie GA, Deary IJ, Ewing FM, et al. Evaluation of serum markers of neuronal damage following severe hypoglycaemia in adults with insulin-treated diabetes mellitus. *Diabetes Metab Res Rev* 1999; **15:** 5-12.

109. Collazos J, Genolla J, Ruibal A. Neuron-specific enolase concentrations in serum in benign liver diseases. *Clin Chem* 1991; **37:** 579-81.

110. Massabki PS, Silva NP, Lourenco DM, Andrade LE. Neuron specific enolase concentration is increased in serum and decreased in platelets of patients with active systemic sclerosis. *J Rheumatol* 2003; **30:** 2606-12.

111. Petrak J, Ivanek R, Toman O, Cmejla R, Cmejlova J, Vyoral D, et al. Deja vu in proteomics. A hit parade of repeatedly identified differentially expressed proteins. *Proteomics* 2008; **8:** 1744-9.

research article

The impact of reconstruction algorithms and time of flight information on PET/CT image quality

Alen Suljic[1], Petra Tomse[2], Luka Jensterle,[2] Damijan Skrk[3]

[1] Faculty of Health Sciences, University of Ljubljana, Slovenia

[2] Department for Nuclear Medicine, University Medical Centre Ljubljana, Slovenia

[3] Slovenian Radiation Protection Administration, Ljubljana, Slovenia

Correspondence to: Alen Suljič, M.Sc., University of Ljubljana, Faculty of Health Sciences, Zdravstvena pot 5, 1000 Ljubljana, Slovenia.
Phone: +386 40 202812; E-mail: alen.alterego@gmail.com

Disclosure: No potential conflicts of interest were disclosed.

Background. The aim of the study was to explore the influence of various time-of-flight (TOF) and non-TOF reconstruction algorithms on positron emission tomography/computer tomography (PET/CT) image quality.

Materials and methods. Measurements were performed with a triple line source phantom, consisting of capillaries with internal diameter of ~ 1 mm and standard Jaszczak phantom. Each of the data sets was reconstructed using analytical filtered back projection (FBP) algorithm, iterative ordered subsets expectation maximization (OSEM) algorithm (4 iterations, 24 subsets) and iterative True-X algorithm incorporating a specific point spread function (PSF) correction (4 iterations, 21 subsets). Baseline OSEM (2 iterations, 8 subsets) was included for comparison. Procedures were undertaken following the National Electrical Manufacturers Association (NEMA) NU-2-2001 protocol.

Results. Measurement of spatial resolution in full width at half maximum (FWHM) was 5.2 mm, 4.5 mm and 2.9 mm for FBP, OSEM and True-X; and 5.1 mm, 4.5 mm and 2.9 mm for FBP+TOF, OSEM+TOF and True-X+TOF respectively. Assessment of reconstructed Jaszczak images at different concentration ratios showed that incorporation of TOF information improves cold contrast, while hot contrast only slightly, however the most prominent improvement could be seen in background variability - noise reduction.

Conclusions. On the basis of the results of investigation we concluded, that incorporation of TOF information in reconstruction algorithm mostly affects reduction of the background variability (levels of noise in the image), while the improvement of spatial resolution due to incorporation of TOF information is negligible. Comparison of traditional and modern reconstruction algorithms showed that analytical FBP yields comparable results in some parameter measurements, such as cold contrast and relative count error. Iterative methods show highest levels of hot contrast, when TOF and PSF corrections were applied simultaneously.

Key words: time of flight; PET/CT; point spread function; reconstruction algorithm; image quality

Introduction

The first advantages of time-of-flight (TOF) technique for positron emission tomography (PET) were presented in the early 1980s. The idea of using the TOF information in PET was implemented in the first generation of the TOF PET scanners using crystal materials with relatively low time resolution.[1,2] TOF PET is characterized by a better trade-off between contrast and noise in the image.[3-7] This property is used in more challenging clinical conditions, allowing shorter examinations at lower count rates, successful scanning of larger patients, clearer characterization of low uptake areas and visualization of smaller lesions.[8-12] Accompanied with the specific point spread function (PSF) correction it produces images with high image quality.[13,14] Current endeavours in research are mainly

FIGURE 1. Triple line insert for spatial resolution measurements and Jaszczak phantom for measurements of described image quality parameters.

oriented towards improving the time resolution. Recent study of TOF PET using Cherenkov light reached coincidence resolution of 71 ps full width at half maximum (FWHM).[15]

Karp *et al.* investigated the benefits of TOF correction in experimental phantoms and concluded that TOF correction leads to a better contrast-to-noise trade-off than non-TOF. They pointed out that complete impact of TOF should not be investigated in terms of a simple sensitivity gain improvement.[10] Akamatsu *et al.* investigated the effect of PSF and TOF corrections on PET/CT image quality with different reconstruction parameters and count rates. They determined that PSF and TOF corrections slightly improve contrast and background variability.[16]

Review of the literature indicates that image quality improvement is expected with incorporating TOF correction in reconstruction algorithm.[16,17] The aim of present research was to evaluate image quality parameters using different reconstruction algorithms, altering phantoms, activity concentration ratios and regions of interest with special focus on TOF information impact.

Materials and methods

All measurements were performed at the Department of Nuclear Medicine, University Medical Centre Ljubljana on Biograph mCT PET/CT scanner, manufactured by Siemens. Scanner combines a 128-slice CT and patented lutetium oxyorthosilicate (LSO) PET system for whole body imaging with included TOF technique. The gantry aperture is 78 cm wide and the tunnel length is 136 cm. This model of PET/CT scanner has incorporated PET Syngo VG30 software. The study was per-

formed on a triple line source phantom and on the Jaszczak phantom. To insure adequate comparison with presented values in literature, the measurements in both phases were performed according to National Electrical Manufacturers Association (NEMA) NU-2-2001 standard.[18]

Measurement of spatial resolution

Spatial resolution was evaluated following the NEMA NU-2-2001 standard using a triple line source of [18]F (activity concentration 7 MBq/ml). Triple line insert phantom (Triple Line Insert, Data Spectrum Co.) was used to obtain three 1 mm diameter parallel lines of tracer material spaced 7.5 cm apart (Figure 1). The total activity was low enough to keep dead time losses and the ratio of randoms to total events below 5%, as suggested by the protocol.[18-20] The acquisition of data was performed with 4.1 ns coincidence window and 12% energy window. The measurements were performed with phantom centre positioned at three locations within PET ring; (1) $x = 0$ and $y = 1$ cm (to avoid the exact centre of the scanner where the sampling density of lines of response may be very high), (2) $x = 0$ and $y = 10$ cm, and (3) $x = 10$ and $y = 0$ cm. The acquired data was reconstructed using analytical filtered back projection (FBP), iterative ordered subsets expectation maximization (OSEM) (4 iterations, 24 subsets) and iterative True-X (4 iterations, 21 subsets) which incorporates PSF correction. All images were reconstructed into a matrix of 400×400 with a 1 mm pixel size. All reconstructions included a Gaussian post-filter of 4 mm FWHM. Values of intrinsic spatial resolution – $FWHM_{int}$ were calculated according to equation in Skreting *et al.*[21], in which $FWHM_{eff}$ is the FWHM of profile measured on the reconstructed image and $FWHM_{filter}$ is the width of the Gaussian reconstruction filter.

$$FWHM_{int} = \sqrt{FWHM_{eff}^2 - FWHM_{filter}^2}$$

Measurements of image quality parameters

Due to the complex interplay of different aspects of imaging system, it is desirable to be able to compare the image quality of different systems using a standardized imaging situation that simulates a clinical imaging condition. In order to evaluate the quality of the image simulating a clinical whole body acquisition, Jaszczak phantom PET/FL-X2/P (Data Spectrum Co.) was used (Figure 1). The phantom consists of the lid, the body of phantom

and the cold spheres insert. Lid has seven little cylinders, six of which are hollow with external diameters of 8 mm, 12 mm, 16 mm and 3 cylinders with diameters of 25 mm. The seventh cylinder is solid and simulates bone on reconstructed image (teflon). The body of the phantom holds the volume of ~ 6 L. The cold insert holds spheres with diameters of 9.5 mm, 12.7 mm, 15.9 mm, 19.1 mm, 25.4 mm and 31.8 mm.[18] The four smallest cylinders (8 mm, 12 mm, 16 mm and 25 mm) and the body of the phantom were filled with a radioactive solution with three different cylinder-to-background activity concentrations of 2:1 (48 kBq/ml:24 kBq/ml), 4:1 (88 kBq/ml: 22 kBq/ml) and 8:1 (144 kBq/ml:18 kBq/ml) in 3 sequential acquisitions. The coincidence and energy window settings remained the same as in spatial resolution measurements. The two larger cylinders were filled with water and air, respectively. The phantom was placed so that the spheres were in the same transversal plane, coinciding with the central plane of the scanner. Corrections (intensity normalization, scatter and random events, dead time losses and attenuation with the CT) were applied in the reconstruction into a matrix of 512 × 512 with 1.6 mm pixel size and Gaussian postfilter of 4 mm of FWHM. We used different image reconstruction algorithms - analytical filtered back projection (FBP), iterative OSEM (4.24) and iterative True-X with PSF correction (4.21). TOF information was alternately incorporated in each reconstruction algorithm. Baseline iterative OSEM (2.8) reconstruction method was added for comparison. Evaluation of image quality was performed by calculation and observation of the following image parameters: percentage of contrast of hot cylinders and cold spheres, percentages of background variability (in the vicinity of hot cylinders and cold spheres) and percentage of relative count error.

Percentage of the contrast of the hot cylinders and cold spheres was determined from the average counts in the cylinders and spheres, as well as in the background which were measured in regions of interest (ROI) with the same size as the cylinders or spheres. Contrast $Q_{H,j}$ for cylinder j was calculated by:

$$Q_{H,j} = \frac{\frac{C_{H,j}}{C_{B,j}} - 1}{\frac{a_H}{a_B} - 1} \times 100\%$$

where $C_{H,j}$ is the average counts in ROI for the cylinder j, $C_{B,j}$ is the average of background ROI, a_H is the activity concentration in cylinders and a_B is the activity concentration in the background (both a_H and a_B were measured in dose calibrator before

PET acquisition). Contrast of spheres $Q_{C,j}$ for each cold sphere j was calculated by:

$$Q_{C,j} = \left(1 - \frac{C_{C,j}}{C_{B,j}}\right) \times 100\%$$

where $C_{C,j}$ is the average counts in the ROI for sphere j and $C_{B,j}$ is the average of the background ROI counts for sphere j.

Percentage of background variability was calculated as the ratio between the standard deviation and the mean value in 12 randomly placed concentric ROI in the background that were at least 15 mm away from any cylinder, sphere or the edge of the phantom. The sizes of ROI corresponded to the diameters of the spheres. The percent background variability N_j for sphere j is calculated as:

$$N_j = \frac{SD_j}{C_{B,j}} \times 100\%$$

where SD_j is the standard deviation of the background ROI counts for sphere j and $C_{B,j}$ is the average of the background ROI counts for sphere j.

The relative count error that evaluates the accuracy of the scatter and attenuation corrections was determined as the average of the relative count errors in 2 planes. This was obtained as the ratio between the mean value of counts in a circular region (of 22 mm or 25 mm in diameter, positioned in the air filled cylinder) and the mean background value (evaluated in 12 regions of the same size). We expected the contribution of scatter and attenuation error that was evaluated for air to be most prominent in the voxels closest to the background which also includes 1.5 mm plastic cylinder wall. Besides estimating the value for purely air medium, we found that it was important to take into account the cylinder wall for comparison. Therefore 2 diameters of ROI were used, including and excluding the cylinder wall (22 mm and 25 mm). The residual error in scatter and attenuation corrections $\Delta C_{air,i}$ for each slice i was calculated as:

$$\Delta C_{air,i} = \frac{C_{air,i}}{C_{B,i}} \times 100\%$$

where $C_{air,i}$ is the average counts in the air filled cylinder ROI and $C_{B,i}$ is the average count of the background ROI for slice i.

Results

Results are presented in the same order as they were presented theoretically in the previous chapter. Spatial resolution results, measured on triple line insert, are followed by contrast, background variability and relative count error results, measured on Jaszczak phantom.

TABLE 1. Measured values of intrinsic spatial resolution in FWHM for various line source positions and reconstruction methods

	FBP	FBP+TOF	OSEM	OSEM+TOF	True-X	True-X+TOF
1 cm offset (x=0, y=1 cm)						
Transverse	5.2 mm	5.1 mm	4.5 mm	4.5 mm	2.9 mm	2.9 mm
10 cm offset (x = 10 cm, y = 10 cm)						
Transverse radial	5.9 mm	5.9 mm	4.8 mm	4.8 mm	2.7 mm	2.8 mm
Transverse tangential	5.9 mm	5.8 mm	5.3 mm	5.8 mm	3.7 mm	3.9 mm

FBP = filtered back projection; FBP+TOF = filtered back projection with incorporated time of flight information; OSEM = ordered subsets expectation maximization; OSEM+TOF = ordered subsets expectation maximization with incorporated time of flight information; True-X = iterative reconstruction method which incorporates point spread function (PSF) correction; True-X + TOF = iterative reconstruction method which incorporates point spread function (PSF) correction with incorporated time of flight information
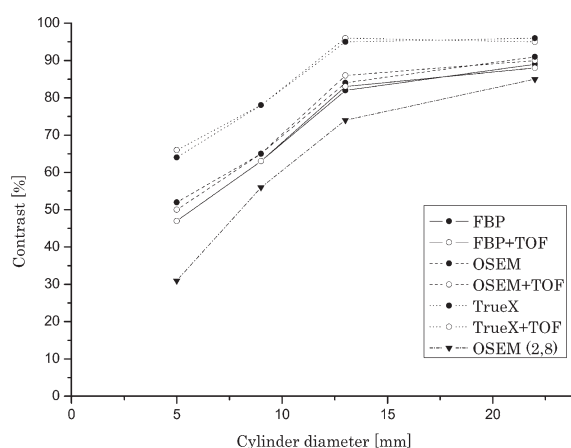
FIGURE 2. Hot contrast in relation with cylinder diameter and reconstruction method (activity concentration ratio 8:1).
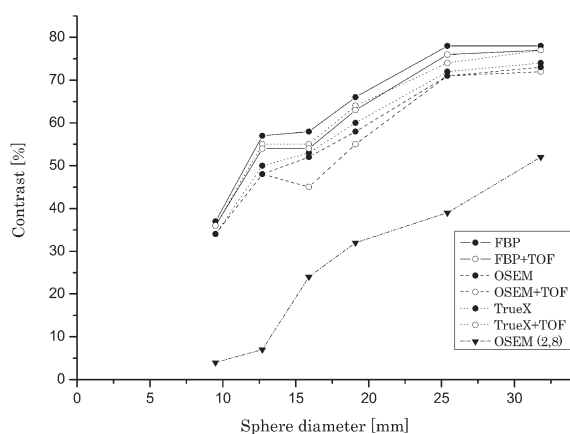
FIGURE 3. Cold contrast in relation with sphere diameter and reconstruction method (activity concentration ratio 1:8).

Spatial resolution

The spatial resolution of a system represents its ability to distinguish between two points after im-age reconstruction. The measurement of spatial resolution characterizes the shape of the reconstructed point spread function at the FWHM level. Such measurement allows a reliable evaluation of scanners, taking into account the variation in spatial resolution with radial distance. The data are taken at low counting rates, so that potential event pileup is not encountered. Table 1 summarizes the results of the spatial resolution measured in air on PET/CT scanner.

Hot and cold contrast

The measured parameters of image quality depend on reconstruction algorithm used. Figures 2 and 3 show the response of observed reconstruction methods in relation to cylinder or sphere diameter and activity concentration ratio between cylinders or spheres and background. Presented activity concentration ratios were chosen for best representation of the results. The iterative algorithm True-X with TOF correction displayed the best results of hot contrast. Slightly lower levels of contrast were shown (with smallest spheres) with iterative OSEM (4.24), followed closely by analytical FBP. Algorithms with incorporated TOF correction displayed slightly better results as their non TOF counterparts. Iterative algorithm True-X with TOF correction displayed the best result of cold contrast, followed closely by analytical FBP. Baseline iterative OSEM (2.8) showed the lowest hot and cold contrast. TOF information had higher impact with cold contrast performance in comparison with hot contrast performance. For all sizes of cylinders and spheres, the hot contrast increased with iterative reconstruction methods, however in cold contrast traditional FBP showed slightly better results, especially for larger spheres.

Background variability

Figures 4 and 5 show variability of background for all reconstruction methods and all (cylinders or spheres) diameters. The TOF correction significantly reduced background variability – up to 50% for all reconstruction algorithms especially with the smallest diameter spheres. The measurement of background variability in the vicinity of cold spheres is not foreseen in the NEMA protocol; however our research shows that the values of background variability in the vicinity of hot cylinders and cold spheres differ by a factor of three. The impact was more prominent for cylinders and spheres of smaller diameters. Baseline OSEM (2.8) produced images with lowest values of background variability, or in other words, highest uniformity and lowest noise levels.

Relative count error

Relative count errors for various reconstruction methods and activity concentration ratios are presented in Table 2. We found some difficulties with positioning ROI in areas with low concentration ratio, since there is a cylinder wall around observed air medium in the background with higher specific activity, which has to be taken into account. This issue was not addressed in standard protocol but as we found it important, we chose to compare measurements with and without 1.5 mm thick cylinder wall accounted in ROI measurements (22 mm and 25 mm). The measurements were made in cylinder filled with air as opposed to the measurements made in lung insert with fixed density 0.3 g/cm^3, cited by NEMA protocol and other authors.[5,17,18,22]

Discussion

The spatial resolution measurements show that PSF modelling successfully counteracts the parallax error and is responsible for spatial resolution improvement throughout field of view. The results are in line with results of other authors and confirmed the accuracy of used methods. Slight misalignments of a line source with the scanner axis leads to degraded resolution compared with that measured with a point source. The spatial resolution measured with a point source, therefore, can be expected to be slightly better than that determined with a line source (approximately few tenths of a millimetre).[23] The objective of the image quality

TABLE 2. Relative count error for various reconstruction methods, performed with regions of interest (ROI) with diameter equal to external diameter of air insert and diameter equal to internal diameter of air insert (in brackets)

	Ratio 1:2	Ratio 1:4	Ratio 1:8
Reconstruction algorithm		ΔC air [%]	
FBP	11.1 (9.8)	16.2 (14.5)	9.7 (8.4)
FBP+TOF	11.1 (12.1)	12.6 (10.2)	9.8 (8.8)
OSEM	15.0 (15.3)	25.0 (23.6)	21.0 (19.8)
OSEM+TOF	15.3 (15.4)	17.7 (15.3)	14.7 (13.8)
True-X	20.4 (20.5)	25.0 (23.5)	20.3 (18.9)
True-X+TOF	14.1 (14.1)	17.2 (14.7)	14.9 (12.3)
OSEM (2,8)	48.0 (46.9)	45.9 (47.5)	49.1 (47.6)

FBP = filtered back projection; FBP+TOF = filtered back projection with incorporated time of flight information; OSEM = ordered subsets expectation maximization; OSEM+TOF = ordered subsets expectation maximization with incorporated time of flight information; True-X = iterative reconstruction method which incorporates point spread function (PSF) correction; True-X+TOF = iterative reconstruction method which incorporates point spread function (PSF) correction with incorporated time of flight information
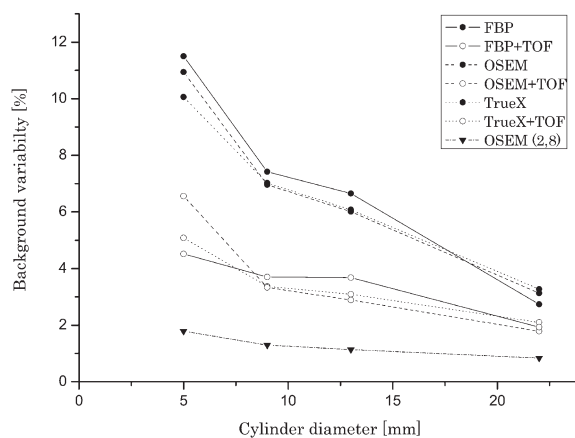
FIGURE 4. Background variability in relation with cylinder diameter and reconstruction method (activity concentration ratio 2:1).
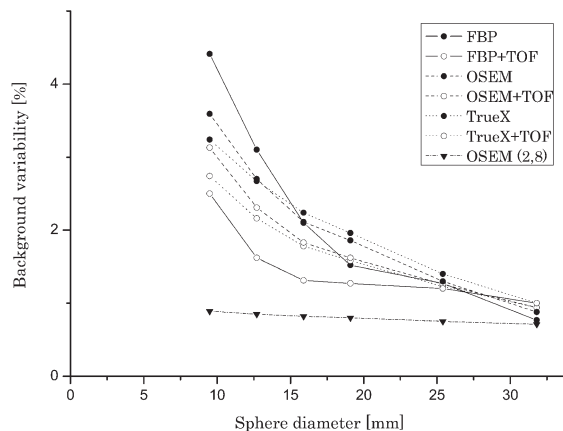
FIGURE 5. Background variability in relation with sphere diameter and reconstruction method (activity concentration ratio 1:2).
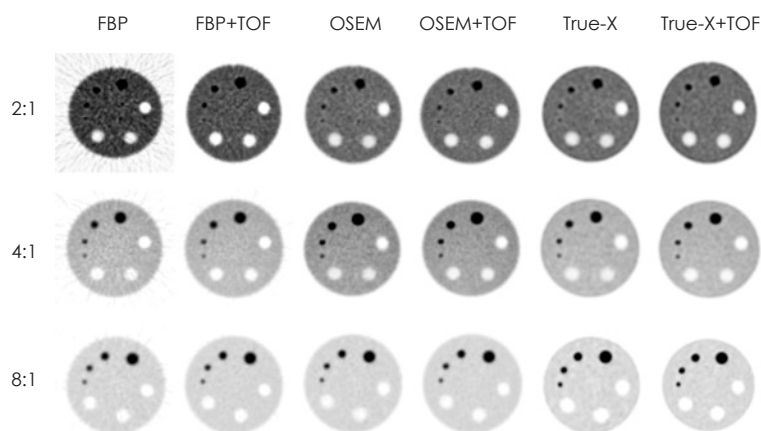
FIGURE 6. Visual assessment of image quality according to the reconstruction method and activity concentration ratio.

FBP = filtered back projection; FBP+TOF = filtered back projection with incorporated time of flight information; OSEM = ordered subsets expectation maximization; OSEM+TOF = ordered subsets expectation maximization with incorporated time of flight information; True-X = iterative reconstruction method which incorporates point spread function (PSF) correction; True-X+TOF = iterative reconstruction method which incorporates point spread function (PSF) correction with incorporated time of flight information

test was to produce images simulating whole body scans with hot and cold lesions. The measurements were extended to include the contrast ratios 2:1, 4:1 and 8:1 between the hot cylinders and background, in addition to evaluation of different modern and especially traditional reconstruction algorithms, not contemplated by NEMA protocol. Results of hot and cold contrast show that incorporation of TOF information only marginally improves contrast recovery. Best results were achieved with iterative reconstruction algorithm incorporating PSF modelling-True-X with TOF information. Baseline OSEM (2.8) produced images with lowest contrast ratio in comparison with other reconstruction methods. The most important improvement of contrast was obtained with the incorporation of PSF in the reconstruction, while TOF having lower impact.

Results of background variability showed that TOF information has the most profound impact. Incorporation of TOF information resulted in up to 50% reduction of background variability with all observed reconstruction algorithms. In clinical application the improvement of background variability means lower patient dose or reduction of the imaging time at the same level of image noise. The background variability in the vicinity of hot inserts was higher up to three times compared to background variability in the vicinity of cold inserts. Best results were achieved with baseline reconstruction algorithm OSEM (2.8) where we reconstructed images with the lowest levels of noise. This algorithm was included in this research

because it was the usual method of reconstruction in the previous generation of PET tomographs.[16] It is important to understand that the background variability parameter presents not only statistical noise but also non uniformities in the image which arise from inaccurate attenuation correction or poor convergence during iterative reconstruction. The background variability does not reflect noise correlations or streak artefacts in the image.[23]

The results of relative count error which provides information of accuracy of attenuation and scatter corrections show, that incorporation of TOF reconstruction in most cases improved (decreased) relative count error, especially at higher activity concentration ratios. Best results were surprisingly obtained with FBP with incorporated TOF correction. The use of PSF correction does not show the improvement of the results, already obtained with TOF correction. The results were similar in evaluation of the cold contrast and the error in the air, since the radioactivity is measured in an image segment in which there is no activity and only the medium varies. The different measurements of relative count error show that the differences between measurements with internal diameter sized ROI and external diameter sized ROI can be as high as 10%.

It is important that the images are also examined visually for inconsistencies and artefacts (Figure 6). Visual assessment of reconstructed Jaszczak images at different activity concentrations showed that incorporation of TOF information in reconstruction algorithm substantially improves contrast levels and lowers noise with analytical FBP. FBP showed the lowest levels of contrast and the highest levels of background variability. Iterative reconstruction algorithm (OSEM) and iterative reconstruction algorithm with PSF modelling-True-X produced images with clearly shaped cylinders and spheres with high contrast and low image noise. TOF information had lower impact on improvement of the images reconstructed with iterative reconstruction methods. TOF information showed best results with low activity concentration ratios and less advanced reconstruction methods, where more noise was present.

Conclusions

The performance characteristics of Siemens Biograph mCT PET/CT scanner were evaluated following the NEMA NU-2-2001 standard, adjusted NEMA NU-2-2001 standard and some additional tests using different methods of topographic reconstruction.. While other studies present either

results with NEMA phantoms, or results with in-house-made phantoms, we found it interesting to compare and present both types of the results, which might be applicable in the institutions where NEMA equipment is not available.

All algorithms offered by the Biograph mCT software were included and applied to the wide range of activity concentration ratios. Thus analytical FBP method as traditional reconstruction method was also included into study in order to compare it with modern iterative reconstruction algorithms, which is novelty compared to results performed by other authors.

Our most important interest was in observing the impact of TOF information. On the basis of measurements evaluation we concluded that incorporation of TOF information in the reconstruction algorithm had the greatest impact on background variability reduction, while improvement of spatial resolution is negligible. The comparison of levels of background variability in the vicinity of hot cylinders revealed that they can be higher up to three times compared to background variability in the vicinity of cold inserts for smallest diameters. Lower levels of background variability in the area of spheres could be obtained using separate phantoms for cylinders and spheres. Measurements of relative count error or accuracy of attenuation and scatter corrections showed that TOF correction improved relative count error, especially with higher activity concentration ratios. We observed substantial difference in relative count error for the cases excluding/including the plastic wall. Relative count error measurements should be performed with the same diameter of ROI as the internal diameter of cylinder. When comparing traditional and modern reconstruction algorithms we found out that analytical FBP yields comparable or even better results in some parameter measurements, such as cold contrast and relative count error. Iterative methods show the highest levels of hot contrast, when PSF and TOF correction were applied simultaneously. However, iterative method with PSF modelling produced higher values of relative count error, which can be decreased with implementing TOF corrections. The impact is especially prominent at higher activity concentration ratios. Baseline iterative OSEM (2.8) showed substantially lower levels of background variability than any other reconstruction algorithm, on the other hand, it was inferior in all other parameter measurements.

References

1. Budinger TF. Time-of-flight positron emission tomography: Status relative to conventional PET. *J Nucl Med* 1983; **24:** 73-8.

2. Boellaard R, Krak NC, Hoekstra OS, Adriaan A. Effects of noise, image resolution, and ROI. *J Nucl Med* 2004; **45:** 1519-27.

3. Cherry SR, Sorenson JA, Phelphs ME. *Physics in nuclear medicine.* Michigan: Saunders; 2003. p. 253-97.

4. Conti M. Focus on time-of-flight PET: the benefits of improved time resolution. *Eur J Nucl Med Mol Imaging* 2011; **38:** 1147-57.

5. Quality assurance for PET and PET/CT systems. *IAEA human health series no.1.* Vienna: IAEA; 2009. p. 2-70.

6. Saha GB. *Basics of PET imaging.* New York: Springer; 2005. p. 59-80.

7. Powsner RA, Powsner ER. *Essential nuclear medicine physics.* Oxford: Blackwell publishing; 2006. p. 116-7.

8. Moses WW. Recent advances and future advances in time-of-flight PET. *Nucl Instrum Methods Phys Res A* 2007; **580:** 919-24.

9. Conti M. State of the art and challenges of time-of-flight PET. *Physica Medica* 2008; **25:** 1-11.

10. Karp JS, Suleman S, Daube-Witherspoon ME, Muehllehner G. Benefit of time-of-flight in PET: experimental and clinical results. *J Nucl Med* 2008; **49:** 462-70.

11. Lois C, Jakoby BW, Long MJ, Hubner KF, Barker DW, Townsend DW. An assessment of the impact of incorporating Time-of-Flight (TOF) information into clinical PET/CT imaging. *J Nucl Med* 2010; **51:** 1-20.

12. Kadrmas DJ, Casey ME, Conti M, Jakoby BW, Lois C, Towsend DW. Impact of time of-flight on PET tumor detection. *J Nucl Med* 2009; **50:** 1315-23.

13. Casey ME. *Point spread function reconstruction in PET.* Knoxville, USA: Siemens Medical Solutions, Inc; 2007. p. 1-7.

14. Chang JK, Laforest R. Evaluation of the HD and HD+TOF reconstructions for Siemens' Biograph-mCT TOF PET scanner. *Nuclear Science Symposium and Medical Imaging Conference (NSS/MIC), 2011 IEEE.* Valencia; 23-29 October 2011. p. 4131-4. DOI: 10.1109/NSSMIC.2011.6153787

15. Korpar S, Dolenec R, Križan P, Pestotnik R, Stanovnik A. Study of TOF PET using Cherenkov light. *Nucl Instrum Methods Phys Res A* 2012; **654:** 532-8.

16. Akamatsu G, Ishikawa K, Mitsumoto K, Taniguchi T, Ohya N, Baba S, et al. Improvement in PET/CT Image Quality with a Combination of Point-Spread Function and Time-of-Flight in Relation to Reconstruction Parameters. *J Nucl Med* 2012; **53:** 1-7.

17. Martí-Climent JM, Prieto E, Domínguez-Prado I, García-Velloso MJ, Rodríguez-Fraile M, Arbizu J, et al. Contribution of time of flight and point spread function modeling to the performance characteristics of the PET/CT Biograph mCT scanner. *Rev Esp Med Nucl Imagen Mol* 2012; **32:** 1-9.

18. National Electrical Manufacturers Association. *NEMA standards publication NU-2-2001. Performance measurements of positron emission tomographs.* Rosslyn, VA: National Electrical Manufacturers Association; 2001. p. 1-39.

19. Prieto E, Martí-Climent JM, Arbizu J, Garrastachu P, Domínguez I, Quincoces G, et al. Evaluation of spatial resolution of a PET scanner through the simulation and experimental measurement of the recovery coefficient. *Comput Biol Med* 2010; **40:** 75-80.

20. Lodge MA, Rahmin A, Wahl RL. A practical, automated quality assurance method for measuring spatial resolution in pet. *J Nucl Med* 2009; **50:** 1307-14.

21. Skretting A. A method for on-site measurement of the effective statial resolution in PET image volumes reconstructed with OSEM and gaussian post-filters. *Radiat Prot Dosimetry* 2010; **139:** 195-8.

22. Jakoby BW, Bercier Y, Conti M, Casey ME, Bendriem B, Towsend DW. Physical and clinical performance of the mCT time-of-flight PET/CT scanner. *Phys Med Biol* 2011; **56:** 2375-89.

23. Daube-Witherspoon ME, Karp JS, Casey ME, DiFilippo FP, Hines H, Muehllehner G, et al. PET Performance Measurements Using the NEMA NU 2-2001 Standard. *J Nucl Med* 2002; **43:** 1398-409.

research article

Careful treatment planning enables safe ablation of liver tumors adjacent to major blood vessels by percutaneous irreversible electroporation (IRE)

Bor Kos[1], Peter Voigt[2], Damijan Miklavcic[1], Michael Moche[2]

[1] University of Ljubljana, Faculty of Electrical Engineering, Ljubljana, Slovenia

[2] Leipzig University Hospital, Department of Diagnostic and Interventional Radiology, Leipzig, Germany

Correspondence to: Michael Moche, M.D., Leipzig University Hospital, Department of Diagnostic and Interventional Radiology, Liebigstraße 20, D-04103 Leipzig, Germany. E-mail: michael.moche@medizin.uni-leipzig.de

Disclosure: DM holds patents on electrochemotherapy that have been licensed to IGEA S.p.a. and is also a consultant to IGEA. The other co-authors have nothing to disclose.

Background. Irreversible electroporation (IRE) is a tissue ablation method, which relies on the phenomenon of electroporation. When cells are exposed to a sufficiently electric field, the plasma membrane is disrupted and cells undergo an apoptotic or necrotic cell death. Although heating effects are known IRE is considered as non-thermal ablation technique and is currently applied to treat tumors in locations where thermal ablation techniques are contraindicated.

Materials and methods. The manufacturer of the only commercially available pulse generator for IRE recommends a voltage-to-distance ratio of 1500 to 1700 V/cm for treating tumors in the liver. However, major blood vessels can influence the electric field distribution. We present a method for treatment planning of IRE which takes the influence of blood vessels on the electric field into account; this is illustrated on a treatment of 48-year-old patient with a metastasis near the remaining hepatic vein after a right side hemi-hepatectomy.

Results. Output of the numerical treatment planning method shows that a 19.9 cm^3 irreversible electroporation lesion was generated and the whole tumor was covered with at least 900 V/cm. This compares well with the volume of the hypodense lesion seen in contrast enhanced CT images taken after the IRE treatment. A significant temperature raise occurs near the electrodes. However, the hepatic vein remains open after the treatment without evidence of tumor recurrence after 6 months.

Conclusions. Treatment planning using accurate computer models was recognized as important for electrochemotherapy and irreversible electroporation. An important finding of this study was, that the surface of the electrodes heat up significantly. Therefore the clinical user should generally avoid placing the electrodes less than 4 mm away from risk structures when following recommendations of the manufacturer.

Key words: irreversible electroporation; liver tumors; colorectal carcinoma; finite element method

Introduction

Irreversible electroporation (IRE) is a tissue ablation method which relies on the phenomenon of electroporation.[1] Electroporation occurs, when cells are exposed to sufficiently strong electric fields. These fields disrupt the plasma membrane and cause increased permeability of the plasma membrane to ions, larger molecules, and even DNA. When the electric field is sufficiently strong, the cells cannot recover from the disruption of the membrane and consequently undergo apoptotic or necrotic cell death.[2,3] When this method is used for curative tumor ablation, it requires the whole tu-

TABLE 1. Parameters of the electrical and thermal model

Property	Value	Reference
σ_L — Liver initial conductivity	0.091 S/m	Haemmerich et al.[10]
σ_L — Liver final conductivity	0.45 S/m	Cukjati[17]
σ_T — Tumor initial conductivity	0.4 S/m	Haemmerich et al.[16]
σ_T — Tumor final conductivity	1.6 S/m	Extrapolated from Cukjati[17]
σ_{Vfinal} — Vessel initial conductivity	0.7 S/m	Marčan et al.[15]
σ_{Vfinal} — Vessel final conductivity	1.05 S/m	Marčan et al.[15]
aT — Tissue conductivity thermal coefficient	1.5 %/K	Haemmerich et al.[16]
C_T — Tissue thermal capacity	3540 J/(kg K)	Hasgall et al.[19]
ρ_T — Tissue density	1079 kg/m³	Hasgall et al.[19]
k_T — Tissue thermal conductivity	0.52 W/(m K)	Hasgall et al.[19]
ω_b —Blood perfusion	1.8 mL /s /100 mL	Hasgall et al.[19]
C_b —Blood thermal capacity	3840 J/(kg K)	Hasgall et al.[19]
ρ_B — Blood density	1060 kg/m³	Garcia et al.[9]
T — Initial tissue temperature	310 K	
q''' — Tissue metabolic heat generation	10740 W/m³	Hasgall et al.[19]
E_a — Activation energy	5.06×10⁵ J/mol	Henriques et al.[20]
ζ — Frequency factor	2.984×10⁸⁰ s⁻¹	Henriques et al.[20]
R — Universal gas constant	8.314 J/(mol*K)	
σ_L — Electrode conductivity	10⁶ S/m	
k_E — Electrode thermal conductivity	15 W/(m K)	Garcia et al.[9]
ρ_E — Electrode density	6000 kg/m³	Garcia et al.[9]
C_E — Electrode thermal capacity	500 J/(kg K)	Garcia et al.[9]

mor to be covered with sufficiently strong electric fields, which requires placement of at least two, but typically four or more electrodes around and/or inside the tumor. The electrodes can be positioned percutaneously under ultrasound or CT guidance, or intra-operatively.[4,5]

IRE relies on applying electric fields in excess of 600 V/cm in the target volume.[6,7] Since tissues are rather good conductors, and tissue conductivity even increases during pulse application, electric fields in tissue are accompanied by significant currents, which can be up to 50 A (maximum current limit of the Nanoknife® device). This leads to large power dissipation in the tissue during the pulses, which can be up to 150 kW during the pulse. However, the pulses are typically equal or less than 100 μs long and always delivered synchronized with the heart rate, which usually is lower than 100 beats per minute. This results in duty cycles of less than 0.1 % and consequently the actual delivered power is less than 15 W, which is between a factor of 5 to 10 less than in thermal ablation methods. Nevertheless, this power dissipation causes a non-negligible temperature rise which can be found most prominently around the tissue-electrode boundary.[8] However, temperature itself is not the primary, nor the desired cell-killing mechanism.[9] In fact, one of the most promising uses of IRE is to treat tumors, which are very close to major blood vessels, bile ducts (in liver), or nerves (in prostate), which limit thermal ablation methods like radiofrequency, laser or microwave ablation.[10–12] The reason for this limitation is on one hand the risk of leaving residual vital tumor due to the heat sink effect induced from the cooling of the vessel. On the other hand, there is a significant risk of heat caused coagulation of sensitive structures like nerves and bile ducts with serious complications for the patient. However, the local electric field distribution, which is the most important factor for successful treatment with IRE is affected by the higher conductivity of blood and blood vessels.[13–15] This means that additional care has to be taken when IRE is performed near blood

vessels, where it is most preferred over the other thermal ablation techniques.

Currently, the manufacturer of the only certified medical device available for IRE treatments (NanoKnife, Angiodynamics, Latham, NY) recommends electrodes for ablation of liver tumors to be no more than 2.2 cm apart, positioned in parallel around the target volume. A total of 90 pulses with voltage to distance ratio of 1500-1700 V/cm, and 90 μs duration are recommended per electrode pair according to System Procedure Guide Software Version 2.2.0. The graphical user interface of the software provides a simple treatment planning option in two dimensions (2D), while not taking into account differences in electric conductivities of tissue between normal and tumor tissue.[16]

In this study we present a method for numerical patient-specific treatment planning for IRE, which takes into account the influence of blood vessels on electric field distribution. The method is illustrated on a 48-years-old. female patient with a recurrent metastasis directly adjacent to the last remaining hepatic vein after previous right-side hemi-hepatectomy and the successful treatment with IRE.

Materials and methods

Electric field computation and temperature distribution computation

Since IRE relies on applying local fields in excess of 600 V/cm in the whole target volume, electrodes need to be introduced in the target volume itself, but preferably minimizing the number of electrodes inserted in the tumor to preclude needle track metastasis seeding. The electric field is however affected by the local conductivity of tissue, which generally varies between different tissues, especially at frequencies, which are present in electroporation pulses (Table 1). Additionally, conductivity of tissue was shown to increase due to the electric field during the pulse delivery due to membrane electroporation.[17,18] Together with the complex geometry of the target location (blood vessels, tumors and liver) this generally requires numerical computation of the electric fields.

In order to differentiate the tissues of different conductivities and separate the target volume from the healthy tissue a segmentation step is required in the treatment planning procedure.

We use a treatment planning procedure based on optimization in Matlab, while electric fields are solved in Comsol Multiphysics. The simulations consist of solving the Laplace equation for electric potential, given boundary conditions for electric potential on the electrodes. A stationary solver is used for the simulations, but iterated 6 times, increasing the conductivity of the tissues above electroporation thresholds between each iteration.[18,21–23] From the electric field simulations, we obtained the electric field distribution and final volumes of tumor and liver covered with fields above the IRE threshold. Since more than one electrode pair is generally required to obtain clinically relevant treatment volumes in IRE, the electric field from each electrode pair are compared and the maximum value at each location is considered when evaluating the total coverage of the target volume.

For verifying the tissue heating during the treatment, the thermal dissipation of the electric field computation step can be used to set a heat source for a Pennes' bioheat equation for a transient solver of temperature fields. To shorten simulation times, a duty-cycle approach is used, wherein we use the thermal dissipation multiplied by the duty cycle of the pulse delivery to model heating. This provides a comparable temperature increase in the bulk tissue[9], but is numerically more stable and much faster. The reason for this is that it does not have to account for the very fast temperature rise during the 90 μs that the pulse is turned on in comparison to the 10000 times longer interval between pulses. All parameters of the electrical and thermal model were taken from the literature and are listed in Table 1.

Patient data

The patient was a 48-years-old female who had previously undergone right hemi-hepatectomy for treatment of metastases of cholangiocellular carcinoma. During follow-up imaging a small (14 × 9 × 15 mm, i.e. 0.96 cm^3) focal recurrent metastasis was detected in the remaining left liver. Since the metastasis was adjacent to the only remaining left hepatic vein it was not surgically resectable. Percutaneous CT guided IRE ablation was selected as the best treatment option to preserve this last liver vein since primary thermal ablations like radiofrequency ablation would have been contraindicated in this constellation. IRE can achieve complete ablation of tumors even nearby major blood vessels, since it is not negatively affected by their cooling effect such as thermal therapies[24] where this so called heat sink effect may lead to incomplete tumor ablation. Furthermore, it is also commonly reported, that it is sparing for larger blood vessels[25] which could have been damaged during

TABLE 2. Reconstructed distances and angles between the electrodes

Electrode pair	Distance [mm]	Angle [°]
1 — 2	18	4.1
1 — 3	14	1.2
1 — 4	12	1.8
2 — 3	15	3.2
2 — 4	12	5.2
3 — 4	17	2.0

FIGURE 1. **(A)** CT image showing position of two of the electrodes (electrodes 1 and 2) inside the liver. **(B)** 3-D model showing the positioning of the electrodes in the model relative to the tumor (green) and the left liver vein (red). The liver, which was also included in the computational model is removed from the image for clarity, since it is completely encompassing the region of interest. The numbers identify each electrode.

thermal ablations. The patient was treated in the scope of the research project GoSmart (funded by the European Commission – grant agreement no. 600641). Ethical approval was obtained from Leipzig University Hospital Institutional Review Board under code AZ206 -13 – 15072013. Informed consent to use their personal data for scientific purposes was obtained from the patient. Treatment was performed using the above-mentioned pulse generator and the ablation protocol recommended from the manufacturer. Electrodes were positioned using CT guidance (Figure 1). Electrode exposure length for the treatment was 2 cm. All data was collected from clinical records or from the generator, where electric pulse data it is saved by default. The data is routinely recorded for improvement of quality, practice and performance of this novel treatment.

For the illustration case, we used MRI images of the patient acquired 3 weeks prior to the treatment. The images were anonymized and uploaded into the web based electric fields visualization tool Visifield (www.visifield.com, University of Ljubljana, Slovenia). Liver was segmented using automatic segmentation method for liver segmentation[26] and the tumor and blood vessel were segmented manually. Interventional CT images obtained during the procedure were used to exactly reconstruct the electrode positions during treatment and to have these available for the numerical simulations. The reconstructed distances between the tips of the electrodes and angles between the tips of the electrodes are given in Table 2. It is also demonstrated, that the radiologist performing the procedure has managed to place the electrodes almost completely in parallel.

The pulse generator measures the pulse voltage and current during electric pulse delivery and stores the results in an xml document, which was parsed into Matlab. The same voltages, as were actually delivered during the actual treatment for each electrode pair were also used in a finite element computational model. The electric field distribution was computed only for the first pulse of each pulse train using a stationary solver, but taking into account increase of conductivity due to electroporation.

Results

A total of 660 pulses were delivered in three sequences to six electrode pairs (pulses are always delivered to pairs of electrodes; sequentially, pairs of two electrodes are selected from available electrodes), with the electrode positioning and num-

TABLE 3. List of delivered pulses and comparison with computed currents

Pulse sequence	Pulse train	Electrode pair	Voltage [V]	No. of pulses	Measured current [A]	Computed current [A]	Error [%]
Test pulses	1	[3,4]	2720	20	26.6	27.4	3
	2	[1,2]	2550	20	21.5	23.9	11
	3	[1,3]	2380	20	23.6	25.8	9
	4	[2,3]	2210	20	21.3	21.0	-2
	5	[4,1]	2200	20	22.5	25.7	14
	6	[2,4]	1650	20	17.4	16.2	-7
Treatment pulses	7	[1,2]	3000	70	30.5	28.4	-7
	8	[3,4]	2720	70	30.5	27.4	-10
	9	[2,3]	2405	70	30.3	22.8	-25
	10	[1,3]	2380	70	30.7	25.9	-16
	11	[2,4]	2200	70	31.1	22.3	-28
	12	[4,1]	2200	70	29.3	25.6	-13
Additional pulses	13	[1,2]	2380	20	24.2	22.1	-9
	14	[3,4]	2380	20	28.5	23.6	-17
	15	[1,3]	1960	20	22.1	20.6	-7
	16	[2,3]	1820	20	20.5	16.8	-18
	17	[2,4]	1540	20	18.9	14.9	-21
	18	[4,1]	1540	20	17.2	17.1	0

FIGURE 2. Coverage progression after delivery of pulses to each electrode pair. The graph shows the combined maximum fields in the tumor following each electrode pair. Electrode pair progression is the same as in Table 3. Arrow indicates the direction of increase of coverage with delivery of successive electric pulses. The graph shows that the first electrode pair already covers the whole tumor with electric fields above the irreversible electroporation threshold.

bering as shown in Figure 1. Initially trains of 20 pulses were delivered (test pulses), then trains of 70 pulses were delivered, with some voltage adjustments (treatment pulses), and finally trains of 20 pulses were delivered (additional pulses) with

lower voltages. Table 3 lists all delivered pulses and pulse parameters.

The root mean square error (RMSE) of the computed currents versus measured currents from the pulse generator is 3.8 A. The cumulative coverage of tumor with electric fields after each electrode pair is shown in Figure 2, while the coverage of liver tissue is shown in Figure 3. While the IRE threshold for tumors has not yet been rigorously determined, we are using a value of 800 V/cm in the following graphs, consistent with previous work.[6,23,27] For liver we used IRE threshold determined from experiments on rabbit livers – 700 V/cm.[21] To be noted however, this value is for pulse trains of 8 pulses. It is very likely that actual IRE thresholds are much lower.[7,28]

In the post-IRE contrast enhanced CT images, a hypodense region can be seen in the area where the treatment was performed. We used this hypodense region to estimate the total IRE lesion as was previously suggested.[29] The volume of this hypodense lesion was 20.03 cm^3. From Figure 3, the volume of the IRE lesion in the liver is 18.4 cm^3. Together with the tumor (0.57 cm^3) in the simulations, the total volume of the computed lesion equals 19.9 cm^3, which is comparable to the lesion size determined by CT.

Figure 4 shows a single slice of temperature data after the 7th pulse treatment set (first train of the treatment pulses, and the train with highest pulse amplitude). The tumor is heated slightly more than the surrounding tissue, as its perfusion is lower, and also the conductivity is higher than that of the liver tissue, which both contributes to a higher Joule heating. Temperatures above 50 C are typically used for indication of thermal tissue damage.[1] Therefore, we also show the volume of tissue above this threshold in Figure 5. Interesting to note is, that temperatures above 70°C are located less than 4 mm from the electrodes. If we approximate this volume with four cylinders, each with a radius of 4 mm and height of 28 mm (length of active electrode region with 4 mm added on either side), the total volume of high temperature caused by the electrodes is 5.6 cm³, which is consistent with the volume of tissue above 50°C shown in Figure 5.

The curve in Figure 5 shows, that the 63% probability of thermal damage, determined by the Arrhenius rate equation, increases strongly in the first 250 s while later the slope levels off. This is caused by the fast increase in temperature around the electrodes, and then a slower increase in temperature in the more distant areas. Finally, the slope gets flatter, since the heating does not extend further from the electroporated area, the pulse amplitudes start to decrease, and diffusion moves the heat into tissue further away.

Discussion

The presented numerical results and clinical follow-up show that IRE is efficient at treating tumors in the immediate vicinity of major blood vessels. Since IRE is unaffected by the cooling of blood vessels, it is supposed to be not limited by their vicinity. The results of our computational model show a good correlation between the modelled IRE, electrical measurements during treatment, and imaging results. The tumor treatment has been classified as a complete ablation, and has shown no recurrence in the 6 months follow-up.

With the number, amplitude, and duration of pulses in the presented treatment, it is therefore clear, that a non-negligible temperature rise occurs. Since IRE has also been classified as a non-thermal tissue ablation technique in the literature[24,30], it needs to be clarified, that non-thermal does not indicate that there is no temperature rise, but rather, that the temperature is not the main mechanism which induces cell death. Our model clearly shows
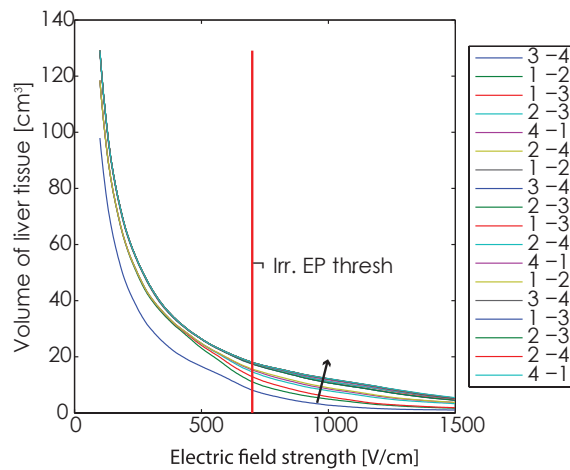
FIGURE 3. Electric field coverage in the liver tissue. The tumor tissue is not included in the volume on this graph. The graph shows the combined maximum fields in the liver following each electrode pair. Electrode pair progression is the same as in Table 3. Arrow indicates the direction of increase of coverage with delivery of successive electric pulses.
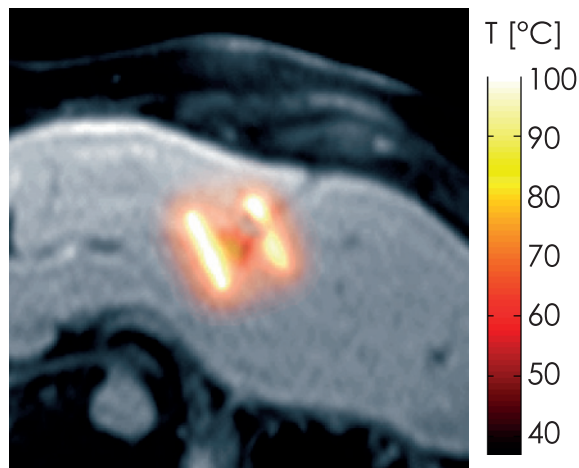
FIGURE 4. One slice showing computed temperature distribution after all pulses from the 7st pulse train (electrode pair 1 – 2 at 3000 V) superimposed on the corresponding MRI slice of the model.

that some areas of the lesion do heat up significantly (Figure 5), and the temperature rise is also consistent with experimental results from the literature.[31] Although our results show, that IRE is not an exclusively nonthermal treatment, *i.e.* there is significant heating present in the vicinity of electrodes, the total treatment volume is significantly higher than the volume based on thermal effects would be expected. A limitation of the model is, that we assumed that pulses were delivered constantly at 1 Hz, while in reality, the pulses were delivered in synchronization with the patient's ECG, which can realistically be up to 100 beats per minute, and would consequently result in a
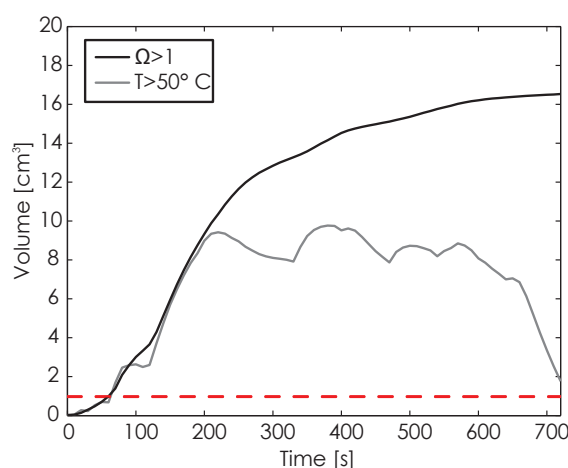
FIGURE 5. Graph of the total volume of tissue with Arrhenius integral above 1, indicating a high probability of thermal damage. Second graph shows the volume of tissue above 50°C, which is consistent with the volume of tissue around the electrodes.

higher temperature rise. In Figure 4, some areas in immediate vicinity of the electrodes are heated to temperatures of more than 100°C, because there was no term for boiling included in the numerical model. In fact, these high temperatures could indicate that some tissue boiling actually occurs near the electrode tips. This could explain the gas bubbles visible in the post-treatment CT images, and which are consistent with reports in the literature.[32] Another reason for these findings could be a gas formation due to electrolysis.[33] However, the temperature drops to below 70°C approximately 4 mm away from the electrodes in this specific case.

The coverage of the target tumor with electric fields was very high. The IRE threshold electric field, which depends on the type of number, duration of pulses, and tissue types of liver tumors has not been firmly established yet.[6] In this work, we assumed a value of 800 V/cm for tumor tissue. Nevertheless it can be seen in Figure 2, that almost the whole tumor is covered by electric field of this strength already in the first two pulse trains between electrode pairs 3-4 and 1-2. That, and the very high temperatures achieved in the model seem to indicate, that the used voltages and pulse numbers[34] were considerably higher than necessary to achieve complete treatment of the tumor.

When liver tumors are surgically treated, at least a safety margin of 0.5 to 1 cm of liver tissue around the tumor is resected to ensure removal of any micrometastases surrounding the tumor and thereby to prevent local tumor recurrence. For the same reason there is a need to achieve a similar

safety margin around the tumor in IRE treatments as well, and the IRE lesion in the presented case is larger than this goal. Assuming an elliptical approximation of the tumor, the volume of an ellipsoid with the semi-axes increased by 1 cm relative to the tumor, the required lesion volume would be 18.05 cm³. This corresponds also to the presented case and should be accounted for every treatment planning.

Conclusions

Treatment planning using accurate computer models was recognized as important for electrochemotherapy and irreversible electroporation.[2,9,23,35,36] On the one hand appropriate numerical treatment planning assures sufficient coverage of the clinical target volume with electric field sufficiently high for efficient tumor treatment also in the vicinity of blood vessels[15] and thereby to prevent local recurrences. On the other hand it enables the prediction and control of temperature thus avoiding thermal tissue damage in critical structures, such as nerves or bile ducts. Regarding the strength of the electric field in the presented case, significant overtreatment can be assumed, since electric fields in the tumor were higher than 900 V/cm. In the future monitoring of electric field in real time[37] and fast near-real time treatment planning will improve the adjustment of the electric pulse parameters. This should allow to preserve the efficiency and reliability of the treatment by avoiding heat induced adverse events. More precise planning will also enable the treatment of larger targets, while limiting thermal damage.[38] An important finding of this study was, that the most heating occurs at the surface of the electrodes. This fact should instruct the clinical user applying the manufacturer recommended voltage settings of the NanoKnife system to avoid placement of the electrodes at a distance of less than 4 mm from at-risk structures in comparable cases in order to avoid thermal damage to these structures.

Acknowledgements

References

1 Davalos R, Mir L, Rubinsky B. Tissue ablation with irreversible electroporation. *Ann Biomed Eng* 2005; **33:** 223-31.

2 Yarmush ML, Golberg A, Serša G, Kotnik T, Miklavčič D. Electroporation-based technologies for medicine: principles, applications, and challenges. *Annu Rev Biomed Eng* 2014; **16:** 295-320.

3 Jiang C, Davalos R, Bischof J. A review of basic to clinical studies of irreversible electroporation therapy. *IEEE Trans Biomed Eng* 2015; **62:** 4-20.

4 Martin RCG. Irreversible electroporation of locally advanced pancreatic head adenocarcinoma. *J Gastrointest Surg* 2013; **17:** 1850-6.

5 Scheffer HJ, Melenhorst MCAM, Vogel JA, van Tilborg AAJM, Nielsen K, Kazemier G, et al. Percutaneous irreversible electroporation of locally advanced pancreatic carcinoma using the dorsal approach: a case report. *Cardiovasc Intervent Radiol* 2015; **38:** 760–5.

6 Qin Z, Jiang J, Long G, Lindgren B, Bischof JC. Irreversible electroporation: an in vivo study with dorsal skin fold chamber. *Ann Biomed Eng* 2013; **41:** 619-29.

7 Neal RE, Garcia PA, Kavnoudias H, Rosenfeldt F, Mclean CA, Earl V, et al. In vivo irreversible electroporation kidney ablation: experimentally correlated numerical models. *IEEE Trans Biomed Eng* 2015; **62:** 561-9.

8 Arena CB, Mahajan RL, Nichole Rylander M, Davalos RV. An experimental and numerical investigation of phase change electrodes for therapeutic irreversible electroporation. *J Biomech Eng* 2013; **135:** 111009.

9 Garcia PA, Rossmeisl JH Jr, Neal RE 2nd, Ellis TL, Davalos RV. A parametric study delineating irreversible electroporation from thermal damage based on a minimally invasive intracranial procedure. *Biomed Eng Online* 2011; **10:** 34.

10 Haemmerich D, Wood BJ. Hepatic radiofrequency ablation at low frequencies preferentially heats tumour tissue. *Int J Hyperth* 2006; **22:** 563-74.

11 Pillai K, Akhter J, Chua TC, Shehata M, Alzahrani N, Al-Alem I, et al. Heat sink effect on tumor ablation characteristics as observed in monopolar radiofrequency, bipolar radiofrequency, and microwave, using ex vivo calf liver model. *Medicine* 2015; **94:** e580.

12 Poulou LS, Botsa E, Thanou I, Ziakas PD, Thanos L. Percutaneous microwave ablation vs radiofrequency ablation in the treatment of hepatocellular carcinoma. *World J Hepatol* 2015; **7:** 1054-63.

13 Golberg A, Bruinsma BG, Uygun BE, Yarmush ML. Tissue heterogeneity in structure and conductivity contribute to cell survival during irreversible electroporation ablation by «electric field sinks». *Sci Rep* 2015; **5:** 8485.

14 Marcan M, Pavliha D, Music MM, Fuckan I, Magjarevic R, Miklavcic D. Segmentation of hepatic vessels from MRI images for planning of electroporation-based treatments in the liver. *Radiol Oncol* 2014; **48:** 267-81.

15 Marčan M, Kos B, Miklavčič D. Effect of blood vessel segmentation on the outcome of electroporation-based treatments of liver tumors. *PloS One* 2015; **10:** e0125591.

16 Haemmerich D, Schutt D, Wright A, Webster J, Mahvi D. Electrical conductivity measurement of excised human metastatic liver tumours before and after thermal ablation. *Physiol Meas* 2009; **30:** 459-66.

17 Cukjati D, Batiuskaite D, Andre F, Miklavcic D, Mir L. Real time electroporation control for accurate and safe in vivo non-viral gene therapy. *Bioelectrochemistry* 2007; **70:** 501-7.

18 Corovic S, Lackovic I, Sustaric P, Sustar T, Rodic T, Miklavcic D. Modeling of electric field distribution in tissues during electroporation. *Biomed Eng OnLine* 2013; **12:** 16.

19 Hasgall P, Neufeld E, Gosselin M, Klingenböck A, Kuster N. IT'IS Database for thermal and electromagnetic parameters of biological tissues. 2011. Available at http://www.itis.ethz.ch/database. Accessed 15 March 2015.

20 Henriques FC. Studies of thermal injury; the predictability and the significance of thermally induced rate processes leading to irreversible epidermal injury. *Arch Pathol* 1947; **43:** 489-502.

21 Sel D, Cukjati D, Batiuskaite D, Slivnik T, Mir LM, Miklavcic D. Sequential finite element model of tissue electropermeabilization. *IEEE Trans Biomed Eng* 2005; **52:** 816-27.

22 Aström M, Zrinzo LU, Tisch S, Tripoliti E, Hariz MI, Wårdell K. Method for patient-specific finite element modeling and simulation of deep brain stimulation. *Med Biol Eng Comput* 2009; **47:** 21-8.

23 Županič A, Kos B, Miklavcic D. Treatment planning of electroporation-based medical interventions: electrochemotherapy, gene electrotransfer and irreversible electroporation. *Phys Med Biol* 2012; **57:** 5425-40.

24 Daniels C, Rubinsky B. Electrical field and temperature model of nonthermal irreversible electroporation in heterogeneous tissues. *J Biomech Eng-Trans ASME* 2009; **131:** 071006.

25 Lee YJ, Lu DSK, Osuagwu F, Lassman C. Irreversible electroporation in porcine liver: short- and long-term effect on the hepatic veins and adjacent tissue by CT with pathological correlation. *Invest Radiol* 2012; **47:** 671-5.

26 Pavliha D, Mušič MM, Serša G, Miklavčič D. Electroporation-based treatment planning for deep-seated tumors based on automatic liver segmentation of MRI images. *PloS One* 2013; **8:** e69068.

27 Miklavcic D, Snoj M, Zupanic A, Kos B, Cemazar M, Kropivnik M, et al. Towards treatment planning and treatment of deep-seated solid tumors by electrochemotherapy. *Biomed Eng Online* 2010; **9:** 10.

28 Long G, Bakos G, Shires PK, Gritter L, Crissman JW, Harris JL, et al. Histological and finite element analysis of cell death due to irreversible electroporation. *Technol Cancer Res Treat* 2014; **13:** 561-9.

29 Zhang Y, White SB, Nicolai JR, Zhang Z, West DL, Kim D, et al. Multimodality imaging to assess immediate response to irreversible electroporation in a rat liver tumor model. *Radiology* 2014; **271:** 721-9.

30 Scheffer HJ, Nielsen K, de Jong MC, van Tilborg AAJM, Vieveen JM, Bouwman A (R. A), et al. Irreversible electroporation for nonthermal tumor ablation in the clinical setting: a systematic review of safety and efficacy. *J Vasc Interv Radiol* 2014; **25:** 997-1011.

31 Wagstaff PGK, de Bruin DM, van den Bos W, Ingels A, van Gemert MJC, Zondervan PJ, et al. Irreversible electroporation of the porcine kidney: Temperature development and distribution. *Urol Oncol* 2015; **33:** 168. e1–168.e7.

32 Dollinger M, Jung E-M, Beyer L, Niessen C, Scheer F, Müller-Wille R, et al. Irreversible electroporation ablation of malignant hepatic tumors: subacute and follow-up CT appearance of ablation zones. *J Vasc Interv Radiol* 2014; **25:** 1589-94.

33 Meir A, Hjouj M, Rubinsky L, Rubinsky B. Magnetic resonance imaging of electrolysis. *Sci Rep* 2015; **5:** 8095.

34 Pucihar G, Krmelj J, Reberšek M, Napotnik TB, Miklavčič D. Equivalent pulse parameters for electroporation. *IEEE Trans Biomed Eng* 2011; **58:** 3279-88.

35 Garcia PA, Pancotto T, Rossmeisl JH, Henao-Guerrero N, Gustafson NR, Daniel GB, et al. Non-thermal irreversible electroporation (N-TIRE) and adjuvant fractionated radiotherapeutic multimodal therapy for intracranial malignant glioma in a canine patient. *Technol Cancer Res Treat* 2011; **10:** 73-83.

36 Miklavčič D, Serša G, Brecelj E, Gehl J, Soden D, Bianchi G, et al. Electrochemotherapy: technological advancements for efficient electroporation-based treatment of internal tumors. *Med Biol Eng Comput* 2012; **50:** 1213-25.

37 Kranjc M, Markelc B, Bajd F, Čemažar M, Serša I, Blagus T, et al. In Situ Monitoring of electric field distribution in mouse tumor during electroporation. *Radiology* 2015; **274:** 115-23.

38 Garcia PA, Davalos RV, Miklavcic D. A numerical investigation of the electric and thermal cell kill distributions in electroporation-based therapies in tissue. *PloS One* 2014; **9:** e103083.

research article

Central nervous system imaging in childhood Langerhans cell histiocytosis – a reference center analysis

Luciana Porto[1], Stefan Schöning[2], Elke Hattingen[1], Jan Sörensen[2], Alina Jurcoane[1], Thomas Lehrnbecher[2]

[1] Neuroradiology Department, Johann Wolfgang Goethe University, Frankfurt/Main, Germany

[2] Pediatric Hematology and Oncology, Hospital for Children and Adolescents, Johann Wolfgang Goethe University, Frankfurt/Main, Germany

Correspondence to: Thomas Lehrnbecher, Pediatric Hematology and Oncology, Hospital for Children and Adolescents, Johann Wolfgang Goethe University, Theodor-Stern-Kai 7, D-60590 Frankfurt, Germany. Phone: +49 69 6301 83481; Fax: +49 69 6301 6700; E-mail: Thomas.Lehrnbecher@kgu.de

Disclosure: No potential conflicts of interest were disclosed.

This work is dedicated to Robert Arceci.

Background. The aim of our study was (1) to describe central nervous system (CNS) manifestations in children with Langerhans cell histiocytosis (LCH) based on images sent to a reference center and meeting minimum requirements and (2) to assess the inter-rater agreement of CNS-MRI results, which represents the overall reproducibility of this investigation.

Methods. We retrospectively reviewed brain MRI examinations in children with LCH, for which MRI minimum requirements were met. Abnormalities were rated by two experienced neuroradiologists, and the inter-rater agreement was assessed.

Results. Out of a total of 94 imaging studies, only 31 MRIs met the minimum criteria, which included T2w, FLAIR, T1w images before/after contrast in at least two different section planes, and thin post contrast sagittal slices T1w through the *sella*. The most common changes were osseous abnormalities, followed by solid enlargement of the pineal gland, thickened enhancing stalk and signal changes of the dentate nucleus. Whereas inter-rater agreement in assessing most of the CNS lesions was relatively high ($\kappa > 0.61$), the application of minimum criteria often did not allow to evaluate the posterior pituitary.

Conclusions. The diversity of radiological protocols from different institutions leads to difficulties in the diagnosis of CNS abnormalities in children with LCH. Although the inter-rater agreement between neuroradiologists was high, not all the LCH manifestations could be completely ruled out when using the minimum criteria. Brain MRIs should therefore follow LCH guideline protocols and include T1 pre-gadolinium sagittal images, and be centrally reviewed in order to improve the comparison of clinical trials.

Key words: Langerhans cell histiocytosis; child; central nervous system; magnetic resonance imaging

Introduction

Langerhans cell histiocytosis (LCH) is a rare disease of the monocyte-macrophage system, seen mainly in children, but which can occur in any age group. The clinical presentation of the disease may range from a self-healing bone-lesion to multi-system life-threatening disease. The choice of appropriate therapy is therefore a significant challenge, with treatment options varying from watch-and-wait to intensive chemotherapy.[1,2] The pathogenesis of LCH remains unresolved, with data supporting both malignant transformation and immune dysregulation.[1,3]

Whereas skin and bone lesions are the most frequent manifestations of LCH, central nervous system (CNS) lesions are less common, and a wide variety of CNS findings have been described by magnetic resonance imaging (MRI).[1,3,4] Unfortunately, many centers often do not follow a standardized protocol when evaluating these patients, or are unaware of potential complications such as degenerative CNS changes.[5] It is thus important to evaluate the reliability of MRI in diagnosing CNS changes. The aim of our study was (1) to describe CNS manifestations of LCH in children based on images sent to a reference center and meeting minimum requirements and, more importantly, (2) to assess the inter-rater agreement of CNS-MRI results, which represents the overall reproducibility of this investigation in this patient population.

Patients and methods

Patients and MR imaging

As the national reference center for German childhood LCH, we regularly receive clinical data and imaging studies from children and adolescents with LCH. We included in our analysis all children with biopsy proven LCH from whom we had received MRI studies during the 2-year period between 2012 to 2014; notably, children could have had also MRI studies performed prior to 2012. Since the centers where the patient was treated often used different MR protocols, we included only patients with the following MR image sequences in the analysis: (1) Sagittal T1-weighted (w) images post contrast, permitting evaluation of the infundibulum (the majority of the images did not include sagittal T1-w pre contrast, with the result that this sequence could not be included as a minimum criterion); (2) T2-w images, fluid attenuated inversion recovery (FLAIR), and (3) T1-w images pre and post contrast in at least two different section planes. Enlargement of the pineal gland was defined as described previously by Sumida *et al.*[6]

Single and multisystem LCH as well as CNS risk lesions were defined according to the guidelines of the LCH study protocols.[4] The study has been approved by the local Ethics committee.

Statistical analysis

In addition to the neuroradiologist who references cerebral MRI studies of children with LCH in Germany (LP), MRIs were assessed by a second senior neuroradiologist. The inter-rater agreement was evaluated by the percent agreement (uncorrected) and the Cohen's Kappa κ index (corrected for chance effects). Substantial or almost perfect agreement was defined for κ values between 0.61–1.0.[7] For the analysis, the software R Statistics 2.15.1 (http://www.R-project.org/) in combination with functions from the packages "irr" and "caret" were used.[8] The results of both the reference neuroradiologist (LP) and the inter-rater agreement are reported.

Results

Patients´ characteristics

Clinical data and imaging studies were available in a total of 94 children with LCH. Cerebral MRI was performed in these children for a variety of reasons such as the presence of neurological abnormalities (*e.g.*, diabetes insipidus (DI)), for further evaluation in patients with involvement of the skull/craniofacial bones, or according to the physician´s discretion (*e.g.* the involvement of the mandibula or the cervical vertebrae). Only brain imaging studies of 31 patients (22 of whom were boys) met the inclusion criteria of the study. Eleven children suffered from unifocal and 5 other from multifocal bone disease. Localized LCH of the skull was seen in 11 patients. Nine children were affected by multisystem LCH. Eleven children suffered from DI, and 2 other children had endocrine disorders other than DI. With the exception of 2 children presenting with absence epilepsy and muscular hypotonia, respectively, no neurological abnormalities were detected in any patient (Table 1).

The median age of the patients at the time of cranial MRI was 7 years (range 0.5–17 years), and the median time between the diagnosis of LCH and cranial MRI was 70 days (range 0–10 years). 11 patients had not received treatment for LCH at the time of MRI.

MR imaging and correlation with clinical data

The most common MRI changes were osseous (55%), followed by solid enlargement of the pineal gland (45%), a thickened enhancing stalk (32%) and signal changes of the dentate nucleus (29%). Occasionally, hyperintensity in the hippocampus, parenchymal/meningeal enhancement and white matter hyperintensity were observed.

TABLE 1. Patients´ characteristics and cerebral magnetic resonance imaging (MRI) finding in 31 children and adolescents with Langerhans cell histiocytosis (LCH)

| ID | Sex | Age at Imaging (yrs) | Time Diagnosis - Imaging | Pattern of LCH[1] | | | DI | Clinical Symptoms | | Therapy[2] | Cerebral MRI Abnormalities | | |
				Single-system	Multi-system	CNS-Risk		Endocrine (other than DI)	Other		Dentate nucleus	Pituitary stalk	Pineal
1	M	17	<10 d	y			y					y	Y
2	M	7	<10 d	y		y				y			
3	M	11	<10 d	y						y			
4	M	15	10 yrs		y		y			y	Y	y	Y
5	F	3	170 d		y					y			Y
6	M	1	<10 d	y									
7	M	3	<10 d	y									
8	M	8	7 yrs		y		y			y		y	Y
9	F	9	18 mths	y		y			Absence seizures	y			Y
10	M	11	8 mths	y				Somatomegaly		y			Y
11	M	15	3 mths	y						y	Y		
12	F	3	3 yrs		y	y	y			y	Y		Y
13	F	14	2 mths	y			y				Y	y	
14	M	3	2 mths		y	y	y		Muscular hypotonia	y		y	Y
15	F	1	10 d	y			y						Y
16	M	3	2 yrs		y					y	Y		
17	M	15	3 yrs	y									
18	M	5	<10 d	y									Y
19	M	1	< 10d	y		y				y	Y		
20	F	10	5 yrs	y			y			y	Y		
21	M	9	<10 d	y		y							
22	F	0,5	< 10d		y	y				y			
23	M	3	2 yrs		y					y	Y		Y
24	F	10	2 mths	y						y			Y
25	M	17	3 yrs		y		y			y		y	
26	M	11	<10 d	y								y	
27	M	6	22 d	y						y			
28	M	5	3 yrs	y			y	Hypopituitarism		y	Y	y	Y
29	M	14	<10 d	y		y				y			
30	M	11	<10 d	y			y					y	
31	F	6	3 mths		y		y					y	y

y represents "present", blanks represent "not present". [1] The pattern of LCH single- and multi-system LCH as well as central nervous system (CNS) risk lesions were defined according to the guidelines of the LCH study protocols [Ref. 5]; [2] Therapy given prior to or at the time of cerebral imaging consisted of regimens according to LCH or to modified LCH protocols; d = day; DI = diabetes insipidus; f = female; m = male; mth = month; yr = year

Tumorous/granulomatous lesions

Hypothalamic-pituitary axis involvement, hypothalamus

Enhancement and thickening of the pituitary stalk > 3 mm were seen in 10 patients (32%) (Table 1). Seven of the 12 available pre contrast MR sagittal images demonstrated loss of bright spot. Nine patients with abnormalities of the pituitary stalk suffered from DI, whereas 1 patient had no clinical manifestation of DI. Seven patients had DI and CNS risk lesions, of whom five patients had additional multisystem LCH.

Pineal abnormalities

Solid enlargement of the pineal gland with enhancement was observed in 14 patients (45%). Enlargement was defined when the height of the pineal gland was more than 3.5 mm in patients younger than two years and as more than 4.5 mm in patients older than 2 years, respectively.[6] In 6 patients, abnormalities were seen in both the pituitary stalk and pinealis, whereas in 12 patients, only one of the structures was affected (pituitary stalk [4], pineal enlarged enhancement [8]).

Extra-axial space involvement

4 patients (13%) presented with dural enhancement. All these patients had osseous lesions combined with epidural and subdural involvement (Figure 1). None of the patients presented with isolated dura-base masses or hypointensity on T2w at the choroid plexus.
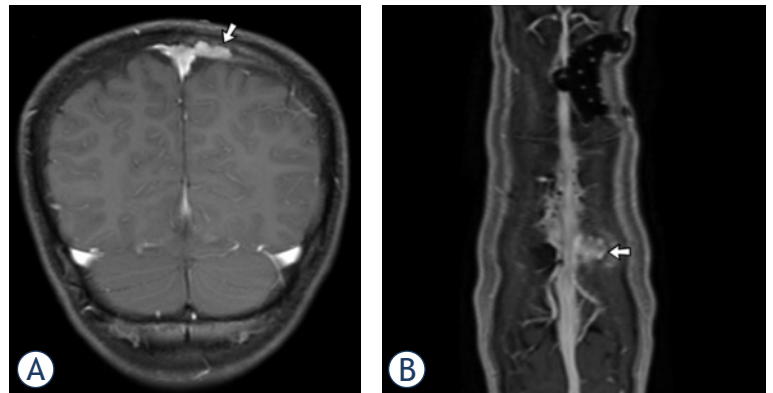
FIGURE 1. T1-w MR-images in an 11-year-old boy with LCH (patient ID #26). **(A)** Coronal enhanced T1-MR image reveals an osseous enhancing mass (arrow) combined with epidural und subdural involvement along the left side of the superior sagittal sinus. **(B)** Enhanced T1-MPRage-Image with reconstruction shows the mass (arrow) closely related to the superior sagittal sinus. Note the infiltration of the dural venous plexus, which is located within the inner portion of the dura. The dural plexus enhances in particular parasagittally on the left, where it connects to the sagittal sinus. There was no thrombus within the sagittal sinus.

Enhancement due to intracerebral granulomatous lesions

5 patients (16%) presented with parenchymal enhancement. Pontine enhancement was seen in 2 cases (Figures 2 and 3), and supratentorial enhancement in 4 patients. One patient presented with simultaneous infra- and supratentorial enhancement.

Lytic lesions of skull

Osseous lesions in the skull, skull base and craniofacial bones were seen in 17 patients (55%); of
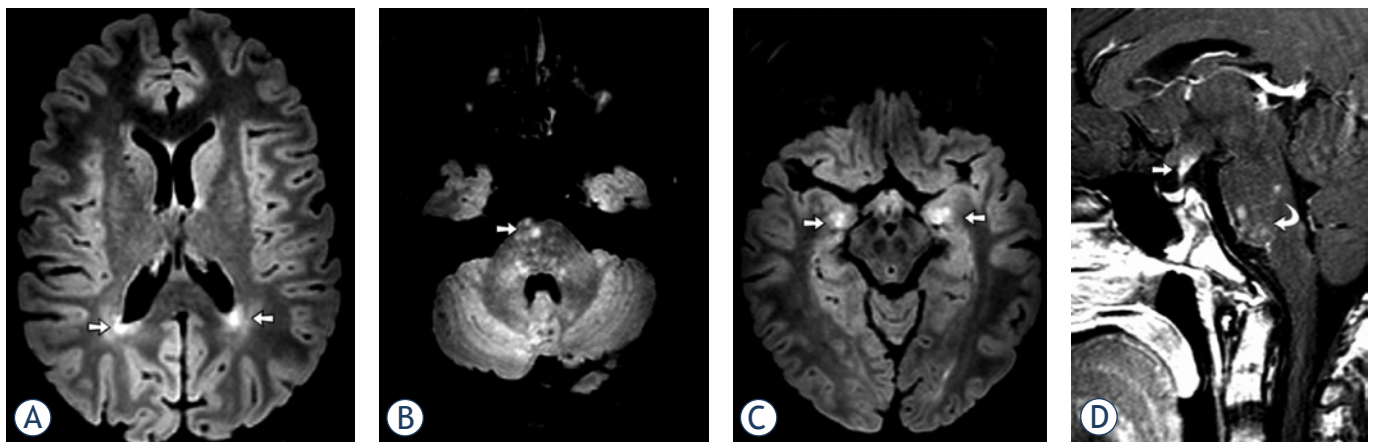
FIGURE 2. Cerebral MRI in a 15-year-old-boy with LCH (patient ID #4). **(A-C)** FLAIR images show high-signal lesions (arrows) in the deep white matter, in pons and hippocampus. After contrast note the parenchymal (partial nodular pattern, curved arrow) and perivascular enhancement. The classical finding, enhancement and thickening of the pituitary stalk, was also present (straight arrow).
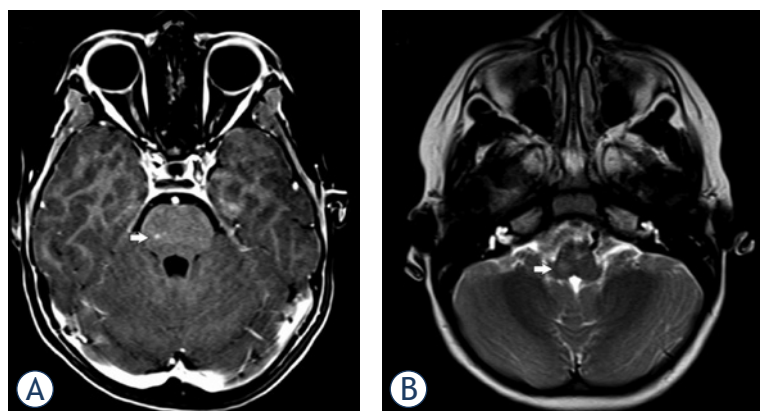
FIGURE 3. Cerebral MRI in a 8-year-old-boy (patient ID #8). **(A)** T1-w image after contrast shows enhancing lesions (arrow) in the pons. **(B)** Additional lesions were seen in medulla oblongata (arrow).
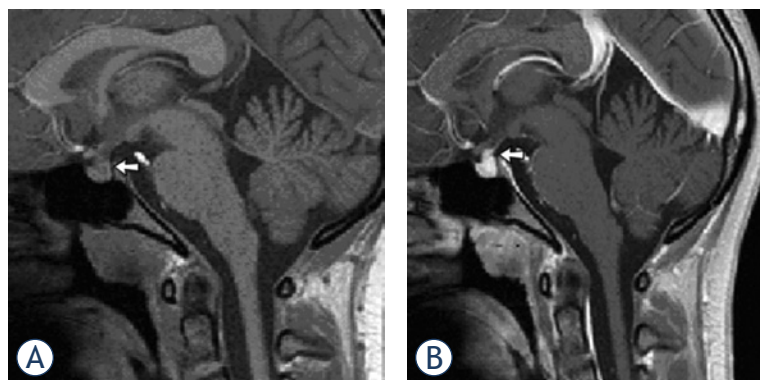
FIGURE 4. Sagittal T1-w MR image in a 14-year-old girl (patient ID #13). **(A)** T1-w image without contrast shows the typical lack of high signal intensity of the posterior pituitary (arrow). **(B)** After contrast note the enhancement and thickening of the pituitary stalk (arrow).

those, 4 had dural infiltration, 4 had extension of the disease within the intraconal space with enhancement, and 3 had bone destruction with involvement of the mastoid.

Non-tumorous, non-granulomatous lesions

Dentate nucleus

The evaluation of the dentate nucleus as a classical location of deep grey matter affected by LCH was limited by artefacts resulting in a relatively low inter-rater agreement ($\kappa < 0.61$). None of the 9 children with dentate nucleus abnormalities showed neurological symptoms such as tremor, dysarthria, or ataxia. Whereas in 6 of the children, LCH had been diagnosed more than 1 year prior to the abnormal MRI finding; the affection of the dentate

nucleus was seen in 1 untreated patient at the time of diagnosis of LCH.

White matter changes

A hyperintense signal on T2w and FLAIR images in the supratentorial white matter were observed in 2 patients (Figure 2) and were likely in 6 patients (representing a total of 25% of patients). The lesions were symmetrical and showed a vascular pattern. These white matter changes were associated with pons involvement in 2 patients, of which one showed enhancement (Figure 2).

Basal ganglia and hypothalamus

Changes in basal ganglia or in the hypothalamus were not observed in any patient.

Atrophy

No signs of cerebellar, midbrain, or supratentorial atrophy were noted for any patient

Inter-rater agreement

The diversity of CNS lesions may lead to difficulties in diagnosis, which may have a significant impact on treatment and outcome. The inter-rater agreement in this study was 69–100%. Substantial inter-rater agreement ($\kappa > 0.61$) was found for the following variables: enlarged pituitary stalk/mass, bone changes, pineal enlarged enhancement, white matter and hippocampal hyperintensity on T2w, as well as for parenchymal and meningeal enhancement. Partial volume effects and artefacts limited the MRI evaluation and the inter-rater reliability in the area of the dentate nucleus ($\kappa = 0.31$). Other variables, such as the hyperintense signal on T2w and FLAIR in the lentiform nucleus, hypothalamus or cerebellum had low occurrence rates and are therefore unreliable agreement indices.

Discussion

Since LCH is a rare disease, research on radiological CNS abnormalities is limited. In addition, the variable quality of diagnostics makes comparing treatment and outcome difficult. Our aim was to describe CNS manifestations in children with LCH based on images sent to a reference center and meeting minimum requirements. The second and more important goal was to evaluate the reliability of the MRI findings based on the inter-rater agreement of two senior neuroradiologists.

Only a total of 33% of the cerebral MRIs sent for reference met the minimum requirements of the study. Unfortunately, we had to omit pre contrast sagittal T1-w as a minimum criterion, since most imaging studies did not include this sequence. The lack of thin T1 sagittal pre contrast images can be explained by the fact that the German public health system only pays for a maximum of 4 MR sequences.

Hypothalamic-pituitary axis

Diabetes insipidus, as the most common endocrinopathy in LCH, is caused by inadequate anti-diuretic hormone (ADH) secretion. Corroborating our data, DI occurs in approximately 25% of all patients with LCH or in approximately 50% of patients with multisystem disease, mainly in those with skull and orbital involvement.[9-12] The typical MRI finding in DI is the lack of high signal intensity of the posterior pituitary on T1w images before contrast ("loss of bright spot"), which correlates with the loss of ADH-containing granules, and is often associated with enhancement and thickening of the pituitary stalk >3 mm (Figure 4).[13] In our series, loss of bright spot was seen in 7 patients, but it is important to note that this result may be biased as usually only children with DI or anterior pituitary hormone deficiency have a typical targeted MRI examination of the pituitary region which includes T1w without gadolinium. Enhancement and thickening of the pituitary stalk were seen in 10 of 31 (32%) of our patients with high inter-rater agreement. Abnormalities of the pituitary stalk were present in 9 of the patients with DI, but notably, also in one patient without DI. Interestingly, over the three year follow-up period, this patient, who received prolonged chemotherapy for primary and relapsed LCH, did not develop DI. Future research is needed to address which children with LCH and associated abnormalities of the pituitary stalk will develop DI at a later time-point,[14] and, more importantly, whether treatment in these children could prevent this specific complication.

Pineal abnormalities

Enhancement of the solid enlarged pineal gland was seen with a high inter-rater agreement in 14 patients (45%), which is considerably higher than reported previously (3% and 15%).[15,16] This difference could be due to several reasons: Firstly, different MRI protocols make it difficult to evaluate pineal enhancement, and the lack of high-resolution thin-section imaging may result in false-negative findings. Secondly, the normal pineal gland tissue

enhances with gadolinium on MRI because of the lack of a blood-brain barrier. This means that contrast enhancement within the pineal gland, especially in teenagers, does not necessarily mean abnormality, *e.g.* infiltration. There is a greater prevalence of ring-like pineal glands in children than in adults, and it was postulated that these glands may form pineal cysts in the future, which would account for the higher percentage enhancing mass in children and teenagers, and of cysts in adulthood and the increased incidence on autopsy reports.[17] It is also important to note that the results of the pineal gland should be interpreted carefully, since there is a large variation of the size of the gland in all age groups.[6]

In contrast to a previous study, we did not find a correlation between abnormalities in the pituitary stalk and the pineal gland.[15] Whereas in 6 patients of our series, both structures showed an abnormality, 12 patients presented with an irregularity in one structure only. It was speculated whether co-existing changes, which have also been observed in other diseases, might be caused by the functional interactions of both structures.[18] However, as noted before, the intrinsic enhancement of the pineal gland makes the evaluation of this structure difficult.

Lytic lesions of skull

Craniofacial involvement is the most common presentation of CNS-LCH. In line with other reports, the frequency of these abnormalities in the present study was 55%.[19,20]

Intracranial non-tumorous lesions including neurodegenerative changes

Intra-axial neurodegenerative parenchymal changes are among the most frequent patterns of CNS-LCH.[16] Neurodegenerative grey-matter changes mainly involve the dentate nucleus and basal ganglia, with a bilaterally symmetrical, hyperintense signal in T1w and T2w as key radiological features.[4] Alterations in the signal-intensity may reflect the loss of neurons, demyelination, gliosis, and inflammation.[4,21] It was speculated that chronic or recurrent granulomatous lesions in the craniofacial bones result in an intracranial process which includes chemokine-mediated tissue damage or an autoimmune response to brain tissue induced by antigen-presentation through Langerhans cells.[4] If this is the case, both the frequency and severity of neurodegenerative lesions might increase with older age of patients with LCH. This hypothesis could explain the lower frequency of grey-matter

changes in the dentate nucleus in our study (29%) compared to a previous analysis (40%).[19] The oldest patient in the present study was 17 years old, whereas Prayer et al included patients up to 47 years of age.[19] In addition, the short follow-up is a limiting factor of our study. On the other hand, it is important to note that the inter-rater agreement assessing the dentate nucleus was moderate due to potential volume effects and artefacts. Interestingly, one 14-year-old patient demonstrated radiological signs of neurodegeneration without having received treatment for LCH. In contrast to a previous study, we did not see a correlation between radiological signs of neurodegeneration and pituitary involvement of LCH.[22] We are currently designing a study which closely monitors children with LCH and radiological signs of neurodegeneration over a long period of time in order to identify risk factors for patients who will ultimately develop clinical symptoms of neurodegeneration.

Inter-rater variability

To date, no study has evaluated the inter-rater variability of CNS abnormalities of children with LCH. This, however, is important, since a valid evaluation is the prerequisite for comparing clinical trials. Although our study demonstrated a high inter-rater agreement for most of the MRI-findings in which minimal criteria were met, the data suggest that cerebral imaging should be centrally referenced as is the case for many pediatric tumors. The inter-rater agreement may even be significantly lower when MRI is performed outside a tertiary referral hospital or by a general radiologist. In addition, it would be interesting to evaluate the inter-rater variability between different reference centers, but this is beyond the scope of this study.

Limitations of this study

As in other studies in children with LCH, cerebral MRI was not performed in all patients, but only in those who had already developed or were at high risk for CNS complications, or according to the treating physician´s discretion. There was therefore an inherent selection bias as not all LCH patients had an MRI.

Although we included only patients with a minimum number of MR-image sequences, the study included imaging from various institutions with heterogeneous protocols making it difficult to assess all the CNS features of LCH. In addition, T1 pre-gadolinium imaging was not performed in most patients and it was therefore often not possible to assess the posterior pituitary bright spot.

Conclusions

The majority of the CNS-images sent for reference did not follow previous guidelines[5], and only one-third of the MRI could be included in this analysis. In order to improve the comparison of clinical trials in the future, all cerebral MRI should meet standardized protocols, which include the assessment of the posterior pituitary bright spot, and should be centrally reviewed. The following protocol is recommended: axial T2w, Fluid Attenuated Inversion Recovery (FLAIR) and T1 w of the entire brain; axial and coronal T1W post contrast of the entire brain (at least one with fat saturation to evaluate lesions of skull). In addition, the hypothalamo-pituitary region should be evaluated with ≤ 3 mm slice thickness with and without contrast enhancement.

In conclusion, (1) CNS manifestations are frequent, but result in variable findings in children with LCH, (2) the assessment of the posterior pituitary was not possible in most of the referred images, and (3), although the inter-rater agreement between neuroradiologists was high, the MRI diagnosis based on referred images was not suitable to rule out all LCH CNS manifestations.

References

1. Delprat C, Arico M. Blood spotlight on Langerhans cell histiocytosis. *Blood* 2014; **124:** 867-72.

2. Badalian-Very G, Vergilio JA, Degar BA, Rodriguez-Galindo C, Rollins BJ. Recent advances in the understanding of Langerhans cell histiocytosis. *Br J Haematol* 2012; **156:** 163-72.

3. Vaiselbuh SR, Bryceson YT, Allen CE, Whitlock JA, Abla O. Updates on histiocytic disorders. *Pediatr Blood Cancer* 2014; **61:** 1329-35.

4. Grois N, Fahrner B, Arceci RJ, Henter JI, McClain K, Lassmann H, et al. Central nervous system disease in Langerhans cell histiocytosis. *J Pediatr* 2010; **156:** 873-81, 881.e1.

5. Haupt R, Minkov M, Astigarraga I, Schafer E, Nanduri V, Jubran R, et al. Langerhans cell histiocytosis (LCH): guidelines for diagnosis, clinical work-up, and treatment for patients till the age of 18 years. *Pediatr Blood Cancer* 2013; **60:** 175-84.

6. Sumida M, Barkovich AJ, Newton TH. Development of the pineal gland: measurement with MR. *Am J Neuroradiol* 1996; **17:** 233-6.

7. Landis J, Koch G. An application of hierarchical kappa-type statistics in the assessment of majority agreement among multiple observers. *Biometrics* 1977; **33:** 363-74.

8. Kuhn M. Building predictive models in R using the caret package. *J Statistical Software* 2008; **28:** 1-26.

9. Nanduri VR, Bareille P, Pritchard J, Stanhope R. Growth and endocrine disorders in multisystem Langerhans' cell histiocytosis. *Clin Endocrinol (Oxf)* 2000; **53:** 509-15.

10. Grois N, Potschger U, Prosch H, Minkov M, Arico M, Braier J, et al. Risk factors for diabetes insipidus in langerhans cell histiocytosis. *Pediatr Blood Cancer* 2006; **46:** 228-33.

11. Donadieu J, Rolon MA, Thomas C, Brugieres L, Plantaz D, Emile JF, et al. Endocrine involvement in pediatric-onset Langerhans' cell histiocytosis: a population-based study. *J Pediatr* 2004; **144:** 344-50.

12. Haupt R, Nanduri V, Calevo MG, Bernstrand C, Braier JL, Broadbent V, et al. Permanent consequences in Langerhans cell histiocytosis patients: a pilot study from the Histiocyte Society-Late Effects Study Group. *Pediatr Blood Cancer* 2004; **42:** 438-44.

13. Tien R, Kucharczyk J, Kucharczyk W. MR imaging of the brain in patients with diabetes insipidus. *Am J Neuroradiol* 1991; **12:** 533-42.

14. Fahrner B, Prosch H, Minkov M, Krischmann M, Gadner H, Prayer D, et al. Long-term outcome of hypothalamic pituitary tumors in Langerhans cell histiocytosis. *Pediatr Blood Cancer* 2012; **58:** 606-10.

15. Grois N, Prosch H, Waldhauser F, Minkov M, Strasser G, Steiner M, et al. Pineal gland abnormalities in Langerhans cell histiocytosis. *Pediatr Blood Cancer* 2004; **43:** 261-6.

16. Chaudhary V, Bano S, Aggarwal R, Narula MK, Anand R, Solanki RS, et al. Neuroimaging of Langerhans cell histiocytosis: a radiological review. *Jpn J Radiol* 2013; **31:** 786-96.

17. Sener RN. The pineal gland: a comparative MR imaging study in children and adults with respect to normal anatomical variations and pineal cysts. *Pediatr Radiol* 1995; **25:** 245-8.

18. Warmuth-Metz M, Gnekow AK, Muller H, Solymosi L. Differential diagnosis of suprasellar tumors in children. *Klin Padiatr* 2004; **216:** 323-30.

19. Prayer D, Grois N, Prosch H, Gadner H, Barkovich AJ. MR imaging presentation of intracranial disease associated with Langerhans cell histiocytosis. *Am J Neuroradiol* 2004; **25:** 880-91.

20. D'Ambrosio N, Soohoo S, Warshall C, Johnson A, Karimi S. Craniofacial and intracranial manifestations of langerhans cell histiocytosis: report of findings in 100 patients. *Am J Roentgenol* 2008; **191:** 589-97.

21. Prosch H, Grois N, Wnorowski M, Steiner M, Prayer D. Long-term MR imaging course of neurodegenerative Langerhans cell histiocytosis. *Am J Neuroradiol* 2007; **28:** 1022-8.

22. Wnorowski M, Prosch H, Prayer D, Janssen G, Gadner H, Grois N. Pattern and course of neurodegeneration in Langerhans cell histiocytosis. *J Pediatr* 2008; **153:** 127-32.

Correlation of diffusion MRI with the Ki-67 index in non-small cell lung cancer

Adem Karaman[1], Irmak Durur-Subasi[1], Fatih Alper[1], Omer Araz[2], Mahmut Subasi[3], Elif Demirci[4], Mevlut Albayrak[4], Gökhan Polat[1], Metin Akgun[2], Nevzat Karabulut[5]

[1] Department of Radiology, Ataturk University, Medical Faculty, Erzurum, Turkey

[2] Department of Pulmonary Diseases, Ataturk University, Medical Faculty, Erzurum, Turkey

[3] Department of Thoracic Surgery, Erzurum Regional Training and Research Hospital, Erzurum, Turkey

[4] Department of Pathology, Ataturk University, Medical Faculty, Erzurum, Turkey

[5] Department of Radiology, Pamukkale University, Medical Faculty, Denizli, Turkey

Background. The primary objective of the study was to evaluate the association between the minimum apparent diffusion coefficient (ADC_{min}) and Ki-67, an index for cellular proliferation, in non-small cell lung cancers. Also, we aimed to assess whether ADC_{min} values differ between tumour subtypes and tissue sampling method.

Methods. The patients who had diffusion weighted magnetic resonance imaging (DW-MRI) were enrolled retrospectively. The correlation between ADC_{min} and the Ki-67 index was evaluated.

Results. Ninety three patients, with a mean age 65 ± 11 years, with histopathologically proven adenocarcinoma and squamous cell carcinoma of the lungs and had technically successful DW-MRI were included in the study. The numbers of tumour subtypes were 47 for adenocarcinoma and 46 for squamous cell carcinoma. There was a good negative correlation between ADC_{min} values and the Ki-67 proliferation index (r = -0.837, p < 0.001). The mean ADC_{min} value was higher and the mean Ki-67 index was lower in adenocarcinomas compared to squamous cell carcinoma (p < 0.0001). There was no statistical difference between tissue sampling methods.

Conclusions. Because ADC_{min} shows a good but negative correlation with Ki-67 index, it provides an opportunity to evaluate tumours and their aggressiveness and may be helpful in the differentiation of subtypes non-invasively.

Key words: diffusion weighted-magnetic resonance imaging; apparent diffusion coefficient; Ki-67 index; adenocarcinoma; squamous cell carcinoma

Introduction

Diffusion weighted magnetic resonance imaging (DW-MRI) is a promising MRI technique used in the evaluation of lung tumours. It has been increasingly used for the detection, differential diagnosis and evaluation of tumour characteristics, including grading and prediction of the therapeutic response.[1-7] DW-MRI is a functional imaging technique that reveals physiological information by quantifying the diffusion of water molecules in tissues. The extent of this diffusion is measured using the apparent diffusion coefficient (ADC). Malignant tissues tend to have a lower ADC and demonstrate higher signal intensity on a DW-MRI image due to their increased cellularity and larger nuclei with abundant macromolecular proteins.[8,9]

The Ki-67 protein (also known as MKI67) is a cellular proliferation marker. During interphase, the Ki-67 antigen can only be detected within the cell nucleus; however, in mitosis, most of the Ki-67 is relocated to the surface of the chromosomes. Ki-67 protein is present during all active phases of the cell cycle (G1, S, G2, and mitosis), but is absent in

resting cells (G0). The Ki-67 proliferation index, one of the biological markers used in histopathological evaluation, is an important criterion in the differentiation of benign and malignant tumours.[10-12] It is also correlated with the clinical course of cancer and has been shown to have prognostic value for treatment response, tumour recurrence and survival in brain, breast, bladder and prostate tumours, meningioma and nephroblastoma.[13-19] The Ki-67 index has also been used routinely in the evaluation of lung tumours and has been shown to be an important prognostic factor for lung cancer.[3,6,20-27] Although a few studies have evaluated the association of ADC with Ki-67 index in lung tumours[3,6], no study has previously investigated differences in the ADC/Ki 67 correlation in different tumour subtypes.

In this study, our primary objective was to evaluate whether there is an association between the minimum ADC (ADC_{min}), determined on DW-MRI, and Ki-67, which is a cellular proliferative index. Our secondary aim was to assess whether ADC_{min} values differ between the adenocarcinomas and squamous cell carcinomas of the lungs and also differ according to the pathologic sampling method used, surgical excision specimen and biopsied material.

Methods

Study population

Between January 2012 and December 2013, records for 104 consecutive patients with histopathologically proven primary adenocarcinoma and squamous cell carcinoma of the lungs, and who had technically successful images on DW-MRI were retrieved from the hospital's pathology database. The patients who were previously treated (n = 5) and\or had an interval of more than 15 days between DW-MRI and biopsy (n = 6) were excluded from the study. All measurements, including calculation of Ki-67 index and ADC_{min} values, were done in the same lesion for each patient. The protocol of the retrospective study was approved by the institutional ethics committee and the requirement for informed consent was waived.

Imaging technique, DW-MRI

It was performed with a 3 tesla scanner (MAGNETOM Skyra, Siemens Healthcare, Erlangen, Germany). Conventional MRI included an axial T1-weighted sequence (repetition time, 104 ms; echo time, 4.92 ms; 1 excitation) and an axial T2-weighted sequence (repetition time, 1400 ms; echo time, 101 ms; 1 excitation). Breath-free DW-MRI was performed in the axial plane using a single-shot, spin-echo echo-planar imaging sequence with the following parameters: repetition time, 6500 ms; echo time, 61 ms; real spatial resolution in the phase-encoding direction, 3.7 mm; flip angle, 90^0; diffusion gradient encoding in three orthogonal directions; b value b = 50, b = 400 and b = 800 s/mm^2; field of view, 380 mm x 380 mm x 310 mm; matrix size, 113 x 192; slice thickness, 6 mm; section gap, 0 mm; 2 signals acquired.

Image analysis

We analysed the lesions using DW-MRI images in association with T1- and T2-weighted images in order to identify accurately. The ADC of the tumour was then calculated to quantitatively analyse the degree of diffusion, using the following formula: $ADC = -\ln(S/S_0) / (b-b_0)$, where S_0 and S are the signal intensities, obtained at three different diffusion gradients (b = 50, b = 400 and b = 800 s/mm^2). The ADC maps were reconstructed at a workstation. While establishing the size and region for the ROI, positioning in the larger area was considered in order to minimize the effect of region on hemodynamic inhomogeneity of tumour by avoiding necrotic, cystic or calcific areas by referring to T2 and T1-weighted images.[28,29] The ADC_{min} values within the ROI were then used in statistical analyses (Figure 1). In analyses workstation (Syngo Via Console, software version 2.0, Siemens AG Medical Solutions, Erlangen, Germany) was used.

Calculation of Ki-67 index

Archived paraffin blocks belonging to the patients were transferred to polylysine glass slides with 4-micron thick sections. Immunochemistry was performed using a Lecia Bond-max automated immunostainer (Leica Microsystems, Newcastle, UK), as described manufacturers protocol. For Ki-67 staining, Ki-67 antibody (NCL-L-Ki67-MM1, monoclonal, 1:60, Novocostra, Newcastle, UK) was used. The sections prepared for examination were evaluated by two pathologists who were blinded to each-other. Firstly, ten areas having highest expression of Ki-67 were determined at low magnification. Then, these areas were further analysed at a single high power field (400 x magnification). Ki-67 expression was defined as the percent of Ki-67-positive tumour cells divided by the total number

of tumour cell within one high power field.[26,30] In the last step, Ki-67 index was calculated as the average percentage of those fields.
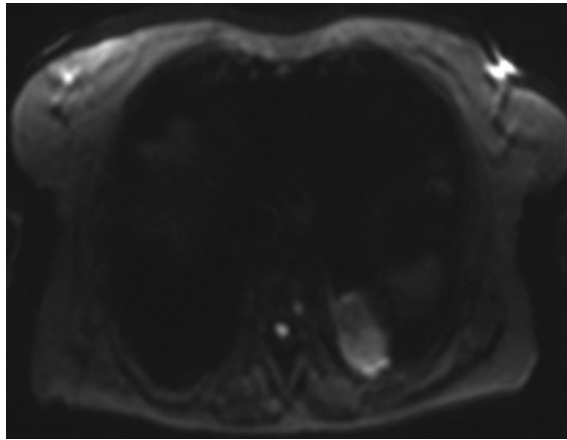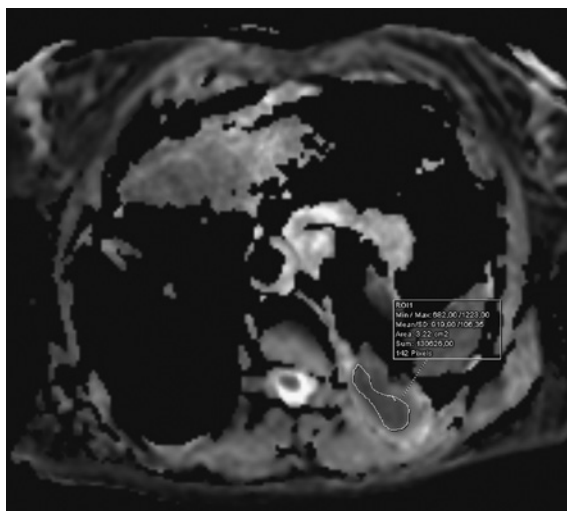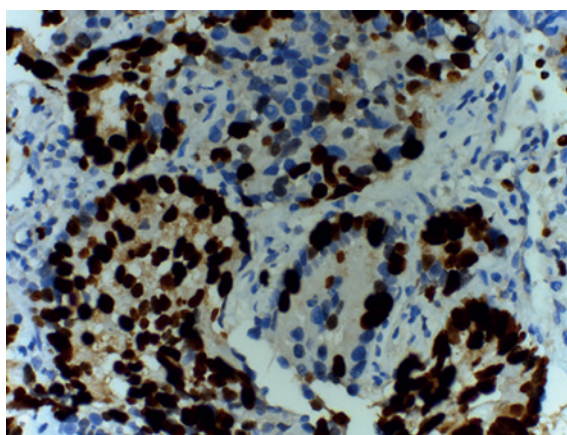
FIGURE 1. Diffusion-weighted (DW)-MRI, apparent diffusion coefficient (ADC) map of a 62-year-old female with adenocarcinoma. **(A)** Tumour shows heterogeneously high signal intensity on DW-MRI, for which the b value is 800 s/mm². **(B)** On the ADC map, the tumour demonstrates heterogeneous diffusion restriction. **(C)** Proliferative index 95% in glandular epithelium (Ki-67X400).

Statistical Analysis

Analyses were performed using IBM SPSS 20.0 for Mac software. The correlation between ADC_{min} and the Ki-67 index was evaluated using Spearman's correlation coefficient. Mann-Whitney U tests were used to assess the difference between the ADC_{min} and the Ki-67 index for the different tumour subtypes. A p value of less than 0.05 was considered statistically significant.

Results

Ninety three patients, with a mean age 65 ± 11 years ranged between 43 and 84, with histopathologically proven primary adenocarcinoma (n = 47) and squamous cell carcinoma (n = 46) of the lungs and had technically successful DW-MRI were included in the study. Histopathological diagnoses were obtained through transthoracic or transbronchial biopsy in 65 subjects and 28 patients underwent surgery.

The mean ADC_{min} value for all the lesions was 0.77 ± 0.15 x 10^{-3} mm²/sec (range, 0.50–1.00 x 10^{-3} mm²/sec). The mean ADC_{min} value for adenocarcinomas was 0.83 ± 0.12 x 10^{-3} mm²/sec and that of squamous cell carcinomas was 0.70 ± 0.16 x 10^{-3} mm²/sec; there was a significant difference between these values (p < 0.0001). The mean Ki-67 was 43.5 ± 22.2 for all the tumours (range, 5–96), with a mean of 30.8 ± 14.1 for adenocarcinomas and 55.9 ± 21.8 for squamous cell carcinoma; the difference between tumour subtypes was significant (p < 0.0001).

There was a negative correlation between ADC_{min} values and the Ki-67 proliferation index (p < 0.001, r = -0.837) (Figure 2). The ADC_{min} values were lower in the cases with higher Ki-67 grades. The mean ADC_{min} values and Ki-67 index for adenocarcinomas and squamous cell carcinomas of the lung are shown in Figure 3. There was no statistical difference of Ki-67 and ADC_{min} values between biopsied material and surgical specimen. The mean Ki-67 was 45.3 ± 22.8 vs 39.3 ± 19.8 and the mean ADC_{min} value was 0.76 ± 0.16x10^{-3} vs 0.78 ± 0.14 x 10^{-3} for biopsied material and surgical specimen, respectively. In the comparative evaluation of correlation between ADC_{min} and the Ki-67 proliferation index that measured either in surgical specimen or biopsied material, the Ki-67 index of surgical specimens was slightly better correlated with ADC_{min} values without statistical significance (r = -0.870 vs. -0.617) compared to biopsied material.
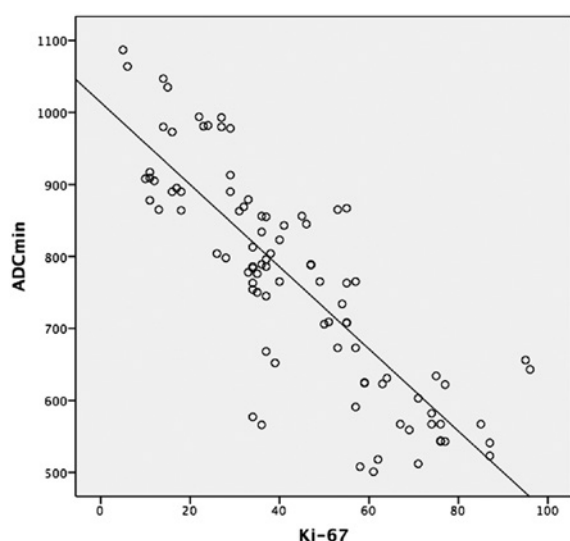
FIGURE 2. The graph shows a negative correlation between the minimum apparent diffusion coefficient (ADC$_{min}$) and the Ki-67 index in lung tumours (r = -0.837, p < 0.001).

FIGURE 3. The graph shows average minimum apparent diffusion coefficient (ADC$_{min}$) values for adenocarcinoma and squamous cell carcinoma according to Ki-67 index. Bars are for ADC$_{min}$ values and line is for Ki-67.

Discussion

Our results showed that there is a negative correlation between the ADC$_{min}$ and the Ki-67 index of lung cancers, which reflects aggressiveness of a tumour. ADC$_{min}$ values for adenocarcinomas were higher than those for squamous cell carcinomas. This finding indicates that ADC$_{min}$ may have a role in discriminating adenocarcinomas from squamous cell carcinomas, as well as being used for evaluating the aggressiveness of the tumour. Also, a low ADC$_{min}$ value can potentially be used as a non-invasive surrogate biomarker for the Ki-67 index for the evaluation of lung tumour characteristics, regardless of subtype.

Lung cancer is the leading cause of cancer-related deaths.[31] Until now, the Ki-67 proliferation index, reflecting aggressiveness of a tumour has been used to determine the prognosis. Malignant tumours are characterized by increased Ki-67 proliferation index due to their cellularity, larger nuclei with more abundant macromolecular proteins, a larger nuclear/cytoplasmic ratio and less extracellular space relative to normal tissue. As these characteristics also restrict the diffusion of water molecules, ADC$_{min}$ decreases in malignant tumours.[8,9,32]

Because ADC$_{min}$ is found to have stronger correlation with Ki-67 index compared to ADC$_{mean}$, we used ADC$_{min}$ in our study.[15] Apparent diffusion coefficient can be used in the non-invasive assessment of suspicious masses, for example, to differentiate metastatic lymph nodes from those that are benign when they cannot be differentiated by size criteria.[5]

ADC values also correlate with tumour grades.[4,17,18] Recent studies have shown that ADC may be more useful than FDG-PET in the differentiation of malignant tumours from benign lesions[3,6] and the new approaches using PET\MRI may provide more promising results in the future.[33] Among primary lung cancers, ADC values are usually low in cases with small cell carcinomas, but the values for adenocarcinomas and squamous cell carcinomas are usually similar.[3,4] However Matoba *et al.* stated that ADCs of well-differentiated adenocarcinoma appear to be higher than those of other histologic lung carcinoma types.[23] Our findings demonstrate that adenocarcinomas showed higher ADC values than squamous cell carcinomas, and had weaker staining diffusivity and intensity of Ki-67.

A high Ki-67 and low ADC$_{min}$ value indicates that a tumour has a high proliferation rate. Ki-67 values obtained using an invasive method reflect only the level in the sampled tissue; this is a particular problem when using biopsy. Since lung carcinomas are not always homogenous, the biopsy site can influence the results. This could be reflected in the fact that in our study the correlation between ADC$_{min}$ and Ki-67 proliferation index was stronger for surgical than for biopsy samples. Unlike these invasive sampling methods, ADC$_{min}$ values obtained by DW-MRI in a non-invasive manner can be calculated from anywhere in the tumour, providing an entire and reproducible assessment of the tumour. Furthermore, since the region with the lowest ADC$_{min}$ value is likely to be the most aggressive portion.[17,34] DWI could also help in the selection of an appropriate biopsy site within the tumour.

An association between the ADC value and the Ki-67 index has been shown for various kinds of tumours[2,14-18,34-38], including lung cancer.[3,6] Wang *et al.*, in their study on DWI in pancreatic endocrine tumours, reported a correlation coefficient of -0.70[2], while Onishi *et al.* reported a correlation coefficient of -0.825 for mucinous breast carcinoma.[15]

Previous studies reporting ADC values of lung carcinoma have been conducted under various magnet strengths, and reported ADC values are lower in magnets with a stronger field. Matoba *et al.* reported mean ADC values of 1.63×10^{-3} mm^2/sec ± 0.5 (mean $\pm$ SD) for squamous cell carcinomas, 2.12×10^{-3} mm^2/sec ± 0.6 for adenocarcinomas, 1.30×10^{-3} mm^2/sec ± 0.4 for large-cell carcinomas, and 2.09×10^{-3} mm^2/sec ± 0.3 for small-cell carcinomas, using a 1.5 T scanner. Usuda *et al.*[6] found that malignant nodules had a mean ADC of $1.27 \pm 0.35 \times 10^{-3}$ mm^2/sec on a 1.5T system. Using a 3.0 T scanner, Zhang *et al.* reported that malignant pulmonary nodules had a mean ADC of $0.87 \pm 0.16 \times 10^{-3}$ mm^2/sec. Similarly, we found a mean ADC$_{min}$ of $0.77 \pm 0.12 \times 10^{-3}$ mm^2/sec in our study conducted on a 3.0 T scanner. These values are lower than those were reported by the studies conducted using 1.5 T systems.[6,23] However, Kivrak *et al.* noted that ADC values vary for different MRI systems with the same magnetic field strength (1.5 T).[39] On the other hand, some authors reported that ADC values might not change for different organ systems under different magnetic fields.[40] However, they only used healthy volunteers and neither pathologic conditions nor image quality was not assessed. Further work is still needed to investigate the effect of magnetic field strength on the ADC of different organ systems.

One of the strongest side of our study was that we used 3 tesla MRI, which has increased signal to noise ratio, spatial resolution, temporal resolution, etc. Thus, decreased imaging time increased patients' cooperation and we had better qualified images. Our study had a few limitations. Our study population was relatively small and, although our results are robust, prospective studies with larger series are warranted to confirm our results. Additionally, to be able to generalize our results to all subtypes of lung cancer, such as small cell carcinomas and the other subtypes of non-small cell lung cancer, which we had very limited number of such cases during the study period, need to be included in future studies. Because we had no data about survival of the cases, we could not conclude any association between ADC$_{min}$ or Ki-67 and survival. However, use of ADC$_{min}$ may provide new insight to the evaluation of lung cancer including benign-malignant discrimination, the possibility of evaluation all lesions and lymph nodes non-invasively, even in the cases that tissue sampling is difficult, as well as predicting the prognosis of tumour by using it as a surrogate marker of Ki-67 index.

In conclusion, our results suggested that ADC$_{min}$ values were inversely correlated with Ki-67 index in non-small cell lung cancer and may be used as a surrogate marker of Ki-67 index in the evaluation of tumour aggressiveness with the advantage of its non-invasiveness and without requirement of tissue sampling of all the lesions.

References

1. Yabuuchi H, Hatakenaka M, Takayama K, Matsuo Y, Sunami S, Kamitani T, et al. Non-small cell lung cancer: detection of early response to chemotherapy by using contrast-enhanced dynamic and diffusion-weighted MR imaging. *Radiology* 2011; **26:** 598-604.

2. Wang Y, Chen ZE, Yaghmai V, Nikolaidis P, McCarthy RJ, Merrick L, et al. Diffusion-weighted MR imaging in pancreatic endocrine tumors correlated with histopathologic characteristics. *J Magn Reson Imaging* 2011; **33:** 1071-9.

3. Zhang J, Cui LB, Tang X, Ren XL, Shi JR, Yang HN, et al. DW MRI at 3.0 T versus FDG PET/CT for detection of malignant pulmonary tumors. *Int J Cancer* 2014; **134:** 606-11.

4. Li F, Yu T, Li W, Zhang C, Cao Y, Su D, et al. Correlation of apparent diffusion coefficient with histologic type and grade of lung cancer. *Zhongguo Fei Ai Za Zhi* 2012; **15:** 646-51.

5. Xu L, Tian J, Liu Y, Li C. Accuracy of diffusion-weighted (DW) MRI with background signal suppression (MR-DWIBS) in diagnosis of mediastinal lymph node metastasis of nonsmall-cell lung cancer (NSCLC). *J Magn Reson Imaging* 2014; **40:** 200-5.

6. Usuda K, Sagawa M, Motono N, Ueno M, Tanaka M, Machida Y, et al. Diagnostic performance of diffusion weighted imaging of malignant and benign pulmonary nodules and masses: comparison with positron emission tomography. *Asian Pac J Cancer Prev* 2014; **15:** 4629-35.

7. Türkbey B, Aras Ö, Karabulut N, Turgut AT, Akpinar E, Alibek S, et al. Diffusion-weighted MRI for detecting and monitoring cancer: a review of current applications in body imaging. *Diagn Interv Radiol* 2012; **18:** 46-59.

8. Koh DM, Collins DJ. Diffusion-weighted MRI in the body: applications and challenges in oncology. *AJR Am J Roentgenol* 2007; **188:** 1622-35.

9. Padhani AR, Liu G, Koh DM, Chenevert TL, Thoeny HC, Takahara T, et al. Diffusion-weighted magnetic resonance imaging as a cancer biomarker: consensus and recommendations. *Neoplasia* 2009; **11:** 102-25.

10. Scholzen T, Gerdes J. The Ki-67 protein: from the known and the unknown. *J Cell Physiol* 2000; **182:** 311-22.

11. Raĭkhlin NT, Bukaeva IA, Smirnova EA, Gurevich LE, Delektorskaia VV, Polotskiĭ BE, et al. Significance of the expression of nucleolar argyrophilic proteins and antigen Ki-67 in the evaluation of cell proliferative activity and in the prediction of minimal (T1) lung cancer. *Arkh Patol* 2008; **70:** 15-18.

12. Gerdes J, Lemke H, Baisch H, Wacker HH, Schwab U, Stein H. Cell cycle analysis of a cell proliferation-associated human nuclear antigen defined by the monoclonal antibody Ki-67. *J Immunol* 1984; **133:** 1710-15.

13. Zhu L, Ren G, Li K, Liang ZH, Tang WJ, Ji YM, et al. Pineal parenchymal tumours: minimum apparent diffusion coefficient in prediction of tumour grading. *J Int Med Res* 2011; **39:** 1456-63.

14. Choi SY, Chang YW, Park HJ, Kim HJ, Hong SS, Seo DY. Correlation of the apparent diffusion coefficiency values on diffusion-weighted imaging with prognostic factors for breast cancer. *Br J Radiol* 2012; **85(1016):** e474-9.

15. Onishi N, Kanao S, Kataoka M, Iima M, Sakaguchi R, Kawai M, et al. Apparent diffusion coefficient as a potential surrogate marker for Ki-67 index in mucinous breast carcinoma, *J Magn Reson Imaging* 2015; **41:** 610-5.

16. Mesko S, Kupelian P, Demanes DJ, Huang J, Wang PC, Kamrava M. Quantifying the ki-67 heterogeneity profile in prostate cancer. *Prostate Cancer* 2013; **2013:** 717080.

17. Kobayashi S, Koga F, Kajino K, Yoshita S, Ishii C, Tanaka H, et al. Apparent diffusion coefficient value reflects invasive and proliferative potential of bladder cancer. *J Magn Reson Imaging* 2014; **39:** 172-8.

18. Tang Y, Dundamadappa SK, Thangasamy S, Flood T, Moser R, Smith T, et al. Correlation of apparent diffusion coefficient with Ki-67 proliferation index in grading meningioma. *AJR Am J Roentgenol* 2014; **202:** 1303-8.

19. Martin B, Paesmans M, Mascaux C, Berghmans T, Lothaire P, Meert AP, et al. Ki-67 expression and patients survival in lung cancer: systematic review of the literature with meta-analysis. *Br J Cancer* 2004; **91:** 2018-25.

20. Usuda K, Zhao XT, Sagawa M, Aikawa H, Ueno M, Tanaka M, et al. Diffusion-weighted imaging (DWI) signal intensity and distribution represent the amount of cancer cells and their distribution in primary lung cancer. *Clin Imaging* 2013**;** **37:** 265-72.

21. Ohno Y, Koyama H, Yoshikawa T, Matsumoto K, Aoyama N, Onishi Y, et al. Diffusion-weighted MRI versus 18F-FDG PET/CT: performance as predictors of tumor treatment response and patient survival in patients with nonsmall cell lung cancer receiving chemoradiotherapy. *AJR Am J Roentgenol* 2012; **198:** 75-82.

22. Tanaka R, Horikoshi H, Nakazato Y, Seki E, Minato K, Iijima M, et al. Magnetic resonance imaging in peripheral lung adenocarcinoma: correlation with histopathologic features. *J Thorac Imaging* 2009; **24:** 4-9.

23. Matoba M, Tonami H, Kondou T, Yokota H, Higashi K, Toga H, et al. Lung carcinoma: diffusion-weighted MR imaging—preliminary evaluation with apparent diffusion coefficient. *Radiology* 2007; **243:** 570-7.

24. Martin B, Paesmans M, Mascaux C, Berghmans T, Lothaire P, Meert AP, et al. Ki-67 expression and patients survival in lung cancer: systematic review of the literature with meta-analysis. *Br J Cancer* 2004; **91:** 2018-25.

25. Warth A, Cortis J, Soltermann A, Meister M, Budczies J, Stenzinger A, et al. Tumour cell proliferation (Ki-67) in non-small cell lung cancer: a critical reappraisal of its prognostic role. *Br J Cancer* 2014; **111:** 1222-9.

26. Tabata K, Tanaka T, Hayashi T, Hori T, Nunomura S, Yonezawa S, et al. Ki-67 is a strong prognostic marker of non-small cell lung cancer when tissue heterogeneity is considered. *BMC Clin Pathol* 2014; **14:** 23-30.

27. Ahn HK, Jung M, Ha SY, Lee JI, Park I, Kim YS, et al. Clinical significance of Ki-67 and p53 expression in curatively resected non-small cell lung cancer. *Tumour Biol* 2014; **35:** 5735-40.

28. Alper F, Kurt AT, Aydin Y, Ozgokce M, Akgun M. The role of dynamic magnetic resonance imaging in the evaluation of pulmonary nodules and masses. *Med Princ Pract* 2013; **22:** 80-6.

29. Karaman A, Kahraman M, Bozdoğan E, Alper F, Akgün M. Diffusion magnetic resonance imaging of thorax. *Tuberk Toraks* 2014; **62:** 215-30.

30. Araz O, Demirci E, Ucar EY, Calik M, Karaman A, Durur-Subasi I, et al. Roles of Ki-67, p53, transforming growth factor-β and lysyl oxidase in the metastasis of lung cancer. *Respirology* 2014; **19:** 1034-9.

31. Siegel R, Naishadham D, Jemal A. Cancer statistics, 2013. *CA Cancer J Clin* 2013; **63:** 11-30.

32. Zhang Z, Zhou Y, Qian H, Shao G, Lu X, Chen Q, et al. Stemness and inducing differentiation of small cell lung cancer NCI-H446 cells. *Cell Death Dis* 2013; **16:** e633.

33. Schaarschmidt BM, Buchbender C, Nensa F, Grueneien J, Gomez B, Köhler J, et al. Correlation of the apparent diffusion coefficient (ADC) with the standardized uptake value (SUV) in lymph node metastases of non-small cell lung cancer (NSCLC) patients using hybrid 18F-FDG PET/MRI. *PLoS One* 2015; **10(1):** e0116277.

34. Yoshida S, Kobayashi S, Koga F, Ishioka J, Ishii C, Tanaka H, et al. Apparent diffusion coefficient as a prognostic biomarker of upper urinary tract cancer: a preliminary report. *Eur Radiol* 2013; **23:** 2206-14.

35. Yoshida S, Koga F, Kobayashi S, Ishii C, Tanaka H, Tanaka H, et al. Role of diffusion weighted magnetic resonance imaging in predicting sensitivity to chemoradiotherapy in muscle-invasive bladder cancer. *Int J Radiat Oncol Biol Phys* 2012; **83:** e21-e7.

36. Wieduwilt MJ, Valles F, Issa S, Behler CM, Hwang J, McDermott M, et al. Immunochemotherapy with intensive consolidation for primary CNS lymphoma: a pilot study and prognostic assessment by diffusion-weighted MRI. *Clin Cancer Res* 2012; **18:** 1146-55.

37. Srinivasan A, Chenevert TL, Dwamena BA, Eisbruch A, Watcharotone K, Myles JD, et al. Utility of pretreatment mean apparent diffusion coefficient and apparent diffusion coefficient histograms in prediction of outcome to chemoradiation in head and neck squamous cell carcinoma. *J Comput Assist Tomogr* 2012; **36:** 131-7.

38. Pope WB, Lai A, Mehta R, Qiao J, Young JR, Xue X, et al. Apparent diffusion coefficient histogram analysis stratifies progression-free survival in newly diagnosed bevacizumab-treated glioblastoma. *AJNR Am J Neuroradiol* 2011; **32:** 882-9.

39. Kıvrak AS, Paksoy Y, Erol C, Koplay M, Özbek S, Kara F. Comparison of apparent diffusion coefficient values among different MRI platforms: a multi-center phantom study. *Diagn Interv Radiol* 2013; **19:** 433-7.

40. Rosenkrantz AB, Oei M, Babb JS, Niver BE, Taouli B. Diffusion-weighted imaging of the abdomen at 3.0 Tesla: image quality and apparent diffusion coefficient reproducibility compared with 1.5 Tesla. *J Magn Reson Imaging* 2011; **33:** 128-35.

research article

The influence of cytokine gene polymorphisms on the risk of developing gastric cancer in patients with Helicobacter pylori infection

David Stubljar[1], Samo Jeverica[1], Tomislav Jukic[2], Miha Skvarc[1], Tadeja Pintar[3], Bojan Tepes[4], Rajko Kavalar[5], Borut Stabuc[6], Borut Peterlin[7], Alojz Ihan[1]

[1] Institute of Microbiology and Immunology, Ljubljana, Slovenia

[2] Medical faculty of Osijek, Osijek, Croatia

[3] Department of Abdominal Surgery, University Clinical Centre Ljubljana, Ljubljana, Slovenia

[4] Abacus Medico Diagnostic Centre Rogaska, Rogaska Slatina, Slovenia

[5] Department of Pathology, University medical Centre Maribor, Maribor, Slovenia

[6] Department of Gastroenterology, University Medical Centre Ljubljana, Ljubljana, Slovenia

[7] Clinical Institute of Medical Genetics, University Clinical Centre Ljubljana, Ljubljana, Slovenia

Background. *Helicobacter pylori* infection is the main cause of gastric cancer. The disease progression is influenced by the host inflammatory responses, and cytokine single nucleotide polymorphisms (SNPs) may have a role in the course of the disease. The aim of our study was to investigate proinflammatory cytokine polymorphisms, previously associated with the development of gastric cancer, in a Slovenian population.

Patients and methods. In total 318 patients and controls were selected for the study and divided into three groups: (i) patients with gastric cancer (n = 58), (ii) patients with chronic gastritis (n = 60) and (iii) healthy control group (n = 200). *H. pylori* infection in patient groups was determined by serology, histology and culture. Four proinflammatory gene polymorphisms were determined (IL-1β, IL-1ra, TNF-α, TLR-4) in all subjects.

Results. We found a statistically significant difference between males and females for the groups (p = 0.025). Odds ratio (OR) for gastric cancer risk for females was 0.557 (95% confidence interval [CI]: 0.233—1.329) and for chronic gastritis 2.073 (95% CI: 1.005—4.277). *IL-1B*-511*T/T homozygous allele for cancer group had OR = 2.349 (95% CI: 0.583—9.462), heterozygous *IL-1B*-511*T had OR = 1.470 (95% CI: 0.583—3.709) and heterozygotes in *TNF-A*-308 genotype for chronic gastritis had OR = 1.402 (95% CI: 0.626—3.139). Other alleles had OR less than 1.

Conclusions. We could not prove association between gastric cancer and chronic gastritis due to *H. pylori* in any cytokine SNPs studied in Slovenian population. Other SNPs might be responsible besides infection with *H. pylori* for the progression from atrophy to neoplastic transformation.

Key words: *Helicobacter pylori;* gene polymorphisms; gastric cancer; chronic gastritis

Introduction

Gastric cancer is the fourth most commonly diagnosed cancer and the second most common cause of cancer-related death worldwide.[1] The incidence of gastric cancer in Slovenia is among the highest in Europe with the crude incidence rate in male population of 28.6/100 000.[2-4] Gastric cancer is multifactorial disease. Environmental and host genetic factors influence the development of gastric cancer. The most important is *Helicobacter pylori* (*H. pylori*) infection. It is belived that roughly 65–80% of gastric cancers are associated with *H. pylori* infection. However, only a minority (1–2%) of infected individuals will develop gastric cancer during their lifetime.[5,6] Gastric carcinogenesis is a

multistep process that starts with chronic active gastritis and continues through the development of gastric atrophy, and metaplasia, to reach gastric cancer stage at the end of that process, lasting tipically between 30–50 years.[7-10] In addition to *H. pylori* infection, several host genetic factors are important for the development of gastric cancer, especially several single nucleotide polymorphisms (SNPs) and/or point mutations in genes that affect gastric acid secretion and innate immune response to infection.[11-14] Polymorphisms in cytokine genes may influence the level of the cytokine production by the host, and consequently influence the disease outcome.[15] The immune response to *H. pylori* is important for the development of gastric cancer due to the recognition of pathogenic elements and induced synthesis and secretion of inflammatory cytokines, resulting inflammation, what can lead to severe gastric immunopathology and cancer.[16]

Interleukin 1b (IL-1b) is the main cytokine secreted in response to *H. pylori* infection. It has a strong pro-inflamatory activity and inhibits gastric acid secretion. IL-1b is 100-times more potent inhibitor of acid secretion than proton pump inhibitors.[17] Inhibition of acid secretion may lead to the spread of bacteria from the antrum to the corpus, and consequently the development of corpus predominant gastritis which further leads to the development of gastric cancer.[18,19] Three polimorphisms were described in the *IL-1B* gene at positions -31, -511 and +3954 from the transcription start site.[18,20] *IL-1B*-31*C and *IL-1B*-511*T alleles are associated with decreased acidity in the stomach (hypochlohydria) in response to the infection with *H. pylori*.[18] IL-1b receptor antagonist (IL-1ra) polymorphisms have also been associated with the level of IL-1b secretion. Genotype *IL-1RN**2 is associated with higher secretion of IL-1b, most probably through the reduction of its receptor antagonist IL-1ra.[20,21]

Tumor necrosis factor-a (TNF-α) is a central mediator of the immune response. Several polymorphisms are known in the promoter region of *TNF-A* gene of which -308*G>A was associated with increased production of TNF-α in response to the infection, and increased gastric cancer risk.[22-24] El-Omar *et al*.[25] and Machado *et al*.[26] found that subject with this polymorphism have almost two-fold increased risk of gastric cancer.

Recently, a functional polymorphism at the position +896, in exon 4 of the *Toll-like receptor-4 (TLR-4)* gene, has been described. This A>G transition results in an alteration of the extracellular domain of TLR-4, that causes hyporesponsiveness to LPS, reduced epithelial TLR-4 density and exaggerated

inflammatory cytokine response.[27] A recent study has reported an association of *TLR-4* gene polymorphisms with gastroduodenal diseases such as gastric atrophy and hypochlorhydria.[28,29] *TLR-4* substitution was associated with noncardia gastric cancer.[30,31]

The aim of our study was to determine the prevalence of the selected pro-inflammatory cytokine polymorphisms in the Slovenian population of patients with gastric cancer and chronic gastritis, and compare its prevalence with the prevalence in the normal healthy population, to see if high incidence of gastric cancer in Slovenian population could be, at least partially, attributed to the higher prevalence of those proinflammatory polymorphisms in the genes for IL-1β, IL-1ra, TNF-α and TLR-4.

Patients and methods

Patients

In total 318 patients and controls were included in the study devided into three groups: (i) consecutive patients with gastric cancer (n = 58), (ii) consecutive patients with chronic gastritis due to *H. pylori* (n = 60) and (iii) healthy control group (n = 200). Study was conducted as a case-control study, where the cancer patients represented one group and the gastritis patients represented the other group. Subjects for the healthy control group were randomly selected from the pool of representative blood samples of Slovenian healthy adults, to be matched for age and sex. All subjects were informed about the inclusion in the study and agreed to it in writing form. National medical ethics committee reviewed and cleared the protocol of the study.

Histopathology, serology and culture

Patients in the gastric cancer group had the histological type of cancer determined using the Lauren's classification that differentiates among intestinal, diffuse and mixed or indetermined type adenocarcinoma. In the group of patients with chronic gastritis two biopsies were obtained from corpus and antrum, and the histological diagnosis was determined in accordance with the Huston modification of Sydney classification for gastritis.[7,32]

Serological confirmation of *H. pylori* infection in the gastric cancer group was confirmed by the quantitative IgG ELISA test GAP®-IgG (Biomerica, USA) from human serum. Test was performed in accordance to instructions by the manufacturer.[33]

TABLE 1. Primers and probes sequences used in the KASP assays

Gene	Probes	Primers
IL-1β -511 C/T	**FAM** 5'-GGGTGCTGTTCTCTGCCTC**G**-3' **VIC** 5'-GGGTGCTGTTCTCTGCCTC**A**-3'	5'-GCCCCAGCCAAGAAAGGTCAATTTT-3'
TNF-α -308 G/A	**FAM** 5'-GGAGGCTGAACCCCGTCC**T**-3' **VIC** 5'-GAGGCTGAACCCCGTCC**C**-'3	5'-GAGGCAATAGGTTTTGAGGGGCAT-3'
TLR-4 +896 A/G	**FAM** 5'-GCATACTTAGACTACTACCTCGATG**A**-3' **VIC** 5'-CATACTTAGACTACTACCTCGATG**G**-3'	5'-CACTCACCAGGGAAAATGAAGAAACATT-3'

H. pylori culture was performed in the gastritis group from two biopsy samples of antrum and corpus, respectively. Biopsy samples were transported to the laboratory in Portagerm pylori transport medium (Biomerieux, France). In the laboratory, samples were homogenized in 1 mL of phosphate buffer (PBS) and 0.5 mL of the homogenate was inoculated onto two selective agar plates: Pylori agar (Biomerieux, France) and Brucella agar supplemented with human blood and antibiotic mixture (BBL, USA). Culture media were incubated at 37 °C for 72 hours in microaerophilic conditions. The identification of typical colonies was confirmed using Gram stain and the proof of enzymes: urease, catalase and oxidase.

Genotyping

Genomic DNA was extracted from the whole blood samples with EDTA using automated system for DNA isolation Magna Pure Compact Nucleic Acid Isolation Kit I (Roche Applied Science, Germany) on fully automated platform MagNa Pure Compact System in accordance to the instructions by the manufacturer.[34] Complete nucleotide sequences of individual genes for inflammatory cytokine *IL-1β* (rs16944), *TNF-α* (rs1800629) and *TLR-4* (rs4986790) were looked into online databases National Center for Biotechnology Information (NCBI; www.ncbi.nlm.nih.gov) and ENSEMBLE (www.ensembl.org). The sequences were examined with the help of the software package Vector NTI Advance 11 (Invitrogen, Carlsbad, CA, USA).[21,25,26] Polymorphisms genotyping was performed using the KASP technology (KBioscience competitive Allele-Specific PCR) using primers and reagents Kasp On Demand (KOD) (KBioscience, UK). 120 bp long reference sequences were sent to the manufacturer, upon which the appropriate primers and probes were designed (Table 1).

The amplification of genomic DNA and the detection of polymorphisms were performed using the real-time polymerase chain reaction (PCR) apparatus LightCycler 480II (Roche Diagnostics GmbH, Germany). A touchdown protocol provided by the manufacturer was used: 94 °C for 15 min; 10 cycles of 94 °C for 10 s, 61 °C for 60 s (the anniling temperature dropped 0.6 °C per cycle to reach the annealing temperature of 55 °C) then; 26 cycles of 94 °C for 10 s, 55 °C for 60 s. *IL-1RN* gene contains a variable number of 86 base pair long tandem repeats (VNTR).[19] Genomic DNA was amplified and PCR products were separated by the 1.5% agarose gel electrophoresis. Primers to detect *IL-1RN**2/2 (TIB Molbiol, Germany) were used. We have used forward primer: 5'-CCCCTCAGCAACACTCC-3', reverse primer: 5'-GGTCAGAAGGGCAGAGA-3'. Cycling conditions for the PCR were 95 °C for 15 min; 30 cycles of 94 °C for 30 s and 61 °C for 30 s; 72 °C for 60 s and 15 min at 72 °C. PCR reaction with the final volume of 25 μl was used, containing 12.5 μl of twice the reaction mixture of HotStartTaq Plus, 0.75 μl of each primer with a concentration of 10 μM, 8.5 μl of ddH$_2$O and 2.5 μl of sample DNA.

There are 5 versions of alleles. Allele 1, 2, 3, 4 and 5 carries 4, 2, 5, 3 and 6 repeats, respectively.[20,35] Due to easier statistical analysis the allele polymorphisms were divided into short and long, the short allele being allele 2 and the long allele being those with 3 repeats or more (alleles 1, 3, 4, and 5).[26]

Statistical analysis

The SPSS Statistics 21 (IBM, USA) software package was used for the statistical analysis. The Hardy-Weinberg equilibrium (HWE) of alleles in each individual locus was assessed. The degrees of freedom for HWE were calculated as the number of genotypes subtracted with the number of alleles. If the value of the c[2] was less than 3.84, the

TABLE 2. Demographic profiles of subjects

Demographic profile	Gastric cancer (n = 58)		Gastritis (n = 60)		Controls
	Intestinal	Diffuse	Atrophic	Metaplastic	/
No. of subjects	32 (55%)	26 (45%)	51 (85%)	9 (15%)	200
Age (years)	52 ± 10	52 ± 10	52 ± 10	58 ± 13	49 ± 5
Gender					
Male	22 (38%)	18 (31%)	20 (33%)	2 (3%)	100 (50%)
Female	10 (17%)	8 (14%)	31 (52%)	7 (12%)	100 (50%)

TABLE 3. Pearson's χ^2 analysis for association between frequencies of cytokine polymorphisms and patients with intestinal type gastric adenocarcinoma, atrophic chronic gastritis and healthy controls

	Intestinal adenocarcinoma		Atrophic gastritis		Controls		Pearson's χ^2	p-value
	(n = 32)		(n = 51)		(n = 108)			
IL-1B -511							8.214	0.084
C/C	10	31.3%	30	58.8%	42	38.9%		
C/T	17	53.1%	18	35.3%	53	49.1%		
T/T	5	15.6%	3	5.9%	13	12.0%		
IL-1RN							4.377	0.357
L/L	17	53.1%	33	64.7%	63	58.3%		
L/2	13	40.6%	15	29.4%	32	29.6%		
2/2	2	6.3%	2	3.9%	13	12.0%		
TNF-A -308							4.796	0.309
G/G	27	84.4%	36	70.6%	83	76.9%		
G/A	5	15.6%	15	29.4%	22	20.4%		
A/A	0	0.0%	0	0.0%	3	2.8%		
TLR-4 +896							3.355	0.500
A/A	30	93.8%	46	90.2%	90	83.3%		
A/G	2	6.3%	5	9.8%	17	15.7%		
G/G	0	0.0%	0	0.0%	1	0.9%		
Gender							7.355	0.025
M	22	68.8%	20	39.2%	60	55.6%		
F	10	31.3%	31	60.8%	48	44.4%		

F = female; M = male

frequencies of the population were in HWE. For all genotypes, the homozygote of the common allele was used as the reference. The *IL-1B, IL-1RN, TNF-A* and *TLR-4* genotype frequencies for each polymorphism were compared by 2-sided Pearson c^2 test, to evaluate the genotype distributions of categorical variables between each group of cases and controls, and to see if there was any association between the tested variables. The odds ratios (ORs) and the 95% confidence interval (95% CI) were assessed using logistic regression analysis with the reference category being healthy controls. ORs for different groups were adjusted for sex only. Statistical differences were considered to be significant at a *P* value < 0.05.

Results

Patients with diagnosed chronic gastritis due to *H. pylori* and gastric cancer were investigated compared to healthy controls. The average age of individuals and gender ratio were comparable in all groups (Table 2). We included 198 subjects and

TABLE 4. Genotype polymorphisms odds ratios (ORs) and 95% confidence intervals (CIs) for gastric cancer and atrophic gastritis subjects

	Intestinal adenocarcinoma (n = 32)	OR	95% CI	p-value	Atrophic gastritis (n = 51)	OR	95% CI	p-value
IL-1B -511								
C/C	10 (31.3)	reference			30 (58.8)	reference		
C/T	17 (53.1)	1.470	0.583-3.709	0.414	18 (35.3)	0.489	0.228-1.050	0.067
T/T	5 (15.6)	2.349	0.583-9.462	0.230	3 (5.9)	0.416	0.099-1.757	0.233
IL-1RN								
L/L	17 (53.1)	reference			33 (64.7)	reference		
L/2	13 (40.6)	1.064	0.436-2.597	0.891	15 (29.4)	1.052	0.473-2.341	0.900
2/2	2 (6.3)	0.394	0.072-2.162	0.394	2 (3.9)	0.400	0.081-1.988	0.263
TNF-A -308								
G/G	27 (84.4)	reference			36 (70.6)	reference		
G/A	5 (15.6)	0.704	0.236-2.099	0.528	15 (29.4)%	1.402	0.626-3.139	0.411
A/A	0 (0.0)	0	0	0	0 (0.0)	0	0	0
TLR-4 +896								
A/A	30 (93.8)	reference			46 (90.2)	reference		
A/G	2 (6.3)	0.326	0.066-1.603	0.168	5 (9.8)	0.499	0.149-1.668	0.259
G/G	0 (0.0)	0	0	0	0 (0.0)	0	0	0
Gender								
M	22 (68.8)	reference			20 (39.2)	reference		
F	10 (31.3)	0.557	0.233-1.329	0.187	31 (60.8)	2.073	1.005-4.277	0.048

Reference category for groups was set to control group. Referent allele was common homozygote; F = female; M = male

controls in the study meeting the necessary initial criteria: 108 healthy control subjects with no underlying conditions, 32 patients with intestinal type of gastric adenocarcinoma and 58 patients with chronic gastritis and positive *H. pylori* infection were included and processed for statistical analysis.

The genotype frequencies distribution among cytokine polymorphisms are presented in Table 3. Comparison of genotype frequencies between intestinal adenocarcinoma group and atrophic gastritis group and healthy controls showed no significant difference (p > 0.05). P-value of 0.084 for IL-1β showed closest statistical difference between the diagnosis severe progression and influence of genetic polymorphisms. However, there was a statistically significant difference between males and females compared between the groups (p = 0.025) (Table 3). The sex-adjusted OR of gastric cancer among *H. pylori* positive subjects was 0.557 (95% CI: 0.233–1.329; p = 0.187) and of chronic gastritis 2.073 (95% CI: 1.005–4.277; p = 0.048). Males were taken as reference.

In the gastric carcinoma patients, *IL-1B*-511*T/T homozygous allele represented 15.6% (5/32) of the case subjects, which was proportionally higher than in control group (12.0%; 13/108), however statistically with an OR of 2.349 (95% CI: 0.583–9.462) was not confirmed. Carriers of heterozygous *IL-1B*-511*T allele in cancer group (53.1%, 17/32) also showed no difference against control group (49.1%, 53/108) despite the OR = 1.470 (95% CI: 0.583–3.709). For atrophic gastritis group there was no statistically difference compared to control group (Table 4). Carriers of the proinflammatory *IL-1B*-511*T allele (both *IL-1B*-511T homozygotes and *IL-1B*-511 heterozygotes) had also no increased risk for gastric cancer (OR = 1.570; 95% CI: 0.644–3.825) or chronic gastritis (OR = 0.480; 95% CI: 0.232–0.996). The associated OR value was even smaller than for homozygotes alone with low frequency of homozygous controls (Table 4). According to Pearson's χ^2 frequency distribution of *IL-1B*-511*T carriers were statistically significant in combination for specific diagnose (p = 0.021; F = 7.760) (data not shown).

The observed associations between *IL-1RN* VNTR genotype carriers *(IL-1RN*L/2)* and the risk of gastric carcinoma or atrophic gastritis had meaningless OR = 1.064 (95% CI: 0.436–2.597), OR = 1.052

TABLE 5. Frequencies of genotype carriers, odds ratios (ORs) and 95% confidence intervals (CIs) for gastric cancer and atrophic gastritis subjects

	Intestinal adenocarcinoma (n = 32)	OR	95% CI	p-value	Atrophic gastritis (n = 51)	OR	95% CI	p-value
IL-1B -511								
C/C	10 (31.3)	reference			30 (58.8)	reference		
T carrier	22 (68.7)	1.570	0.644-3.825	0.321	21 (41.2)	0.480	0.232-0.996	0.049
IL-1RN								
L/L	17 (53.1)	reference			33 (64.7)	reference		
2 carrier	15 (46.9)	0.947	0.408-2.200	0.900	17 (33.3)	0.905	0.429-1.912	0.794
TNF-A -308								
G/G	27 (84.4)	reference			36 (70.6)	reference		
A carrier	5 (15.6)	0.590	0.201-1.730	0.336	15 (29.4)	1.217	0.556-2.667	0.623
TLR-4 +896								
A/A	30 (93.8)	reference			46 (90.2)	reference		
G carrier	2 (6.3)	0.318	0.068-1.487	0.145	5 (9.8)	0.435	0.135-1.407	0.165
Gender								
M	22 (68.8)	reference			20 (39.2)	reference		
F	10 (31.3)	0.561	0.237-1.329	0.189	31 (60.8)	2.068	1.015-4.213	0.045

Reference category for groups was set to control group. Referent allele was common homozygote; F = female; M = male

(95% CI: 0.473–2.341), respectively. Furthermore short allele had no statistical association with developing the disease.

In a logistic regression model that included the other genetic markers (*TNF-A* and *TLR-4*), there were no statistical significant differences adjusted to control group and common alleles. Heterozygotes in *TNF-A*-308 genotype had also no statistically significant excess for the chronic gastritis (OR = 1.402; 95% CI: 0.626–3.139) (Table 3). *TNF-A*-308*A carriers (both *TNF-A*-308*A homozygotes and *TNF-A*-308 heterozygotes) had even less probability with an OR of 1.217 (95% CI: 0.556–2.667) for gastritis (Table 5).

Pearson correlation model for all *IL-1B*-511, *IL-1RN* VNTR, *TNF-A*-308 and *TLR-4*+896 genotypes was performed and showed no statistical significance between them (p > 0.01). However correlation between *IL-1B* and *IL-1RN* was found (Pearson's R = 0.300; p < 0.001). Furthermore, there was no evidence of the association between the 55 (28.9%) carriers of *IL-1B*-511*T and *IL-1RN*2 alleles (OR = 1.489; 95% CI: 0.660-3.361) for the risk of gastric cancer (data not shown). There was also no association for chronic gastritis. Moreover, combined T and 2 allele carriers had even lesser risk associated with developing gastric cancer than each allele separately.

Discussion

This is the first study on Slovenian population that checked variants or polymorphisms in genes responsible for cytokine secretion that may contribute to the different outcomes of infection and the development of gastric lesions. Our results showed that there was a statistical difference between genders on the outcome of infection with *H. pylori* (p = 0.025). Males were more predominant to develop gastric cancer than females (female OR = 0.557). Meanwhile females had 2-fold greater probability to develop chronic gastritis (OR = 2.073; 95% CI: 1.005–4.277). Our results were consistent with reported results in studies stated by Chandanos and Lagergren[4], and Dixon et al.[32] All investigated polymorphism unfortunately showed no associations with disease prediction.

IL-1B polymorphisms were not statistically associated with the prediction of each diagnose as accoording, however p-value to determine association between polymorphism and outcome of infection (diagnose severity: gastritis or cancer) was 0.084. Frequency distribution in our population showed that *IL-1B*-511*C homozygote allele was most frequent in chronic gastritis group (58.8%). According to our knowledge such results were not found in any other study. Genotype frequencies for cancer

group were coincided with control group. Studies in Caucasian and Asian populations have shown that polymorphisms in the genes *IL-1B* and *IL-1RN* were in conjunction with an increased risk for hypochlohydria and gastric carcinoma.[13] According to our findings, individuals carrying the *IL*-1B-511*T/T allele compared to control group showed an increased OR for gastric cancer. Heterozygotes for *IL-1B* gene (*IL-1B*-511*T carriers) and both homozygotes and heterozygotes for T allele, also showed increased OR for developing gastric cancer. Although the OR values were evaluated it would be exaggerated to affirm that these polymorphisms could indicate on the risk for developing intestinal adenocarcinoma, because the power of our statistical anysis was really poor with p-values less then 0.05 and wider 95% CI. However allele combination (T/T and C/T) showed statistically significant association with diagnose prediction (p = 0.021). Percent of *IL-1B*-511*T carriers in cancer group has reached almost 69% of tested individuals.

El-Omar *et al*.[24] have identified the inflammatory profile of genetic polymorphisms in the genes for IL-1β (*IL-1B* -511*T) and IL-1ra (*IL-1RN**2/2) to increase the risk of developing gastric cancer.[17] In our population there was 40.6% of short allele carriers diagnosed with cancer but no statistical difference to predict the disease was observed (Table 4). The correlated association between *IL-1B* and *IL-1RN* proinflammatory genotypes (*IL-1B*-511*T carriers and *IL-1RN**2 homozygotes) and risk for gastric cancer was also determined (p < 0.001 and Pearson's R = 0.300). These results indicated that *IL-1RN**2/2 gene is recessive in combination with T carriers in *IL-1B*.[36] The genotype frequencies for individuals with gastric cancer or even chronic gastritis were even smaller than in control group. Results should be taken caustiously because in our population only 2% of cancer patients or patients with gastritis and 12% of controls had *IL-1RN**2/2.

The present study has showed that *TLR-4* polymorphism is not associated with the development of the premalignant gastric abnormalities of hypochlorhydria and atrophy, or with increased risk of gastric adenocarcinoma. No association was seen with cancer although this polymorphism has been associated with risk of other inflammatory conditions. The polymorphism was associated with hyporesponsiveness to bacterial LPS.[37] The association of the *TLR-4*+896A>G polymorphism identifies subjects who have an increased risk of severe inflammation and subsequently, development of hypochlorhydria and gastric atrophy, which are regarded as the most important precancerous ab-

normalities.[27] However, our results were comparable to those by Garza-Gonzales[28] that the *TLR-4* polymorphism did not play a role in the development of gastric premalignancies.

H. pylori infection also enhances the mucosal production of TNF-α. TNF-α is not as potent inhibitor of gastric acid secretion as IL-1β.[38] Although El-Omar *et al*.[20] and Machado *et al*.[26] found an almost two-fold increase in risk for gastric cancer, several studies have not found an association between *TNF-A*-308*A and gastric cancer risk.[39-41] The *TNF-A*-308*A allele has been found in association with an increased risk of *cagA* positive infections and gastric cancer by Zambon *et al*.[23] and Yea *et al*.[42] also found no significant association between the *TNF-A*-308 polymorphism and the severity of gastric disease (carcinoma, gastritis, gastric ulcers, duodenal ulcers). However our results have not confirmed that and were coincided with results of Tseng *et al*.[43], who investigated polymorphisms in Jamaican children. Meanwhile the G allele has been found to be associated with peptic ulcer, which commonly accompanies gastritis[32], and concomitant *H. pylori* infection, compared to those without ulcerations.[44] Mucosal expression levels of TNF-α was lower in *H. pylori*-infected individuals with duodenal ulcers. Heterozygous G carriers in our population were slightly drawn near with development of chronic gastritis (OR = 1.402; 95% CI: 0,626–3,139), but again the p-value was 0.411 and the association was not confirmed.

The reduced number of samples available for statistical analysis may have harmed our results. We have found no indications that the infection with *H. pylori* in a given inflammatory genotype of could result in an inflammatory response, and then gastritis or cancer. We have also showed that the presence of *IL-1B*-511 genotype for the inflammatory cytokine was inclined to the difference between intestinal type of gastric cancer, chronic gastritis and healthy controls. However statistically it was not associated entirely and could not be used to identify people at increased risk. On the other hand, cytokine gene polymorphisms represent just one component of complex interactions among host, pathogen, and environmental factors involved in gastric carcinogenesis, what was definitly confirmed with statistical difference between genders. Only combination of *H. pylori* and host-associated risk factors do not always allow evaluation of gastric carcinoma risk. The progression from atrophy to neoplastic transformation depends on other factors, including diet and different pathogenesis of *H. pylori* strains.[5,7] Ando *et*

al.[45] have found that patients who develop duodenal ulcer disease are protected from gastric cancer. Both conditions are associated with *H. pylori*, but duodenal ulcers are associated with an antrum predominant gastritis, low prevalence of gastric atrophy, and very high acid secretion. On the contrary, gastric cancer patients develop corpus predominant gastritis, multifocal atrophic gastritis, and hypochlorhydria. Proinflammatory genotypes of the *IL-1B* gene, through its induction of gastric atrophy and gastric acid inhibition, increase the risk of gastric atrophy.

The number of cases in our study was small. In the study, in cancer group, we only included patients with intestinal type of gastric cancer, however in gastritis group we included all gastritis types, not only those with accompanied atrophy. Individuals with extensive corpus gastritis develop hypochlorhydria and gastric atrophy, which are presumptive precursors of gastric cancer.[20] Another drawback is that we have not determined bacterial strain (*vac A, cag A*) as it was done by Figueiredo *et al.*[46] and Zambon *et al.*[23] Anyway, now we have learnt that the assessment of patients with *H. pylori* infection and its strain is very important and concluded that eradication of bacteria has essential meaning. We recommend that not only screening for *H. pylori* also the strain determination should have some diagnostic value, especially in the patients who already developed gastritis. Furthermore, for such patients assessment of disease progression (atrophic or metaplastic gastritis) could be followed by polymorphism determination. The statistical power of our pilot study was very poor and we could not evaluate it to the whole Slovenian population, but for further polymorphism investigations it is necessary to include more patients with different disease progression. Our study design was considered good, because our study population was not heterogenic. Untill now we cannot predict the disease based only on single polymorphism.

Conclusions

Altogether, our findings indicated that host genotype as well as *H. pylori* infection could be important for greater risk for developing gastric cancer. However, those parameters alone could not predict the incidence of the disease. For more accurate analysis of the impact of genetic polymorphisms and identification of people with an increased risk for developing the disease, it would be necessary to expand the study and include a larger number of subjects, especially patients with gastric cancer.

References

1. Ferlay J, Shin HR, Bray F, Forman D, Mathers C, Parkin DM. Estimates of worldwide burden of cancer in 2008: GLOBOCAN 2008. *Int J Cancer* 2010; **127:** 2893-917.

2. Cancer in Slovenia 2009. Ljubljana: Institute of Oncology Ljubljana, Epidemiology and Cancer Registry, Cancer Registry of Republic of Slovenia. 2013 [cited 2013 Nov 25]. Available from: http://www.onko-i.si/eng/crs.

3. Tepeš B, Kavalar R. [Gastric cancer, screening possibilities and proposals for endoscopic and histologic follow-up of premalignant gastric lesions]. [Slovenian]. *Zdrav Vestn* 2010; **79:** 366-74.

4. Chandanos E, Lagergren J. Oestrogen and the enigmatic male predominance of gastric cancer. *Eur J Cancer* 2008; **44:** 2397-403.

5. Kusters JG, van Vliet AHM, Kuipers EJ. Pathogenesis of Helicobacter pylori infection. *Clin Microbiol Rev* 2006; **19:** 449-90.

6. Kodama M, Murakami K, Sato R, Okimoto T, Nishizono A, Fujioka T. Helicobacter pylori-infected animal models are extremely suitable for the investigation of gastric carcinogenesis. *World J Gastroenterol* 2005; **11:** 7063-71.

7. Manxhuka-Kerliu S, Telaku S, Devolli-Disha E, Ahmetaj H, Sahatciu-Meka V, Kerliu A, et al. 2009. Helicobacter pylori gastritis updated Sydney classification applied in our material. *Prilozi* 2009; **30:** 45-60.

8. Ishihara S, Rumi MA, Kadowaki Y, Ortega-Cava CF, Yuki T, Yoshino N, et al. Essential role of MD-2 in TLR4-dependent signaling during Helicobacter pylori-associated gastritis. *J Immunol* 2004; **173:** 1406-16.

9. Lu W, Pan H, Zhang L, Lin D, Miao X, You W. Genetic polymorphisms of interleukin IL-1B, IL-1RN, IL-8, IL-10 and tumor necrosis factor α and risk of gastric cancer in a Chinese population. *Carcinogenesis* 2005; **26:** 631-6.

10. Correa P, Haensze, W, Cuello C, Tannenbaum S, Archer M. A model for gastric cancer epidemiology. *Lancet* 1975; **2:** 58-60.

11. Jorge YC, Duarte MC, Silva AE. Gastric cancer is associated with *NOS2* -954G/C polymorphism and environmental factors in a Brazilian population. *BMC Gastroenterol* 2010; **10:** 64-84.

12. Murphy G, Thornton J, McManus R, Swan N, Ryan B, O'Morain CA, et al. Association of gastric disease with polymorphisms in the inflammatory related genes IL-1B, IL-1RN, IL-10, TNF and TLR4. *Eur J Gastroenterol Hepatol* 2009; **21:** 630-5.

13. Melo Barbosa HP, Martins LC, Dos Santos SE, Demachki S, Assumpção MB, Aragão CD, et al. Interleukin-1 and TNF-α polymorphisms and Helicobacter pylori in a Brazilian Amazon population. *World J Gastroenterol* 2009; **15:** 1465-71.

14. Kamangar F, Abnet CC, Hutchinson AA, Newschaffer CJ, Helzlsouer K, Shugart YY, et al. Polymorphisms in inflammation-related genes and risk of gastric cancer (Finland). *Cancer Causes Control* 2006; **17:** 117-25.

15. Moorchung N, Srivastava AN, Gupta NK, Ghoshal UC, Achyut BR, Mittal B. 2007. Cytokine gene polymorphisms and the pathology of chronic gastritis. *Singapore Med J* 2007; **48:** 447-54.

16. Skvarc M, Stubljar D, Kopitar AN, Jeverica S, Tepes B, Kos J, et al. Inhibition of cathepsin X enzyme influences the immune response of THP-1 cells and dendritic cells infected with Helicobacter pylori. *Radiol Oncol* 2013; **47:** 258-65.

17. Ito H, Kaneko K, Makino R, Konishi K, Kurahashi T, Yamamoto T, et al. Interleukin-1beta gene in esophageal, gastric and colorectal carcinomas. *Oncol Rep* 2007; **18:** 473-81.

18. Xue H, Lin B, Ni P, Xu H, Huang G. Interleukin-1B and interleukin-1 RN polymorphism and gastric carcinoma risk: A meta-analysis. *J Gastroenterol Hepatol* 2010; **25:** 1604-17.

19. Sitarz R, de Leng WWJ, Polak M, Morsink FHM, Bakker O, Polkowski WP, et al. IL-1B −31T>C promoter polymorphism is associated with gastric stump cancer but not with early onset or conventional gastric cancers. *Virchows Arch* 2008; **453:** 249-55.

20. El-Omar EM, Carrington M, Chow WH, McColl KEL, Breamk JH, Young H, et al. Interleukin-1 polymorphisms associated with increased risk of gastric cancer. *Nature* 2000; **404:** 398-402.

21. Cauci S, Santolo MD, Ryckman KK, Williams SM, Banfi G. Variable number of tandem repeat polymorphism of the interleukin-1 receptor antagonist gene IL-1RN: a novel association with the athlete status. *BMC Med Genet* 2010; **11:** 29-40.

22. Crusius JB, Canzian F, Capellá G, Peña AS, Pera G, Sala N, et al. Cytokine gene polymorphisms and the risk of adenocarcinoma of the stomach in the European prospective investigation into cancer and nutrition (EPIC-EURGAST). *Ann Oncol* 2008; **19:** 1894-902.

23. Zambon CF, Basso D, Navaglia F, Belluco C, Falda A, Fogar P, et al. Pro- and anti-inflammatory cytokines gene polymorphisms and Helicobacter pylori infection: interactions influence outcome. *Cytokine* 2005; **29:** 141-52.

24. Hou L, El-Omar EM, Chen J, Grillo P, Rabkin CS, Baccarelli A, et al. Polymorphisms in Th1-type cell-mediated response genes and risk of gastric cancer. *Carcinogenesis* 2007; **28:** 118-23.

25. El-Omar EM, Rabkin CS, Marilie DG, Vaughan TL, Harvey AR, Schoenberg JB, et al. Increased risk of noncardia gastric cancer associated with proinflammatory cytokine gene polymorphisms. *Gastroenterology* 2003; **124:** 1193-201.

26. Machado JC, Figueiredo C, Canedo P, Pharoah P, Carvalho R, Nabais S, et al. A proinflammatory genetic profile increases the risk for chronic atrophic gastritis and gastric carcinoma. *Gastroenterology* 2003; **125:** 364-71.

27. Hold GL, Rabkin CS, Chow WH, Smith MG, Gammon MD, Risch HA, et al. A functional polymorphism of toll-like receptor 4 gene increases risk of gastric carcinoma and its precursors. *Gastroenterology* 2007; **132:** 905-12.

28. Garza-Gonzalez E, Bosques-Padilla FJ, Mendoza-Ibarra SI, Flores-Gutierrez JP, Maldonado-Garza HJ, Perez-Perez GI. Assessment of the toll-like receptor Asp299Gly, Thr399Ile and interleukin-8 -251 polymoprhisms in the risk for the development of distal gastric cancer. *BMC Cancer* 2007; **7:** 70.

29. Hishida A, Matsuo K, Goto Y, Mitsuda Y, Hiraki A, Naito M, et al. Toll-like receptor 4 +3725 G/C polymorphism, Helicobacter pylori seropositivity, and the risk ofgastric atrophy and gastric cancer in Japanese. *Helicobater* 2009; **14:** 47-53.

30. Achyut BR, Ghoshal UC, Moorchung N, Mittal B. Association of toll-like receptor-4 (Asp299Gly and Thr399Ileu) gene polymorphisms with gastritis and precancerous lesions. *Hum Immunol* 2007; **68:** 901-7.

31. El-Omar EM, Ng MT, Hold GL. Polymorphisms in Toll-like receptor genes and risk of cancer. *Oncogene* 2008; **27:** 244-52.

32. Dixon MF, Genta R, Yardley JH, Correa P. Classification and grading of gastritis: The updated Sydney system. *Am J Surg Pathol* 1996; **20:** 1161-81.

33. Szeto ML, Lee CK, Yee YK, Li K., Lee WK, Lee CC, et al. Evaluation of five commercial serological tests for the detectionof Helicobacter pylori infection in Chinese. *Aliment Pharmacol Ther* 2001; **15:** 703-6.

34. Kirchgesser M, Adem C, Baumgartner A, Girgnhuber H, Malmberg W, Schmitt I, et al. Automated isolation of DNA from tissue samples in 35-50 minutes: Fast and easy purification combining the MagNA Lyser and the MagNA Pure Compact System. *Biochemica* 2006; **1:** 9-10.

35. Highet AR, Gibson CS, Goldwater PN. Variant interleukin 1 receptor antagonist gene alleles in sudden infant death syndrome. *Arch Dis Child* 2010; **95:** 1009-12.

36. Machado JC, Pharoah P, Sousa S, Carvalho R, Oliveira C, Figueiredo C, et al. Interleukin 1B and interleukin 1RN polymorphisms are associated with increased risk of rastric carcinoma. *Gastroenterology* 2001; **121:** 823-9.

37. Kutikhin AG. Impact of Toll-like receptor 4 polymorphisms on risk of cancer. *Hum Immunol* 2011; **72:** 193-206.

38. Queiroz DM, Guerra JB, Rocha GA, Rocha AM, Santos A, De Oliveira AG, et al. *IL1B* and *IL1RN* polymorphic genes and Helicobacter pylori cagA strains decrease the risk of reflux esophagitis. *Gastroenterology* 2004; **127:** 73-9.

39. Wu MS, Chen LT, Shun CT, Huang SP, Chiu HM, Wang HP, et al. Promoter polymorphisms of tumor necrosis factor-alpha are associated with risk of gastric mucosa-associated lymphoid tissue lymphoma. *Int J Cancer* 2004; **110:** 695-700.

40. Garza-Gonzalez E, Bosques-Padilla FJ, El-Omar E, Hold G, Tijerina-Menchaca R, Maldonado-Garza HJ, et al. Role of the polymorphic IL-1B, IL-1RN and TNF-A genes in distal gastric cancer in Mexico. *Int J Cancer* 2005; **114:** 237-41.

41. Achyut BR, Tripathi P, Ghoshal UC, Moorchung N, Mittal B. Interleukin-10 (-819 C/T) and tumor necrosis factor-alpha (-308 G/A) gene variants influence gastritis and lymphoid follicle development. *Dig Dis Sci* 2008; **53:** 622-9.

42. Yea SS, Yang YI, Jang WH, Lee YJ, Bae HS, Paik KH. Association between TNF-alpha promotor polymorphism and Helicobacter pylori cagA subtype infection. *J Clin Pathol* 2001; **54:** 703-6.

43. Tseng FC, Brown EE, Maiese EM, Yeager M, Welch R, Gold BD, et al. Polymorphisms in cytokine genes and risk of Helicobacter pylori infection among Jamaican children. *Helicobacter* 2006; **11:** 425-30.

44. Chakravorty M, Datta De D, Choulhury A, Santra A, Roychoudhury S. Association of specific haplotype of TNFalpha with Helicobacter pylori-mediated duodenal ulcer in eastern Indian population. *J Genet* 2008; **87:** 299-304.

45. Ando T, El-Omar EM, Goto Y, Nobata K, Watanabe O, Maeda O, et al. Interleukin 1B proinflammatory genotypes protect against gastro-oesophageal reflux disease through induction of corpus atrophy. *Gut* 2006; **55:** 158-64.

46. Figueiredo C, Machado JC, Pharoah P, Seruca R, Sousa S, Carvalho R, et al. Helicobacter pylori and interleukin 1 genotyping: An opportunity to identify high-risk individuals for gastric carcinoma. *J Natl Cancer Instit* 2002; **94:** 1680-7.

case report

Inflammatory myofibroblastic tumor of the pancreatic head – a case report of a 6 months old child and review of the literature

Ales Tomazic[1], Diana Gvardijancic[1], Joze Maucec[1], Matjaz Homan[2]

[1] Department of Abdominal Surgery, University Medical Center Ljubljana, Ljubljana, Slovenia

[2] Department of Gastroenterology, Hepatology and Nutrition, University Children's Hospital, Ljubljana, University Medical Center Ljubljana, Ljubljana, Slovenia

Background. Inflammatory myofibroblastic tumors are rare in the pediatric population. Most common localizations were reported in the lungs. A localization in the pancreas needs differentiation from other tumors and chronic pancreatitis. Treatment is surgical resection, although there are reports of treatment with oral steroids and radiation therapy.

Case report. A 6-month-old child was treated due to a tumor in the head of the pancreas. On admission he was jaundiced with pruritus. US and MRI confirmed pancreatic tumor. Preoperative biopsy wasn't conclusive regarding the nature of the tumor. Duodenopancreatectomy was performed. Postoperative course was uneventful. Histologic examination confirmed the diagnosis of inflammatory myofibroblastic tumor. On follow up, he remained with no evidence of recurrence.

Conclusions. A literature review revealed 10 cases of pancreatic inflammatory myofibroblastic tumors in the pediatric age group. Our patient is the youngest reported. Despite major resection, there were no complications. However, management of this child might be possible with steroids, but conservative treatment might be insufficient, especially in aggressive forms of tumors.

Key words: child; inflammatory myofibroblastic tumor; duodenopancreatectomy

Introduction

Inflammatory myofibroblastic tumors (IMT's) are rare solid lesions that occur primarily in visceral and soft tissue. Most frequently they occur in the first two decades of life. The most common localizations of IMTs have been reported in lung, mesentery and omentum.[1] These lesions have also been termed inflammatory pseudotumors, fibroxanthomas, fibrous histiocytomas, postinflammatory tumors and plasma cell granulomas. There are few hypotheses of the etiological factors responsible for development of the IMT. IMT can develop as a consequence of an inflammatory reaction to an underlying low grade malignancy. *Human herpes viruses*

3 and 8, *Eikenella corrodens* and *Epstain Barr virus* have been also proposed as possible infectious triggers of the IMT.[2,3,4] It is speculated that the disease is provoked by deregulation of cytokine production caused by infection.

Clinically and radiologically, an IMT can be confused with malignancy. A localization of IMT in the pancreas is very rare and needs differentiation from other tumors and chronic pancreatitis.

The macroscopic appearance of IMT is usually well-circumscribed or multinodular, white, firm mass. Histological, IMT is composed of spindle-shaped myofibroblasts or fibroblasts accompanied by a mixed inflammatory infiltrate of eosinophils, plasma cells, and lymphocytes.[1,5] Treatment is
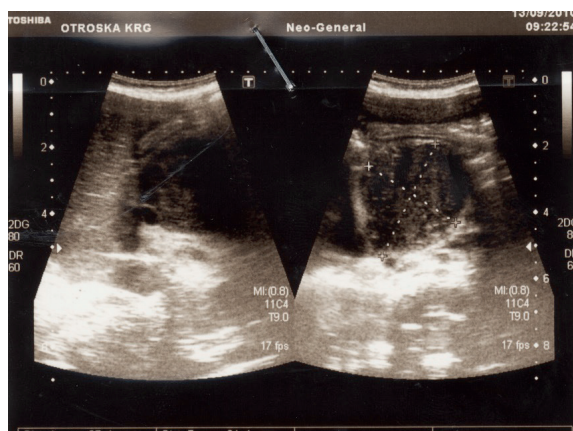
FIGURE 1. Ultrasound has identified 40 mm large mass in the region of the head of the pancreas.
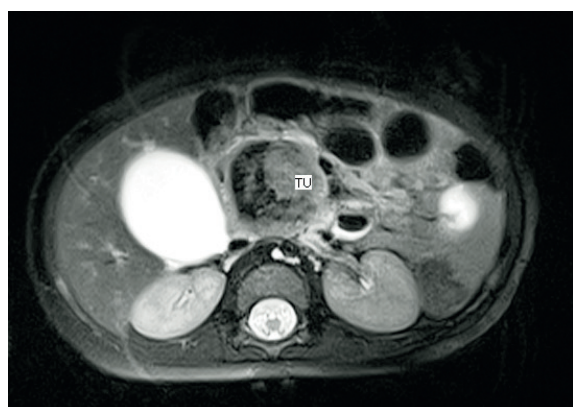
(A)

(B)

FIGURE 2. MRI confirmed well circumscribed tumor mass, with a diameter of 37 mm. The origin of the mass was in the head of the pancreas and in the uncinate process. There was no infiltration of the surrounding tissue. Tumor impressed the caval vein and pushed the superior mesenteric artery and vein ventraly and lateraly. **(A)** Coronal plane. **(B)** Sagital plane.

usually in the form of surgical resection, although there are recent reports of treatment with oral steroids.[6] Some authors report also palliative treatment with radiation therapy.[7]

We present a case of 6 months old male, who was referred to our department due to an IMT of the pancreatic head, which caused jaundice and pruritus. To the best of our knowledge, this is the youngest child with this type of tumor published so far in the literature.

Case report

A 6-months old boy was transferred to our hospital with a 4-days history of jaundice and pruritus. On examination he was jaundiced with no organomegaly. There was a rash on the trunk and extremities. Liver function tests revealed a direct bilirubin level of 109 μmol/L (normal below 17), alkaline phosphatas level of 11.62 μkat/L (normal up to 1.74) and γGT level of 3.23 μkat/L (normal up to 0.63).

An ultrasound scan (US) of his abdomen identified a 40 mm large mass in the head of the pancreas. The common bile duct was dilated, the gallbladder was extremely enlarged, but there was no dilatation of intrahepatic bile ducts and pancreatic duct (Figure 1). The results of US-guided fine needle aspiration biopsy wasn't conclusive regarding the nature of the tumor. MRI confirmed well circumscribed tumor mass, with a diameter of 37 mm. The tumor originated from the head of the pancreas and uncinate process. 3D reconstruction showed no infiltration in the surrounding tissue, including major vessels (Figure 2). However, there was evidence, that the tumor impressed on the caval vein

FIGURE 3. Surgical specimen of the duodenopancreatectomy. Left is duodenum, right gallbladder, up stomach and in the middle head of the pancreas with tumor.

and pushed the superior mesenteric artery and vein ventrally and laterally.

Whipple's procedure was performed due to biliary obstruction and possible malignancy (Figure 3).

Histological examination revealed an infiltrative growth in the pancreatic head, mainly surrounding and destroying pancreatic acini (Figure 4), but also encroaching on papila of Vater and duodenal wall. The lesion was composed of bland spindle cells forming a storiform (Figure 5) and vague fascicular growth pattern, admixed with areas displaying more epithelioid morphology (Figure 6) and variably prominent inflammatory cell infiltrate (Figure 7), composed of lymphocytes, plasma cells and eosinophilic granulocytes (Figure 8).

By immunohistochemistry, the lesional cells were smooth muscle actin positive proliferation of bland spindle cells forming a storiform and vague fascicular growth pattern, admixed with areas displaying more epithelioid morphology and variably prominent inflammatory cell infiltrate, composed of lymphocytes, plasma cells and eosinophilic granulocytes, while stainings for cytokeratins, S100, desmin, H-caldesmon and ALK were negative, confirming myofibroblastic differentiation of the lesional cells. Although the histological and immunohistochemical features were suggestive of inflammatory myofibroblastic tumour, an unusual form of chronic pancreatitis could not be reliably excluded.

The postoperative course was uneventful. The boy was discharged on the 14th postoperative day. Over the next 3.5 years of follow up, he remains well and with no clinical or radiological evidence of recurrence.

Discussion and review of literature

Pancreatic tumors are rare in childhood, accounting for only 0.2% of childhood malignancies.[8] Inflammatory myofibroblastic tumors are usually benign solid lesions of unclear etiology, commonly found in the lungs. The term inflammatory myofibroblastic tumor, commonly referred to as inflammatory pseudotumor in the previous literature, was initially proposed in 1990 in the study of inflammatory lesions of the pulmonary system.[9] The majority of the cases that were reported in the literature as »inflammatory pseudotumor« of the pancreas, would probably now be classified as autoimmune pancreatitis and in rare cases they represent
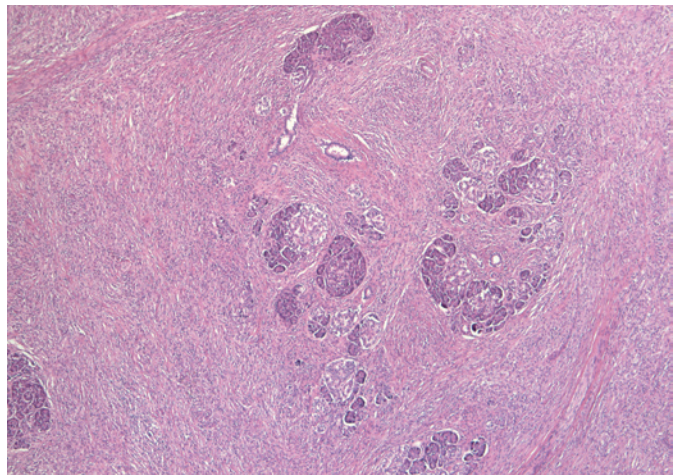

FIGURE 4. Spindle cell proliferation in the pacreatic head, growing in between and into the pacreatic acini.
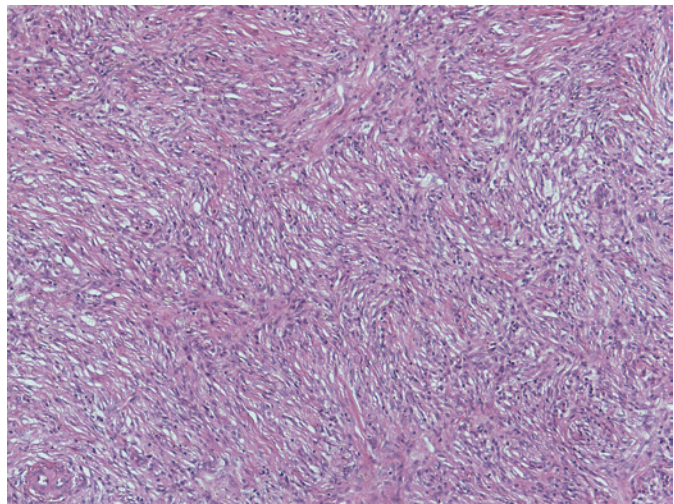

FIGURE 5. Bland spindle cell proliferation with vague storiform growth pattern.
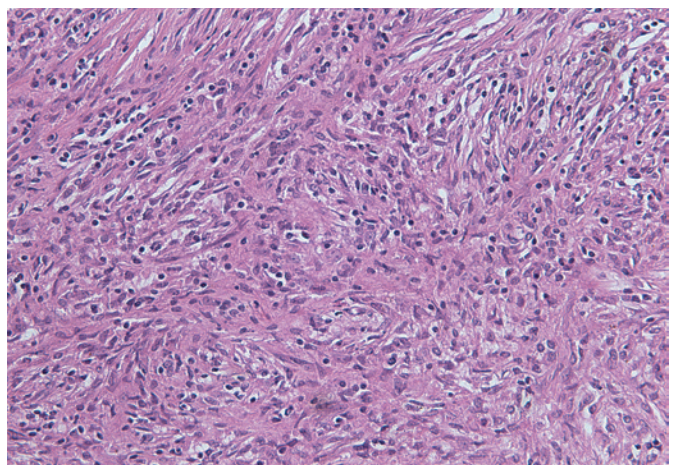
FIGURE 6. An admixture of spindled and more epithelioid lesional cells admixed with inflammatory cell infiltrate.
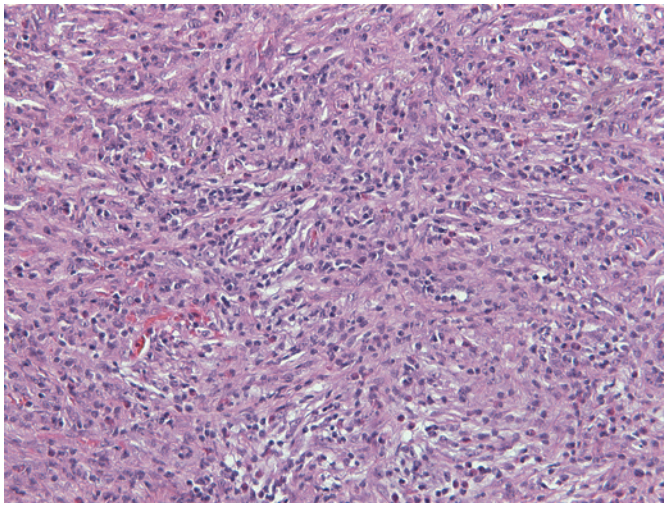
FIGURE 7. Prominent inflammatory cell infiltrate was present in several areas within the lesional cell proliferation.
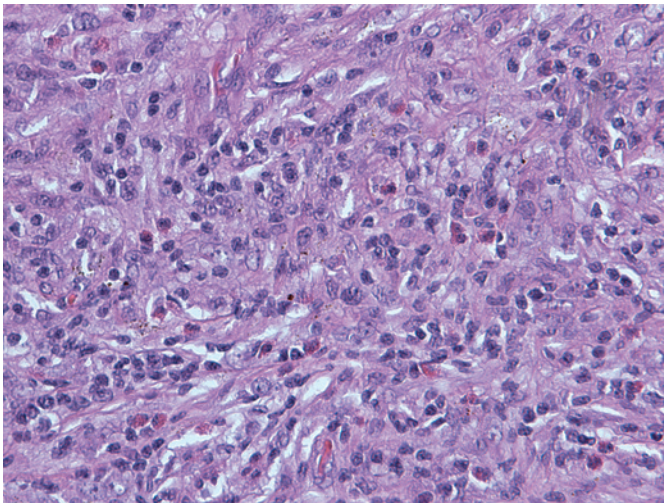
FIGURE 8. Note numerous eosinophilic granulocytes within the inflammatory cell component.

true »inflammatory myofibroblastic tumors«.[10,11] Another nosological problem with inflammatory myofibroblastic tumor is differentiation from inflammatory fibrosarcoma, which was first reported as an invasive tumor with greater atypia of constituent fibroblasts or myofibroblasts than seen in inflammatory myofibroblastic tumor.[12] According to Coffin, inflammatory myofibroblastic tumors are characterized with local invasion, vascular invasion and multifocal onset.[13] Invasion of retroperitoneal connective tissue, duodenal wall and Vater's papilla was also seen in our case. This indicated, that the lesion was neoplastic. However in inflam-

matory fibrosarcoma, more aggressive behaviour is seen, including higher incidence of recurrence and death.[12] Inflammatory myofibroblastic tumor and inflammatory fibrosarcoma have been speculated to be two lesions occupying the same spectrum, with reported cases of inflammatory myofibroblastic tumors probably including some low-grade examples of inflammatory fibrosarcoma.[14]

Histologically, inflammatory myofibroblastic tumors are characterized by irregular proliferation of myofibroblasts intermixed with inflammatory cells, mainly lymphocytes and plasmacytes. They are subcategorized into fibrohystiocytic type, plasma cell granuloma type, largely sclerosed or fibrosed type, hypocellular fibrous type and myxoid/vascular type.[15] Discovery of cytogenetic aberrations in inflammatory myofibroblastic tumors and the recognition of ALK gene rearrangements solidified the concept of inflammatory myofibroblastic tumor as a neoplastic lesion. It most frequently occurs in the lung or the mesenterium of children or young adults and rarely metastasizes (<5%).[16] The liver is also relatively frequently involved[17], but other sites such as the stomach[18], spleen[19], bladder[20], kidney[21], maxillary sinuses[22], heart[23], parapharyngeal space[24], retrorectal space[25] and peripheral nerve[26] have also been recorded.

Only 28 cases of pancreatic inflammatory myofibroblastic tumors have been reported so far, 60% being located in the pancreatic head.[7] Inflammatory fibroblastic tumor equally affects males and females. The age distribution resembled that of in pulmonary system ranging 2.5 to 70 years.[27] A literature review revealed 10 documented cases of pancreatic inflammatory myofibroblastic tumor in the pediatric age group (Table 1).

Compared to this data, our patient is the youngest child with inflammatory myofibroblastic tumor of the pancreas reported in the literature. The main features at presentation were pruritus, jaundice, abdominal mass, lethargy, vomiting, fever and anemia.[6] Curative resection is treatment of choice for inflammatory myofibroblastic tumors. Whipple's procedure or distal pancreatectomy is performed, according to the site of the tumor. The prognosis of inflammatory myofibroblastic tumors is generally good, with rare incidence of malignant transformation.[28] However, a significant recurrence rate of 25% was reported.[29] It was suggested that the presence of atypia, ganglion-like cells and p53 expression may suggest more aggressive behaviour.[30,31] These lesions may be indistinguishable from inflammatory fibrosarcoma due to a high degree of clinical and morphological overlap.[28]

TABLE 1. Reported cases of pediatric pancreatic inflammatory myofibroblastic tumors in the literature

Age	Sex	Location	Presentation	Treatment	Reference
10	F	body	Abdominal mass	Distal pancreatectomy	Abrebanel et al. 1984
2.5	F	body	Anemia, fever, abdominal mass	Distal pancreatectomy	Scott et al. 1988
5	F	head	vomiting	Whipple	Stringer et al. 1992
8	F	head	Jaundice, anemia, weight loss	Whipple	Uzoaru et al. 1993
8	F	body	Abdominl mass	Distal pancreatectomy	Shankar eta al. 1998
11	F	head	Jaundice, pruritus, anorexia, pain	Whipple	McLain et al. 2000
4	F	head	Malaise, lethargy	Whipple	Slavotinek et al. 2000
11	M	body	Lethargy, anemia, abdominal mass	Distal pancreatectomy	Morris-Stiff et al. 1998
13	F	head	Jaundice, vomiting, weight loss	Whipple	Dagash eta l. 2009
10	M	head	Jaundice, pain	Steroids	Dagash eta l. 2009

Besides surgical resection, alternative therapeutic regimens are still lacking. While systemic immunosuppresive treatment with steroids, chemotherapy and radiation therapy have been reported for unresected or recurrent cases of extrapancreatic inflammatory myofibroblastic tumors.[28,32,33]

In the literature there are only two reported cases of pancreatic inflammatory myofibroblastic tumors that were not treated with resection.[6,7] The first reported case was a child treated with high dose steroids. The mass gradually resolved and the patient remains disease free 6 years after treatment.[6] The second case was an adult treated with palliative radiation and corticoid therapy because of unresectable mass in the head of the pancreas.[7] In this case, long term results were not published.

Chronic pancreatitis could not be completely excluded according to histological examination. Anyway, specific causative factor for chronic pancreatitis was not identified. In addition, pediatric patients present with chronic pancreatitis much later (average age 6 ± 4 years) than it developed in our patient (6 months).[34]Therefore, chronic pancreatitis was very unlikely the reason for pancreatic head mass in our patient.

Conclusions

We report a case of pancreatic inflammatory myofibroblastic tumors in a six month old male child treated with surgical resection. This is the first case report of an infant with IMT. In addition, the tumor is rarely described in the pancreas. Despite major surgery no complications evolved in long term follow up.

References

1. Coffin CM, Humphrey PA, Dehner LP. Extrapulmonary inflammatory myofibroblastic tumor: a clinical and pathological survey. *Semin Diagn Pathol* 1998, **15:** 85-101.

2. Slavotinek JP, Bourne AJ, Sage MR, Freeman JK. Inflammatory pseudotumour of the pancreas in a child. *Pediatr Radiol* 2000; **30:** 801-3.

3. Gomez-Roman JJ, Sanchez-Velasco P, Ocejo-Vinyals G, Hernandez-Nieto E, Leyva-Cobian F, Val-Bernal JF. Human herpesvirus-8 genes are expressed in pulmonary inflammatory myofibroblastic tumor (inflammatory pseudotumor). *Am J Surg Pathol* 2001; **25:** 624-9.

4. Lewis JT, Gaffney RL, Casey MB, Farrell MA, Morice WG, Macon WR. Inflammatory pseudotumor of the spleen associated with a clonal Epstein-Barr virus genome. Case report and review of the literature. *Am J Clin Pathol* 2003; **120:** 56-61.

5. Gomez-Roman JJ, Ocejo-Vinyals G, Sanchez-Velasco P, Nieto EH, Leyva-Cobian F, Val-Bernal JF. Presence of human herpesvirus-8 DNA sequences and overexpression of human IL-6 and cyclin D1 in inflammatory myofibroblastic tumor. *Lab Invest* 2000; **80:** 1121-6.

6. Dagash H, Koh C, Cohen M, Sprigg A, Walker J. Inflammatory myofibroblastic tumor of the pancreas: a case report of 2 pediatric cases-steroids or surgery? *J Ped Surg* 2009; **44:** 1839-41.

7. Schutte K, Kandulski A, Kuester D, Meyer F, Wieners G, Schulz HU, et al. Inflammatory myofibroblastic tumor of the pancreatic head: An unusual cause of recurrent acute pancreatitis- case presentation of a palliative approach after failed resection and review of the literature. *Case Rep Gastroenterol* 2010; **4:** 443-51.

8. Mammen A, Kalisadan V, Beasley SW. Rare pancreatic tumors in children (other than nesidioblastosis). *Aust N Z J Surg* 1997; **67:** 720-1.

9. Petinato G, Manivel JC, De Rosa N, Dehner LP. Inflammatory myofibroblastic tumor (plasma cell granuloma). Clinicopathologic study of 20 cases with immunohistocemical and structural observations. *Am J Clin Pathol* 1990; **94:** 538-46.

10. Volkan Adsay N, Bastruk O, Klimstra DS, Kloppel G. Pancreatic pseudotumors: non-neoplastic solid lesions of the pancreas that clinically mimic pancreas cancer. *Sem Diagn Pathol* 2004; **21:** 260-7.

11. Petter LM, Martin JK, Menke DM. Localized lymphoplasmacellular pancreatitis forming a pancreatic inflammatory pseudotumor. *Mayo Clin Proc* 1998; **73:** 447-50.

12. Meis JM, Enzinger FM. Inflammatory fibrosarcoma of the mesentery and retroperitoneum; A tumor closely simulating inflammatory pseudotumor. *Am J Surg Pathol* 1991; **15:** 1146-56.

13. Coffin CM, Waterson J, Priest JR, Dehner LP. Extrapulmonary inflammatory myofibroblastic tumor (inflammatory pseudotumor); A clinicopathologic and immunohistochemical study of 84 cases. *Am J Surg Pathol* 1995; **19:** 859-72.

14. Nakamura Y, Inui K, Yoshino J, Tokoro T, Sabater L, Takeda S, et al. Inflammatory myofibroblastic tumor (inflammatory fibrosarcoma) of the pancreas: A case report. *Hepato-Gastroenetrology* 2005; **52:** 625-8.

15. Travis WD, Colby TV, Koss MN, Rosado-de-Christenson ML, Muller NL, King TE. Miscellaneous disease of uncertain etiology. In: Atlas of Nontumor Pathology. Non-neoplastic Disorders of the Lower Respiratory Tract. 1st ed. King DW, ed. American Registry of Pathology and Armed Forced Institute of Pathology, Washington DC, 2002. p. 857-900.

16. Coffin CM, Hornick JL,Fletcher CDM. Inflammatory myofibroblastic tumor: comparison of clinicopathologic, histologic, and immunohistochemical features including ALK expression in atypical and aggressive cases. *Am J Surg Pathol* 2007; **31:** 509-20.

17. Krech RH, Erhardt-Domagalsky M, Neumann H. Inflammatory pseudotumor of the liver. Morphologic and cytophotometry studies and differential diagnosis. *Pathologe* 1995; **16:** 415-20.

18. Taratuta E, Krinsky G, Genega E, Roche K, Geneisier N. Pediatric inflammatory pseudotumor of the stomach: contrast-enhanced CT and MR imaging findings. *Am J Radiol* 1996; **167:** 919-20.

19. Glazer M, Sagar V. SPECT imaging of the spleen in inflammatory pseudotumor. Correlation with ultrasound, CT, and MRI. *Clin Nucl Med* 1993; **18:** 527-9.

20. Foschini MP, Scarpellini F, Rinaldi P, Mancini AF, Accinelli G, Eusebi V. Inflammatory pseudotumor of the urinary bladder . Study of 4 cases and review of the literature. *Pathologica* 1995; **87:** 653-8.

21. Vujanic GM, Berry PJ, Frank JD. Inflammatory pseudotumor of the kidney with extensive metaplastic bone. *Pediatr Pathol* 1992; **12:** 557-61.

22. Som PM, Brandwein MS, Maldijan C, Reino AJ, Lawson W. Inflammatory pseudotumor of the maxillary sinus: CT and MR findings in six cases. *Am J Radiol* 1994; **163:** 689-92.

23. Jenkins PC, Dickinson AE, Flanagan MF. Cardiac inflammatory pseudotumor: rapid appearance in an infant with congenital heart disease. *Pediatr Cardiol* 1996; **17:** 399-401.

24. Hytiroglou P, Brandwein MS, Strauchen JA, Mirante JP, Urken ML, Biller HF. Inflammatory pseudotumor of the parapharyngeal space: Case report and review of the literature. *Head Neck* 1992; **14:** 230-4.

25. Georgia JD, Lawrence DP, DeNobile JW. Case report. Inflammatory pseudotumor in the retrorectal space: CT and MR appearance. *J Comput Assist Tom* 1996; **20:** 410-2.

26. Weiland TL, Scheithauer BW, Rock MG, Sargent JM. Inflammatory pseudotumor of nerve. *Am J Surg Pathol* 1996; **20:** 1212-8.

27. Hassan KS, Cohen HI, Hassan FK, Hassan SK. Unusual case of inflammatory myofibroblastic tumor associated with spontaneous splenic rupture. *World J Emerg Surg* 2010; **5:** 28.

28. DiFiore LW, Goldblum JR. Inflammatory myofibroblastic tumor of the small intestine. *J Am Coll Surg* 2002; **194:** 502-6.

29. Wreesmann V, van Eijck CH, Naus DC, van Velthuysen ML, Jeekel J, Mooi WJ. Inflammatory pseudotumor (inflammatory myofibroblastic tumor) of the pancreas: a case report of six cases associated with obliterative phlebitis. *Histopathology* 2001; **38:** 105-10.

30. Biselli R, Ferlini C, Fattorossi A, Boldrini R, Bosman C. Inflammatory myofibroblastic tumor (inflammatory pseudotumor): DNA flow cytometric analysis of nine pediatric cases. *Cancer* 1996; **77:** 778-84.

31. Hussong JW, Brown M, Perkins SL, Dehner LP, Coffin CM. Comparison of DNA ploidy, histologic and clinical outcome in inflammatory myofibroblastic tumors. *Mod Pathol* 1999; **12:** 279-86.

32. Tang TT, Segura AD, Oechler HW, Harb JM, Adair SE, Gregg DC, et al. Inflammatory myofibrohistiocytic proliferation simulating sarcoma in children. *Cancer* 1990; **65:** 1626-34.

33. Doski JJ, Priebe CJ, Driessnack M, Smith T, Kane P, Romero J. Corticosteroids in the management of unresected plasma cell granuloma (inflammatory pseudotumor) of the lung. *J Pediatr Surg* 1991; **26:** 1064-6.

34. Clifton MS, Pelayo JC, Cortes RA, Grethel EJ, Wagner AJ, Lee H, et al. Surgical treatment of childhood recurrent pancreatitis. *J Pediatr Surg* 2007; **42:** 1203-7.

research article

Neoadjuvant chemotherapy in 13 patients with locally advanced poorly differentiated thyroid carcinoma based on Turin proposal - a single institution experience

Nikola Besic[1], Marta Dremelj[2], Andreja Schwartzbartl-Pevec[3], Barbara Gazic[4]

[1] Department of Surgery, [2]Department of Radiotherapy, [3]Department of Nuclear Medicine, [4]Department of Pathology, Institute of Oncology Ljubljana, Ljubljana, Slovenia

Correspondence to: Prof. Nikola Bešić, M.D., Ph.D., Department of Surgical Oncology, Institute of Oncology Ljubljana, Zaloška 2, SI-1000 Ljubljana, Slovenia. Phone: +386 1 5879 953; Fax: +386 1 5879 400; E-mail: nbesic@onko-i.si

Disclosure: No potential conflicts of interest were disclosed.

Background. There is a paradigm that chemotherapy is ineffective in thyroid carcinoma. The aim of our study was to find out whether neoadjuvant chemotherapy before thyroid surgery had an effect on the size of primary tumour in patients with poorly differentiated thyroid carcinoma (PDTC) based on Turin proposal.

Patients and methods. Altogether, 13 patients (8 women, 5 men; median age 61 years) with PDTC based on Turin proposal were treated with neoadjuvant chemotherapy between 1986 and 2005. Tumour diameter was from 4.5 to 18 cm (median 9 cm). Regional and distant metastases were detected in 6 and 9 patients, respectively. Eight patients had pT4 tumour.

Results. Altogether, 29 (range 1–5) cycles of chemotherapy were given. Tumour diameter decreased in all the patients and by more than 30% in 5 patients (= 38%). Two of these five patients had also preoperative external beam irradiation (EBRT). Total thyroidectomy, lobectomy and neck dissection were performed in 10, 3 and 5 cases, respectively. R0 and R1 resection was done in 5 and 8 cases, respectively. Eight patients had postoperative EBRT of the neck and upper mediastinum. The 5-year and 10-year cause-specific survival rates of patients were 66% and 20%, respectively.

Conclusions. After neoadjuvant chemotherapy a partial tumour regression was observed in 38% of patients with PDTC based on Turin proposal.

Key words: poorly differentiated thyroid carcinoma; neoadjuvant; chemotherapy; survival; pathology

Introduction

A clinicopathologic entity of poorly differentiated thyroid carcinoma (PDTC) was proposed by Sakamoto *et al.* 30 years ago.[1] They found that the differences in the survival rates among well differentiated, poorly differentiated and anaplastic carcinomas were significant and of value in determining management and survival of thyroid cancer patients.[1] The World Health Organization (WHO) classification of tumours of endocrine organs in 2004 introduced PDTC as a separate entity and de-

fined it as a follicular-cell neoplasm showing limited evidence of structural follicular cell differentiation, and morphologically and behaviourally at an intermediate position between differentiated (follicular and papillary carcinomas) and undifferentiated (anaplastic) carcinoma.[2] At an international consensus meeting, uniform diagnostic criteria for PDTC (Turin Proposal criteria) were defined in the presence of solid/trabecular/insular growth pattern, absence of conventional nuclear features of papillary carcinoma, and in the presence of at least one of the following features: convoluted nuclei,

mitotic activity ≥3/10 high-power fields, or tumour necrosis.[3]

PDTC is a rare disease that carries a poor prognosis.[4] The incidence of PDTC as defined by the Turin Proposal criteria in Japan, USA and Northern Italy was 0.3%, 1.8% and 6.7%, respectively.[5,6] In the literature, there are only limited data on the treatment of patients with PDTC.[7-11] Recently, Ibrahimpasic *et al.* reported the results of treatment of 27 patients with PDTC presenting with gross extrathyroidal extension during the period 1986-2009 at the Memorial Sloan-Kettering Cancer Center.[9] The majority of their patients (60%) who presented with or subsequently developed distant metastases eventually died of distant disease, therefore they concluded that systemic therapies to target distant metastatic disease are required to achieve improvements in the outcome.[9] The aim of the present study was to find out whether neoadjuvant chemotherapy before thyroid surgery had an effect on the size of primary tumour in patients with locally advanced and/or initially metastatic PDTC based on Turin proposal.

Patients and methods

During the period 1979-2005, 45 patients (33 women, 12 men; mean age 61.6 years) were treated with neoadjuvant chemotherapy for thyroid carcinoma at our tertiary comprehensive cancer center.[12,13] Among them, 13 patients (8 women, 5 men; median age 61 years) had poorly differentiated thyroid carcinoma. They were initially treated during the period 1986-2005. The histological slides of all 13 patients with PDTC, who were the subject of this study, were reviewed by a pathologist experienced in thyroid pathology. All tumours fulfilled the Turin proposal criteria.[3]

In all patients in the primary chemotherapy group, the tumour was considered inoperable because of infiltration into the surrounding tissues. Altogether, ten patients were treated with neoadjuvant chemotherapy, while two patients were treated with preoperative chemotherapy and preoperative external beam radiotherapy (EBRT). Surgery was performed whenever the tumour was reduced after chemotherapy and/or EBRT and the surgeon deemed it resectable. The median interval between the beginning of chemotherapy and the surgical procedure was 30 days (range 8–85 days).

Data on the patients' gender, age, history and extent of the disease, morphological characteristics, therapy, locoregional control, and survival were collected. The tumour size, presence of regional or distant metastases and residual tumour after surgery were assessed by TNM clinical classification according to the Union for International Cancer Control (UICC) criteria from 2009.[14] Clinical characteristics of patients with PDTC based on Turin proposal and therapy are presented in Table 1.

The aim of the study was to evaluate the effect of chemotherapy in patients with PDTC. Because of rarity of PDTC we collected data of patients who were treated at our Institute and were included in the following consecutive clinical trials: Rational diagnostic and therapy of patients with thyroid tumours (J3-7842), Importance of cytomorphology, measurements of DNA, Ki 67 and apoptosis for planning and evaluation of effect of chemotherapy in thyroid carcinoma (J3-3026), Genetic and radio-nuclear methods in diagnostics and therapy of thyroid carcinoma (J3-3460), all supported by the Ministry of Science of Slovenia. The Medical Ethics Committee of the Republic Slovenia and the Protocol Review Board and Ethics Committee of the Institute of Oncology Ljubljana reviewed and approved all three studies, which were performed in accordance with the ethical standards laid down in an appropriate version of the 1964 Declaration of Helsinki. These studies were conducted with the understanding and consent of the involved human subjects. Our chart review for the present publication was approved by the Institutional Review Board.

Surgery

Surgery was considered the most effective treatment of PDTC and has therefore remained its mainstay. At our Institute, treatment of each patient with advanced thyroid carcinoma depends on the decision of the multidisciplinary team consisting of a surgical oncologist, a specialist in nuclear medicine, a medical oncologist and a radiotherapist. Our patients were treated with surgery, radioiodine (RAI), EBRT, chemotherapy, or a combination of these modalities as dictated by the circumstances.[12] Before RAI ablation of thyroid remnant and RAI therapy all patients were on low-iodine diet for two weeks in order to achieve moderate iodine deficiency.[15]

Chemotherapy and radiotherapy

The treatment was started with a non-toxic schedule (*i.e.* 2 mg vinblastine over 12- or 24-h infusions in 1000 mL of 0.9% saline) as already reported

TABLE 1. Clinical characteristics and therapy of patients with poorly differentiated thyroid carcinoma (PDTC) based on Turin proposal

Patient no.	Gender	Age	Histology of primary PDTC	TNM	Effect of chemotherapy (RECIST)	Preoperative EBRT (neck)	Surgical treatment	Residual tumour after surgery	RAI ablation of thyroid remnant	RAI therapy (number)	EBRT (neck)	Disease specific survival (months)	Cause of death
1	F	62	Hurthle cell	T3N1M1	SD	no	TT+mRND	R1	yes	0	no	131	DM
2	F	80	Papillary	T3N1M1	PR	no	TT+mRND	R1	yes	2	yes	24	DM
3	F	78	Papillary	T3N1M1	SD	no	TT+mRND	R1	yes	0	yes	26	DM+LR
4	F	45	Follicular	T4N0M0	SD	no	TT	R1	yes	1	yes	119	DM
5	F	47	Hurthle cell	T4N0M1	SD	no	TT	R1	yes	5	no	52	DM
6	M	69	Follicular	T4N1M0	PR	yes	TT	R1	yes	0	yes	101	Other causes
7	M	65	Papillary	T4N1M1	SD	no	lobectomy+mRND	R1	yes	2	yes	49	Other causes
8	M	61	Follicular	T4N0M0	PR	no	lobectomy	R0	yes	3	yes	104	DM
9	M	56	Papillary	T4N1M1	SD	no	lobectomy+mRND	R1	yes	6	yes	92	DM
10	F	57	Papillary	T4N0M0	PR	yes	TT	R0	yes	2	yes	103	DM
11	F	63	Follicular	T3N0M1	SD	no	TT	R0	yes	3	no	183	DM
12	F	37	Follicular	T3N0M1	SD	no	TT	R0	yes	1	no	54	DM
13	M	59	Follicular	T4N0M1	PR	no	TT	R0	yes	7	no	118	DM

DM = distant metastases; F = female; LR = locoregional disease; M = male; mRND = modified radical neck dissection; PR = partial response; RAI = radioiodine; SD = stable disease; TT = total thyroidectomy

in our previous publications.[8,12,13,16] Vinblastine shows a cytostatic effect in cell lines models, which is reflected in rapid decrease of relative cell viability during prolonged exposure.[17] At all tested concentrations, the relative cell viability was reduced by 20% or more already after 48 h exposure.[17] However, vinblastine may cause cardiac arrhythmia, therefore we did not use vinblastine in a patient (number 7) with ischemic heart disease. Instead, in this patient, 20 mg of adriamycin in a 2-hour infusion was used once a week. In such doses, adriamycin does not cause nausea, vomiting, alopecia, hematopoietic side effects or congestive heart failure according to our extensive experience with adriamycin in patients with anaplastic thyroid carcinoma. The tumour increased in one of our patients (number 8) despite treatment with vinblastine, therefore a combination of vinblastine and cisplatin of 90 mg over a 24-h infusion with EBRT was used. After treatment with this combination, the tumour size decreased by more than half.

Hematologic (anaemia, leukopenia, neutropenia, and thrombocytopenia) and non-hematologic (nephrotoxicity defined by serum creatinine level, alopecia, and nausea/vomiting) toxic effects were evaluated according to the National Cancer Institute - Common Toxicity Criteria, version 4.0.

The local effect of chemotherapy used to be assessed by clinical findings only. The size of the primary tumour was measured clinically each day during the first week after chemotherapy and once a week thereafter during the visits to the outpatient clinic and before the next cycle of chemotherapy. Resectability of a tumour was clinically evaluated by a surgeon once a week. The extent of the disease and the potential effectiveness of chemotherapy were evaluated before the first chemotherapy and before the surgical procedure by clinical examination, X-ray, CT scan, ultrasonography and/or serum thyroglobulin (Tg) concentration measurements, as dictated by the circumstances. The overall effect of chemotherapy on the primary tumour size was defined according to Response Evaluation Criteria in Solid Tumours (RECIST) criteria[18]: (1) progressive disease (PD): at least a 20% increase in the sum of longest diameter of target lesions, taking as reference the smallest sum of longest diameter recorded before the treatment started; (2) stable disease (SD): neither sufficient shrinkage to qualify for partial regression nor sufficient increase to qualify for progressive disease; (3) partial response (PR): at least a 30% decrease in the sum of the longest diameter of target lesions; and as (4) complete response if the tumour disappeared.

TABLE 2. Presence of distant metastases in 13 patients with poorly differentiated thyroid carcinoma (PDTC) based on Turin proposal treated with neoadjuvant chemotherapy

Factor	Subgroup	Without metastases (N = 4)	With metastases (N = 9)	p-value
Mean age (years)		59	62	0.64
Mean tumour size (cm)		10	9.7	0.64
Gender	Female	2	6	1.00
	Male	2	3	
Age (years)	44 or less	0	1	1.00
	45 or more	4	8	
Tumour diameter (cm)	0 ≤ 4	0	0	1.00
	More than 4	4	8	
pT tumour stage	pT3	0	5	0.105
	pT4	4	4	
N stage	N0	3	4	0.56
	N1 or N2	1	5	
M stage	M0	4	0	-
	M1	0	9	
Thyroid surgical procedure	Total or near-total thyroidectomy	3	7	1.00
	Lobectomy	1	2	
Residual tumour after surgery	R0	2	3	1.00
	R1	2	6	
Neck dissection	No	4	4	0.105
	Yes	0	5	
Radioiodine ablation after surgery	No	0	0	1.00
	Yes	4	9	
Therapy with radioiodine	No	1	2	1.00
	Yes	3	7	
Effect of chemotherapy	< 50% or no effect	1	7	0.22
	50–99%	3	2	
Recurrence	No	1	0	
	Yes - distant	3	0	
	Disease present permanently	0	9	
Outcome	Death of disease	3	8	1.00
	Death of other causes	1	1	
Disease-free interval in months: mean (range)		106 (101–119)	-	-
Cause-specific survival in months: mean (range)		106 (101–119)	81 (24–183)	0.75

According to our study protocol, if primary tumour progressed after chemotherapy, the patient was treated with a combination of EBRT and chemotherapy. Two patients received preoperative EBRT with a median dose of 35 Gy (range 30–40 Gy) over three to four weeks. In one patient, intubation was necessary one week after the initiation of external irradiation with a daily dose of 2.5 Gy. Altogether, eight patients had preoperative and/or postoperative EBRT of the neck and superior mediastinum with a total tumour dose of 30.6–59.4 Gy (median 50 Gy). The radiation field included the whole neck up to the level of the mastoid process, bilateral supraclavicular and infraclavicular regions, and the superior mediastinum using a ^{60}Co unit and two opposed fields.

Follow-up and survival

For all patients, follow-up examinations were performed at our Institute at least once a year. They consisted of obtaining a detailed medical history, a physical exam, and determination of the serum Tg concentration. Whenever the Tg concentration was elevated, imaging (X-ray, ultrasound, RAI scintigraphy, computed tomography, magnetic resonance imaging, bone scintigraphy and/or positron emission tomography - computed tomography (PET-CT) scan) was performed to determine the location and extent of residual disease or suspected recurrence.

Disease-specific survival was defined as the period from the first day of treatment with preopera-

tive chemotherapy to the death or last follow-up of the patient. Overall survival was defined as the period from the first day of primary treatment preoperative chemotherapy to death of any cause or the last follow-up. Disease-free interval was defined as the period from the beginning of chemotherapy to recurrence or the last follow-up. The disease-free interval excludes those patients with distant metastases at initial presentation.

Statistical analysis

Characteristics of patients and treatments were compared by Fisher's exact or chi-square test, where appropriate. The age of the patients and size of their tumours were compared using the Mann-Whitney rank-sum test. Survival and disease-free intervals were compared using a log-rank test. Survival curves were calculated according to the Kaplan-Meier method. For statistical analysis, SPSS 16.0 for Windows was used.

Results

Patients

Tumour diameter was from 4.5 to 18 cm (median 9 cm). Regional and distant metastases were detected in 6 and 9 patients, respectively. Six patients had lung metastases and three patients had bone metastases. Eight (61%) patients had pT4 tumour (Table 2).

Actual chemotherapy and toxicity

Chemotherapy consisted of vinblastine, vinblastine with adriamycin or vinblastine with cisplatin in 11, 1 and 1 cases, respectively. The interval between the first chemotherapy and surgical procedure was 1–12 weeks (median 4 weeks). Altogether, 29 (range 1–5) cycles of chemotherapy were given.

The following toxic effects of cisplatin were observed in our patient number 8: leukopenia grade 1, nausea/vomiting grade 1-2, nephrotoxicity grade 1 and alopecia grade 1. None of other patients had any toxic side effects of chemotherapy because doses of chemotherapy used were very low.

Response to treatment, survival, additional treatment and follow up

Survival of patients with PDTC according to the effect of chemotherapy is presented in Figure 1.
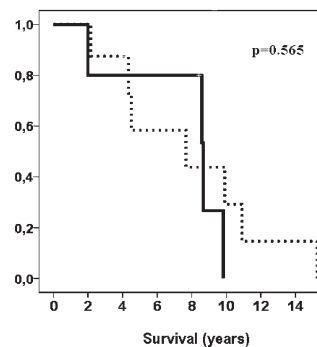
Solid line = partial response; dashed line = stable disease

FIGURE 1. Survival of patients with poorly differentiated thyroid carcinoma (PDTC) according to the effect of chemotherapy.
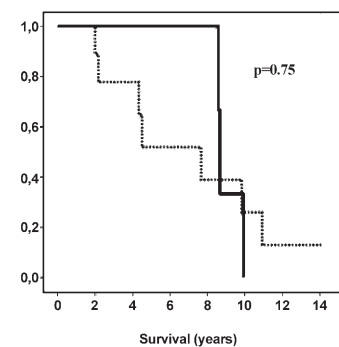
Solid line = M0, dashed line = M1

FIGURE 2. Survival of patients with poorly differentiated thyroid carcinoma (PDTC) and presence of metastases.

Tumour size decreased in all of patients, but PR was observed in 5 patients (38%). Two of these five patients had also preoperative EBRT.

Total thyroidectomy, lobectomy and neck dissection were performed in 10, 3 and 5 cases, respectively. R0 and R1 resection was done in 5 and 8 cases, respectively.

Radioiodine (RAI) therapy was used in patients with initially distant metastatic disease and distant dissemination during follow-up in 7 out of 9 and 3 out of 3 patients, respectively. They received 1–7 (median 2.5) therapies with RAI in a dose of 3.7–7.4 GBq. Eight patients received postoperative EBRT of the neck and upper mediastinum.

Distant metastases were diagnosed in three patients during follow-up of 7–189 months (median 118 months).

Ten patients died of distant metastases, one of distant metastases with small locoregional recurrence, and two patients died of other causes. The 5-year and 10-year cause-specific survival rates of patients were 66% and 20%, respectively. Survival of patients with PDTC based on Turin proposal and presence of metastases are shown in Figure 2.

Discussion

Fortunately, aggressive locally advanced differentiated, poorly differentiated and anaplastic thyroid carcinomas are rare. However, because of this rarity, it is very unlikely that randomized trials will be conducted in patients with these rare tumours. One way to test the effectiveness of the therapy is to use a specific drug in a neoadjuvant setting. In

two of our previous studies, we found out that neoadjuvant chemotherapy reduced the size of primary tumour by more than half in 44% of patients with differentiated thyroid carcinoma.[12,13]

The aim of the present study was to report the effectiveness of neoadjuvant chemotherapy in reducing the size of primary tumour in patients with locally advanced and/or initially metastatic PDTC based on Turin proposal. We found that in 38% of patients with PDTC based on Turin proposal, neoadjuvant chemotherapy decreased the size of primary tumour and PR was achieved. Based on this data we believe that chemotherapy may be the treatment of choice in locoregionally advanced and metastatic PDTC. Our data are not the only ones that oppose the paradigm that chemotherapy is ineffective in well, moderately or poorly differentiated thyroid carcinoma. Santini *et al.* reported a 37% response rate after a combination of carboplatin, epirubicin and thyroid-stimulating hormone (TSH) stimulation in fourteen patients with PDTC and RAI-resistant diffuse lung metastases.[19] Carboplatin (300 mg/m^2) and epirubicin (75 mg/m^2) were given at 4- to 6-week intervals for a total of six courses. To raise serum TSH, either endogenous TSH stimulation was obtained by reducing the daily dose of L-thyroxin therapy or exogenous TSH stimulation was induced by recombinant human TSH. Lung computed tomography scans before and after therapy showed that one patient had a complete remission, while five patients had a partial remission.[19]

We believe that extensive surgery is not enough to obtain long-lasting locoregional control of disease in advanced PDTC. Namely, Ibrahimpasic *et al.* reported that 19 patients had only microscopic residual disease and 8 (42%) of them had locoregional recurrence.[9] They also reported that 63% of patients had only RAI therapy, 11% underwent RAI therapy and EBRT, while 11% had only EBRT.[9] On the other hand, our 8 patients with microscopic residual disease after thyroid surgery received a more extensive additional therapy: all of them had initial chemotherapy, postoperative RAI ablation of thyroid remnant and EBRT. Additionally, 5 patients (62.5%) also received RAI therapy. A more extensive additional therapy in our patients might be the reason that locoregional recurrence occurred in only 25% of cases.

Locoregional recurrence of thyroid carcinoma may lead to an uncontrollable disease and frequently often correlates with poor outcome. EBRT is used to prevent locoregional recurrence. According to the American Thyroid Association

guidelines[20], EBRT treatment of the primary tumour should be considered in patients aged over 45 years with grossly visible extrathyroidal extension at the time of surgery and a high likelihood of microscopic residual disease, or in patients with gross residual tumour in whom further surgery or RAI would likely be ineffective. In a recent review article, Sanders *et al.* concluded that EBRT should probably be considered also in patients with PDTC who have pT3 carcinoma, extracapsular extension of lymph node disease or extensive lymph node involvement.[7]

One reason that supports the initial multimodal approach is the fact that PDTC is often composed of a poorly differentiated as well as moderately differentiated component. It is well known that poorly differentiated cells are sensitive to chemotherapy. Neoadjuvant chemotherapy proved to be effective in all our patients, while in 38% PR of primary tumour was observed. RAI was used whenever possible to treat the differentiated component of PDTC.

Our study has several limitations. It is not randomized and there is no control group of patients (without chemotherapy). Furthermore, number of patients is too small to draw any conclusions whether the prognosis of R0 tumours is superior to that of R1 tumours and whether R1 tumours can be controlled by EBRT. However, we believe that in order to prevent locoregional recurrence and/or dissemination, the initial treatment should be based on prognostic and predictive factors also in patients with thyroid carcinoma. This principle is widely applied to many solid malignancies, *i.e.* breast cancer, colorectal cancer, head and neck cancer and many others. For example, after surgical procedure, a patient with breast cancer will also be treated with EBRT, chemotherapy, hormonal therapy and targeted therapy based on prognostic and predictive factors.[21]

However, American Thyroid Association and European Thyroid Association guidelines for treatment of differentiated thyroid carcinoma do not recommend initial multimodal approach in more aggressive types of differentiated thyroid carcinoma.[21,22] It is well known that PDTC based on Turin proposal and anaplastic thyroid carcinoma are aggressive tumours that cause locoregional recurrence and dissemination[4], therefore, we believe that an adequate initial multimodal treatment is justified. Naturally, in locoregionally advanced and/or metastatic PDTC, multimodal treatment should be used whenever possible. With such an approach, excellent locoregional

control of disease was achieved in our patients. None of our patients had uncontrollable locoregional PDTC.

In locally advanced patients with PDTC based on Turin proposal from the Memorial Sloan-Kettering Cancer Center[9], 5-year disease-specific survival was only 49%, while it was 66% in our patients, although initially distant metastases were more common in our series (37% *vs.* 61%). Possibly, longer survival of our patients was a result of our multimodal treatment approach. All our patients had initial chemotherapy, and 92% of them received adjuvant therapy: 31% RAI only, 15% EBRT only, while as many as 46% received both RAI therapy and EBRT. On the other hand, only 77% of patients reported by Ibrahimpasic *et al.* underwent adjuvant therapy: 55% RAI only, 11% EBRT only, while only 11% underwent both RAI therapy and EBRT.[9]

Jung *et al.* reported treatment results in 49 patients with PDTC not based only on Turin proposal.[23] RAI therapy was used in 38 patients. Patients with RAI therapy had significantly longer survival in comparison to patients without RAI therapy (5-year survival: 73% vs. 60%).[22] However, in a multivariate analysis, RAI therapy was not an independent factor for survival.[22] Similarly, Lai *et al.* reported that RAI therapy was not an independent prognostic factor for survival in a retrospective review consisting of 82 patients with insular carcinoma, possibly because patients with worse-prognosis tumours were selected for a more extensive adjuvant treatment, obscuring any potential benefit.[10] RAI scanning was performed at the Memorial Sloan-Kettering Cancer Center in eight patients with PDTC based on Turin proposal with distant metastases at presentation, and seven (87.5%) patients had RAI-avid metastases.[9] Similarly, at our institute, 83% of cases with distant disease had RAI-avid metastases, so these patients underwent RAI therapy.

Like many others studies[7,9,10,23] ours also shows that distant disease is the main cause of death in patients with locally advanced and metastatic PDTC. Initially or after disease progression, PDTC was a systemic disease in 92% of our patients. In order to treat systemic PDTC based on Turin proposal effectively, not only RAI but also other systemic treatment modalities are needed. Of course, there is a place for targeted therapy in PDTC, but at present time, there are only limited data about its use in poorly differentiated thyroid carcinoma.[24] Sorafenib was reported to be effective treatment in radioiodine-refractory PDTC.[25]

Conclusions

After neoadjuvant chemotherapy and preoperative EBRT a partial response of primary tumour was observed in 38% of patients with PDTC based on Turin proposal. Surgical procedure is the mainstay of treatment in PDTC, but postoperative RAI therapy, EBRT, or both, seem to be associated with prolonged survival.

Acknowledgement

References

1. Sakamoto A, Kasai N, Sugano H. Poorly differentiated carcinoma of the thyroid. A clinicopathologic entity for a high-risk group of papillary and follicular carcinomas. *Cancer* 1983; **52:** 1849-55.

2. Sobrinho-Simões M, Albores-Saavedra J, Tallini G. Poorly differentiated carcinoma. In: DeLellis RA, Lloyd RV, Heitz U, Eng C, editors, *Pathology and genetics. Tumours of endocrine organs.* Lyon: World Health Organization, IARC Press, France; 2004. p. 73-6.

3. Volante M, Collini P, Nikiforov YE, Sakamoto A, Kakudo K, Katoh R, et al. Poorly differentiated thyroid carcinoma: the Turin proposal for the use of uniform diagnostic criteria and an algorithmic diagnostic approach. *Am J Surg Pathol* 2007; **31:** 1256-64.

4. Patel KN, Shaha AR. Poorly differentiated and anaplastic thyroid cancer. *Cancer Control* 2006; **13:** 119-28.

5. Asioli S, Erickson LA, Righi A, Jin L, Volante M, Jenkins S. Poorly differentiated carcinoma of the thyroid: validation of the Turin proposal and analysis of IMP3 expression. *Mod Pathol* 2010; **23:** 1269-78.

6. Ito Y, Hirokawa M, Fukushima M, Inoue H, Yabuta T, Uruno T, et al. Prevalence and prognostic significance of poor differentiation and tall cell variant in papillary carcinoma in Japan. *World J Surg* 2008; **32:** 1535-43.

7. Sanders EM Jr, LiVolsi VA, Brierley J, Shin J, Randolph GW. An evidence-based review of poorly differentiated thyroid cancer. *World J Surg* 2007; **31:** 934-45.

8. Auersperg M, Us-Krasovec M, Petric G, Pogacnik A, Besic N. Results of combined modality treatment in poorly-differentiated and anaplastic thyroid carcinoma. *Wien Klin Wochenschr* 1990; **102:** 267-70.

9. Ibrahimpasic T, Ghossein R, Carlson DL, Chernichenko N, Nixon I, Palmer FL, et al. Poorly differentiated thyroid carcinoma presenting with gross extrathyroidal extension: 1986-2009 Memorial Sloan-Kettering Cancer Center experience. *Thyroid* 2013; **23:** 997-1002.

10. Lai HW, Lee CH, Chen JY, Tseng LM, Yang AH. Insular thyroid carcinoma: collective analysis of clinicohistologic prognostic factors and treatment effect with radioiodine or radiation therapy. *J Am Coll Surg* 2006; **203:** 715-22.

11. Justin EP, Seabold JE, Robinson RA, Walker WP, Gurll NJ, Hawes DR. Insular carcinoma: a distinct thyroid carcinoma with associated iodine-131 localization. *J Nucl Med* 1991; **32:** 1358-63.

12. Besic N, Auersperg M, Dremelj M, Vidergar-Kralj B, Gazic B. Neoadjuvant chemotherapy in 16 patients with locally advanced papillary thyroid carcinoma. *Thyroid* 2013; **23:** 178-84.

13. Besic N, Auersperg M, Gazic B, Dremelj M, Zagar I. Neoadjuvant chemotherapy in 29 patients with locally advanced follicular or Hürthle cell thyroid carcinoma: a phase 2 study. *Thyroid* 2012; **22:** 131-7.

14. Sobin LH, Gospodarowitz MK, Witekind C. Thyroid gland (ICD-O C73). In: Sobin LH, Gospodarowitz MK, Witekind C, editors. *TNM classification of malignant tumours.* 7th edition. New York: Wiley Blackwell; 2009. p. 58-62.

15. Dobrenic M, Huic D, Zuvic M, Grosev D, Petrovic R, Samardzic T. Usefulness of low iodine diet in managing patients with differentiated thyroid cancer - initial results. *Radiol Oncol* 2011; **45:** 189-95.

16. Auersperg M, Us-Krasovec M, Pogacnik A, Hocevar M, Novak B, Besic N, et al. Induction chemotherapy in primarily inoperable differentiated thyroid carcinomas. *Radiol Oncol* 1993; **27:** 187-91.

17. Zager V, Cemazar M, Hreljac I, Lah TT, Sersa G, Filipic M. Development of human cell biosensor system for genotoxicity detection based on DNA damage-induced gene expression. *Radiol Oncol* 2010; **44:** 42-51.

18. Eisenhauer EA, Therasse P, Bogaerts J, Schwartz LH, Sargent D, Ford R, et al. New response evaluation criteria in solid tumours: revised RECIST guideline (version 1.1). *Eur J Cancer* 2009; **45:** 228-47.

19. Santini F, Bottici V, Elisei R, Montanelli L, Mazzeo S, Basolo F. Cytotoxic effects of carboplatinum and epirubicin in the setting of an elevated serum thyrotropin for advanced poorly-differentiated thyroid cancer. *J Clin Endocrinol Metab* 2002; **87:** 4160-5.

20. Cooper DS, Doherty GM, Haugen BR, Kloos RT, Lee SL, Mandel SJ, et al. Revised American Thyroid Association Management guidelines for patients with thyroid nodules and differentiated thyroid cancer. *Thyroid* 2009; **19:** 1167-214.

21. Marinko T, Dolenc J, Bilban-Jakopin C. Cardiotoxicity of concomitant radiotherapy and trastuzumab for early breast cancer. *Radiol Oncol* 2014; **48:** 105-12.

22. Pacini F, Schlumberger M, Dralle H, Elisei R, Smit JW, Wiersinga W, et al. The European Thyroid Cancer Taskforce: European consensus for the management of patients with differentiated thyroid carcinoma of the follicular epithelium. *Eur J Endocrinol* 2006; **154:** 787-803.

23. Jung TS, Kim TY, Kim KW, Oh YL, Park do J, Cho BY, et al. Clinical features and prognostic factors for survival in patients with poorly differentiated thyroid carcinoma and comparison to the patients with the aggressive variants of papillary thyroid carcinoma. *Endocr J* 2007; **54:** 265-74.

24. Kim KB, Cabanillas ME, Lazar AJ, Williams MD, Sanders DL, Ilagan JL, et al. Clinical responses to vemurafenib in patients with metastatic papillary thyroid cancer harboring BRAF(V600E) mutation. *Thyroid* 2013; **23:** 1277-83.

25. Liu M, Shen Y, Ruan M, Li M, Chen L. Notable decrease of malignant pleural effusion after treatment with sorafenib in radioiodine-refractory follicular thyroid carcinoma. *Thyroid* 2014; **24:** 1179-83.

research article

Fibulin-3 as a biomarker of response to treatment in malignant mesothelioma

Viljem Kovac[1], Metoda Dodic-Fikfak[2], Niko Arneric[2], Vita Dolzan[3], Alenka Franko[2]

[1] Institute of Oncology Ljubljana, Zaloška cesta 2, Ljubljana, Slovenia

[2] Clinical Institute of Occupational Medicine, University Medical Center Ljubljana, Ljubljana, Slovenia

[3] Pharmacogenetics Laboratory, Institute of Biochemistry, Faculty of Medicine, University of Ljubljana, Ljubljana, Slovenia

Correspondence to: Assist. Prof. Alenka Franko, M.D., Ph.D., Clinical Institute of Occupational Medicine, University Medical Center Ljubljana, Poljanski nasip 58, Ljubljana, Slovenia. Phone: +386 1 522 2119; Fax: +386 1 522 2478; Email: alenka.franko@siol.net

Disclosure: No potential conflicts of interest were disclosed.

Background. Fibulin-3 is a new potential biomarker for malignant mesothelioma (MM). This study evaluated the potential applicability of fibulin-3 plasma levels as a biomarker of response to treatment and its prognostic value for progressive disease within 18 months. The potential applicability of fibulin-3 in comparison with or in addition to soluble mesothelin-related peptides (SMRP) was also assessed.

Patients and methods. The study included 78 MM patients treated at the Institute of Oncology Ljubljana between 2007 and 2011. Fibulin-3 levels in plasma samples obtained before treatment and in various responses to treatment were measured with the enzyme-linked immunosorbent assay.

Results. In patients evaluated before the treatment, fibulin-3 levels were not influenced by histopathological sub-types, tumour stages or the presence of metastatic disease. Significantly higher fibulin-3 levels were found in progressive disease as compared to the levels before treatment (Mann-Whitney [U] test = 472.50, p = 0.003), in complete response to treatment (U = 42.00, p = 0.010), and in stable disease (U = 542.00, p = 0.001). Patients with fibulin-3 levels exceeding 34.25 ng/ml before treatment had more than four times higher probability for developing progressive disease within 18 months (odds ratio [OR] = 4.35, 95% confidence interval [CI] 1.56–12.13). Additionally, patients with fibulin-3 levels above 34.25 ng/ml after treatment with complete response or stable disease had increased odds for progressive disease within 18 months (OR = 6.94, 95% CI 0.99–48.55 and OR = 4.39, 95% CI 1.63–11.81, respectively).

Conclusions. Our findings suggest that in addition to SMRP fibulin-3 could also be helpful in detecting the progression of MM.

Key words: fibulin-3; biomarker; malignant mesothelioma; response to treatment.

Introduction

Malignant mesothelioma (MM) is an aggressive malignant disease that has been associated with occupational and environmental exposure to asbestos.[1-8] Most commonly it arises from serosal cells of the pleura and less frequently from peritoneum or other serosal surfaces such as pericardium and tunica vaginalis.[6,9]

Malignant mesothelioma remains a fatal disease that is hard to treat with favourable outcome.[9,10] Hence, potential new biomarkers for earlier diag-

nosis and following the response to treatment have been intensively investigated. One of the most extensively studied blood-based biomarkers is soluble mesothelin-related peptides (SMRP); however, the poor sensitivity limits its added value to early diagnosis.[10,11] Nevertheless, the results of our previous study suggest that SMRP may be a useful tumour marker for detecting the progression of MM and evaluating tumour response to treatment.[12]

Fibulin-3, also known as epidermal growth factor containing fibulin-like extracellular matrix protein 1 (EFEMP1), is suggested to be a new potential

biomarker for MM.[13] Fibulin- 3 belongs to a family of extracellular matrix glycoproteins[14] that have recently been shown to act as tumour suppressors or activators in different cancers.[15-17] It has restricted expression in the body and is predominately localized in the extracellular matrix of elastic tissue.[18] The levels of fibulin-3 expression have been found to be decreased in many cancer types due to promoter hypermethylation and have been correlated with poor survival of patients with lung cancer[19,20], breast cancer[21], and hepatocellular carcinoma.[22] On the other hand, an increase in fibulin-3 was observed in malignant gliomas[23], cervical carcinomas[24], and pancreatic cancer.[25]

Fibulin-3 was first studied as a biomarker of MM by Pass *et al.* who reported that plasma fibulin-3 levels can distinguish a healthy person with exposure to asbestos from patients with MM.[13] They found that in conjunction with fibulin-3 levels in pleural effusions, plasma fibulin-3 levels can further differentiate MM effusion from other malignant and benign effusions.[13] Recent studies identified soluble mesothelin as a superior diagnostic biomarker for MM compared to fibulin-3, whereas fibulin-3 provided superior prognostic information compared to mesothelin.[26]

According to our knowledge and available literature, fibulin-3 has not been studied so far as a biomarker for evaluating tumour response to treatment. This study aimed to determine fibulin-3 levels in plasma of patients with MM before treatment and in various responses to treatment (complete response, partial response, stable disease, and progressive disease), to evaluate its potential applicability as a biomarker of tumour response to treatment, and to assess if plasma level of fibulin-3 could predict the probability of progressive disease after the response to treatment in the period of 18 months. We also assessed the potential applicability of fibulin-3 as a biomarker of tumour response to treatment in comparison with or in addition to SMRP.

Patients and methods

Patients

A panel study was performed. Patients eligible for inclusion in the study had histologically proven MM and each subject acted as her/his own control in an ongoing longitudinal study.[12] Briefly, the study included 78 patients with MM treated at the Institute of Oncology Ljubljana in the period between March 2007 and June 2011.

Eligibility criteria included biopsy-proven MM. In all patients, thoracoscopy or laparoscopy/laparotomy was performed. The immunohistochemistry methods were used (Cytokeratin 5/6 [CK5/6], Epithelial Membrane Antigen [EMA], Calretinin, Vimentin, Wilms tumour gene–1 [WT1], CD15, Ber-EP4, B72.3, MOC-31, actin, desmin, S-100, Carcinoembryonic Antigen [CEA], thyroid transcriptor factor1 [TTF-1]). The patients had no history of another cancer during the past 5 years or breast cancer ever; the Eastern Cooperative Oncology Group (ECOG) performance status (PS) was 0–2.

Tumour extension was classified according to TNM classification, based on the results from chest and upper abdominal CT scan and thoracoscopy.[27] For comparison with subsequent scanning, the thickness of the tumour on three CT levels was recorded considering the modified RECIST criteria.[28] Sporadically a NMR was done to evaluate the operability of some patients[29] and a PET-CT was also done in some patients to evaluate the extent of disease and response to treatment like in patients with lung cancer.[30]

The patients were treated with 4 to 9 cycles of chemotherapy comprising cisplatin and low dose gemcitabine in prolonged infusion, or cisplatin and pemetrexed.[31-34] In one patient with pleural MM, extrapleural pleuropneumonectomy was carried out before chemotherapy and in four patients with pleural MM, it was carried out after chemotherapy. Peritonectomy was performed in two patients with peritoneal MM before chemotherapy and in three patients after chemotherapy. Four patients received best supportive care only. Twenty-nine patients with pleural MM were treated with second-line chemotherapy and two of them received palliative radiotherapy.[12]

For all the patients, data on smoking were obtained using a standardized questionnaire. The duration of smoking and the number of pack-years of smoking were calculated for each subject.[35,36] To determine occupational and/or environmental asbestos exposure, a semi-quantitative method was used as previously described.[12]

Methods

Blood specimen collection was carried out in patients before treatment (before the 1st cycle of chemotherapy or surgery) and/or after treatment (after the third and/or the sixth cycle of chemotherapy or surgical procedure) and/or at the progress of the disease. In total, 135 blood samples from 78 pa-

TABLE 1. Fibulin-3 levels (ng/ml) before treatment at different histopathological subtypes, at different tumour stages and according to the presence of metastatic disease in patients with malignant mesothelioma

Characteristics	Mean	SD	Median	Range	Inter-quartile	Mann-Whitney (U) test	p value
Subtype							
Epitheloid (N = 25)	41.52	24.26	36.42	1.65–92.32	23.00–58.14	69.00[a]	0.789
Biphasic (N = 6)	41.04	16.57	35.24	22.72–65.22	28.41–59.41	2.00[b]	0.286
Sarcomatoid (N = 2)	27.36	1.60	27.36	26.23–28.49	26.23–27.36	17.50[c]	0.519
Tumour stage[d]							
I[e] (N = 1)							
II (N = 8)	28.88	8.32	28.67	15.69–40.78	21.98–35.32	32.00[f]	0.156
III (N = 13)	46.39	28.09	47.41	1.65–92.32	22.03–66.43	42.00[g]	0.817
IV (N = 7)	40.97	21.71	30.31	22.72–84.33	28.49–54.93	19.00[h]	0.320
Metastatic disease							
Present (N = 7)	40.97	21.70	30.31	22.72–84.33	28.49–54.93	73.00[i]	0.854
Not present (N = 22)	39.89	23.38	35.25	1.65–92.32	22.21–54.12		

N = number of plasma samples; [a] Mann-Whitney (U) test calculated for epitheloid subtype vs. biphasic subtype; [b] Mann-Whitney (U) test calculated for biphasic vs. sarcomatoid subtype; [c] Mann-Whitney (U) test calculated for epitheloid subtype vs. sarcomatoid subtype; [d] Pleural malignant mesothelioma only; [e] Stage I was found only in one patient with fibulin-3 level 43.44 ng/ml; [f] Mann-Whitney (U) test calculated for stage II vs. III; [g] Mann-Whitney (U) test calculated for stage III vs. IV; [h] Mann-Whitney (U) test calculated for stage II vs. IV; [i] Mann-Whitney (U) test calculated for metastatic disease present vs. not present

tients were collected in different periods of disease and treatment.

Plasma was prepared immediately after blood sampling and stored in aliquots frozen at -30 ℃ until the fibulin-3 assay was performed. Fibulin-3 levels in plasma were measured with the use of enzyme-linked immunosorbent assay (Uscn Life Science Inc., Wuhan, China). The median value of fibulin-3 in complete response or after the surgery was chosen as the cut-off level.

For all the patients, the information on SMRP levels was available from our previous study[12] for the same time-points before and/or after treatment. A level of 1.50 nmol/L was considered as a cut-off value for positive SMRP. Using receiver operating characteristic (ROC) curve analysis, we determined the fibulin-3 cut-off values for prediction of disease progression. We compared serum levels in progressive disease with levels in complete response, partial response or stable disease and calculated the area under the curve (AUC), sensitivity and specificity. As our aim was to determine the usefulness of serum fibulin-3 for screening for progressive disease, cut-off value with at least 80% sensitivity was selected to limit the potential for false negative results. On the other hand, lower specificity would not be as problematic, as patients would have a more detailed check-up after initial screening.

Statistics and ethical consideration

Standard descriptive statistics were used to describe each variable. Mann-Whitney test (U) test was performed to determine the differences in fibulin-3 levels before treatment and in various responses to treatment. The correlations between fibulin-3 and SMRP levels were calculated using Pearson's correlation coefficient. Logistic regression analysis was used to assess the odds for different responses to treatment.

Prior to inclusion, all patients were fully informed about the study and signed informed consent to participate. The study was approved by the Slovenian Ethics Committee for Research in Medicine and was carried out according to the Helsinki Declaration.

Results

Patients

The study included 78 patients with MM, 57 (73%) male and 21 (27%) female. The overall median (min–max range) age was 66 (23–84) years. Among them, 35 (44.9%) were ever smokers and 43 (55.1%) of them never smoked. The median duration of smoking was 18 (1–69) years, the median number of smoked cigarettes per day was 20 (1–29) and

TABLE 2. Fibulin-3 levels (ng/ml) before treatment and in different responses to treatment in 78 patients with MM

Disease phase	Mean	SD	Median	Range	Inter-quartile	Mann-Whitney (U) test	p value
All phases (N = 135)	44.57	21.31	40.78	0.00–105.00	29.18–56.27		
Before treatment (N = 33)	40.57	22.26	35.09	1.65–92.32	24.23–56.21	877.00[a]	0.598
Complete response or after surgery (N = 5)	32.43	9.98	34.25	18.16–45.50	23.55–40.40		
Partial response (N = 13)	45.13	26.48	41.18	0.00–105.00	27.90–56.42		
Stable disease (N = 39)	40.00	16.11	37.10	6.52–73.44	29.40–47.56		
Progressive disease (N = 45)	53.56	21.67	47.19	16.26–105.00	37.78–67.93	813.00[b]	0.001

N = number of plasma samples; [a] Mann-Whitney (U) test calculated for fibulin-3 before treatment vs. stable disease + partial response + complete response or after surgery; [b] Mann-Whitney (U) test calculated for fibulin-3 in progressive disease vs. stable disease + partial response + complete response or after surgery

TABLE 3. The odds for developing different responses to treatment for fibulin-3 levels > 34.25 ng/ and SMRP levels >1.50 nmol/L in univariate and multivariate analysis

	Univariate analysis		Multivariate analysis	
	Fibulin-3 OR (95% CI)	SMRP OR (95% CI)	Fibulin-3 OR (95% CI)	SMRP OR (95% CI)
Before treatment vs. complete response	0.63 (0.09–4.26)	0.14 (0.01–1.43)	0.74 (0.1–5.48)	0.15 (0.02–1.48)
Before treatment vs. partial response	1.51 (0.41–5.58)	0.67 (0.18–2.45)	1.56 (0.42–5.84)	0.64 (0.17–2.39)
Before treatment vs. stable disease	0.99 (0.39–2.51)	0.74 (0.29–1.91)	1.04 (0.41–2.67)	0.73 (0.28–1.93)
Before treatment vs. progressive disease	4.35 (1.56–12.13)	5.86 (1.68–22.40)	3.74 (1.28–10.93)	4.94 (1.35–18.08)
Complete response vs. progressive disease	6.94 (0.99–48.55)	41.00 (3.65–461.03)	7.77 (0.58–104.98)	43.99 (3.07–629.57)
Partial response vs. progressive disease	2.89 (0.75–11.19)	8.79 (1.97–39.28)	2.90 (0.65–13.00)	8.81 (1.89–41.11)
Stable disease vs. progressive disease	4.39 (1.63–11.81)	7.92 (2.37–26.46)	3.52 (1.22–10.14)	6.58 (1.90–22.83)

CI = confidence interval; OR = odds ratio; SMRP = soluble mesothelin-related peptides

the median pack-years of smoking amounted to 15 (1–45).

Asbestos exposure was confirmed in 67 (85.9%) of the patients with MM. The assessed exposure was low in 24 (30.8%) patients, median in 21 (26.9%) patients, and high in 22 (28.2%) patients, while in 11 patients (14.1%) asbestos exposure could not be proven with certainty. In the exposed group, the median duration of exposure was 90.50 (0.1–528) months.

Regarding the location of the disease, 70 (89.7%) patients had pleural and 8 (10.3%) peritoneal MM. Epitheloid MM was found in 64 (82.0%), biphasic in 7 (9.0%), and sarcomatoid in 7 (9.0%)

patients. Five (6.4%) patients were diagnosed with stage I, 17 (21.8%) with stage II, 28 (35.9%) with stage III and 20 (25.6%) with stage IV, while 8 (10.3%) patients had MM of peritoneum and therefore, the stage could not been determined. The median survival of all patients was 20.1 (2.8–86.1) months.

Among 33 patients evaluated before treatment, no significant differences in fibulin-3 levels were observed between histopathological subtypes or between tumour stages. Fibulin-3 levels before treatment were not significantly different between patients with and without evidence of metastatic disease (U = 73.00, p = 0.854) (Table 1).

The results of descriptive statistics for fibulin-3 levels before treatment and/or in different responses to treatment for all 78 malignant mesothelioma patients are presented in Table 2. No significant difference was observed between the fibulin-3 levels before treatment as compared to the levels in patients in complete response to treatment (U = 71.00, p = 0.641), partial response to treatment (U = 186.00, p = 0.496), or stable disease (U = 597.00, p = 0.603). On the other hand, significantly higher fibulin-3 levels were found in progressive disease as compared to the levels before treatment (U = 472.50, p = 0.006). Fibulin-3 levels were also significantly higher in progressive disease as compared to the levels in complete response to treatment (U = 42.00, p = 0.020) or stable disease (U = 542.00, p = 0.002), while no significant difference was observed between progressive disease and partial response to treatment (U = 229.00, p = 0.241).

No correlation (r = 0.364, p < 0.001) was detected between fibulin-3 levels and SMRP levels as determined at the same time-points in our previous study.[12]

In ROC curve analysis comparing progressive disease with complete response, partial response or stable disease, AUC for fibulin-3 was 68.3% (95% CI = 57.9–78.7, p = 0.002). Cut-off value of 34.25 ng/ml had sensitivity of 82.2%, thus passing the sensitivity threshold of 80%. On the other hand, specificity for this cut-off value was 47.7% (Figure 1). For mesothelin levels, AUC was 84.2% (95% CI = 76.8–91.7, p < 0.001, Figure 1). Previously determined cut-off value of 1.5 nmol/L had high sensitivity of 91.1% and specificity of 49.1%, thus also limiting the chance of false negative results.

For further logistic regression analysis, fibulin-3 levels were categorized into two categories based on ROC curve analysis: ≤ 34.25 ng/ml and > 34.25 ng/ml. Patients with fibulin-3 levels before treatment exceeding 34.25 ng/ml had more than four times higher probability for developing progressive disease during the period of 18 months (OR = 4.35, 95% CI 1.56–12.13, p = 0.005). However, fibulin-3 levels before treatment were not associated with complete response to treatment (OR = 0.63, 95% CI 0.09–4.26, p = 0.633), partial response to treatment (OR = 1.51, 95% CI 0.41–5.58, p = 0.540), or stable disease (OR = 0.99, 95% CI 0.39–2.51, p = 0.984). Nevertheless, patients with fibulin-3 levels higher than 34.25 ng/ml after the treatment with complete response to treatment or with stable disease showed increased odds for developing progressive disease during the period of 18 months (OR = 6.94, 95% CI 0.99–48.55, p = 0.051 and OR
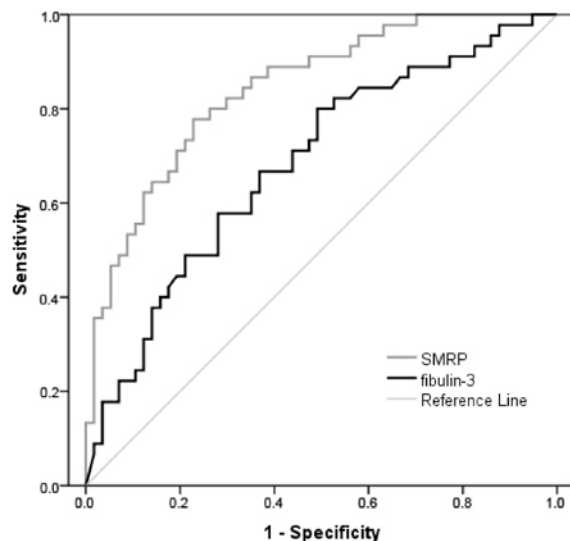

FIGURE 1. Receiver operating characteristic (ROC) curve for mesothelin-related peptides (SMRP) and fibulin-3 serum levels comparing values at progressive disease with values at complete response, partial response or stable disease.

= 4.39, 95% CI 1.63–11.81, p = 0.003 respectively) (Table 3).

The analysis also showed that patients with pre-treatment SMRP levels >1.50 nmol/L had almost six times higher odds for progressive disease during the period of 18 months (OR = 5.86, 95% CI 1.68–22.40, p = 0.005). Additionally, patients with SMRP levels >1.50 nmol/L after the treatment and with complete response to treatment, partial response to treatment, and stable disease were at higher risk for developing progressive disease compared with those with SMRP ≤ 1.50 nmol/L during the period of 18 months (OR = 41.00, 95% CI 3.65–461.03, p = 0.003, OR = 8.79, 95% CI 1.97–39.28, p = 0.004, and OR = 7.92, 95% CI 2.37–26.46, p = 0.001 respectively) (Table 3).

To evaluate the combined effect of fibulin-3 and SMRP levels in evaluating tumour response to treatment, we constructed multivariate logistic regression models that included two categories of fibulin-3 (> 34.25 ng/ml vs. ≤ 34.25 ng/ml) and two categories of SMRP (>1.50 nmol/L vs. ≤ 1.50 nmol/L). The odds for developing different responses to treatment (complete response, partial response, stable disease, progressive disease) did not change considerably compared to the results of univarate logistic regression analysis when pretreatment fibulin-3 and SMRP were both above the respective cut-off levels (34.25 ng/ml and 1.50 nmol/L respectively). Similarly, the probability for developing progressive disease did not change significantly

compared with the results of univarate logistic regression analysis when fibulin-3 and SMRP were both above the respective cut-off levels in different responses to treatment (Table 3).

Discussion

As expected the occupational and/or environmental exposure to asbestos was confirmed in almost 86% of patients with MM. This is in agreement with the results of the studies published so far that have proposed asbestos as a major cause for developing this aggressive disease.[1-8]

Fibulin-3 has recently been suggested as a new tumour biomarker for MM.[13,26] Pass et al. presented that plasma fibulin-3 levels can distinguish an asbestos exposed healthy person from patients with MM.[13] Creaney et al. recognized soluble mesothelin as a superior diagnostic biomarker for MM compared with fibulin-3, while fibulin-3 was indicated to provide superior prognostic information compared with mesothelin.[26] However, to our knowledge and available literature, fibulin-3 has not been studied yet as a biomarker for evaluating tumour response to treatment.

The results of the current study show significantly higher fibulin-3 levels in progressive disease as compared with the levels before treatment, in complete response to treatment, and in stable disease, which indicates that fibulin-3 could be helpful in identifying the progression of MM. On the other hand, no significant difference was observed between the fibulin-3 levels before treatment as compared with the levels in complete response to treatment, partial response to treatment, and stable disease. The results of our previous study investigating SMRP as a tumour biomarker for MM, showed significantly higher SMRP levels before treatment than the levels in complete response, partial response, and a borderline significant difference between levels before treatment and stable disease.[12] These findings suggest SMRP not only as a superior diagnostic biomarker for MM compared with fibulin-3 as presented in the study of Creaney et al.[26], but also as a superior biomarker for evaluating tumour response to treatment.

An important finding of the current study shows that the probability for the development of progressive disease during the period of 18 months was more than four times higher when fibulin-3 levels before treatment exceeded 34.25 ng/ml, and almost five times higher when SMRP level before treatment was higher than 1.50 nmol/L. The analysis also showed increased odds for developing progressive disease during the period of 18 months when fibulin-3 levels after the treatment and with complete response to treatment or stable disease were higher than 34.25 ng/ml. The same holds true of SMRP levels above 1.50 nmol/L in complete response, partial response, and stable disease. These results suggest that in addition to SMRP, the fibulin-3 levels before treatment, in complete response to treatment, and in stable disease could help predict the risk of developing progressive disease in MM. When including fibulin-3 levels above 34.25 ng/ml and SMRP levels above 1.50 nmol/L in multivariate logistic regression models, the odds for both fibulin-3 and SMRP did not change significantly, suggesting independent effects. However, we have to indicate that the confidence intervals were wide because the number of involved subjects was low.

In conclusion, the findings of our current study show that in addition to SMRP[12], fibulin-3 could also be helpful in detecting the progression of MM. Contrary to SMRP[12], fibulin-3 has not been proven as a useful biomarker for evaluating tumour response to treatment. The results of the present study also indicate that fibulin-3 levels before treatment, in complete response to treatment, and in stable disease could be beneficial in predicting the risk of developing progressive disease in patients with MM. To increase the power of the study and to validate these results, a larger sample size is needed.

Acknowledgements

References

1. Berry M. Mesothelioma incidence and community asbestos exposure. Environ Res 1997; **75:** 34-40.

2. Iwatsubo Y, Pairon JC, Boutin C, Menard O, Massin N, Caillaud D, et al. Pleural mesothelioma: dose-response relation at low levels of asbestos exposure in a French population-based case-control study. Am J Epidemiol 1998; **148:** 133-42.

3. Howel D, Gibbs A, Arblaster L, Swinburne L, Schweiger M, Renvoize E, et al. Mineral fibre analysis and routes of exposure to asbestos in the development of mesothelioma in an English region. *Occup Environ Med* 1999; **56:** 51-8.

4. Agudo A, González CA, Bleda MJ, Ramirez J, Hernandez S, Lopez F, et al. Occupation and risk of malignant pleural mesothelioma: a case-control study in Spain. *Am J Ind Med* 2000; **37:** 159-68.

5. Magnani C, Dalmasso P, Biggeri A, Ivaldi C, Mirabelli D, Terracini B. Increased risk of malignant mesothelioma of the pleura after residential or domestic exposure to asbestos: a case-control study in Casale Monferrato, Italy. *Environ Health Perspect* 2001; **109:** 915-9.

6. Zellos L, Christiani DC. Epidemiology, biologic behaviour, and natural history of mesothelioma. *Thorac Surg Clin* 2004; **14:** 469-77.

7. Pan XL, Day HW, Wang W, Beckett LA, Schenker MB. Residential proximity to naturally occurring asbestos and mesothelioma risk in California. *Am J Respir Crit Care Med* 2005; **172:** 1019-25.

8. Maule MM, Magnani C, Dalmasso P. Modeling mesothelioma risk associated with environmental asbestos exposure. *Environ Health Perspect* 2007; **115:** 1066-71.

9. Robinson BW, Lake RA. Advances in malignant mesothelioma. *N Engl J Med* 2005; **353:** 1591-603.

10. Kovac V, Zwitter M, Zagar T. Improved survival after introduction of chemotherapy for malignant pleural mesothelioma in Slovenia: population-based survey of 444 patients. *Radiol Oncol* 2012; **46:** 136-44.

11. Hollevoet K, Reitsma JB, Creaney J, Grigoriu BD, Robinson BW, Scherpereel A, et al. Serum mesothelin for diagnosing malignant pleural mesothelioma: an individual patient data meta-analysis. *J Clin Oncol* 2012; **30:** 1541-9.

12. Franko A, Dolzan V, Kovac V, Arneric N, Dodic-Fikfak M. Soluble mesothelin-related peptides levels in patients with malignant mesothelioma. *Dis Markers* 2012; **32:** 123-31.

13. Pass HI, Levin SM, Harbut MR, Melamed J, Chiriboga L, Donington J, et al. Fibulin-3 as a blood and effusion biomarker for pleural mesothelioma. *N Engl J Med* 2012; **367:** 1417-27.

14. Timpl R, Sasaki T, Kostka G, Chu ML. Fibulins: a versatile family of extracellular matrix proteins. *Nat Rev Mol Cell Biol* 2003; **4:** 479-89.

15. Argraves WS, Greene LM, Cooley MA, Gallagher WM. Fibulins: physiological and disease perspectives. *EMBO Rep* 2003; **4:** 1127-31.

16. Zhang Y, Marmorstein LY. Focus on molecules: fibulin-3 (EFEMP1). *Exp Eye Res* 2010; **90:** 374-5.

17. Kim IG, Kim SY, Choi SI, Lee JH, Kim KC, Cho EW. Fibulin-3-mediated inhibition of epithelial-to-mesenchymal transition and self-renewal of ALDH+ lung cancer stem cells through IGF1R signaling. *Oncogene* 2014; **33:** 3908-17.

18. Kobayashi N, Kostka G, Garbe JH, Keene DR, Bachinger HP, Hanisch FG, et al. A comparative analysis of the fibulin protein family. Biochemical characterization, binding interactions, and tissue localization. *J Biol Chem* 2007; **282:** 11805-16.

19. Yue W, Dacic S, Sun Q, Landreneau R, Guo M, Zhou W, et al. Frequent inactivation of RAMP2, EFEMP1 and Dutt1 in lung cancer by promoter hypermethylation. *Clin Cancer Res* 2007; **13:** 4336-44.

20. Xu S, Yang Y, Sun YB, Wang HY, Sun CB, Zhang X. Role of fibulin-3 in lung cancer: in vivo and in vitro analyses. *Oncol Rep* 2014; **31:** 79-86.

21. Sadr-Nabavi A, Ramser J, Volkmann J, Naehrig J, Wiesmann F, Betz B, et al. Decreased expression of angiogenesis antagonist EFEMP1 in sporadic breast cancer is caused by aberrant promoter methylation and points to an impact of EFEMP1 as molecular biomarker. *Int J Cancer* 2009; **124:** 1727-35.

22. Nomoto S, Kanda M, Okamura Y, Nishikawa Y, Qiyong L, Fujii T, et al. Epidermal growth factor-containing fibulin-like extracellular matrix protein 1, EFEMP1, a novel tumor-suppressor gene detected in hepatocellular carcinoma using double combination array analysis. *Ann Surg Oncol* 2010; **17:** 923-32.

23. Hu B, Thirtamara-Rajamani KK, Sim H, Viapiano MS. Fibulin-3 is uniquely upregulated in malignant gliomas and promotes tumor cell motility and invasion. *Mol Cancer Res* 2009; **7:** 1756-70.

24. En-lin S, Sheng-guo C, Hua-qiao W. The expression of EFEMP1 in cervical carcinoma and its relationship with prognosis. *Gynecol Oncol* 2010; **117:** 417-22.

25. Seeliger H, Camaj P, Ischenko I, Kleespies A, De Toni EN, Thieme SE, et al. EFEMP1 expression promotes in vivo tumor growth in human pancreatic adenocarcinoma. *Mol Cancer Res* 2009; **7:** 189-98.

26. Creaney J, Dick IM, Meniawy TM, Leong SL, Leon JS, Demelker Y, et al. Comparison of fibulin-3 and mesothelin as markers in malignant mesothelioma. *Thorax* 2014; **69:** 895-902.

27. UICC International Union Against Cancer. Pleurak mesothelioma. In: Sobin LH, Gospodarowicz MK, Wittekind C, editors. *TNM classification of malignant tumours*, 7th edition. Chichester: Wiley-Blackwell; 2009. p. 147-50.

28. Byrne MJ, Nowak AK. Modified RECIST criteria for assessment of response in malignant pleural mesothelioma. *Ann Oncol* 2004; **15:** 257-60.

29. Podobnik J, Kocijancic I, Kovac V, Sersa I. 3T MRI in evaluation of asbestos-related thoracic diseases - preliminary results. *Radiol Oncol* 2010; **44:** 92-6.

30. Zwitter M, Stanic K, Rajer M, Kern I, Vrankar M, Edelbaher N, et al. Intercalated chemotherapy and erlotinib for advanced NSCLC: high proportion of complete remissions and prolonged progression-free survival among patients with EGFR activating mutations. *Radiol Oncol* 2014; **48:** 361-8.

31. Vogelzang NJ, Rusthoven JJ, Symanowski J, Denham C, Kaukel E, Ruffie P, et al. Phase III study of pemetrexed in combination with cisplatin versus cisplatin alone in patients with malignant pleural mesothelioma. *J Clin Oncol* 2003; **21:** 2636-44.

32. Goricar K, Kovac V, Dolzan V. Polymorphisms in folate pathway and pemetrexed treatment outcome in patients with malignant pleural mesothelioma. *Radiol Oncol* 2014; **48:** 163-72.

33. Lee CW, Murray N, Anderson H, Rao SC, Bishop W. Outcomes with first-line platinum-based combination chemotherapy for malignant pleural mesothelioma: A review of practice in British Columbia. *Lung Cancer* 2009; **64:** 308-13.

34. Kovac V, Zwitter M, Rajer M, Marin A, Debeljak A, Smrdel U, et al. A phase II trial of low-dose gemcitabine in prolonged infusion and cisplatin for malignant pleural mesothelioma. *Anticancer Drugs* 2012; **23:** 230-8.

35. Ferris BG. Epidemiology Standardization Project (American Thoracic Society). *Am Rev Respir Dis* 1978; **118:** 1-20.

36. Dodic Fikfak M, Kriebel D, Quinn MM, Eisen EA, Wegman DH. A case control study of lung cancer and exposure to chrysotile and amphibole at a Slovenian asbestos-cement plant. *Ann Occup Hyg* 2007; **51:** 261-8.

research article

Impact of tumour volume on prediction of progression-free survival in sinonasal cancer

Florian Hennersdorf[1], Paul-Stefan Mauz[2], Patrick Adam[3], Stefan Welz[4], Anne Sievert[2], Ulrike Ernemann[1], Sotirios Bisdas[1]

[1] Department of Diagnostic and Interventional Neuroradiology, University Hospital Tübingen, Germany

[2] Department of Otorhinolaryngology, University Hospital Tübingen, Germany

[3] Institute of Pathology, University Hospital Tübingen, Germany

[4] Department of Radiation Oncology, University Hospital Tübingen, Germany

Background. The present study aimed to analyse potential prognostic factors, with emphasis on tumour volume, in determining progression free survival (PFS) for malignancies of the nasal cavity and the paranasal sinuses.

Patients and methods. Retrospective analysis of 106 patients with primary sinonasal malignancies treated and followed-up between March 2006 and October 2012. Possible predictive parameters for PFS were entered into univariate and multivariate Cox regression analysis. Kaplan-Meier curve analysis included age, sex, baseline tumour volume (based on MR imaging), histology type, TNM stage and prognostic groups according to the American Joint Committee on Cancer (AJCC) classification. Receiver operating characteristic (ROC) curve analysis concerning the predictive value of tumour volume for recurrence was also conducted.

Results. The main histological subgroup consisted of epithelial tumours (77%). The majority of the patients (68%) showed advanced tumour burden (AJCC stage III-IV). Lymph node involvement was present in 18 cases. The mean tumour volume was 26.6 ± 21.2 cm³. The median PFS for all patients was 24.9 months (range: 2.5–84.5 months). The ROC curve analysis for the tumour volume showed 58.1% sensitivity and 75.4% specificity for predicting recurrence. Tumour volume, AJCC staging, T- and N- stage were significant predictors in the univariate analysis. Positive lymph node status and tumour volume remained significant and independent predictors in the multivariate analysis.

Conclusions. Radiological tumour volume proofed to be a statistically reliable predictor of PFS. In the multivariate analysis, T-, N- and overall AJCC staging did not show significant prognostic value.

Key words: tumour volume; sinonasal carcinoma; prognostic value

Introduction

With an annual incidence rate of 0.5–1.0 per 100.000, malignancies of the nasal cavity and paranasal sinuses are rare entities constituting only 3% of head and neck carcinomas and 0.5% of all malignant tumours.[1] Sinonasal neoplasms show a wide variety of histological subtypes comprising carcinomas, melanomas, lymphomas, sarcomas and esthesioneuroblastomas.[1] Unspecific related symptoms and asymptomatic tumour growth within the large air-filled spaces of the viscerocranium result in late diagnosis and poor prognosis.[1,2] 5-year survival rates reported in the literature range from 10–75% and depend significantly on tumour histology.[3] Despite different subgroups, sinonasal tumours are commonly uniformly staged according to the TNM classification as published by the American Joint Committee on Cancer (AJCC).[4] Retrospective studies have identified patient age, sex and tumour stage as predictive factors for progression-free and overall survival.[5-11] Specifically, poor outcome was

observed when cervical lymph node involvement was present.[7] However, preliminary evidence has shown no reliable prognostic value of the widely used staging systems.[4,10]

In the present work, we sought to validate and extend previous evidence regarding the prognostic factors in sinonasal malignancies by examining the prognostic value of epidemiological (age, sex) and clinical (staging systems) criteria in conjunction with baseline imaging parameters like tumour volume based on MR imaging.

Patients and methods

Patients

We conducted a retrospective analysis of all patients who were imaged, diagnosed, and treated with sinonasal tumours between March 2006 and October 2012 at the Head and Neck Cancer centre at University Hospital Tübingen. The study was conducted according to the Helsinki Declaration. Each patient's informed consent was obtained and Institutional Review Board approval was granted. It also approved the use of images and medical records. The inclusion criteria were: a) primary malignancy of the sinonasal tract with histological verification; b) patients undergone either primary surgery, primary radiotherapy or combined adjuvant radiotherapy with or without concomitant chemotherapy; c) baseline MRI with gadolinium-enhanced T1-weighted sequences for tumour volumetry, performed not longer than 1 week before surgical resection; d) adequate clinical follow-up on a 3- or 6-month time interval. Informed consent was obtained from all patients for the MR exams.

Imaging studies and tumour volumetry

All MR imaging examinations were performed by using the same 1.5 T MR scanners (Avanto and Aera, Siemens Medical Systems, Erlangen, Germany), with a 12-channel-array head coil. Along with a number of conventional T2- and T1-sequences before and after contrast agent, 3D isotropic T1-weighted image datasets (TR/TE 1300/2.6 ms, voxel size 1 mm^3) were acquired after intravenous administration of gadobutrol. Apart from the head and neck MRI studies, patients received whole-body CT imaging with iodinated contrast agent in order to exclude distant disease. Radiological tumour volumetry in the contrast-enhanced 3D T1-weighted images was performed offline by two radiologists in consensus using a dedicated workstation and commercially available software (Advantage Windows, GE Medical Systems, Milwaukee, WI).

Therapy

Standard treatment for epithelial tumours consisted of radical surgery and depending on tumour stage of subsequent radiotherapy with doses of 50–67 Gy. Chemotherapy was not part of the standard therapeutic regimen and was only administered on adjuvant setting or for palliation to the patients with advanced tumour stages (stage IV). In these cases protocols containing cisplatin or carboplatin were used. Only patients with sinonasal lymphoma received chemotherapy according to the rituximab, cyclophosphamide, doxorubicin, vincristine, prednisone (R-CHOP) protocol as the standard therapeutic regimen.

Statistical analysis

Progression-free survival (PFS) was defined as the number of months between the tumour resection and the diagnosis of locoregional tumour progress in follow-up surveillance and was analysed using the Kaplan-Meier method with log-rank (Mantel-Cox) test. Univariate and multivariate Cox regression analysis with forward entry (Wald test) was conducted and the metrics were primarily treated as continuous or categorical variables without predetermined cut-off values. The model, adjusted for age and sex, included baseline tumour volumetry, tumour histology and histological grading, T-stage and N-stage as "stand-alone" parameters, TNM and stage grouping according to the AJCC classification. Receiver operating characteristic (ROC) curve analysis for the prediction of locoregional recurrence was conducted to determine the cut-off value of tumour volume that yielded optimal sensitivity and specificity. Overall survival was not used as an outcome owing to the small number of patients being observed for five years or longer and to variations in treatment after patients experienced a disease progression, which would confound the direct evaluation of the stated hypothesis. Data normality was examined by Kolmogorov- Smirnov test and Q-Q plots. All statistical computations were conducted with commercially available software (MedCalc Statistical Software version 12.7.2, MedCalc Software bvba, Ostend, Belgium) and results were declared statistically significant at the 2-sided 5% comparison-wise significance level ($P < 0.05$).
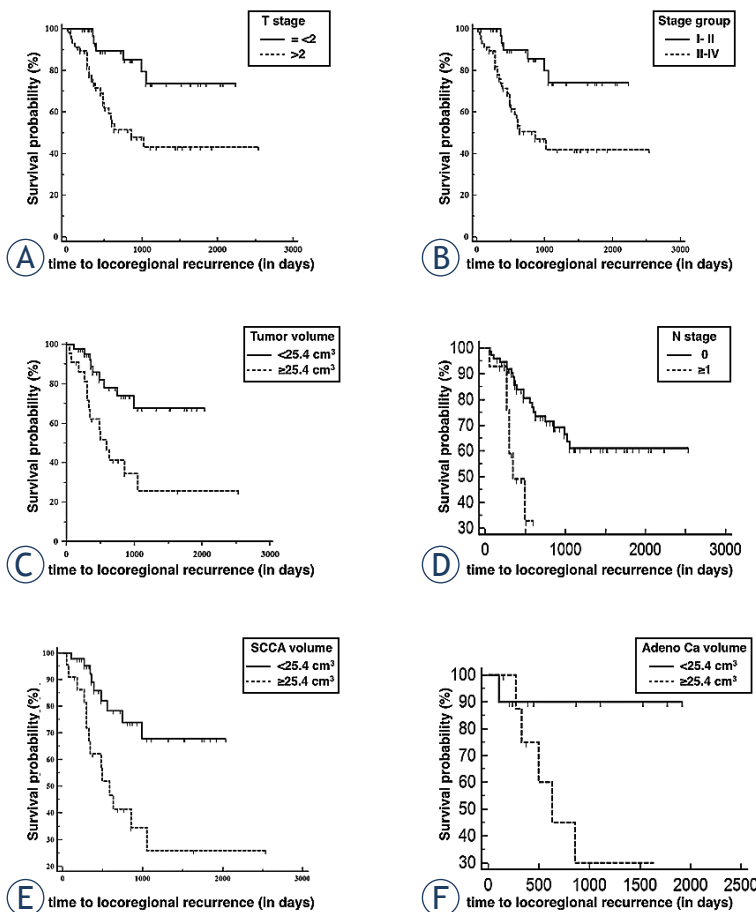
FIGURE 1. Kaplan-Meier survival curves for locoregional recurrence according to T-stage groups **(A)**, American Joint Committee on Cancer (AJCC) stage groups **(B)**, radiologic tumour volume **(C)** and N-stages **(D)**. Subgroup analyses by tumour volume for squamous cell carcinoma **(E)** and adenoracinoma **(F)**.

Results

One-hundred and six patients (45 females, 61 males) were identified (mean age: 64.8 years, range: 31–77 years). The main histological subgroup consisted of carcinomas comprising squamous cell carcinomas (SCCA) (42 cases), adenocarcinomas (22 cases), adenoid cystic carcinomas (3 cases), anaplastic carcinomas (2 cases), neuroendocrine carcinomas (5 cases) as well as other rare subtypes (8 cases). The remaining tumour entities included melanomas (10 cases), sarcomas (4 cases) and one esthesioneuroblastoma. Patients diagnosed with lymphoma or plasmocytoma (6 and 3 respectively) were excluded from the analysis due to the completely different therapeutic approach. Comprising 55% of patients, the nasal cavity was the more common site of origin compared to 38% of tumours originating in the paranasal sinuses. In 7 patients the tumour

could not be assigned to being nasal or paranasal in origin due to advanced tumour stage. The majority of the patients (68%) showed advanced tumour burden (stage III-IV). The distribution of T stages was as follows: 16% T1, 22% T2, 11% T3 and 41% T4. Most tumours were graded G2 (55%) and G3 (28%). Cervical lymph node involvement was present in 18 cases. The mean (± standard error, SE) radiological volume of primary tumours was 26.6 ± 21.2 cm³. Tumour cells at the surface of the resection margin (R1) occurred in 13 cases, consisting of 8 epithelial tumours and 5 other than epithelial. The median PFS for all patients was 24.9 months (range: 2.5–84.5 months). Six patients with advanced disease in the primary radiological staging received only palliative care and had short overall survival and thus, were excluded from further analysis in order to avoid statistical bias. Therefore a total of 91 patients were included into the statistical analysis. To further exclude bias due to different tumour subtypes we conducted subgroup analyses including only SCCA (42 patients) and adenocarcinomas (22 patients). In subgroup analysis patients with R1 resections were also excluded.

Kaplan-Meier analysis demonstrated a significant ($P = 0.003$) prolongation of the PFS in patients with T1-T2 tumours (mean PFS 68.6 months, standard error [SE] 5.7 months, 95% confidence interval [CI] 57.5–79.8) compared to those with T3-T4 tumours (mean PFS of 44.9 months, SE 5.6 months, 95% CI 34–55.9). Similarly, AJCC stage I-II patients had mean PFS of 68.9 months (SE 5.6, 95% CI 57.9–79.9) vs. 43.3 months (SE 5,6, 95% CI 32,3–54) for patients with AJCC stage III-IV tumours ($P = 0.002$). Tumour volume < 25.4 cm³ was associated with a mean PFS of 63 months (SE 5.1 months, 95% CI 53–73.1), whereas patients with larger tumour volumes had significantly lower PFS of 38.7 months (SE 6.4 months, 95% CI 26.1–51.3) ($P = 0.004$). Figure 1 shows Kaplan- Meier curves for T-stages (A), AJCC stage groups (B), different tumour volumes (C) and for N- stages (D) in all studied patients. In addition, Kaplan- Meier curves for different tumour volumes for SCCA subgroup (E, $P = 0.0001$) and adenocarcinoma subgroup (F, $P = 0.057$) are shown.

ROC curves for the sum of covariates are presented in Figure 2: for all studied patients (A) and separately for those with epithelial tumours (SCCA and adenocarcinoma). The ROC curve analysis for the tumour volume revealed 25.4 cm³ as the trade-off value with optimal sensitivity (58.1%) and specificity (75.4%) rates for predicting locoregional recurrence. Furthermore,

TABLE 1. Univariate analysis of prognostic factors for progression-free-survival. The statistically significant predictors are indicated in bold italics

Prognostic factors	P-value	Hazards ratio (95% CI)
Age (in years)		
< 67	0.32	
≥ 67		
Sex		
Male	0.06	
Female		
Histology		
Epithelial	0.49	
Non-epithelial		
T stage		
T ≤ 2	*0.02*	0.23 (0.11–0.68)
T > 2		
N stage		
N = 0	*0.002*	4.56 (1.75–11.94)
N = 1		
AJCC		
AJCC = 1	*0.004*	0.27 (0.11–0.65)
AJCC > 1		
Volume (in cm³)		
< 25.4	*0.0072*	2.66 (1.31–5.41)
≥ 25.4		

AJCC = American Joint Committee on Cancer; CI = confidence interval

FIGURE 2. Multiple receiver operating characteristic (ROC) curves for the sum of covariates for all patients **(A)** and for the squamous cell carcinoma and adenocarcinoma subgroups **(B)** demonstrating that radiologic tumour volume has the largest area under the curve (AUC).

multiple ROC curve analyses demonstrated that the largest area under the curve (AUC) was observed for tumour volume (0.687, SE 0.0857, 95% CI 0.519–0.855) followed by AJCC stage (0.607, SE 0.0824, 95% CI 0.445–0.768).

The significant prognostic factors were entered into a multivariate model (overall model fit: $P = 0.0008$) where T-stage and AJCC stage were not significant covariates ($P ≥ 0.09$). On contrary, positive lymph node status at diagnosis proved to be a significant predictor for tumour recurrence ($P = 0.04$, odds ratio 2.6, 95% CI 1.06–13.6). Also, tumour volume was a significant predictor for tumour progression ($P = 0.03$, odds ratio 1.05, 95% CI 0.15–6.7). The subgroup analyses revealed similar results to those for all patients. Notably, when the SCCA-adenocarcinoma subgroup of patients with complete tumour resection (R0) where included in a univariate analysis, tumour volume was highly significant for predicting PFS with a P-value of 0.0003. In the multivariate analysis for these patients, tumour volume remained the strongest prognostic parameter ($P = 0.01$, overall model fit < 0.0001).

Discussion

Prognosis of malignant neoplasms of the nasal cavity and paranasal sinuses is moderate to poor de-
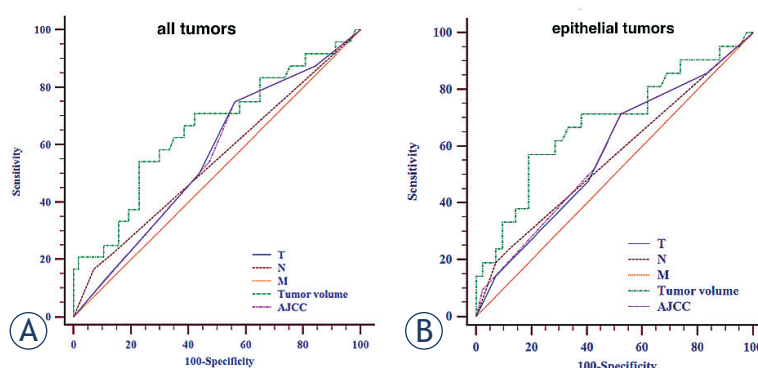
pending on factors such as histology, tumour stage and patient's age.[2,12-14] The crucial point in managing sinonasal tumours is local tumour control.[15] Despite improvement in therapy only marginal improvement of survival has been achieved over the past decades.[3,15] The standard therapeutic regimen includes surgery followed by radiotherapy. The potential benefit of chemotherapy administered neoadjuvantly and/or concomitantly in treating epithelial neoplasms has been shown to be only marginal and is therefore controversial.[5]

Consistent with the literature epithelial neoplasms were the most common entity constituting more than two thirds of all tumours with SCCA being the most frequent histology in our population. Adenoid cystic carcinoma which is commonly found to be the second most frequent entity after SCCA was markedly underrepresented with only 3% of cases. Surprisingly, we had only one case of esthesioneuroblastoma but as much as 5 patients with neuroendocrine carcinoma. Though we did not perform revision of histologies, this aberration might be explained by observation of Cohen *et al.* Who reviewed 12 patients previously diagnosed with olfactory neuroblastoma. In this study only 2 cases were confirmed as neuroblastoma whereas 10 patients had in fact other tumours such as neuroendocrine carcinoma or others.[16] Consistently with this theory, we found 5 cases of neuroendocrine carcinoma. In agreement with the literature, our population showed a male: female ratio of 3:2.[15]

The lag time between initial symptoms onset and surgery of tumours in nasal cavity or paranasal sinuses is crucial for surgeon to obtain clear margins. Usually, many tumours undergo surgery in advanced stage, which precludes margin-free

tumour eradication.[5] On the other hand, surgery is the most effective treatment modality.[3] Therefore, to plan optimal oncologic treatment it is important to know factors with impact on the patient's prognosis. Many potential factors for an unfavorable outcome such as stage of disease, histology, intracranial extension and recently molecular markers such as EGFR have been studied in the literature.[15,17] Our results indicate that besides the known predictive factors, including T-, N-, M- and overall AJCC-stage[15], tumour volume is an important predictive factor that should be encountered in the staging system in future. Compared to N- and M-stage status, which are rarely positive in sinonasal tumours except in some rare histologic types, tumour volume seems to be a robust predictive biomarker.

Khademi *et al.* found only therapy response and stage of disease as independent predictors on multivariate analysis.[15] In our dataset, neither T- nor overall AJCC- staging system proved to be significant on multivariate analysis which is in accordance to previously published data.[4,10] However, radiologic tumour volume and N-stage showed the highest significance in predicting PFS, though N-stage outperformed tumour volume.

The mains limitation of our study is that multiple histological subgroups were analysed together. Due to small patient numbers subgroup analysis was only possible for SCCA and adenocarcinoma where the results from the overall analysis were confirmed (see Figure 1). The outstanding significance of radiological tumour volume is somehow surprising taking into account that T-staging system incorporates detailed information of local tumour extension such as orbital or skull base involvement whereas radiologic volumetry reflects only tumour size. As mentioned above, the prognosis is mostly influenced by ability to assure local tumour control with radical surgical resection being often limited due to the close proximity of midfacial anatomic structures and the skull base. Therefore, it appears reasonable that tumour size plays an essential role in patient's outcome.

Based on presented results, we recommend using imaging-based tumour volumetry as an essential factor when planning therapeutic strategy and aggressiveness of oncologic therapy. Although our data are mainly based on SCCA and adenocarcinoma histologies, we consider our results to be a reasonable platform to integrate primary tumour volume into therapeutic considerations when dealing with other, non-epithelial histological entities.

References

1. Dulguerov P, Jacobsen MS, Allal AS, Lehmann W, Calcaterra T. Nasal and paranasal sinus carcinoma: are we making progress? A series of 220 patients and a systematic review. *Cancer* 2001; **92:** 3012-29.

2. Schröck A, Göke F, van Bremen T, Kirsten R, Jakob M, Ehrenberg T, et al. [Sinonasal tract malignancies: a 14-year single institution experience]. [German]. *HNO* 2012; **60:** 1041-6.

3. Turner JH, Reh DD. Incidence and survival in patients with sinonasal cancer: a historical analysis of population-based data. *Head Neck* 2012; **34:** 877-85.

4. *AJCC cancer staging manual.* Edge S, Byrd DR, Compton CC, Fritz AG, Greene FL, Trotti A, editors. 7th edition. New York: Springer-Verlag; 2010.

5. Airoldi M, Garzaro M, Valente G, Mamo C, Bena A, Giordano C, et al. Clinical and biological prognostic factors in 179 cases with sinonasal carcinoma treated in the Italian Piedmont region. *Oncology* 2009; **76:** 262-9.

6. Sung MW, Kim KH, Kim JW, Min YG, Seomg WJ, Roh JL, et al. Clinicopathologic predictors an dimpact of distant metastasis from adenoid cystic carcinoma of the head and neck. *Arch Otolaryngol Head Neck Surg* 2003; **129:** 1193-7.

7. Bhattacharyya N. Cancer of the nasal cavity: survival and factors influencing prognosis. *Arch Otolaryngol Head Neck Surg* 2002; **128:** 1079-83.

8. Jethanamest D, Vila PM, Sikora AG, Morris LG Predictors of survival in mucosal melanoma of the head and neck. *Ann Surg Oncol* 2011; **18:** 2748-56.

9. Alvarez I, Suárez C, Rodrigo JP, Nuñez F, Caminero MJ. Prognostic factors in paranasal sinus cancer. *Am J Otolaryngol* 1995; **16:** 109-14.

10. Suarez C, Llorente JL, Fernandez De Leon R, Maseda E, Lopez A. Prognostic factors in sinonasal tumors involving the anterior skull base. *Head Neck* 2004; **26:** 136-44.

11. Lee CH, Hur DG, Roh HJ, Rha KS, Jin HR, Rhee CS, et al. Survival rates of sinonasal squamous cell carcinoma with the new AJCC staging system. *Arch Otolaryngol Head Neck Surg* 2007; **133:** 131-4.

12. Dirix P, Nuyts S, Geussens Y, Jorissen M, Vander Poorten V, Fossion E, et al. Malignancies of the nasal cavity and paranasal sinuses: long-term outcome with conventional or three-dimensional conformal radiotherapy. *Int J Radiat Oncol Biol Phys* 2007; **69:** 1042-50.

13. Snyers A, Janssens GO, Twickler MB, Hermus AR, Takes RP, Kappelle AC, et al. Malignant tumors of the nasal cavity and paranasal sinuses: long-term outcome and morbidity with emphasis on hypothalamic-pituitary deficiency. *Int J Radiat Oncol Biol Phys* 2008; **73:** 1343-51.

14. Guntinas-Lichius O, Kreppel MP, Stuetzer H, Semrau R, Eckel HE, Mueller RP. Single modality and multimodality treatment of nasal and paranasal sinuses cancer: a single institution experience of 229 patients. *Eur J Surg Oncol* 2007; **33:** 222-8.

15. Khademi B, Moradi A, Hoseini S, Mohammadianpanah M. Malignant neoplasms of the sinonasal tract: report of 71 patients and literature review and analysis. *Oral Maxillofac Surg* 2009; **13:** 191-9.

16. Cohen ZR, Marmor E, Fuller GN, DeMonte F. Misdiagnosis of olfactory neuroblastoma. *Neurosurg Focus* 2002; **12(5):** e3.

17. Takahashi Y, Bell D, Agarwal G, Roberts D, Xie TX, El-Naggar A, et al. Comprehensive assessment of prognostic markers for sinonasal squamous cell carcinoma. *Head Neck* 2013; **36:** 1094-102.

Comparison of hybrid volumetric modulated arc therapy (VMAT) technique and double arc VMAT technique in the treatment of prostate cancer

Christopher Amaloo[1], Daryl P. Nazareth[2], Lalith K. Kumaraswamy[3]

[1] Department of Radiation Medicine, Roswell Park Cancer Institute, Buffalo, NY, USA
[2] Department of Radiation Medicine, Roswell Park Cancer Institute and Department of Biophysics and Physiology, University at Buffalo, Buffalo, USA
[3] Department of Radiation Medicine and Department of Cell Stress Biology, Roswell Park Cancer Institute, Buffalo, USA

Correspondence to: Assist. Prof. Lalith K. Kumaraswamy, M.Sc., DABR, Department of Radiation Medicine, Roswell Park Cancer Institute, Elm and Carlton Streets, Buffalo, NY 14263, USA; or Department of Cell Stress Biology, Roswell Park Cancer Institute, Buffalo, NY 14263, USA. Email: lalith.kumaraswamy@roswellpark.org

Background. Volumetric modulated arc therapy (VMAT) has quickly become accepted as standard of care for the treatment of prostate cancer based on studies showing it is able to provide faster delivery with adequate target coverage and reduced monitor units while maintaining organ at risk (OAR) sparing. This study aims to demonstrate the potential to increase dose conformality with increased planner control and OAR sparing using a hybrid treatment technique compared to VMAT.

Methods. Eleven patients having been previously treated for prostate cancer with VMAT techniques were replanned with a hybrid technique on Varian Treatment Planning System. Multiple static IMRT fields (2 to 3) were planned initially based on critical OAR to reduce dose but provide some planning treatment volume (PTV) coverage. This was used as a base dose plan to provide 30-35% coverage for a single arc VMAT plan.

Results. The clinical VMAT plan was used as a control for the purposes of comparison. Average of all OAR sparing between the hybrid technique and VMAT showed the hybrid plan delivering less dose in almost all cases except for V80 of the bladder and maximum dose to right femoral head. PTV coverage was superior with the VMAT technique. Monitor unit differences varied, with the hybrid plan able to deliver fewer units 37% of the time, similar results 18% of the time, and higher units 45% of the time. On average, the hybrid plan delivered 10% more monitor units.

Conclusions. The hybrid plan can be delivered in a single gantry rotation combining aspects of VMAT with regions of dynamic intensity modulated radiation therapy (IMRT) within the treatment arc.

Key words: VMAT; hybrid; prostate; planning

Introduction

Prostate cancer is one of the most prevalent malignant diseases that occur among men with a new case diagnosed every 2.2 minutes, affecting 1 in 6 men in their lifetime.[1,2] Traditionally, radiotherapy has been a vital part of the treatment of prostate cancer with three-dimensional conformal radio-therapy (3D-CRT) as the historical standard. Data from dose escalation studies suggests an association between increased dose and an improvement in prostate cancer control[3] with an increased efficacy in prostate-specific antigen (PSA) control at the cost of increased toxicity.[4,5] By utilizing techniques such as intensity modulated radiation therapy (IMRT) or volumetric modulated arc therapy

(VMAT) with image guided radiotherapy (IGRT), the amount of normal tissue treated can be reduced and thus limit this increased toxicity.[6,7] Due to these improved outcomes, IMRT and VMAT techniques are becoming the new standard for curative external beam radiation therapy.[7-9] Given the widespread and prolific nature of the disease, it has proven to be a vital site for the validation of new treatment modalities. Previous studies have shown that VMAT offers reduced monitor units (MU) and delivery time in comparison to IMRT[10-15], at the cost of low dose spillage and potentially reduced conformation of dose for all treatment sites.

RapidArc® is a form of VMAT that delivers intensity modulated radiation arcs by simultaneously changing gantry speed, multileaf collimator (MLC) position, and dose rate.[11] While this technique offers increased dose conformality and sparing of organs at risk (OAR) compared to 3D-CRT[16], one drawback of such a technique is the spread of low dose to the surrounding normal tissue.[11-17] In the treatment of prostate cancer, the spread of such a large low dose region can lead to issues with the intestinal tract, causing such secondary issues as diarrhea, intestinal strictures, and incontinence.[9,18] In order to reduce the low dose volume, and achieve better control to the respective OARs, a hybrid technique was developed similar in nature to Chan *et al.* with the use of dynamic IMRT in place of 3D conformal fields.[19] Our hybrid technique features a pair of non-opposing dynamic IMRT fields where the beam axis covers the planning treatment volume (PTV) while minimizing the overlap with the OARs. It contributed approximately 1/3 of the total

dose to the targets, with the remaining 2/3 of the dose coming from a single overlaying VMAT arc.

The aim of this study is to retrospectively compare the dosimetric parameters of this hybrid treatment technique combining the use of dynamic IMRT fields supplementing a single modulated arc pass to the standard VMAT plan containing two full arcs frequently utilized clinically at our institute for the treatment of prostate cancer.

Methods

Eleven patients, previously treated at our institute for prostate cancer, were chosen for this study. A variety of treatment plans were chosen to include a combination of patient size, target size, and compromised critical OARs that require special consideration. Patient age ranged from 60 to 81 with a mean age of 68. Patients had PSA scores ranging from of 4.4 to 24.4, with Gleason scores from 6 to 9 (Table 1).

All patients were treated clinically with a VMAT technique, utilizing two arcs to achieve a conformal dose to the target structure. These patients were then retrospectively re-planned with a hybrid technique on Varian Eclipse Treatment Planning Software (TPS) (Varian Medical Systems, Palo Alto, CA) Version 10.0. The hybrid technique consisted of dual dynamic IMRT fields with geometry designed to limit OAR dose but provide some PTV coverage. Dose was calculated and subsequently used as a base dose plan, providing initial coverage for a single overlay volume modulated arc.

Patients were simulated with a GE Lightspeed computed tomography simulator in the supine position on a flat tabletop. A custom formed vacloc bag was utilized to ensure consistent setup and stabilization. The bladder at time of simulation was filled to a degree that was maintainable and reproducible for daily treatment. CT slices were acquired at a thickness of 2.5 mm covering a region from above the iliac crests superiorly to below the perineum inferiorly.

A physician contoured the gross tumor volume (GTV) to include all known disease, as defined by the planning CT, encompassing the entirety of the prostate gland. A urethrogram was used in planning to aid in delineation of the inferior border of the prostate to include a volume 5 mm superior to the tip of the dye. The clinical treatment volume (CTV) is the GTV and areas of microscopic disease extension including the proximal 1 cm of the seminal vesicles. The PTV included a 1 cm radial expan-

TABLE 1. Patient characteristics

Pt number	Staging	Gleason score	PSA	Age
1	T1c	4+3=7/10	6.0	70
2	T1c	3+3=6/10	4.4	67
3	T1c	3+4=7/10	9.9	61
4	T2a	4+5=9/10	24.4	81
5	T2c	3+3=6/10	10.8	67
6	T2a	5+4=9/10	9.5	74
7	T1c	3+4=7/10	6.1	70
8	T1c	4+3=7/10	8.8	60
9	T1c/T2a	4+3=7/10	4.8	69
10	T1c	4+3=7/10	6.8	63
11	T2b/T3a	4+5=9/10	14.2	63

PSA = prostate-specific antigen; Pt = patient

sion of the CTV in all directions, except a posterior margin of 6 mm, to allow for treatment set up variation as well as internal motion of organs. The confidence in the reduced size of the posterior margin is due, in part, to IGRT techniques of weekly CBCT and daily kV orthogonal matching to imbedded radiopaque fiducial prostate seed markers.

OARs contoured on the treatment planning CT include the left and right femoral heads to the level of the ischial tuberosity, the bladder, and the rectum from the superior rectosigmoid flexure to the inferior level of the ischial tuberosities. Additionally, an external body structure was also contoured as a normal tissue for the purposes of dose volume histogram (DVH) analysis. All structures contoured exist as solid organs in their entirety.

The prescription dose was 1.8 Gy per fraction for 44 fractions (79.2 Gy total dose) to cover 95% of the PTV, with the maximum dose in the PTV no more than 107% of the prescription dose.

VMAT planning

All treatment planning was performed on Varian Eclipse TPS 10.0. The original VMAT plans were copied and dose was calculated based on the previously generated arc parameters with the following criteria: The treatment isocenter was placed at the center of the PTV. Two full arcs were planned using the Eclipse Arc Geometry Tool, with the initial arc rotating clockwise from 181° to 179°, a collimator rotation of 30° and the second arc rotating counter clockwise from 179° back to 181° with a collimator rotation of 320°.

Additional structures created for planning purposes only included a radial expansion of 1 mm on the PTV to enhance dose coverage and fall off. Regions of overlap between treatment volumes and OARs were contoured to control dose effectively within these areas. Additionally, to better control dose to the rectum, two additional structures were contoured as illustrated in Figure 1. Rectum_Out was a radial expansion of 5 mm on the rectum minus the overlap contour, subsequently cropped out of the overlap area with an additional 1 cm margin. Rectum_Mid was a radial expansion of 5 mm on the rectum minus the overlap contour, subsequently cropped out of both the overlap area with a 3 mm margin and Rectum_Out. Finally, support structures were added to account for the treatment couch in the path of the arcs.

Within the VMAT optimizer, using calculation model algorithm PRO_10028, upper and lower dose constraints were set on all tumor and treat-
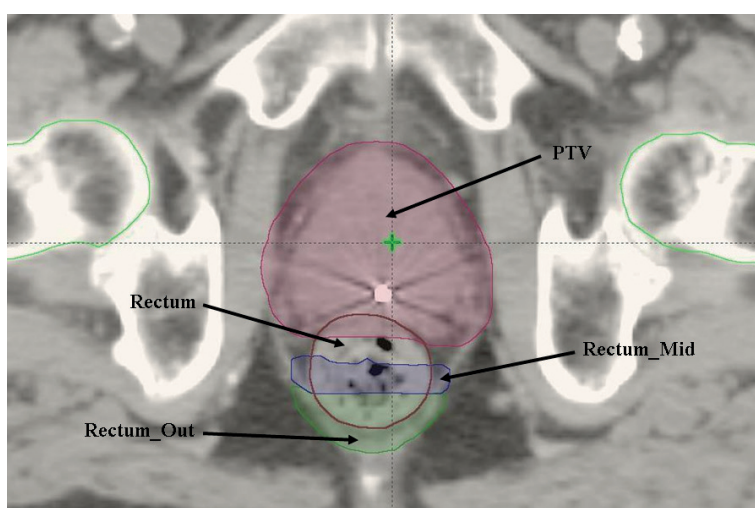

FIGURE 1. Diagram showing additional structures to control rectal dose.

ment volumes and expansions thereof. Coverage of targets thus defined received topmost priority, with OARs receiving lesser priority in the order of rectum, bladder, and finally, bilateral femoral head and necks. The Normal Tissue Objective was utilized, with a priority value matching that of the target coverage, with automatic tissue sparing selected.

Dose was calculated for an intermediate optimization, and final dose calculated after the VMAT optimizer was run a second time to completion. A normalization point was selected such that 100% of the prescribed dose would be delivered to 95% the PTV.

Hybrid planning

The hybrid planning technique was comprised of two dynamic IMRT fields with a single overlying volume modulated arc delivered to the same isocenter as in the VMAT plans. Beam arrangement of the dynamic fields was chosen such that the majority of the PTV on the central axis received coverage while minimizing direct OAR exposure within the fields. Directly opposed fields were avoided, and in general, left and right anterior oblique fields gave the best geometry.

The two dynamic IMRT fields provided approximately 1/3 of the total dose, with the remaining dose supplied by the overlying arc. The IMRT fields served as a base dose for the VMAT optimizer, with the same structures and constraints as utilized for the VMAT planning process.

Again, dose was calculated for an intermediate optimization, and final dose calculated with the
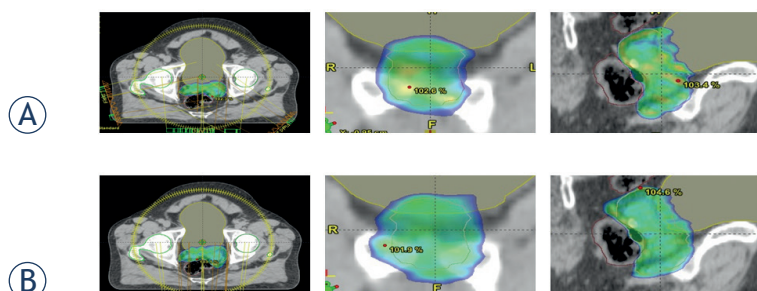
FIGURE 2. Dose distribution for typical hybrid **(A)** and 2 arc volumetric modulated arc therapy (VMAT) **(B)**. plans with color wash of 95% of the prescription dose.
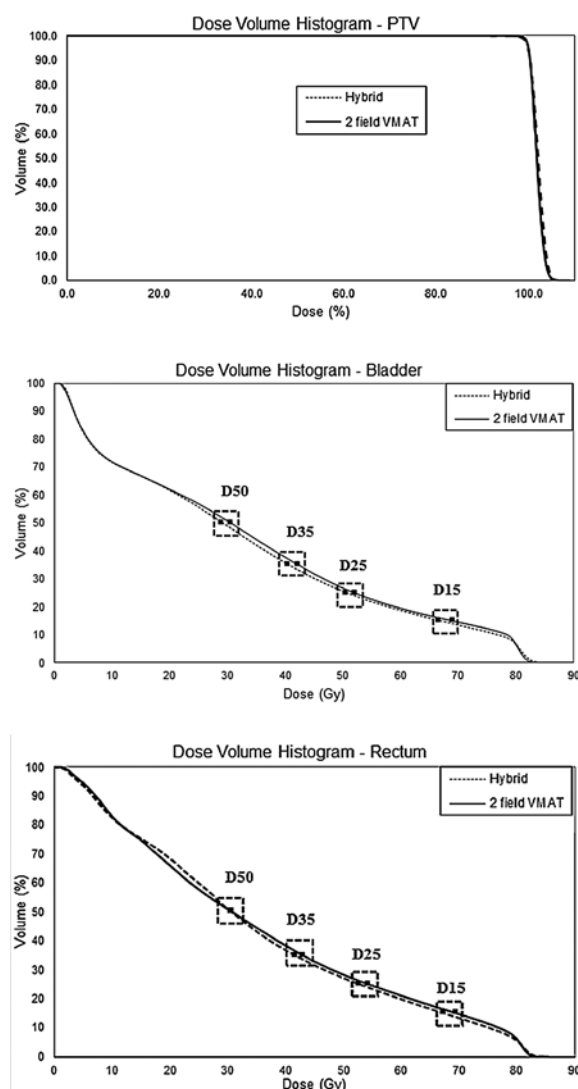

FIGURE 3. Dose volume histogram (DVH) comparison of some planning treatment volume (PTV), rectum, and bladder between the hybrid technique and the two field volumetric modulated arc therapy (VMAT) technique.

VMAT optimizer run to completion on a second pass. A normalization point was chosen to achieve the same coverage as in the VMAT plan.

Isodose lines were analyzed and, if possible, the IMRT fluences were adjusted manually to increase target coverage or reduce hot spots.

Analysis

For each case, the two competing treatment plans were compared on the basis of several criteria. For target coverage, PTV min (D2), max (D98), and mean, as recommended by ICRU 83[20] for dose reporting, as a percentage of prescribed dose were cross referenced against a conformality index (CI) as defined below. For OAR analysis, the data was examined based on the specific organ tolerances as per tables in RTOG 0815. For the rectum, the DVH points of D15, D25, D35, and D50 as well as the V80, V75, V70 and V65 were examined. For the bladder, the DVH points of interest were again D15, D25, D35, and D50 as well as V75, V70, V65, and V60. For the bilateral femora both the max and mean values were compared. To gauge low dose to the body, the body V5 and V10 was used as a point of comparison, as well as a calculation for integral dose (ID) as defined below. Finally, a monitor unit comparison was made between the hybrid and VMAT plan as an indicator of modulation.

$$CI = VRx \, / \, V\_PTV \qquad [1]$$

Where V_{Rx} is the volume in cc receiving the prescription dose, and V_{PTV} is the PTV volume in cc.

$$ID = Vp\overline{D} \qquad [2]$$

Where V, p, and $\overline{D}$ are respectively the volume, density of the organ, and mean organ dose.

Results

Dose color wash at 95% of the prescription dose is shown for the hybrid treatment and for the double arc VMAT comparison in Figure 2. The breakdown of target coverage with CI, PTV minimum, maximum, and mean along with MU delivered and ID are shown in Table 2. The OAR study parameters for the two techniques are tabulated in Table 3 with corresponding differences. The average DVHs for the PTV and bladder and rectum are shown in Figure 3.

Target coverage

The hybrid plan had better conformality compared to the double arc VMAT plan with a relative improvement of 5.5% in CI. All of the plans were con-

TABLE 2. Planning treatment volume (PTV) coverage, monitor units, and integral dose for delivery of plans

Pt number	Modality	CI	PTV-min	PTV-max	PTV-mean	MU	Integral dose
1	Hybrid	0.98	92.8%	108.5%	103.0%	686	308.1
	VMAT	1.08	95.5%	108.1%	101.4%	867	303.7
2	Hybrid	0.99	91.3%	107.1%	102.3%	817	186.5
	VMAT	1.15	97.5%	107.6%	102.0%	697	198.8
3	Hybrid	1.00	94.4%	107.6%	102.3%	616	255.8
	VMAT	1.05	96.2%	106.2%	101.3%	592	255.3
4	Hybrid	1.05	95.0%	107.7%	102.5%	743	200.3
	VMAT	1.08	97.5%	109.4%	101.5%	574	196.3
5	Hybrid	1.07	94.9%	106.6%	102.4%	521	232.0
	VMAT	1.12	96.9%	106.9%	101.3%	796	233.1
6	Hybrid	1.15	96.8%	111.0%	101.6%	600	216.3
	VMAT	1.32	91.6%	109.8%	102.0%	602	208.6
7	Hybrid	0.97	94.2%	107.1%	102.8%	542	201.3
	VMAT	0.97	94.7%	106.1%	102.3%	487	201.8
8	Hybrid	1.03	95.2%	110.0%	102.6%	729	133.5
	VMAT	1.03	94.8%	107.4%	101.7%	598	132.2
9	Hybrid	1.09	95.3%	109.7%	102.3%	786	254.7
	VMAT	1.17	97.4%	106.2%	101.6%	622	263.5
10	Hybrid	1.13	96.2%	109.3%	101.8%	603	178.5
	VMAT	1.03	92.6%	107.3%	102.2%	610	175.6
11	Hybrid	1.00	96.0%	106.6%	102.1%	521	165.6
	VMAT	1.14	98.1%	106.0%	101.7%	587	175.5
AVE	Hybrid	1.04	94.74%	108.29%	102.34%	651.27	212.05
	VMAT	1.10	95.71%	107.36%	101.73%	639.27	213.13

AVE = average; CI = confidence interval; MU = monitor units; Pt = patient; VMAT = volumetric modulated arc therapy

sidered acceptable with 95% of the PTV volume receiving 100% of the prescribed dose, but the VMAT plan achieved better dose homogeneity with an increase in 1% to PTV minimum and a reduction of 1% in PTV maximum (Table 2).

Organs at risk

Critical structure dose constraints followed RTOG protocol 0815 such that volumes of 15%, 25%, 35%, and 50% shall receive doses less than 80, 75, 70 and 65 Gy for the bladder and 75, 70, 65, 60 Gy for the rectum, respectively. The clinical VMAT plan served as control for the purposes of comparison. On average, the hybrid technique provided greater OAR sparing for both the rectum and bladder at all volumes and doses of interest (Table 3). For the volume constraints, the p-value of each difference is provided. A low p-value indicates that the VMAT and hybrid values are statistically significantly different.

Monitor units, integral dose, low dose spillage

Monitor unit differences varied, with the hybrid plan able to deliver fewer MU 45% of the time. Integral dose was slightly lower with the hybrid plan. For low doses of radiation to the whole body, the hybrid plan fared slightly better than the double arc VMAT plans, with a reduction in V5 of 0.8%, and a reduction in V10 of 1.9% on average (Table 2, 3).

Discussion

Previous studies comparing VMAT to IMRT for prostate treatment have highlighted the fact that VMAT delivery is more efficient than that of IMRT.[16, 21-33] However, all of these studies have

TABLE 3. Organ-at-Risk constraints for bladder, rectum, femora and body

	Dose Constraints											
	Bladder				Rectum				Left F. Head		Right F. Head	
	D50	D35	D25	D15	D50	D35	D25	D15	Max	Mean	Max	Mean
VMAT (Gy)	30.66	42.35	52.12	69.11	30.75	42.98	54.31	69.50	38.49	17.31	37.13	17.18
HYBRID (Gy)	29.10	40.56	50.62	66.72	30.66	41.69	52.83	67.34	44.86	15.41	46.02	18.25
DIFF (Gy)	1.56	1.79	1.50	2.40	0.09	1.28	1.48	2.16	-6.37	1.90	-8.89	-1.07

	Volume Constraints										
	Bladder				Rectum					Body	
	V65	V70	V75	V80	V50	V60	V65	V70	V75	V5	V10
VMAT (%)	16.92	14.60	12.28	6.73	28.08	21.15	17.97	14.92	11.57	25.34	20.40
HYBRID (%)	15.88	13.40	10.96	6.43	26.24	19.47	16.10	12.93	9.69	24.51	18.51
DIFF (P-Val)	1.04 (0.36)	1.20 (0.32)	1.32 (0.27)	0.30 (0.39)	1.84 (0.31)	1.68 (0.25)	1.87 (0.17)	1.99 (0.09)	1.88 (0.06)	0.84	1.89

DIFF = difference; f. = femur; VMAT = volumetric modulated arc therapy

mixed dosimetric results. Some studies have shown better sparing of OARs with IMRT[23], while some have shown equivalent sparing of OARs.[26,33] For example, the study by Ishii et al.[33] showed that PTV coverage was similar between RapidArc, 7 field IMRT, and 9 field IMRT. For the rectum D_{mean}, V_{65Gy} and V_{45Gy} and bladder V_{45Gy}, their results indicated that 9 field IMRT plans had significantly lower values than the RapidArc and 7 field IMRT. Our aim was to develop a technique that would further reduce the delivery time and maintain the same level of dosimetric outcome as the conventional RapidArc delivery.

The hybrid technique enables the planner to more easily control dose to critical OARs. The use of dynamic IMRT allows for additional input into the TPS and serves as a portal for the planner to more directly control dose distributions. The combination of directly changing fluencies for the IMRT portion of delivery, as well as a choice of beam geometry allows the planner to better control where dose falls. Greater OAR sparing was seen in the hybrid technique for both bladder and rectum points across the range of interest.

The hybrid technique provides greater conformality compared to the standard VMAT. As IGRT localization improves, this allows for reduced OAR volumes exposed to escalated doses, potentially reducing toxicity to normal tissues. This not only creates the opportunity for reduced patient complications, but also room for dose escalation leading to potential increased local control. One way of measuring the dose-modulation potential of a plan

delivery modality is to consider the number of control points it allows. The control points are created by the TPS software and contained in a treatment plan's DICOM file. Each control point specifies the state of the linac at a given instant of treatment (i.e., jaw settings, MLC positions, MUs, gantry angle and rotation speed, etc.). An IMRT plan and full-arc VMAT plan contain 320 and 178 control points, respectively. Therefore, a hybrid plan contains 2x320+178 = 818 control points, while double-arc VMAT plan contains 178x2 = 356 control points. Thus, the hybrid plan provides better dose modulation and control of dose fall off around the PTV.

With Varian Eclipse treatment planning, the hybrid plan was created utilizing separate optimizers from the constituent VMAT and IMRT portions. With this method of planning, the IMRT base dose plan is unaware of the subsequent VMAT arc and therefore cannot effectively yield homogeneous coverage to the PTV. This inhomogeneous base dose presents an additional restriction on the VMAT optimizer to achieve constraints as seen by the decrease in PTV homogeneity of 2% with the hybrid technique.

A typical prostate VMAT field has a beam on time of 1.2 minutes (72 seconds) during treatment. Since most of our prostate VMAT plans require two arcs to achieve a homogeneous dose distribution to the target, the combined beam on time is about 2.4 minutes (144 seconds). The hybrid plan, on the other hand, can be delivered in one gantry sweep consisting of two dynamic IMRT fields with a single overlying VMAT field. A typical dynam-

ic IMRT field from this technique has a beam on time of 0.3 minute. Therefore, the hybrid technique would have a typical total beam on time of 1.2 min + 0.3 min + 0.3 min = 1.8 min, or 108 seconds, which is approximately 0.5 min lower than the typical prostate VMAT delivery in our clinic. Thus, this reduction in time would reduce the chance of intra-fraction motion and increasing patient comfort. Delivery of the treatment in one gantry rotation can also reduce machine wear and potential downtime for machine maintenance.

Total MUs for both techniques are similar, but with a lower ID with the hybrid technique, as well as reduced volume receiving 5 Gy and 10 Gy overall. This is critical due to the radiosensitivity of the OAR's, particularly the rectum and bladder.

Conclusions

Dosimetrically the hybrid and double arc VMAT plans are similar, with the hybrid plan achieving better constraints on the OARs without significantly higher MUs.

Clinically, the hybrid plan offered slightly poorer homogeneity compared with the VMAT plans, yielding a greater shoulder on the PTV coverage. This issue is due to the nature of the two disparate optimizers attempting to achieve overall dose homogeneity. Changing the nature of the optimization to a single overall algorithm would correct the difficulty in achieving completely uniform coverage.

The hybrid treatment delivered in a single gantry rotation with short pauses for small IMRT corrections could potentially reduce treatment time and increase target localization compared to multiple arc VMAT, while providing superior sparing of critical OARs. It not only allows for increased conformality of dose over VMAT while maintaining reduced treatment times over full IMRT, but also provides more planner control in the area of low dose spillage.

References

1. Cutler SJ, Scotto J, Devesa SS, Connelly RR. Third national cancer survey-an overview of available information. *J Natl Cancer I* 1974; **53:** 1565-75.

2. Parkin DM, Bray F, Ferlay J, Pisani P. Global cancer statistics, 2002. *CA: Cancer J Clin* 2005; **55:** 74-108.

3. Zelefsky M, Leibel S, Gaudin P, Kutcher G, Fleshner N, Venkatramen ES, et al. Dose escalation with three-dimensional conformal radiation therapy affects the outcome in prostate cancer. *Int J Radiat Oncol* 1998; **41:** 491-500.

4. Peeters ST, Heemsbergen WD, Koper PC, van Putten WL, Slot A, Dielwart MF, et al. Dose-response in radiotherapy for localized prostate cancer: results of the Dutch multicenter randomized phase III trial comparing 68 Gy of radiotherapy with 78 Gy. *J Clin Oncol* 2006; **24:** 1990-6.

5. Pollack A, Zagars GK, Starkschall G, Childress CH, Kopplin S, Boyer AL, et al. Conventional vs. conformal radiotherapy for prostate cancer: preliminary results of dosimetry and acute toxicity. *Int J Radiat Oncol* 1996; **34:** 555-64.

6. De Meerleer GO, Vakaet LA, De Gersem WR, De Wagter C, De Naeyer B, De Neve W. Radiotherapy of prostate cancer with or without intensity modulated beams: a planning comparison. *Int J Radiat Oncol* 2000; **47:** 639-48.

7. De Meerleer G, Vakaet L, Meersschout S, Villeirs G, Verbaeys A, Oosterlinck W, et al. Intensity-modulated radiotherapy as primary treatment for prostate cancer: acute toxicity in 114 patients. *Int J Radiat Oncol* 2004; **60:** 777-87.

8. Zelefsky MJ, Fuks Z, Hunt M, Yamada Y, Marion C, Ling CC, et al. High-dose intensity modulated radiation therapy for prostate cancer: early toxicity and biochemical outcome in 772 patients. *Int J Radiat Oncol* 2002; **53:** 1111-6.

9. Zelefsky MJ, Chan H, Hunt M, Yamada Y, Shippy AM, Amols H. Long-term outcome of high dose intensity modulated radiation therapy for patients with clinically localized prostate cancer. *J Urology* 2006; **176:** 1415-9.

10. Cozzi L, Dinshaw KA, Shrivastava SK, Mahantshetty U, Engineer R, Deshpande DD, et al. A treatment planning study comparing volumetric arc modulation with RapidArc and fixed field IMRT for cervix uteri radiotherapy. *Radiother Oncol* 2008; **89:** 180-91.

11. Wolff D, Stieler F, Welzel G, Lorenz F, Abo-Madyan Y, Mai S, et al. Volumetric modulated arc therapy (VMAT) vs. serial tomotherapy, step-and-shoot IMRT and 3D-conformal RT for treatment of prostate cancer. *Radiother Oncol* 2009; **93:** 226-33.

12. Wu QJ, Yoo S, Kirkpatrick JP, Thongphiew D, Yin FF. Volumetric arc intensity–modulated therapy for spine body radiotherapy: comparison with static intensity-modulated treatment. *Int J Radiat Oncol* 2009; **75:**1596-604.

13. Clivio A, Fogliata A, Franzetti-Pellanda A, Nicolini G, Vanetti E, Wyttenbach R, et al. Volumetric-modulated arc radiotherapy for carcinomas of the anal canal: A treatment planning comparison with fixed field IMRT. *Radiother Oncol* 2009; **92:** 118-24.

14. Bertelsen A, Hansen CR, Johansen J, Brink C. Single arc volumetric modulated arc therapy of head and neck cancer. *Radiother Oncol* 2010; **95:** 142-8.

15. Boylan CJ, Golby C, Rowbottom C. GA VMAT planning solution for prostate patients using a commercial treatment planning system. *Phys Med Biol* 2010; **55:** N395.

16. Palma D, Vollans E, James K, Nakano S, Moiseenko V, Shaffer R, et al. Volumetric modulated arc therapy for delivery of prostate radiotherapy: comparison with intensity-modulated radiotherapy and three-dimensional conformal radiotherapy. *Int J Radiat Oncol* 2008; **72:** 996-1001.

17. Wagner D, Christiansen H, Wolff H, Vorwerk H. Radiotherapy of malignant gliomas: comparison of volumetric single arc technique (RapidArc), dynamic intensity-modulated technique and 3D conformal technique. *Radiother Oncol* 2009; **93:** 593-6.

18. Bentzen SM, Constine LS, Deasy JO, Eisbruch A, Jackson A, Marks LB, et al. Quantitative Analyses of Normal Tissue Effects in the Clinic (QUANTEC): an introduction to the scientific issues. *Int J Radiat Oncol* 2010; **76:** S3-9.

19. Chan OS, Lee MC, Hung AW, Chang AT, Yeung RM, Lee AW. The superiority of hybrid-volumetric arc therapy (VMAT) technique over double arcs VMAT and 3D-conformal technique in the treatment of locally advanced non-small cell lung cancer–A planning study. *Radiother Oncol* 2011; **101:** 298-302.

20. International Commission on Radiation Units and Measurements. Prescribing, recording, and reporting photon-beam intensity-modulated radiation therapy (IMRT). ICRU Report 83. *J ICRU* 2010; **10:** 1-106.

21. Viani GA, Silva LGB, Stefano EJ. High-dose conformal radiotherapy reduces prostate cancer-specific mortality: results of a meta-analysis. *Int J Radiat Oncol* 2012; **83:** e619-25.

22. Kjaer-Kristoffersen F, Ohlhues L, Medin J, Korreman S. RapidArc volumetric modulated therapy planning for prostate cancer patients. *Acta Oncol* 2009; **48:** 227-32.

23. Yoo S, Wu J, Lee R, Yin FF. Radiotherapy treatment plans with rapidarc for prostate cancer involving seminal vesicles and lymph nodes. *Int J Radiat Oncol* 2010; **76:** 935-42.

24. Zhang P, Happersett L, Hunt M, Jackson A, Zelefsky M, Mageras G. Volumetric modulated arc therapy: planning and evaluation for prostate cancer cases. *Int J Radiat Oncol* 2010; **76:** 1456-62.

25. Aznar MC, Petersen PM, Logadottir A, Lindberg H, Korreman SS, Kjaer-Kristoffersen F, et al. Rotational radiotherapy for prostate cancer in clinical practice. *Radiother Oncol* 2010; **97:** 480-4.

26. Davidson MTM, Blake S, Batchelar DL, Cheung P, Mah K. Assessing the role of volumetric modulated arc therapy (VMAT) relative to IMRT and helical tomotherapy in the management of localized, locally advanced, and post-operative prostate cancer. *Int J Radiat Oncol* 2011; **80:** 1550-8.

27. Hardcastle N, Tome WA, Foo K, Miller A, Carolan M, Metcalfe P. Comparison of prostate IMRT and VMAT biologically optimized treatment plans. *Med Dosim* 2011; **36:** 292-8.

28. Kopp RW, Duff M, Catalfamo F, Shah D, Rajecki M, Ahmad K. VMAT vs. 7-field-IMRT: assessing the dosimetric parameters of prostate cancer treatment with a 292-patient sample. *Med Dosim* 2011; **36:** 365-72.

29. Sale C, Moloney P. Dose comparisons for conformal, IMRT and VMAT prostate plans. *J Med Imaging Radiat Oncol* 2011; **55:** 611-21.

30. Myerhaug S, Chan G, Craig T, Weinberg V, Cheng C, Roach M, et al. A treatment planning and acute toxicity comparison of two pelvic nodal volume delineation techniques and delivery comparison of intensity-modulated radiotherapy versus volumetric modulated arc therapy for hypofractionated high-risk prostate cancer radiotherapy. *Int J Radiat Oncol* 2012; **82:** e657-62.

31. Sze HCK, Lee MCH, Hung WM, Yau TK, Lee AWM. RapidArc radiotherapy planning for prostate cancer: single-arc and double-arc techniques vs. intensity-modulated radiotherapy. *Med Dosim* 2012; **37:** 87-91.

32. Fontenot JD, King ML, Johnson SA, Wood CG, Price MJ, Lo KK. Single-arc volumetric-modulated arc therapy can provide dose distributions equivalent to fixed-beam intensity-modulated radiation therapy for prostatic irradiation with seminal vesicle and/or lymph node involvement. *Br J Radiol* 2012; **85:** 231-6.

33. Ishii K, Ogino R, Okada W, Nakahara R, Kawamorita R, Nakajima T. A dosimetric comparison of RapidArc and IMRT with hypofractionated simultaneous integrated boost to the prostate for treatment of prostate cancer. *Br J Radiol* 2013; **86:** 20130199.

research article

Rounded leaf end effect of multileaf collimator on penumbra width and radiation field offset: an analytical and numerical study

Dong Zhou, Hui Zhang, Peiqing Ye

Department of Mechanical Engineering, Tsinghua University, Beijing, China

Correspondence to: Prof. Peiqing Ye, Ph.D., Department of Mechanical Engineering, Tsinghua University, Beijing, China.
Phone: +86 010 6277 3269; E-mail: yepq@tsinghua.edu.cn

Background. Penumbra characteristics play a significant role in dose delivery accuracy for radiation therapy. For treatment planning, penumbra width and radiation field offset strongly influence target dose conformity and organ at risk sparing.

Methods. In this study, we present an analytical and numerical approach for evaluation of the rounded leaf end effect on penumbra characteristics. Based on the rule of half-value layer, algorithms for leaf position calculation and radiation field offset correction were developed, which were advantageous particularly in dealing with large radius leaf end. Computer simulation was performed based on the Monte Carlo codes of EGSnrc/BEAMnrc, with groups of leaf end radii and source sizes. Data processing technique of curve fitting was employed for deriving penumbra width and radiation field offset.

Results. Results showed that penumbra width increased with source size. Penumbra width curves for large radius leaf end were U-shaped. This observation was probably related to the fact that radiation beams penetrated through the proximal and distal leaf sides. In contrast, source size had negligible impact on radiation field offset. Radiation field offsets were found to be constant both for analytical method and numerical simulation. However, the overall resulting values of radiation field offset obtained by analytical method were slightly smaller compared with Monte Carlo simulation.

Conclusions. The method we proposed could provide insight into the investigation of rounded leaf end effects on penumbra characteristics. Penumbra width and radiation field offset calibration should be carefully performed to commission multileaf collimator for intensity modulated radiotherapy.

Key words: multileaf collimator; rounded leaf end effect; penumbra width; radiation field offset; Monte Carlo simulation

Introduction

Multileaf collimator system was introduced as a replacement of shielding block for beam shaping and beam intensity modulation, which has become an essential component for modern radiation therapy and a standard of care for radiation oncology facilities.[1] Penumbra characteristics of multileaf collimator are closely related to healthy tissues involvement, which is of interest to medical physicists, dosimetrists and radiation oncologists.[2]

Single-focused multileaf collimator is characterized by linear leaf motion perpendicular to collimator rotation axis, which has been widely used by virtue of its compact space and simplified structures. The rounded leaf end design of single-focused multileaf collimator for following beam divergence has a strong impact on penumbra characteristics.[3] In order to avoid tumour underdose and normal tissue overdose, the rounded leaf end effect of single-focused multileaf collimator on penumbra characteristics should be carefully modelled
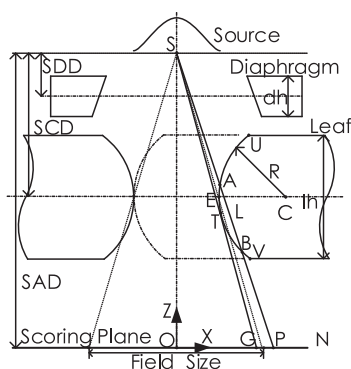
FIGURE 1. Components of treatment head are comprised of source, diaphragm, multileaf collimator, and scoring plane. Leaf positions on scoring plane are classified into nominal leaf position N, geometric leaf position G and physical leaf position P.

SAD = source to axis distance; SCD = source to collimator distance; SDD = source to diaphragm distance

in treatment planning system, otherwise it would result in dose error particularly when sharp dose gradient is intended for stereotactic body radiotherapy.

For the purpose of precision radiation therapy, intensive research efforts have been made on the dosimetric measurement and Monte Carlo simulation of multileaf collimator systems.[4,5] Studies have revealed that dosimetric characteristics of multileaf collimator are influenced by the factors, including but not limited to geometry of treatment modality, radiation source properties, leaf end shape and leaf position with respect to central axis.[6] It was found that dosimetric penumbra of multileaf collimator is the combined effect of geometric penumbra, transmission penumbra and phantom scatter.[7] Quality assurance has been implemented to determine penumbra width and the offset between light field edge and radiation field edge during commissioning of multileaf collimator.[8,9] Results have shown that penumbra width and radiation offset are leaf position dependent and largely attributed to leaf end shape. It is reported that the projected leaf position on scoring plane, light field edge and radiation field edge follow a nonlinear relationship. Calibrations of leaf position offset and radiation field offset were performed to minimize the error between planned doses and delivered doses.[10,11] Rule of half-value layer[12] has been proposed for calculation of radiation field offset based on geometrical approach.[13] However, previous studies were confined to single source energy distribution, normally simplified as Gaussian shaped, and limited leaf ends in the shape of circular arc were investigated. There is a lack of consistency in the quantitative study into rounded leaf end effect on penumbra characteristics of multileaf collimator in literature. Besides, there is no literature available, to our knowledge, reporting on algorithms of leaf position calculation and radiation field offset correction for large radius leaf end.

Consequently, the aim of this study was to explore the rounded leaf end effect and efforts were made to reveal the source energy distribution and leaf end shape related penumbra characteristics. An analytical method for radiation field offset correction was developed and numerical simulation with various leaf end radii and source sizes was conducted based on Monte Carlo codes.

Materials and methods

In this section, leaf positions are classified and geometry based algorithms for radiation field offset correction are developed. With treatment head modelling, Monte Carlo simulation is introduced to investigate the rounded leaf effect on penumbra characteristics. Data processing techniques for deriving penumbra width and radiation field offset are proposed.

Algorithms for leaf position calculation and radiation field offset correction

Leaf positions on scoring plane are divided into projected leaf end position (nominal leaf position), light field edge (geometric leaf position), and radiation field edge (physical leaf position).[14] Nominal leaf position is usually calibrated so that it corresponds to the light field edge or the radiation field edge. In this study, nominal leaf position is designated to coincide with the projected leaf position without calibration.

As depicted in Figure 1, mechanical leaf position is referred to as the leaf tip location relative to collimator rotation axis, which is shown as point E. Nominal leaf position, geometric leaf position and physical leaf position on the scoring plane are represented by point N, point G, and point P, respectively. Leaf position offset (LPO) is defined as the distance between geometric leaf position and nominal leaf position. Radiation field offset (RFO) is defined as the distance between physical leaf position and geometric leaf position. The term of physical-nominal offset (PNO) is proposed, which is defined as the distance between physical leaf position and nominal leaf position.

Place the origin of coordinate in coincidence with isocenter O. Therefore, the Z-coordinates are zero for point N, G and P. Point N is obtained by projecting of mechanical leaf position E onto the scoring plane. Point G is obtained by deriving the tangent line of circular arc leaf end from source S. Point P is obtained by rule of half-value layer.

Equations for the LPO, RFO and PNO derivation are presented,

$$\begin{cases} LPO = x_G - x_N \\ RFO = x_P - x_G \\ PNO = x_P - x_N \end{cases} \tag{1}$$

Algorithms for calculation the X-coordinates of leaf positions are illustrated as follows. Consider a specific nominal leaf position, which is designated as point N in Figure 1, Point E is obtained by back-projecting leaf end point N onto the collimator middle plane, that is

$$x_E = x_N \times \frac{SCD}{SAD} \tag{2}$$

where SCD is used to stand for source to collimator distance, while SAD stands for source to axis distance. The circular arc center C is shifted to the positive side of point E with a length of radius R, that is,

$$x_C = x_E + R \tag{3}$$

Denote the distance between source S and arc centre C as D, which is used as a reference,

$$D = \sqrt{(x_S - x_C)^2 + (z_S - z_C)^2} \tag{4}$$

Firstly, point G is obtained by deriving the tangent line of circular arc leaf end from source S. The relationship between point G and point T is,

$$x_G = x_T \times \frac{SAD}{SAD - z_T} \tag{5}$$

Thus, the prerequisite for point G derivation is to obtain point T. The X-coordinate of point T should satisfy the condition of $x_T < x_C$. Point T can be obtained by the following equations,

$$\begin{cases} (x_T - x_C)^2 + (z_T - z_C)^2 = R^2 \\ (z_T - z_S)(z_T - z_C) + (x_T - x_S)(x_T - x_C) = 0 \end{cases} \tag{6}$$

In case that the tangent point falls out of circular arc or S falls within circle, denote the tangent point as the intersection point of circular arc with proximal or distal leaf side. The intersection points are depicted as point U and point V, respectively. Algorithm is illustrated as follows, for leaf height of lh,

$$x_T = \begin{cases} x_T, & \text{if } z_T \in [z_C - lh/2, z_C + lh/2] \\ x_C - \sqrt{R^2 - (lh/2)^2}, & \text{otherwise} \end{cases} \tag{7}$$

$$z_T = \begin{cases} z_C + lh/2, & \text{if } D \le R \\ z_C + lh/2, & \text{if } D > R \text{ and } z_T > z_C + lh/2 \\ z_C - lh/2, & \text{if } D > R \text{ and } z_T < z_C - lh/2 \\ z_T, & \text{if } D > R \text{ and } z_T \in [z_C - lh/2, z_C + lh/2] \end{cases} \tag{8}$$

Secondly, point P is obtained by the half-value layer rule. Draw a secant line from source S to the

point P, the secant point A and B fall on the left side of C, that is, $x_A < x_C$, $x_B < x_C$. Find the equation of secant line satisfying the condition that path length AB equals half-value layer L,

$$\begin{cases} L = -\ln(0.5)/\mu \\ (z_A - z_B)^2 + (x_A - x_B)^2 = L^2 \end{cases} \tag{9}$$

where path length is calculated according to the inverse exponential power law and m denotes the attenuation coefficient of tungsten leaf. A, B and S are on the secant line. It is written in the following form,

$$(z_A - z_S)(x_B - x_S) - (z_B - z_S)(x_A - x_S) = 0 \tag{10}$$

Suppose the A and B are both on the circular arc, that is,

$$\begin{cases} (x_A - x_C)^2 + (z_A - z_C)^2 = R^2 \\ (x_B - x_C)^2 + (z_B - z_C)^2 = R^2 \end{cases} \tag{11}$$

Combine [9], [10] and [11] into a system of nonlinear equations, solve it with iterative methods. In case that the resulting A or B is not on circular arc, conditional statements are performed as follows.

If the resulting $Z_A > Z_C + lh/2$ or $D < R$, it means point A should be on the proximal leaf side. Substitute equation [12] for [11] in the system of equations and solve it.

$$\begin{cases} (x_A - x_C)^2 + (z_A - z_C)^2 = R^2 \\ (x_B - x_C)^2 + (z_B - z_C)^2 = R^2 \end{cases} \tag{12}$$

Else, if $Z_B < Z_C - lh/2$, substitute equation [13] for [11] in the system of equations and solve it.

$$\begin{cases} (x_A - x_C)^2 + (z_A - z_C)^2 = R^2 \\ z_B = z_C - lh/2 \end{cases} \tag{13}$$

Else, return with the solutions of equations.

Monte Carlo simulation

Numerical simulation is performed based on Monte Carlo codes EGSnrc/BEAMnrc.[15,16] Multileaf collimator component module of VARMLC is adopted. Leaf ends in the shape of circular arc are used, with radius values in a range of 4 cm to 25 cm. The geometry of Monte Carlo simulation is depicted as Figure 1. Multileaf collimator is comprised of 40 pairs of leaves. Symmetric field size of 10x10 is adopted, which remains constant for different leaf positions. It means that the central 10 pairs of leaves shift for field shaping, while the peripheral leaves stay still in close state. For central leaf pair, the gap between leading leaf and trailing leaf corresponds to the square field edge of 10 cm, measured along leaf travel direction on scoring plane. Diaphragms are extracted to the maximum position in order to

TABLE 1. Parameters for Monte Carlo simulation

Parameter	Value	Unit
Source to axis distance	100	cm
Source to collimator distance	46	cm
Source to diaphragm distance	33.9	cm
Diaphragm height	7.8	cm
Leaf height	8	cm
Leaf pairs	40	-
Leaf density	19.3	g/cm^3
Attenuation coefficient m	0.96	cm^{-1}
Maximum field size	40	cm
Photon source average energy	1.5	MeV
Source divergence angle	15.8°	-
Recording histories	10^9	-

avoid interference with radiation beams. Source sizes with a range of 0.5 to 3 mm full width at half maximum (FWHM) are adopted. Parameters for configuration are listed in Table 1.

Data processing

Data processing software BEAMDP is utilized for deriving energy fluence versus position from the acquired phase space files grouped by source size and leaf end radius. Curve fitting is performed to obtain penumbra characteristics, including penumbra width and radiation field offset. Figure 2 shows a sample result for data processing.

Normalize the Monte Carlo data by scaling between 0 and 1. The penumbra width is referred to as the distance between relative intensity of 0.2 and 0.8, and the radiation field edge is referred to as the position with relative intensity of 0.5. Gaussian function is employed for curve fitting, with the following equation:

$$f(x) = \sum_{i=1}^{n} a_i e^{-\left((x-b_i)/c_i\right)^2}$$

[14]

Three-peak Gaussian curve fitting is used for the sample data, with coefficients listed in Table 2. Result shows that the goodness of fit is 0.0154 measured by Root Mean Squared Error. Penumbra width is 1.98 mm and radiation field edge is at 9.932 cm, with PNO offset of 0.68 mm.

FIGURE 2. Data processing for leaf end radius of 10 cm with nominal leaf position at 10 cm and source size of 2 mm full width at half maximum.

MC = Monte Carlo

Results

Penumbra width

The results of penumbra width are illustrated as Figure 3A. Note that penumbra width varies according to field location, leaf end radius and source size. The minimum and maximum penumbra width are obtained with source sizes of 0.5 mm and 3 mm FWHM, respectively. Figures 3B, 3C and 3D show penumbra width for leaf end radius of 4, 15, 25 cm, respectively. Observe that penumbra width is a function of distance from central axis. The overall trend is that penumbra width with positive distance from central axis is smaller than its negative counterpart.

Figure 4 shows the penumbra width with for source size of 1 mm FWHM. Curve E with leaf end radius of 15 cm demonstrates the minimum sum of penumbra width, which is the optimum in terms of penumbra characteristics. Observe that for large radius leaf end and nominal leaf position far from central axis, penumbra width curve are U-shaped, as shown by curve F and curve G.

FIGURE 3A-D. (A). 3D graph of penumbra width with source size of 0.5 to 3 mm full width at half maximum. **(B).** Penumbra width for leaf end of radius 4 cm. **(C).** Penumbra width for leaf end of radius 15 cm. **(D).** Penumbra width for leaf end of radius 25 cm.

Radiation field offset

Results of physical-nominal offset are depicted in Figure 5A. It is noted that source size has little impact on physical-nominal offset and the surfaces of PNO with source size of 0.5, 1, 2, 3 mm FWHM coincide with each other. Physical-nominal offset maximum of -10.1 mm is obtained at radius of 25 cm with nominal leaf position at -20 cm. Figures 5B, 5C and 5D show PNO for source size of 0.5 to 3 mm with leaf end radius of 4 cm, 15 cm and 25 cm, respectively. Observe that the maximum discrepancy of PNO curves occurs at central axis for radius of 4 cm, which is 0.4 mm.

Figure 6 shows the physical-nominal offset of Monte Carlo simulation and calculation using analytical method for source size of 1 mm FWHM. Note that PNO curve for small radius tends to be flat, and leaf end with large radius follows a quasi-quadratic function between PNO and leaf projected position. Although overall trends of calculation curves are in good agreements with Monte Carlo data, the results of Monte Carlo data are slightly larger compared with analytical values, with maximum discrepancy of 2 mm found for curve pair G at the point with a distance of -20 cm from central axis.

As illustrated in Figure 7, the analytical results agree well with Monte Carlo simulation for leaf end of radius 15 cm with source size of 1 mm. The curves of calculation PNO and RFO are shifted upwards with a constant gap of 0.16 mm, compared with simulation PNO and RFO. Note that the RFO curve is almost parallel with axis, which implies that a constant RFO value could be assigned and physical-nominal offset could be quickly deduced from leaf position offset. The RFO values derived from analytical method and numerical simulation are 0.10 and 0.26 mm, respectively.

Figure 8 shows the radiation offset results using Monte Carlo simulation and analytical method. It is noted that the RFO values of Monte Carlo data are slightly larger than the calculation data. As for leaf end with radius of 25 cm, the curve of radiation field offset is U-shaped with maximum RFO of 2 mm.

Discussion

The results demonstrate that algorithms for leaf position calculation and radiation field offset correction serve well the purpose of investigating rounded leaf end effect on penumbra characteristics. Compared with previous works[10-14], the algorithms we proposed are advantageous particularly

TABLE 2. Three-peak Gaussian curve fitting coefficients

Coefficient	Value	Coefficient	Value	Coefficient	Value
a_1	0.406	a_2	0.397	a_3	0.996
b_1	9.813	b_2	9.586	b_3	9.054
c_1	0.169	c_2	0.269	c_3	0.668
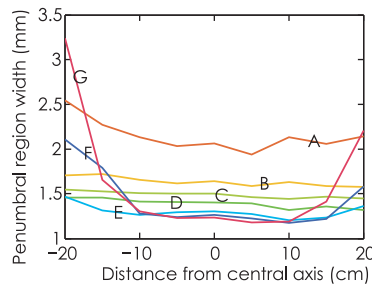
FIGURE 4. Penumbra width for source size of 1mm full width at half maximum. Curve A to G denote radius of 4, 6, 8, 10, 15, 20, 25 cm.
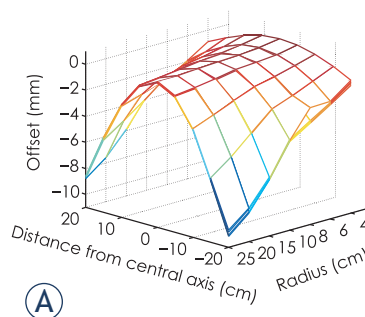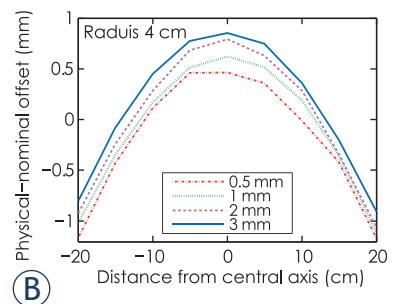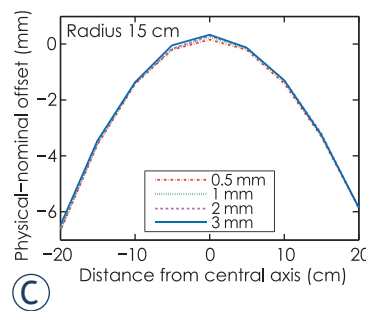
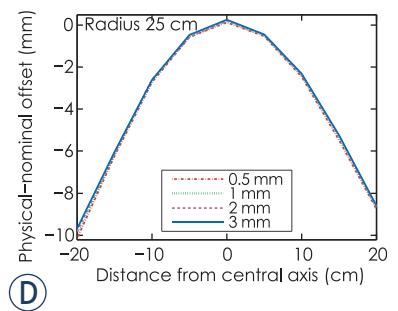**FIGURE 5A-D. (A).** 3D graph of physical-nominal offset with source size of 0.5, 1, 2, 3 mm full width at half maximum. **(B).** physical-nominal offset (PNO) for radius of 4 cm. **(C).** PNO for radius of 15 cm. **(D).** PNO for radius of 25 cm. Source size ranges from 0.5 to 3 mm.

in dealing with large radius leaf end. It is shown that penumbra width of multileaf collimator is a function of radiation source size, geometry of treatment head, leaf end shape and projected leaf position on scoring plane. Optimal radius of leaf end shape could be found by examining the penumbra width curves of Monte Carlo simulation. The results also reveal that radiation source size has a
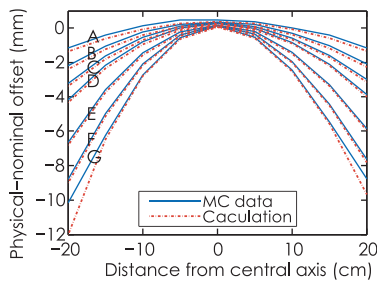
FIGURE 6. Physical-nominal offset for 1mm full width at half maximum source. Curve pair A to G are referred to as circular arc leaf ends with radius of 4, 6, 8, 10, 15, 20, 25 cm, for Monte Carlo (MC) simulation (solid line) and analytical method (dashed line).
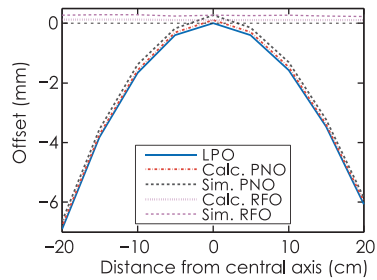

FIGURE 7. Comparison of leaf position offset (LPO), physical-nominal offset (PNO) and radiation field offset (RFO) for leaf end of radius 15 cm with source size of 1 mm.
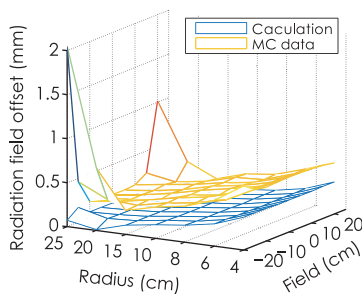
Calc. = calculation; Sim. = simulation

FIGURE 8. Comparison of radiation field offset (RFO) for Monte Carlo simulation and analytical method with source size of 1 mm full width at half maximum.

MC = Monte Carlo

Monoenergetic photon source is designated as Gaussian shaped with full width at half maximum in a range of 0.5 mm to 3 mm, which is in accordance with the dosimetric results.[17] Average source energy of 1.5 MeV is adopted corresponding to 6MeV medical linear accelerator. However, energy spectrum and angular distribution of radiation beams would be implemented in the future works, which is not a trivial task.

For leaf end with large radius, the U-shaped curves appear both for penumbra width and radiation field offset, which are not preferred for clinical application. This observation is probably related with the fact that radiation beams penetrated through the proximal and distal leaf sides.

Although the fluence energy distribution has been intensively studied, the round leaf end effect on penumbra characteristics in phantom or *in vivo* has not been explored, which could be realized by dose calculation algorithms in future works. Scatter effect on dose profile could be calculated using kernel-based convolution and superposition algorithms.

It is noted that the results of RFO correction algorithm are generally in good agreement with numerical simulation. However, the values obtained using analytical method are slightly smaller compared with the corresponding Monte Carlo results, which means that analytical method may underestimates radiation field offset. In order to better predict the radiation field offset, analytical RFO can be placed to match numerical RFO by moving in the direction of from irradiation area to shielded area. This observation implies that analytical method should be applied with care. The error between analytical and numerical methods is probably related the empirical rule of half-value layer or "geometric optics" formulae. A simple physical explanation for the underestimation is given as follows.

Denote P as the physical leaf position obtained by "geometric optics" formulae, which means the path length AB equals half value layer. Denote P_{50} as the radiation field edge, or physical leaf position, obtained by Monte Carlo simulation. Consequently, the question being proposed could be rephrased as "why is $x_P < x_{P_{50}}$?".

Firstly, as illustrated in Figure 9, draw a line CJ from circle arc centre C that is perpendicular with path length AB, with intersection point of K. Denote the length of JK as *H*. It is obvious that *H* is monotonically decreasing for R > 0. For clinical application, leaf end radius is commonly larger than half of leaf width. The maximum of *H* is written,

negligible impact on radiation field offset, while for penumbra width, source size counts.

In our study, virtual source model (VSM) is applied, which has been intensively reported by previous studies.[16] The VSM technique for dose calculation is computational efficient and able to simulate the same dose profile without explicitly taking into consideration the realistic treatment head geometry. Virtual source in our study is Gaussian shaped. However, for realistic treatment head, source energy distribution could more complex than single Gaussian source. In order to accommodate realistic system properties, firstly, virtual source modelling should be conducted to identifying focal source and extra-focal source energy distribution. Secondly, Monte Carlo simulation would be performed according to results of VSM. The geometry of treatment head for numerical simulation is simplified so that the impact of treatment head components, such as primary collimator and flattening filter, on extra-focal radiation, is minimized. However, it is quick to implement by modifying the component properties in Monte Carlo simulation codes.

$$H = R - \left|\overrightarrow{CK}\right| = R - \sqrt{R^2 - \left(\left|\overrightarrow{AB}\right|/2\right)^2} < 8/2 - \sqrt{(8/2)^2 - \left(-\ln(0.5)/0.96/2\right)^2} = 0.016 \text{ cm} \qquad [15]$$

Normally, source energy distribution for treatment modality is with FWHM ranging from 1 to 3 mm. Note that the H is small compared with source size.

Secondly, suppose that source energy distribution is approximately symmetric about central axis. Divide source energy into three parts, the left part S_1, the middle part S_2 and the right part S_3 with respect to the central axis. Denote that total source energy as 1, it is written that,

$$S_1 + S_2 + S_3 = 1 \qquad [16]$$

$$S_1 = S_3 \qquad [17]$$

The attenuation weight for the beams from source part S_1, S_2 and S_3 to the point P are defined as w_1, w_2 and w_3, respectively. The rule of half value layer tells that $w_2 = 0.5$. On account that H is small, beams irradiate from the left part of source are supposed to reach P without attenuation, that is $w_1 = 1$, while for the right part, beams penetrate through leaf entity to reach P with path length larger than half value layer, that is, $0 < w_3 < 0.5$. Consequently, the radiation intensity E_P of point P is written as follows,

$$E_P = w_1 S_1 + w_2 S_2 + w_3 S_3 > S_1 + 0.5 \cdot S_2 = 0.5 \cdot (S_1 + S_2 + S_3) = 0.5 \quad (18)$$

Therefore, it is implied that the physical edge of radiation field P_{50} should be on the right side of P, that is, $x_P < x_{P_{50}}$. This is a simple physical explanation why "geometric optics" formulae systematically underestimate the physical-nominal offset. Since the segmentation of source energy is coarse, further study is suggested with Ray Tracing algorithm, which is implemented by computation of the weighed beam integral based on the law of exponential attenuation. It is suggested that modifications for analytical RFO correction should be performed in order to fit in well with treatment modalities. Path length larger than the half-value layer would be beneficial.

The rounded leaf end design of multileaf collimators leads to partial transmission of radiation beams, which have a significant impact on dose delivery accuracy of IMRT, SBRT and VMAT. Based on Monte Carlo simulation for SBRT multileaf collimator, Asnaashari et al.[5] have revealed that dosimetric penumbra is influenced by source energy, beam collimators and field size. This observation is in good agreement with our study. It is suggested that dosimetric characteristics of multileaf collimator should be calibrated and comprehensive rou-
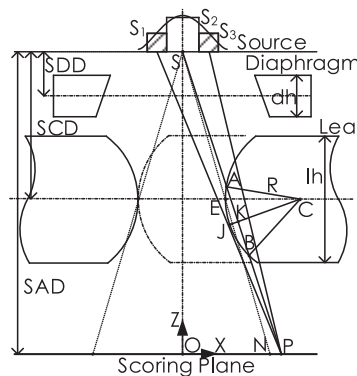

FIGURE 9. Geometry of treatment head for simple physical explanation of why the rule of half value layer systematically underestimates the physical-nominal offset.

SAD = source to axis distance; SCD = source to collimator distance; SDD = source to diaphragm distance

tine quality assurance should be performed before they are implemented for IMRT applications.[3] Further study is needed both for theoretical investigation and dosimetric measurement of rounded leaf end effect.

In our study, penumbra width and radiation field offset of single leaf are intensively studied. In contrast, Szpala et al.[11] investigated the value of dosimetric leaf gap (DLG) for leaf pairs in treatment planning. It was demonstrate that the DLG depends on the size of mulileaf collimator slit. Such effect is probably caused by scatter variation from the opposite leaf with different slit widths. Furthermore, they proposed a method by expanding the DLG parameter from a single value to a function of distance from the nominal leaf position and displacement of the opposite leaf. However, efforts should made to improve dose calculation accuracy in VMAT treatment planning, not merely by adjusting single parameter, such as leaf transmission or DLG. Better modeling rounded leaf end effect is of significance for future works.

Conclusions

In summary, the algorithms we proposed for leaf position calculation and radiation field offset correction are effective for leaf end with large radius. Results of Monte Carlo simulation show that source size influences penumbra width, while for radiation field offset, the source size impact is negligible. Penumbra width performance could be improved by carefully choosing the radius of circular arc leaf end. In this study, the leaf positions, including mechanical leaf position, nominal leaf position, geometric leaf position and physical

leaf position are classified and rigorously deduced. Correction of leaf position offset, radiation field offset and physical-nominal offset are realized based on analytical method. In general, results of analytical method agree well with numerical simulation. However, a slight gap exists between analytical radiation field offset and numerical radiation field offset, which implies that modification should be introduced when applying the empirical rule of half-value layer. For better treatment planning, the rounded leaf end effect on penumbra characteristics should be taken with care in order to achieve dose delivery accuracy.

Acknowledgments

References

1. Jeraj M, Robar V. Multileaf collimator in radiotherapy. *Radiol Oncol* 2004; **3:** 235-40.

2. Clark BG, Teke T, Otto K. Penumbra evaluation of the varian millennium and BrainLAB M3 multileaf collimators. *Int J Radiat Oncol Biol Phys* 2006; **66(4 Suppl):** S71-5.

3. Pasquino M, Borca VC, Catuzzo P, Ozzello F, Tofani S. Transmission, penumbra and leaf positional accuracy in commissioning and quality assurance program of a multileaf collimator for step-and-shoot IMRT treatments. *Tumori* 2006; **92:** 511-16.

4. Mohan R, Jayesh K, Joshi RC, Al-idrisi M, Narayanamurthy P, Majumdar SK. Dosimetric evaluation of 120-leaf multileaf collimator in a Varian linear accelerator with 6-MV and 18-MV photon beams. *J Med Phys* 2008; **33:** 114-8.

5. Asnaashari K, Chow JCL, Heydarian M. Dosimetric comparison between two MLC systems commonly used for stereotactic radiosurgery and radiotherapy: A Monte Carlo and experimental study. *Phys Medica* 2013; **29:** 350-6.

6. Topolnjak R, van der Heide UA. An analytical approach for optimizing the leaf design of a multi-leaf collimator in a linear accelerator. *Phys Med Biol* 2008; **53:** 3007-21.

7. Sun J, Zhu Y. Study of dosimetric penumbra due to multileaf collimation on a medical linear accelerator. *Int J Radiat Oncol Biol Phys* 1995; **32:** 1409-17.

8. Bailey D, Kumaraswamy L, Podgorsak M. A fully electronic intensity-modulated radiation therapy quality assurance (IMRT QA) process implemented in a network comprised of independent treatment planning, record and verify, and delivery systems. *Radiol Oncol* 2010; **44:** 124-30.

9. Sumida I, Yamaguchi H, Kizaki H, Koizumi M, Ogata T, Takahashi Y, et al. Quality assurance of MLC leaf position accuracy and relative dose effect at the MLC abutment region using an electronic portal imaging device. *J Radiat Res* 2012; **53:** 798-806.

10. Graves MN, Thompson AV, Martel MK, McShan DL, Fraass BA. Calibration and quality assurance for rounded leaf-end MLC systems. *Med Phys* 2001; **28:** 2227-33.

11. Szpala S, Cao F, Kohli K. On using the dosimetric leaf gap to model the rounded leaf ends in VMAT/RapidArc plans. *J Appl Clin Med Phys* 2014; **15:** 4484.

12. Boyer AL, Li S. Geometric analysis of light-field position of a multileaf collimator with curved ends. *Med Phys* 1997; **24:** 757-62.

13. Wu JM, Lee TF, Yeh SA, Hsiao KY, Chen HH, Chao PJ, et al. A Light-Field-Based Method to Adjust On-Axis Rounded Leaf End MLC Position to Predict Off-Axis MLC Penumbra Region Dosimetric Performance in a Radiation Therapy Planning System. *Biomed Res Int* 2013; **2013:** 461801.

14. Vial P, Oliver L, Greer PB, Baldock C. An experimental investigation into the radiation field offset of a dynamic multileaf collimator. *Phys Med Biol* 2006; **51:** 5517-38.

15. Rogers DWO, Walters B, Kawrakow I. *BEAMnrc Users manual NRCC report PIRS-0509(A)revL*. Ottawa: National Research Council of Canada; 2013.

16. Rucci A, Carletti C, Cravero W, Strbac B. Use of IAEA's phase-space files for the implementation of a clinical accelerator virtual source model. *Phys Medica* 2014; **30:** 242-8.

17. Sterpin E, Chen Y, Lu W, Mackie TR, Olivera GH, Vynckier S. On the relationships between electron spot size, focal spot size, and virtual source position in Monte Carlo simulations. *Med Phys* 2011; **38:** 1579-86.

research article

A comparison of the quality assurance of four dosimetric tools for intensity modulated radiation therapy

Jaeman Son[1,2], Taesung Baek[1,4], Boram Lee[1,5], Dongho Shin[2], Sung Yong Park[3], Jeonghoon Park[2], Young Kyung Lim[2], Se Byeong Lee[2], Jooyoung Kim[2], Myonggeun Yoon[1]

[1] Department of Bio-Convergence Engineering, Korea University, Seoul, Korea

[2] Proton Therapy Center, National Cancer Center, Goyang, Korea

[3] McLaren Proton Therapy Center, Karmanos Cancer Institute, Flint, MI, USA

[4] Department of Radiation Oncology, Ilsan Hospital, Goyang, Korea

[5] Department of Radiation Oncology, Sun Hospital, Daejeon, Korea

Background. This study was designed to compare the quality assurance (QA) results of four dosimetric tools used for intensity modulated radiation therapy (IMRT) and to suggest universal criteria for the passing rate in QA, irrespective of the dosimetric tool used.

Materials and methods. Thirty fields of IMRT plans from five patients were selected, followed by irradiation onto radiochromic film, a diode array (Mapcheck), an ion chamber array (MatriXX) and an electronic portal imaging device (EPID) for patient-specific QA. The measured doses from the four dosimetric tools were compared with the dose calculated by the treatment planning system. The passing rates of the four dosimetric tools were calculated using the gamma index method, using as criteria a dose difference of 3% and a distance-to-agreement of 3 mm.

Results. The QA results based on Mapcheck, MatriXX and EPID showed good agreement, with average passing rates of 99.61%, 99.04% and 99.29%, respectively. However, the average passing rate based on film measurement was significantly lower, 95.88%. The average uncertainty (1 standard deviation) of passing rates for 6 intensity modulated fields was around 0.31 for film measurement, larger than those of the other three dosimetric tools.

Conclusions. QA results and consistencies depend on the choice of dosimetric tool. Universal passing rates should depend on the normalization or inter-comparisons of dosimetric tools if more than one dosimetric tool is used for patient specific QA.

Key words: intensity modulated radiation therapy; quality assurance; dosimetric tool; gamma index

Introduction

Radiation therapy is one of the most widely used cancer treatment methods. Among the methods used are 3D conformal radiation therapy (3D CRT), intensity modulated radiotherapy (IMRT), and particle beam therapy. IMRT uses a multi-leaf collimator (MLC) to vary the intensity of the beam delivered to the tumour.[1] Since IMRT requires fine control of the MLC during irradiation, cau-tion must be exercised in delivering radiation.[2-4] Treatment quality assurance (QA) is therefore necessary to determine the difference between calculated and actual dose distributions.[5,6]

QA for conventional IMRT treatment is widely performed using an ion chamber and film, with the ion chamber used to measure absolute dose at each location and film used for 2D relative dose comparisons.[7-9] Although film has the great advantage of high resolution, it has several disadvantages,

including the need to change film for every beam test and its dependence on beam energy, processing conditions, and external light. Recently developed radiation therapy methods have greater accuracy, with new dosimetry tools developed to overcome the disadvantages of film measurements. Among these tools are a diode detector-based 2D diode array dosimeter[10] (MapCheck2; Sun Nuclear Corporation, Melbourne, Florida), a 2D ion chamber array dosimeter[11] (I'mRT MatriXX; IBA) and portal dosimetry using an electronic portal imaging device[12] (EPID). The gamma evaluation method is generally used to verify the actual dose distribution that will be delivered to the patient during IMRT.[13] This method is based on a comparison of the calculated 2D dose map from treatment planning system (TPS) with the measured 2D dose map from each dosimetric tool. Although there is no general consensus, QA results are considered acceptable when the passing rate is greater than 95% using as criteria a tolerance of dose difference (DD) of 3% and a tolerance for distance to agreement (DTA) of 3 mm.[14]

Table 1 shows an example of QA results using film, Mapcheck, MatriXX and portal dosimetry based on gamma evaluation for 10 randomly selected treatment plans undergoing IMRT at four different institutions in Korea. Each of 4 hospitals sorted out 10 IMRT QA results using one of four dosimetric tools and analysed the passing rates depending on the QA tools. Therefore, this data shows the general passing rates of IMRT QA depending on the dosimetric tools. The mean ± standard deviation (SD) passing rates ($\gamma\% \leq 1$) for film, Mapcheck, MatriXX and EPID were 96.80 ± 0.94%, 98.90 ± 0.55%, 99.40 ± 0.48% and 97.10 ± 1.12%, respectively. Thus, passing rates are dependent on the dosimetric tool used, with mean passing rates being lowest for film and highest for MatriXX. This example suggests that passing rates of 95% for film measurement and portal dosimetry are not equivalent.[15,16] Many institutions, however, have not set an acceptance level for each tool but have universally set 95% as the acceptance level for all tools. The current emphasis on treatment QA for patients suggests the need for specific guidelines for each specific dosimetric tool. Although guidelines have been proposed[17], they were only for acceptable doses and allowable errors for each body part, and did not include passing rates for different dosimetric tools.

In this study, four different dosimetric tools were used for quality assurance method of IMRT plans from five patients and their patient spe-

TABLE 1. Average passing rates for film, diode array (Mapcheck), ion chamber array (MatriXX) and electronic portal imaging device (EPID) for intensity modulated radiation therapy (IMRT) quality assurance (QA) in four different institutions in Korea

	Film	Mapcheck	MatriXX	EPID
Mean	96.80	98.90	99.40	97.10
Standard deviation	0.94	0.55	0.48	1.12

cific QA results were compared. The correlations among these dosimetric tools were used to determine reasonable tolerance levels for each.

Materials and methods

The IMRT plans for five patients undergoing radiation therapy, modelled using the Eclipse treatment planning system Ver. 8.9. (Varian Medical Systems, Salt Lake City, UT, USA) with anisotropic analytical algorithm (AAA), were used for this study.[18] Figure 1 shows the experimental setup of IMRT QA with film, Mapcheck, MatriXX and EPID. The gamma index method was used to compare the TPS dose with measured doses, using dose difference (DD) criteria of 3% and distance-to-agreement criteria (DTA) of 3 mm. The reference dose map was the calculated dose maps from TPS in our analysis. The gamma index value was calculated at all 2-dimensional points, with the percentage of points with a gamma index value ≤ 1 and meeting the DD and DTA criteria being the passing rate. The passing rates of the four dosimetric tools were compared.

Film QA

The traditional method of QA for IMRT is 2-dimensional testing using film. We used commercial Gafchromic EBT2 film (International Specialty Products, New Jersey, USA)[19] and an Epson Expression 10000-XL flatbed film scanner (Epson, California, USA), with a resolution of 0.38 x 0.38 mm². Film was calibrated using an ion chamber, with more calibration points used for low dose areas to enhance accuracy. Doses were measured at a source to axis distance (SAD) of 100 cm, with film located at a depth of 10 cm of solid slab phantom and a gantry angle of 0°. Radiological Imaging Technology IMRT software (Ver. 5.2, Colorado Springs, CO, USA) was used to verify dose delivery after the beam measurement.

MapCheck QA

MapCheck2 (Sun Nuclear; Melbourne, FL, USA) is a relatively new dosimetric tool, consisting of diode detectors in a 2D array and a field size of 32 cm x 26 cm. The matrix is composed of 1,527 diodes, spaced 7.07 mm apart, with each having an active detector area of 0.64 mm^2 and the entire matrix having active detector size of 24.4 x 24.4 cm^2.[20] Similar to film QA, dose was measured at 8 cm depth of Mapcheck dedicated phantom, Mapphan (Sun Nuclear, Melbourne, FL, USA) at a gantry angle of 0°. Mapcheck dedicated software (MapCHECK2, Ver 5.01.05, Sun Nuclear, Melbourne, FL, USA), was used to verify the dose delivery after the beam measurement.

MatriXX QA

The MatriXX (IBA Dosimetry GmbH, Schwarzenbruck, Germany) is similar to Mapcheck but has ionization chambers rather than diode detectors in a 2D array.[21,22] Although MatriXX has fewer ion chambers than Mapcheck has diode detectors, the ion chambers yield more stable data than the diodes.[23] The 1,024 ionization chambers of MatriXX are aligned in a parallel pattern in a 32 x 32 grid, with the diameter, height, volume and detector spacing of each ion chamber being 4.5 mm, 7.62 mm, 0.08 cc and 7.62 mm, respectively. The gantry angle was 0° and the beam was investigated using a 5 cm solid water phantom on top of the MatriXX. OmniPro-I'mRT (Ver 1.7.0021, IBA Dosimetry, Germany), a MatriXX-dedicated software program, was used to verify dose delivery after beam irradiation.

EPID QA (portal dosimetry)

We used an aSi-based EPID (aS500, Varian Medical Systems, Palo Alto, CA) attached to a Varian Clinac iX Linear accelerator (Varian Medical Systems, Palo Alto, CA, USA).[12] This EPID has a resolution of 0.784 x 0.784 mm^2 with an array of 512 x 384 pixels, thus having higher resolution than Mapcheck or MatriXX, and a field size of 40 x 30 cm^2. The source to axis distance (SAD) was set at 100 cm and the beam was investigated at a gantry angle of 0°. Measurement with EPID was measured with no phantom and EPID dedicated software (Eclipse, Ver 8.9, Varian Medical System, USA) was used to verify dose delivery after the beam measurement.
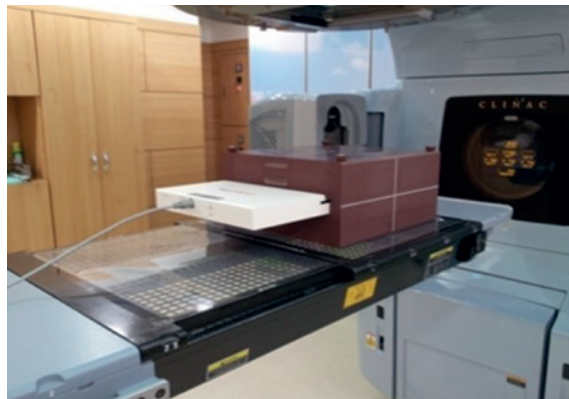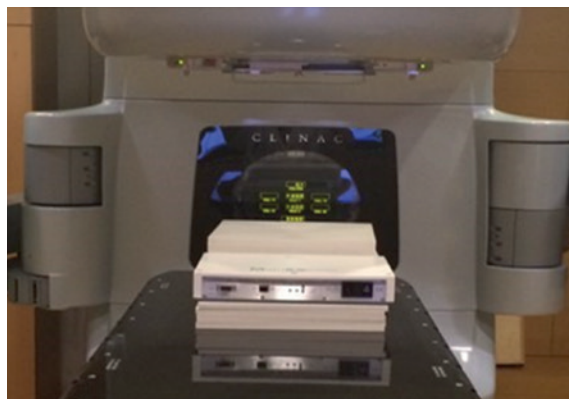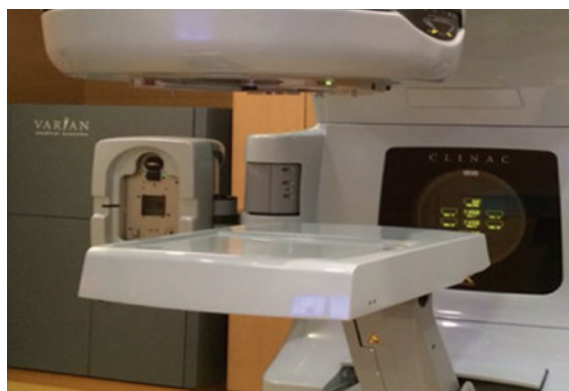
FIGURE 1. Pictures of the experimental setup for IMRT QA using various dosimetric tools. **(A)** Film, **(B)** Mapcheck, **(C)** ion chamber array (MatriXX), **(D)** Portal dosimetry.

TABLE 2. Mean passing rates based on the gamma index method for the treatment fields of each patient using film, diode array (Mapcheck), ion chamber array (MatriXX), and electronic portal imaging device (EPID)

	Patient 1	Patient 2	Patient 3	Patient 4	Patient 5	Mean
Film	97.42	95.42	95.83	94.80	95.92	95.88
Mapcheck	100.00	99.45	100.00	98.90	99.70	99.61
MatriXX	99.10	99.26	98.84	98.82	99.20	99.04
EPID	99.42	99.12	99.20	99.52	99.20	99.29

Results

Doses calculated using TPS were compared with doses measured by the four dosimetric tools based on gamma evaluation (3%/3mm, threshold 15%). Figure 2 shows examples of gamma evaluation results using film, Mapcheck, MatriXX and EPID for IMRT QA. Although Table 1 shows the general passing rates of IMRT QA depending on the dosimetric tools, the result can be dependent on the patient selected in each institution. To clarify the dependency of QA result on dosimetric tools, one should carry out IMRT QA of *same* patient using *different* dosimetric tools. Table 2 shows the mean passing rates, based on the gamma index method, for the treatment fields of each patient using film,

Mapcheck, MatriXX, and EPID. The values measured with the four dosimetry tools showed good agreement with the calculated values for all five patients. The mean ± standard deviation (SD) passing rates ($\gamma\% \leq 1$) for film, Mapcheck, MatriXX and EPID for 30 IMRT fields of five patients were 95.88 ± 0.87%, 99.61 ± 0.41%, 99.04 ± 0.18% and 99.29 ± 0.15%, respectively. Although all four dosimetry tools met the acceptable passing rate of 95%, these tools showed some differences in measuring the same beam, with the gamma index being much lower for film than for the three other tools.

To show fluctuations for each dosimetric tool, we assessed the passing rates of three consecutive measurement results using film, Mapcheck, MatriXX and EPID based on gamma index values for 6 fields of patient 1 from Table 2. This means that QA was carried out 3 times, repetitively. As shown in Table 3, the gamma index results were similar, regardless of the number of measurements, for Mapcheck, MatriXX and EPID. Film, however, showed higher a standard deviation (i.e., fluctuation) for three consecutive measurements than for the other dosimetirc tools. For example, the fluctuation of film measurement for field 1 was 0.59 which is much higher than 0.00, 0.00, 0.05 for Mapcheck, MatriXX and EPID, respectively.
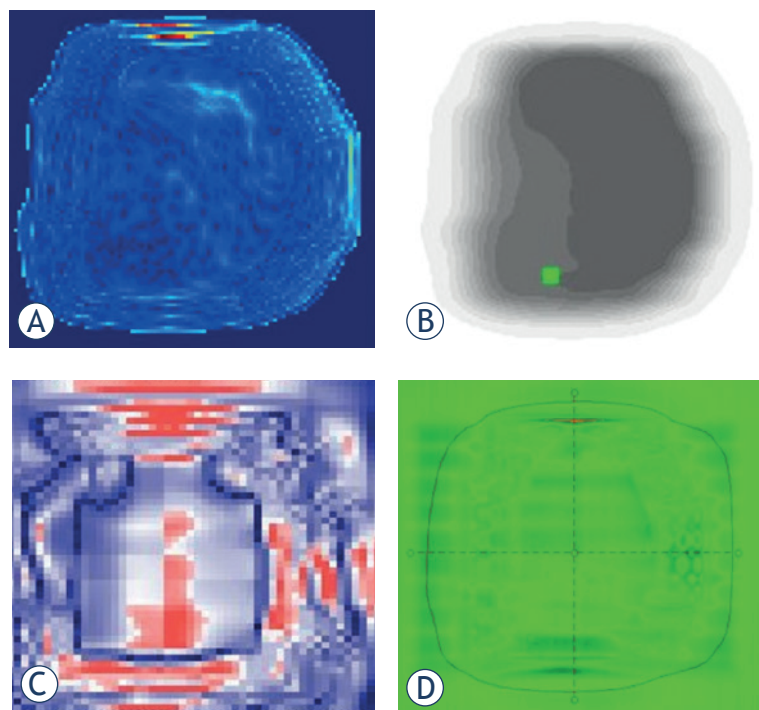
Discussion

This comparison of gamma indices for EBT film, Mapcheck, MatriXX, and EPID showed differences in dose distribution when using these various dosimetric tools to carry out the quality assurance for the same patients undergoing IMRT. Even with using the same dosimetry tool, the results differed slightly for each measurement of the same field.

The passing rates based on film measurement were much lower than those using the three other dosimetric tools (Table 2). To check the uncertainty of film for the exact same beam, QA was carried out *only one time* but *3 films* were inserted in the

FIGURE 2. 2D images of the passing rate based on gamma evaluation for various dosimetric tools. **(A)** Film, **(B)** diode array (Mapcheck), **(C)** ion chamber array (MatriXX), **(D)** Portal dosimetry.

TABLE 3. Passing rates of three consecutive measurement results using film, diode array (Mapcheck), ion chamber array (MatriXX) and electronic portal imaging device (EPID) based on gamma index values for 6 fields of patient 1. The data shown for patient 1 in Table 2 is the average of first measurement set of data in Table 3

	Measurement	Field 1	Field 2	Field 3	Field 4	Field 5	Field 6
Film	1st	98.95	98.97	91.20	97.86	98.88	98.66
	2nd	97.90	98.93	91.18	98.74	98.28	98.71
	3rd	97.58	98.42	91.15	99.24	98.65	98.26
	Mean (SD)	98.14 (0.59)	98.77 (0.25)	91.18 (0.02)	98.61 (0.57)	98.60 (0.25)	98.54 (0.20)
Mapcheck	1st	100.00	100.00	100.00	100.00	100.00	100.00
	2nd	100.00	100.00	100.00	100.00	100.00	100.00
	3rd	100.00	100.00	100.00	100.00	100.00	100.00
	Mean (SD)	100.00 (0.00)	100.00 (0.00)	100.00 (0.00)	100.00 (0.00)	100.00 (0.00)	100.00 (0.00)
MatriXX	1st	99.29	98.41	99.57	99.30	99.10	98.97
	2nd	99.30	99.25	99.57	99.28	99.06	99.01
	3rd	99.29	99.24	99.58	99.29	99.00	98.99
	Mean (SD)	99.29 (0.00)	98.97 (0.39)	99.57 (0.00)	99.29 (0.01)	99.05 (0.04)	98.99 (0.02)
EPID	1st	99.80	99.40	99.60	98.90	98.80	100.00
	2nd	99.90	99.60	99.70	99.20	99.10	100.00
	3rd	99.80	99.60	99.45	99.05	98.90	99.90
	Mean (SD)	99.83 (0.05)	99.53 (0.09)	99.58 (0.10)	99.05 (0.12)	98.93 (0.12)	99.97 (0.05)

SD = standard deviation

phantom. To irradiate the exactly same beam, one should remove the unstable low dose part of the beam caused by scattering, leakage, etc. To do that, we did carry out QA *not with individual field* but *with composite fields*, which may remove the low dose part in the analysis. Assessment of the passing rates based on gamma evaluation showed uncertainties ranging from 0.11 to 0.39 (Table 4). Despite these uncertainties, however, the results were reasonably stable, suggesting that a single measurement would be sufficient for QA.

In general, uncertainties tend to be higher for low dose film measurements.[20] We therefore investigated a beam with a universally-tripled-beam intensity (i.e., tripled monitor unit) on each field to confirm the decrease of gamma index with low dose. Table 5 shows the passing rate using film measurements for 3-fold increased beam intensity for 6 fields of patient 1, 2, 4. Compared with the results shown in Table 3, the mean passing rate increased, indicating that, in general, high and stable gamma index results with film can be obtained at higher beam intensity (i.e., increased monitor units), comparable to the results from the three other dosimetric tools. Table 5 also shows that standard deviation is decreased with increased beam intensity. Therefore, QA using film should be

TABLE 4. Passing rates based on gamma evaluation using 3 films in the same location for intensity modulated radiation therapy (IMRT) quality assurance (QA) of each patient

	Patient 1	Patient 2	Patient 3	Patient 4	Patient 5
Film	98.36	95.29	98.51	98.08	99.41
	97.47	95.47	98.55	98.19	99.14
	97.63	95.65	98.87	98.36	99.27
Mean	97.82	95.47	98.64	98.21	99.27
SD	0.39	0.15	0.16	0.12	0.11

performed at a sufficiently high intensity beam to reduce the uncertainties from low doses. Although raising the threshold level will lead to clearing of low dose, it may not appropriate since it can cause only the high dose area to be set as region of interest. If one wants to use normal treatment MU in QA, careful calibration of film should be used to decrease the standard deviation of film for low dose area.

While the QA results based on Mapcheck, MatriXX and EPID showed good agreement among themselves by showing average passing rates of 99.61%, 99.04% and 99.29%, respectively, the aver-

TABLE 5. Passing rates of film measurements based on gamma evaluation for 3-fold increased beam intensity (i.e., monitor unit) for 6 fields of patient 1

	Field1	Field2	Field3	Field4	Field5	Field6	Mean	SD
Patient1	99.23	99.45	99.20	99.09	99.04	99.21	99.20	0.13
Patient2	98.63	98.04	98.03	97.91	96.80	97.15	97.76	0.61
Patient4	98.77	98.67	99.23	99.40	99.93	98.30	99.05	0.53

age passing rate based on film measurement was significantly lower, 95.88%. The QA result seems to depend on the unique characteristics of each dosimetric tool such as depth of measurement, its resolution, etc. These experimental results suggest that the criteria of the passing rate based on film measurement should be decreased about 3% compared to the criteria for other dosimetric tools. If one wants to use universal criteria for the passing rate for all four dosimetric tools, one should increase the beam intensity about three times if the film is used as a measurement tool. Further study is needed to suggest the more reliable universal passing rate with large number of case studies.

Conclusions

We have used film, Mapcheck, MatriXX and EPID to evaluate their dosimetric properties for IMRT QA. While the measured dose maps with Mapcheck, MatriXX and EPID agreed well with the calculated dose maps of TPS, the passing rate was noticeably lower for film measurements. It seems that different passing rates in QA results may partially stem from the different resolution (or measured dose matrix) of four dosimetric tools. Use of film for IMRT QA should be implemented using beams of sufficiently high intensity to be compatible with the results of Mapcheck, MatriXX, and EPID. Our results suggest that setting an acceptance level based on the correlation of various dosimetric tools is a more correct method than simply setting the same acceptance level for all of these tools.

Acknowledgment

References

1. Lee N, Terezakis S. Intensity-modulated radiation therapy. *J Surg Oncol* 2008; **97:** 691-6.

2. Langer M, Brown R, Urie M, Leong J, Stracher M, Shapiro J. Large scale optimization of beam weights under dose-volume restrictions. *Int J Radiat Oncol Biol Phys* 1990; **18:** 887-93.

3. Morrill SM, Lane RG, Wong JA, Rosen II. Dose-volume considerations with linear programming optimization. *Med Phys* 1991; **18:** 1201-10.

4. Langer M, Leong J. Optimization of beam weights under dose-volume restrictions. *Int J Radiat Oncol Biol Phys* 1987; **13:** 1255-60.

5. Van Esch A, Bohsung J, Sorvari P, Tenhunen M, Paiusco M, Iori M, et al. Acceptance tests and quality control (QC) procedures for the clinical implementation of intensity modulated radiotherapy (IMRT) using inverse planning and the sliding window technique: experience from five radiotherapy departments. *Radiother Oncol* 2002; **65:** 53-70.

6. Palta JR, Liu C, Li JG. Quality assurance of intensity-modulated radiation therapy. *Int J Radiat Oncol, Biol, Phys* 2008; **71:** S108-12.

7. Tsai Ph D J-S, Wazer MD DE, Ling MD MN, Wu MD JK, Fagundes MD M, DiPetrillo MD T, et al. Dosimetric verification of the dynamic intensity-modulated radiation therapy of 92 patients. *Int J Radiat Oncol Biol Phys* 1998; **40:** 1213-30.

8. Fraass B, Doppke K, Hunt M, Kutcher G, Starkschall G, Stern R, et al. American Association of Physicists in Medicine Radiation Therapy Committee Task Group 53: quality assurance for clinical radiotherapy treatment planning. *Med Phys* 1998; **25:** 1773-829.

9. Ezzell GA, Galvin JM, Low D, Palta JR, Rosen I, Sharpe MB, et al. Guidance document on delivery, treatment planning, and clinical implementation of IMRT: Report of the IMRT subcommittee of the AAPM radiation therapy committee. *Med Phys* 2003; **30:** 2089.

10. Jursinic PA, Nelms BE. A 2-D diode array and analysis software for verification of intensity modulated radiation therapy delivery. *Med Phys* 2003; **30:** 870-9.

11. Poppe B, Blechschmidt A, Djouguela A, Kollhoff R, Rubach A, Willborn KC, et al. Two-dimensional ionization chamber arrays for IMRT plan verification. *Med Phys* 2006; **33:** 1005-15.

12. Van Esch A, Depuydt T, Huyskens DP. The use of an aSi-based EPID for routine absolute dosimetric pre-treatment verification of dynamic IMRT fields. *Radiother Oncol* 2004; **71:** 223-34.

13. Low DA, Harms WB, Mutic S, Purdy JA. A technique for the quantitative evaluation of dose distributions. *Med Phys* 1998; **25:** 656-61.

14. Howell RM, Smith I, Jarrio CS. Establishing action levels for EPID-based QA for IMRT. *J Appl Clin Med Phys* 2008; **9:** 16-25.

15. Ezzell GA, Burmeister JW, Dogan N, LoSasso TJ, Mechalakos JG, Mihailidis D, et al. IMRT commissioning: Multiple institution planning and dosimetry comparisons, a report from AAPM Task Group 119. *Med Phys* 2009; **36:** 5359.

16. Basran PS, Woo MK. An analysis of tolerance levels in IMRT quality assurance procedures. *Med Phys* 2008; **35:** 2300-7.

17. Nelms BE, Simon JA. A survey on IMRT QA analysis. *J Appl Clin Med Phys* 2007; **8:** 2448.

18. Bragg CM, Wingate K, Conway J. Clinical implications of the anisotropic analytical algorithm for IMRT treatment planning and verification. *Radiother Oncol* 2008; **86:** 276-84.

19. Zeidan OA, Stephenson SA, Meeks SL, Wagner TH, Willoughby TR, Kupelian PA, et al. Characterization and use of EBT radiochromic film for IMRT dose verification. *Med Phys* 2006; **33:** 4064-72.

20. Letourneau D, Gulam M, Yan D, Oldham M, Wong JW. Evaluation of a 2D diode array for IMRT quality assurance. *Radiother Oncol* 2004; **70:** 199-206.

21. Saminathan S, Manickam R, Chandraraj V, Supe SS. Dosimetric study of 2D ion chamber array matrix for the modern radiotherapy treatment verification. *J Appl Clin Med Phys* 2010; **11:** 3076.

22. Herzen J, Todorovic M, Cremers F, Platz V, Albers D, Bartels A, et al. Dosimetric evaluation of a 2D pixel ionization chamber for implementation in clinical routine. *Phys Med Biol* 2007; **52:** 1197-208.

23. Li JG, Yan G, Liu C. Comparison of two commercial detector arrays for IMRT quality assurance. *J Appl Clin Med Phys* 2009; **10:** 2942.

Erratum

The corresponding author should be Santanu Chakraborty instead of Jillian Mclean.

The corresponding author should be:

Dr. Santanu Chakraborty, Department of Radiology, University of Ottawa, Department of Medical Imaging, The Ottawa Hospital, 1053 Carling Avenue, Ottawa, ON K1Y 4E9, Canada. Phone: (613) 737 8571; Fax: (613) 761 4476; E-mail: schakraborty@toh.on.ca

Z obsevanjem pospešena diferenciacija matičnih celic

Mieloch AA, Suchorska WM

Izhodišča. Učinkovita diferenciacija matičnih celic je zelo pomembna v regenerativni medicini. V mnogih raziskavah so preučevali usmerjeno diferenciacijo matičnih celic in izdelali učinkovito zaporedje postopkov. Kljub temu je potrebno, da te postopke izboljšujemo. V članku razlagamo, kako z obsevanjem pospešujemo diferenciacijo matičnih celic in kakšni molekularni procesi pri tem potekajo. Opisujemo z ionizirajočim sevanjem inducirane odgovore različnih vrst matičnih celic. Opredeljujemo vlogo proteina p53 pri diferenciaciji embrionalnih in somatskih matičnih celicah. Na koncu postavimo hipotezo o vlogi mitohondrijev pri razvoju matičnih celic in pri odgovoru na ionizirajoče sevanje.

Zaključki. Kljub temu, da poznamo nevarnost poškodb in nevarnost genomske nestabilnosti zaradi ionizirajočega sevanja, pa lahko ionizirajoče sevanje ob primerni dozi postane učinkovito orodje za spodbujanje usmerjene diferenciacije nekaterih vrst matičnih celic.

Gama-enolaza. Dobro poznan tumorski označevalec, z manj poznano vlogo pri raku

Vižin T, Kos J

Izhodišča. Gama-enolaza, poznana tudi kot nevronska specifična enolaza (NSE), je encim glikolitične poti, ki se izraža predvsem v nevronih in celicah nevroendokrinega sistema. Kot tumorski označevalec jo uporabljamo ob diagnozi raka in napovedi izida bolezni pri bolnikih z rakom, mehanizmi preko katerih je vključena v napredovanje malignega procesa pa ostajajo nepojasnjeni. Gama-enolaza je kot citoplazemski encim vključena v povečano aerobno glikolizo, ki je glavni vir energije rakavih celic in podpira njihovo proliferacijo. Različne lokalizacije gama-enolaze v patofizioloških stanjih pa nakazujejo na dodatne funkcije.

Zaključki. Ugotovili so, da C-končni del molekule, ki ni povezan z glikolitično aktivnostjo, spodbuja preživetje nevronskih celic z uravnavanjem signalnih poti, ki so odvisne od receptorja nevronskega rastnega faktorja, kar vodi tudi v obsežno preoblikovanje aktinskega citoskeleta. Ta dodatna funkcija gama-enolaze je lahko pomembna tudi pri rakavih celicah bodisi za zaščito celic pred stresnimi pogoji in terapijo raka bodisi za spodbujanje migracije in invazije tumorskih celic. Gama-enolaza ima zato najverjetneje večfunkcijsko vlogo pri napredovanju raka, saj podpira povečane presnovne zahteve tumorskih celic, jih ščiti v stresnih pogojih ter spodbuja njihovo invazijo in migracijo.

Vpliv rekonstrukcijskega algoritma in vključitve informacije časa preleta na kakovost slik PET/CT

Suljič A, Tomše P, Jensterle L, Škrk D

Izhodišča. Namen raziskave je bil ugotoviti vpliv različnih rekonstrukcijskih algoritmov z in brez vključitve informacije časa preleta (TOF, *time of flight*) na kakovost slik pozitronske emisijske tomografije z računalniško tomografijo (PET/CT).

Materiali in metode. Meritve smo opravili s trilinijskim fantomom, ki je imel kapilare notranjega premera ~ 1 mm, in s standardnim fantomom Jaszczak. Zajete podatke smo rekonstruirali z analitičnim algoritmom filtrirane povratne projekcije (FBP), iterativnim algoritmom ukazane pričakovane maksimizacije (OSEM, *Ordered Subsets Expectation Maximization*) (4 iteracije, 24 podmnožic), iterativnim algoritmom *True-X*, ki vključuje specifično funkcijo razširitve točke (PSF, *point spread function*), in izhodiščnim iterativnim algoritmom OSEM (2 iteraciji, 8 podmnožic).

Rezultati. Meritve prostorske ločljivosti izražene v polni širini pri polovičnem maksimumu (FWHM, *full width at half maximum*) so dosegle vrednosti 5,2 mm pri FBP; 4,5 pri OSEM in 2,9 pri *True-X*; pri FBP+TOF je bila vrednost prostorske ločljivosti 5,1 mm, pri OSEM+TOF 4,5 mm in pri *True-X*+TOF 2,9 mm. Ocena parametrov rekonstruiranih slik so pokazale, da informacija TOF predvsem izboljša hladni kontrast, medtem ko je vpliv izboljšanja pri vročem kontrastu manjši. Največje izboljšanje se pokaže pri variabilnosti ozadja (zniževanju šuma).

Zaključki. Rezultati raziskave kažejo, da vključitev informacije TOF v rekonstrukcijski algoritem ne izboljša prostorske ločljivosti. Informacija TOF ima največji vpliv pri zniževanju variabilnosti ozadja oz. nivoja šuma na sliki. Primerjava med tradicionalnimi in modernimi rekonstrukcijskimi metodami je pokazala, da analitična FBP prikaže primerljive ali celo boljše rezultate pri meritvah hladnega kontrasta in relativne napake števnosti (*relative count error*). Iterativne metode so prikazale najvišje ravni kontrastne ločljivosti, ko smo informaciji TOF in PSF upoštevali hkrati.

Natančno načrtovanje zdravljenja omogoča varno ablacijo jetrnih tumorjev v bližini večjih žil s perkutano ireverzibilno elektroporacijo

Kos B, Voigt P, Miklavčič D, Moche M

Izhodišča. Ireverzibilna elektroporacija je metoda, ki jo lahko uporabljamo za ablacijo tkiva na osnovi elektroporacije. Kadar celice izpostavimo dovolj močnemu električnemu polju, poškodujemo celično membrano in celice odmrejo po mehanizmu apoptotične ali nekrotične celične smrti. Čeprav med terapijo z ireverzibilno elektroporacijo prihaja do segrevanja tkiva, metodo uvrščamo med netermične metode ablacije tkiva in jo največ uporabljamo na mestih, kjer so termične metode kontraindicirane.

Materiali in metode. Proizvajalec trenutno edinega generatorja električnih pulzov za ireverzibilno elektroporacijo priporoča razmerje napetost-razdalja med elektrodami 1500 do 1700 V/cm za zdravljenje tumorjev v jetrih. Vendar pa lahko bližina žil vpliva na porazdelitev električnega polja in posledično na izid terapije. Predstavljamo metodo za načrtovanje zdravljenja ireverzibilne elektroporacije, ki upošteva vpliv žil na električno polje in ilustriramo metodo na primeru 48 letne bolnice z metastazo v neposredni bližini zadnje preostale hepatične vene po desni hemihepatektomiji.

Rezultati. Rezultati numerične metode za načrtovanje zdravljenja kažejo, da je bila z električnimi pulzi ustvarjena 19,9 cm^3 velika lezija in da je bila celotna tumorska masa pokrita z električnim poljem vsaj 900 V/cm. Volumen lezije v modelu se dobro ujema z volumnom lezije vidne na računalniškotomografskih slikah s kontrastom zajetih neposredno po terapiji z ireverzibilno elektroporacijo. V bližini elektrod prihaja do pomembnega dviga temperature, vendar ostane hepatična vena pretočna tudi po terapiji; po šestih mesecih sledenja ni dokazov o ponovitvi bolezni.

Zaključki. Načrtovanje zdravljenja z natančnimi računalniškimi modeli prepoznavamo kot pomembno za uspešno zdravljenje z ireverzibilno elektroporacijo. Pomemben rezultat raziskave je, da v okolici elektrod prihaja do bistvenega segrevanja. Zato naj se klinični uporabniki izogibajo vstavljanju elektrod manj kot 4 mm stran od rizičnih struktur, kadar sledijo navodilom proizvajalca.

Slikovna diagnostika histiocitoze Langerhansovih celic pri otrocih. Analiza referenčnega centra

Porto L, Schöning S, Hattingen E, Sörensen J, Jurcoane A, Lehrnbecher T

Izhodišča. Namen raziskave je bil (1) opisati histiocitozo Langerhansovih celic pri otrocih v centralnem živčnem sistemu na osnovi minimalnega števila opravljenih sekvenc MRI, zbranih v referenčnem centru ter (2) na osnovi izvidov MRI oceniti medsebojno usklajenost ocenjevalcev.

Bolniki in metode. Retrospektivno smo analizirali posnetke MRI otrok s histiocitozo Langerhansovih celic, ki so izpolnjevali kriterije minimalnega števila opravljenih sekvenc MRI. Spremembe centralnega živčnega sistema sta ločeno opisala dva izkušena nevroradiologa, na podlagi česar smo presodili medsebojno usklajenost ocenjevalcev.

Rezultati. Od 94 opravljenih slikanj MRI jih je le 31 izpolnjevalo kriterije minimalnega števila opravljenih sekvenc MRI za vključitev v raziskavo. Ti kriteriji so bili: T2 poudarjeno slikanje, metoda MR za izločanje signalnih tekočin (angl. FLAIR), T1 poudarjeno slikanje pred/po kontrastu v vsaj dveh različnih ravninah ter tanke po-kontrastne T1 poudarjene rezine v sagitalni ravnini skozi sello. Najpogosteje opažene spremembe so bile spremembe kostnega mozga, nato solidno povečanje češarike, zadebeljen in obarvan infundibulum ter spremenjen signal dentatnega jedra. Medsebojna usklajenost ocenjevalcev večine sprememb centralnega živčnega sistema je bila razmeroma visoka (κ > 0,61). Uporabo minimalnih kriterijev MRI pogosto ni omogočila ocene posteriorne hipofize.

Zaključki. Raznolikost radioloških protokolov v različnih institucijah otežuje diagnostiko sprememb v centralnem živčnem sistemu pri otrocih s histiocitozo Langerhansovih celic. Medsebojna usklajenost med nevroradiologi je bila razmeroma visoka, kljub temu pa na osnovi minimalno izpolnjenih kriterijev MRI ni bilo mogoče izključiti vseh pojavnih oblik histiocitoze Langerhansovih celic. Ustrezen predpisani postopek MRI naj bi zato vključeval T1 poudarjeno predkontrastno slikanje v sagitalni ravnini po priporočilih za diagnosticiranje histiocitoze Langerhansovih celic. Potrebna je tudi centralna preverba slikovnih preiskav, ki bi omogočila lažjo primerjavo kliničnih raziskav.

Soodvisnost difuzijskega magnetnoresonančnega slikanja in indeksa Ki-67 pri nedrobnoceličnem raku pljuč

Karaman A, Durur-Subasi I, Alper F, Araz O, Subasi M, Demirci E, Albayrak M, Polat G, Akgun M, Karabulut N

Izhodišča. Primarni cilj raziskave je bil oceniti povezavo med minimalno difuzijsko konstanto (*angl. minimum apparent diffusion coefficient,* ADC_{min}) in indeksom celične proliferacije Ki-67 pri nedrobnoceličnem pljučnem raku. Zanimalo nas je tudi, ali se vrednost ADC_{min} razlikuje pri različnih histoloških tipih in različnih tkivnih vzorčenjih.

Metode. V raziskavo smo retrospektivno vključili bolnike, pri katerih smo predhodno naredili difuzijsko poudarjeno magnetno resonančno slikanje (*angl. diffusion weighted magnetic resonance imaging,* DW-MRI). Ocenili smo soodvisnost med ADC_{min} in indeksom Ki-67.

Rezultati. Analizirali smo 93 bolnikov s povprečno starostjo 65 ± 11 let. Pri 47 smo patohistološko dokazali žlezni in pri 46 skvamoznocelični rak pljuč. Pri vseh smo naredili preiskavo DW-MRI. Ugotovili smo izrazito negativno soodvisnost med vrednostmi ADC_{min} in proliferativnim indeksom Ki-67 (r = -0,837; p < 0,001). Povprečna vrednost ADC_{min} je bila višja in povprečna vrednost indeksa Ki-67 nižja pri žleznem raku, če smo ga primerjali s skvamoznoceličnim (p < 0,0001). Nismo našli statistično značilne razlike pri različnih tkivnih vzorčenjih.

Zaključki. ADC_{min} je pokazal znatno negativno soodvisnost z indeksom Ki-67, zato bi lahko bil način za ocenjevanje agresivnosti tumorja in bi na neinvazivni način prispeval k lažji opredelitvi vrste tumorja.

Vpliv polimorfizmov citokinskih genov na razvoj želodčnega raka pri bolnikih z okužbo Helicobacter pylori

Štubljar D, Jeverica S, Jukić T, Skvarč M, Pintar T, Tepeš B, Kavalar R, Štabuc B, Ihan A

Izhodišča. Baktetrija *Helicobacter pylori* je glavni vzrok za nastanek želodčnega raka. Na napredovanje bolezni predvsem vplivajo vnetni odzivi gostitelja, pri katerih imajo ključno vlogo polimorfizmi citokinskih genov. Namen raziskave je bil v slovenski populaciji bolnikov preučiti polimorfizme vnetnih citokinov, ki so povezani z razvojem želodčnega raka.

Bolniki in metode. V klinično raziskavo smo vključili 318 bolnikov in kontrolnih primerov. Razdelili smo jih v tri skupine: (i) bolniki z rakom želodca (n = 58), (ii) bolniki s kroničnim gastritsom (n = 60) in (iii) zdrava kontrolna skupina (n = 200). *Helicobacter pylori* smo v prvih dveh skupinah bolnikov določili s serološkimi in histološkimi preiskavami ter dokazovanjem bakterije na kulturi. Genske polimorfizme štirih provnetnim citokinov (IL-1β, IL-1 ra, TNF-a in TLR-4) smo določili pri vseh osebah.

Rezultati. Ugotovili smo statistično pomembne razlike med moškimi in ženskami (p = 0,025). Razmerje obetov (RO) za tveganje za nastanek želodčnega raka pri ženskah je bilo 0,557 (95% interval zaupanja [CI]: 0,233—1,329) in kroničnega gastritisa 2,073 (95% CI: 1,005—4,277). *IL-1B*-511*T/T homozigotni alel za skupino raka je imel RO = 2,349 (95% CI: 0,583—9,462), heterozigoten *IL-1B*-511*T pa RO = 1,470 (95% CI: 0,583—3,709). Heterozigoti v *TNF-A*-308 genotipu za kronični gastritis so imeli RO = 1,402 (95% CI: 0,626—3,139). Med drugimi aleli je bilo razmerje obetov manjše kot 1.

Zaključki. Čeprav smo odkrili statistično pomambno razliko med moškimi in ženskami, pa v slovenski populaciji nismo uspeli dokazati povezave med želodčnim rakom in kroničnim gastritsom zaradi okužbe s *Helicobacter pylori* ter polimorfizmi citokinskih genov. Zaključili smo, da so drugi genski polimorfizmi - poleg okužbe s *Helicobacter pylori* - lahko odgovorni za razvoj atrofije črevesne sluznice v neoplastično transformacijo

Inflamatorni miofibroblastni tumor v glavi trebušne slinavke. Prikaz primera pri 6-mesečnem otroku in pregled literature

Tomažič A, Gvardijančič D, Maučec J, Homan M

Izhodišča. Inflamatorni miofibroblastni tumorji so pri otrocih redki. Najpogosteje se pojavijo v pljučih. Če se pojavijo v glavi trebušne slinavke, jih je diferencialno diagnostično potrebno ločiti od drugih vrst tumorjev in kroničnega pankreatitisa. Običajna metoda zdravljenja je kirurška resekcija, v zadnjem času so opisana tudi zdravljenja s steroidi in obsevanjem.

Prikaz primera. Šest mesecev starega dečka smo zdravili zaradi tumorja v glavi trebušne slinavke. V klinični sliki sta bila ob sprejemu izražena pruritus in ikterus. Ultrazvok in magnetnoresonančna preiskava sta odkrili tumor v glavi trebušne slinavke. Preoperativna biopsija ni jasno opredelila izvora tumorja. Dečku smo naredili duodenopankreatektomijo. Pooperativni potek je minil brez zapletov. Patohistološki pregled resektata je potrdil diagnozo inflamatornega miofibroblastnega tumorja. Na kontrolnih pregledih ni bilo znakov za ponovitev bolezni.

Zaključki. Pri pregledu literature smo zasledili 10 primerov inflamatornih miofibroblastnih tumorjev v trebušni slinavki pri otrocih, vendar še nikoli pri dojenčku. Kljub večji resekciji pooperativnih zapletov ni bilo. Zdravljenje bi bilo morda mogoče tudi s steroidi, vendar bi bil takšen pristop vprašljiv, posebej pri agresivnih oblikah tumorjev.

Neoadjuvantna kemoterapija pri 13 bolnikih z lokalno napredovalim slabo diferenciranim rakom ščitnice opredeljenim s torinskimi izhodišči. Izkušnje posamične bolnišnice

Besić N, Dremelj M, Schwartzbartl-Pevec A, Gazić B

Izhodišča. Uveljavljeno je prepričanje, da kemoterapija ni učinkovita pri zdravljenju raka ščitnice. Namen raziskave je bil ugotoviti, ali neoadjuvantna kemoterapija pred operacijo ščitnice vpliva na velikost primarnega tumorja pri bolnikih s slabo diferenciranim rakom ščitnice (SDRŠ) opredeljenim s torinskimi izhodišči.

Bolniki in metode. Skupno 13 bolnikov (8 žensk, 5 moških; srednja starost 61 let) s slabo diferenciranim rakom ščitnice opredeljenim s torinskimi izhodišči smo v obdobju od leta 1986 do 2005 zdravili z neoadjuvantno kemoterapijo. Premer tumorja je bil 4,5–18 cm (srednji 9 cm). Šest bolnikov je imelo zasevke v področnih bezgavkah, 9 bolnikov pa oddaljene zasevke. Osem bolnikov je imelo tumor pT4.

Rezultati. Bolniki so prejeli 29 (razpon 1–5) krogov kemoterapije. Premer tumorja se je zmanjšal pri vseh bolnikih, za več kot 30 % pa pri 5 bolnikih (38%). Dva od teh petih bolnikov smo obsevali z zunanjim žarkovnim snopom. Totalno tiroidektomijo smo naredili pri 10 bolnikih, lobektomijo pri treh in modificirano disekcijo vratnih bezgavk pri petih bolnikih. Histopatološki pregled je pokazal, da je bila v 5 primerih resekcija R0, v 8 primerih pa R1. Osmim bolnikom smo z zunanjim žarkovnim snopom pooperativno obsevali vrat in zgornji mediastinum. Petletno specifično preživetje bolnikov glede raka je bilo 66 %, 10-letno pa 20 %.

Zaključki. Po neadjuvantni kemoterapiji se je tumor zmanjšal za več kot 30% pri 38% bolnikih s slabo diferenciranim rakom ščitnice opredeljenim s torinskimi izhodišči.

Fibulin-3 kot tumorski označevalec odgovora na zdravljenje pri bolnikih z malignim mezoteliomom

Kovač V, Dodič-Fikfak M, Arnerić N, Dolžan V, Franko A

Izhodišča. Fibulin-3 je novi možni tumorski označevalec pri bolnikih z malignim mezoteliomom. V raziskavi smo želeli ovrednotiti morebitno uporabo plazemskega nivoja fibulina-3 pri ocenjevanju odgovora na zdravljenje in njegovo napovedno vrednost za napredovanje bolezni do 18 mesecev po diagnozi malignega mezotelioma. Primernost fibulina-3 smo tudi primerjali s topnimi z mezotelinom povezanimi peptidi (SMRP) in ocenili njihovo skupno napovedno vrednost.

Bolniki in metode. V raziskavo smo vključili 78 bolnikov z malignim mezoteliomom, ki smo jih zdravili na Onkološkem inštitutu Ljubljana v letih 2007 do 2011. Nivo plazemskega fibulina-3 smo določevali pred zdravljenjem in pri različnih odgovorih na zdravljenje. Uporabljali smo encimski imunski test.

Rezultati. Pred zdravljenjem se nivo plazemskega fibulina-3 ni razlikoval glede na histološki podtip, tumorski stadij in prisotnost oddaljenih zasevkov. Statistično značilno višji nivo pa smo ugotovili pri napredovanju bolezni v primerjavi z nivojem pred zdravljenjem (test Mann-Whitney [U] = 472,50, p = 0,003) ter v primerjavi z nivojem ob popolnem odgovoru na zdravljenje (U = 42,00, p = 0,010) in pri stagnaciji bolezni (U = 542,00, p = 0,001). Bolniki, pri katerih je nivo fibulina-3 pred zdravljenjem presegel 34,25 ng/ml, so imeli več kot štirikrat večjo verjetnost, da bo bolezen napredovala v času 18 mesecev (razmerje obetov [OR] = 4,35; 95 % interval zaupanja [CI] 1,56–12,13). Prav tako so bolniki z višjim nivojem fibulina-3 po zdravljenju in s popolnim odgovorom na zdravljenje ali stagnacijo bolezni imeli večjo verjetnost, da bo bolezen napredovala v času 18 mesecev (OR = 6,94; 95 % CI 0,99–48,55 in OR = 4,39; 95 % CI 1,63–11,81).

Zaključki. Raziskava je pokazala, da bi fibulin-3 ob SMRP lahko bil dodatni tumorski označevalec za ugotavljanje napredovanja bolezni pri bolnikih z malignim mezoteliomom.

Vpliv tumorskega volumna na napoved preživetja brez napredovanja bolezni pri sinonazalnem raku

Hennersdorf F, Mauz PS, Adam P, Welz S, Sievert A, Ernemann U, Bisdas S

Izhodišča. Namen raziskave je bil analizirati napovedne dejavnike, s poudarkom na tumorskem volumnu, ki vplivajo na preživetje brez napredovanja bolezni pri raku nosne votline in obnosnih votlin.

Bolniki in metode. Retrospektivno smo analizirali 106 bolnikov s primarnim sinonazalnim rakom, ki smo jih zdravili in spremljali med marcem 2006 in oktobrom 2012. Možne napovedne dejavnike za preživetje brez ponovitve bolezni smo vključili v univariatno in multivariatno Coxovo regresijsko analizo. S Kaplan-Meierjevo metodo smo izračunali, kakšen vpliv na preživetje so imeli starost, spol, izhodiščni tumorski volumen (ki smo ga odčitali iz magnetnoresonančnih slik), histološki tip, stadij TNM in napovedne skupine po razvrstitvi Ameriškega odbora za raka (*American Joint Committee on Cancer,* AJCC). Analizirali smo tudi krivulje za občutljivost in specifičnost (*receiver operating characteristic,* ROC), s katerimi smo opredelili napovedno vrednost tumorskega volumna.

Rezultati. Najštevilčnejša histološka podskupina so bili epitelijski tumorji (77 %). Večina bolnikov (68 %) je imela napredovale tumorje (stadij AJCC II-IV). 18 bolnikov je imelo prizadete bezgavke. Povprečen tumorski volumen je bil 26,6 ± 21,2 cm³. Srednji čas preživetja brez ponovitve bolezni je bil 24,9 mesecev (razpon: 2,5–84,5 mesecev). Analiza krivulj ROC za tumorski volumen je pri ponovitvi bolezni pokazala občutljivost 58,1 % in specifičnost 75.4 %. V univariatni analizi so bili značilni napovedni dejavniki tumorski volumen, stadij AJCC, stadij T in stadij N. V multivariatni analizi sta bila značilna in neodvisna napovedna dejavnika pozitiven bezgavčni status in tumorski volumen.

Zaključki. Radiološki tumorski volumen se je pokazal statistično zanesljiv napovedni dejavnik preživetja brez ponovitve bolezni. Stadij T, stadij N in celokupni stadij AJCC v multivariatni analizi niso zadržali napovedne vrednosti.

Primerjava hibridne volumetrične modulirane ločne radioterapevtske tehnike (VMAT) in dvoločne tehnike VMAT za zdravlejnje raka prostate

Amaloo C, Nazareth D, Kumaraswamy LK

Izhodišča. Volumetrično modulirano ločno terapijo (*angl.* VMAT) so hitro sprejeli kot standarden način zdravljenja raka prostate. Raziskave so pokazale, da VMAT lahko zagotovi hitrejše obsevanje ob ustrezni pokritosti tarče in znižanem številu monitorskih enot ter ohranjeni zaščiti kritičnih organov. Namen raziskave je bil predstaviti zmožnost hibridne radioterapevtske tehnike, da zagotovi (v primerjavi z VMAT) večjo konformnost ob hkratni boljši kontroli načrtovanja in zaščiti kritičnih organov.

Metode. Pri 11 bolnikih, ki smo jih predhodno zdravili zaradi raka prostate s tehniko VMAT, smo ponovno načrtovali obsevanje s hibridno tehniko in s pomočjo Varianovega načrtovalnega sistema (*Varian Treatment Planning System*). Multipla statična polja (2 do 3) intenzitetno modulirane radioterapije (*angl.* IMRT) smo načrtovali glede na kritične organe. Na ta način smo zmanjšali obsevalno dozo vendar načrtovali dovolj veliko dozo na obsevalne tarčne volumne (planirane tarčne volumne, PTV). Tako smo dosegli bazično načrtovano dozo, ki je predstavljala 30–35 % doze za posamični ločni plan obsevanja tehnike VMAT.

Rezultati. Klinični načrt obsevanja VMAT smo uporabili za kontrolo oz. primerjavo. Primerjava povprečnih doz pri hibridni tehniki in VMAT, ki so jih prejeli rizični organi, je pokazala, da s hibridnim načrtom obsevanja dosežemo nižjo dozo pri vseh primerih, razen pri V80 za mehur in za desno glavo stegnenice. Obsevalna doza na PTV je bila primernejša pri tehniki VMAT.

Zaključki. Hibridni načrt je lahko izsevan v času ene same rotacije gantrija, pri čemer so prvine VMAT znotraj terapevtskega loka kombinirane z vložki dinamične IMRT.

Učinek zaokroženega konca lističev pri večlistnem kolimatorju na širino polsence in na premik meje obsevalnega polja. Analitična in numerična analiza

Zhou D, Zhang H, Ye P

Izhodišča. V radioterapiji imajo značilnosti polsence pomembno vlogo pri natančni aplikaciji doze. Ob načrtovanju zdravljenja širina polsence in premik meje obsevalnega polja znatno vplivata na konformnost dozne porazdelitve v področjih tarče in kritičnih organov.

Metode. V raziskavi analitično in numerično ocenjujemo učinek zaokroženih koncev lističev na značilnosti polsence. Izhajajoč iz pravila razpolovne debeline smo razvili algoritme za izračun lege lističev in korekcije meje obsevalnega polja, kar je še posebej pomembno v primeru lističev z velikim polmerom. Naredili smo računalniško simulacijo, ki je temeljila na programih Monte Carlo EGSnrc/BEAMnrc za različne polmere koncev lističev in različne velikosti virov sevanja. Za izračun širine polsence in premika meje obsevalnega polja smo uporabili tehniko obdelave podatkov s prileganjem krivulji.

Rezultati. Rezultati so pokazali, da se širina polsence povečuje z velikostjo vira. Krivulje širine polsence za lističe velikih polmerov so imele obliko črke U. To je bilo verjetno povezano z dejstvom, da žarki prehajajo na proksimalni in distalni strani lističa. Nasprotno pa je imela velikost vira zanemarljiv vpliv na premik meje obsevalnega polja. Premiki meje obsevalnega polja so bili v primeru analitične in numerične simulacije nespremenjeni. Kljub temu so bile celokupne končne vrednosti premikov meje obsevalnega polja, ki smo jih pridobili z analitično metodo, nekoliko manjše kot vrednosti pridobljene s simulacijo Monte Carlo.

Zaključki. Predlagana metoda bi lahko omogočila vpogled v raziskovanje učinkov zaokroženih koncev lističev na značilnosti polsence. Ob pripravi večlistnega kolimatorja za potrebe intenziteto modulirajoče radioterapije mora biti širina polsence in kalibracija premikov meje obsevalnih polj opravljena natančno.

Primerjava zagotavljanja kakovosti štirih dozimetričnih orodij pri intenzitetno moduliranem obsevanju

Son J, Baek T, Lee B, Shin D, Park SY, Park J, Lim YK, Lee SB, Kim J, Yoon M

Izhodišča. Raziskavo smo zasnovali, da bi primerjali rezultate štirih dozimetričnih orodij zagotavljanja kakovosti, ki jih uporabljamo pri intenzitetno moduliranem obsevanju (IMRT) in da bi predlagali univerzalne kriterije za zagotavljanje kakovosti, ne glede na dozimetrična orodja, ki jih uporabljamo.

Materiali in metode. Izbrali smo trideset polj načrtov IMRT pri petih bolnikih in nadaljevali s postopki za zagotavljanje kakovosti. Uporabili smo (1) obsevanje na radiokromatskem filmu, (2) diodno matriko (Mapcheck), (3) matriko ionske celice (MatriXX) in (4) napravo za elektronsko portalno slikanje (EPID). Izmerjene doze iz štirih dozimetričnih orodij smo primerjali z dozo, ki smo jo izračunali s sistemom načrtovanja zdravljenja. Stopnje menjavanja (*passing rates*) štirih dozimetričnih orodij smo izračunali z metodo indeksa gama, ob uporabi razlike v odmerku 3 % in dogovorne razdalje do 3 mm kot merila.

Rezultati. Rezultati zagotavljanja kakovosti, ki so temeljili na Mapcheck, MatriXX in EPID so pokazali dobro ujemanje s povprečnimi stopnjami menjavanja 99,61 %, 99,04 % in 99,29 %. Povprečna stopnja menjavanja, ki temeljila na merjenju radiokromatskega filma, pa je bila precej nižja, 95,88 %. Povprečna negotovost (1 standardni odklon) za minljive stopnje pri 6 intenzitetno modulirajočih področjih je bila okrog 0,31 pri merjenju s filmom in večja kot pri drugih treh dozimetričnih orodjih.

Zaključki. Rezultati zagotavljanja kakovosti in doslednosti so odvisni od izbire dozimetričnega orodja. Univerzalna stopnja menjavanja bi morala biti odvisna od normalizacije ali medsebojnih primerjav dozimetričnih orodij, če uporabljamo več kot eno dozimetrično orodje za zagotavljanje kakovosti pri posameznem bolniku.
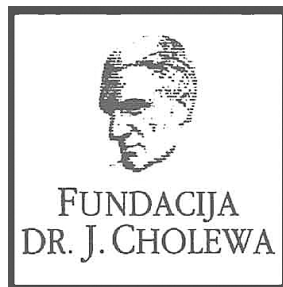
## Fundacija Doc. dr. Josip Cholewa

RAZPISUJE

denarno pomoč za sofinanciranje materialnih stroškov pri znanstveno-raziskovalnih delih s področja onkologije.

Prijava naj vsebuje:

1. kratko obrazložitev znanstveno-raziskovalnega dela s finančno konstrukcijo

2. kratko biografijo in bibliografijo prosilca/prosilcev

Prijave, prosimo, pošljite do **30. 9. 2015** na naslov Združenje Fundacija Doc.dr. Josip Cholewa, Dunajska cesta 106, 1000 Ljubljana

Uporabljena moška slovnična oblika se enakovredno nanaša na oba spola.

Fundacija "Docent dr. J. Cholewa" je neprofitno, neinstitucionalno in nestrankarsko združenje posameznikov, ustanov in organizacij, ki želijo materialno spodbujati in poglabljati raziskovalno dejavnost v onkologiji.
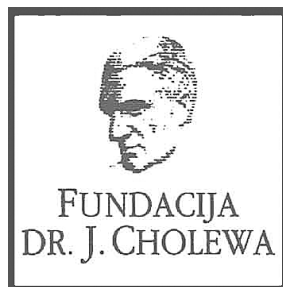
Activity of "Dr. J. Cholewa" Foundation for Cancer Research and Education – a report for the third quarter of 2015

The "Docent Dr. J. Cholewa Foundation for Cancer Research and Education" is named after Dr. Josip Cholewa, one of the first researchers in cancer in Slovenia and the founder of the "Banovinski Inštitut za raziskovanje in zdravljenje novotvorb" in 1937, that later became the Institute of Oncology in Ljubljana, Slovenia. His laboratory and clinical research work was based on an innovative and far-reaching multidisciplinary approach that included studies on prevention, detection and treatment of cancer. This pioneering approach facilitated the understanding of the complexities of all the problems and troubles experienced by cancer patients, their doctors and other medical staff when facing this disease. It could also be regarded as a harbinger of the progress observed in a large part of the world in the last half of the previous century. Therefore, the Foundation is a non-profit, non-political and non-government organisation that helps professionals, institutions and individuals obtaining financial help for cancer research and education in the Republic of Slovenia with the goal of continuing and expanding the great work and efforts of Dr. Josip Cholewa.

The "Docent Dr. J. Cholewa Foundation for Cancer Research and Education" hopes and strives to provide at least part of the financial support needed by qualified individuals and organisations interested in cancer research in the Republic of Slovenia. One of the objectives of the Foundation is to facilitate the transmission of the latest diagnostic and therapy procedures to the clinical environment in Slovenia, thus benefiting the ever increasing number of patients with various types of cancer in Slovenia. With this in mind, it is important to note that the incidence rates of many cancer, like colon, prostate and breast cancer have kept rising in recent decades in Slovenia.

The Foundation continues to provide financial support to "Radiology and Oncology", an international scientific journal that is edited and published in Ljubljana, Slovenia. It publishes scientific research articles, reviews, case reports, short reports and letters to the editor about research and studies in experimental and clinical oncology, supportive therapy, radiology, radiophyics, prevention and early diagnostics of different types of cancer. It is an open access journal freely available in pdf format and with a respectable Science Citation Index Impact factor. All the abstracts in "Radiology and Oncology" are available in Slovenian and the journal can thus provide sufficient scientific information from various fields of high quality cancer research to interested lay public in Slovenia.

The "Docent Dr. J. Cholewa Foundation for Cancer Research and Education" has thus an important role in support of cancer research, cancer education and many of the related fields in the Republic of Slovenia.

Andrej Plesničar, M.D., M.Sc.
Borut Štabuc, M.D., Ph.D.
Tomaž Benulič, M.D.
Viljem Kovač, M.D., Ph.D.

TANTUM VERDE®

Lajšanje bolečine in oteklin pri vnetju v ustni votlini in žrelu, ki nastanejo zaradi okužb in stanj po operaciji in kot posledica radioterapije (t.i. radiomukozitis).

Tantum Verde 1,5 mg/ml oralno pršilo, raztopina

Kakovostna in količinska sestava
1 ml raztopine vsebuje 1,5 mg benzidaminijevega klorida, kar ustreza 1,34 mg benzidamina. V enem razpršku je 0,17 ml raztopine. En razpršek vsebuje 0,255 mg benzidaminijevega klorida, kar ustreza 0,2278 mg benzidamina. En razpršek vsebuje 13,6 mg 96 odstotnega etanola, kar ustreza 12,728 mg 100 odstotnega etanola, in 0,17 mg metilparahidroksibenzoata (E218).

Terapevtske indikacije
Samozdravljenje: lajšanje bolečine in oteklin pri vnetju v ustni votlini in žrelu, ki so lahko posledica okužb in stanj po operaciji. Po nasvetu in navodilu zdravnika: lajšanje bolečine in oteklin v ustni votlini in žrelu, ki so posledica radiomukozitisa.

Odmerjanje in način uporabe
Uporaba 2- do 6-krat na dan (vsake 1,5 do 3 ure). Odrasli: 4 do 8 razprškov 2- do 6-krat na dan. Otroci od 6 do 12 let: 4 razprški 2- do 6-krat na dan. Otroci, mlajši od 6 let: 1 razpršek na 4 kg telesne mase; do največ 4 razprške 2 do 6-krat na dan.

Kontraindikacije
Znana preobčutljivost za zdravilno učinkovino ali katerokoli pomožno snov.

Posebna opozorila in previdnostni ukrepi
Pri manjšini bolnikov lahko resne bolezni povzročijo ustne/žrelne ulceracije. Če se simptomi v treh dneh ne izboljšajo, se mora bolnik posvetovati z zdravnikom ali zobozdravnikom, kot je primerno. Zdravilo vsebuje aspartam (E951) (vir fenilalanina), ki je lahko škodljiv za bolnike s fenilketonurijo. Zdravilo vsebuje izomalt (E953) (sinonim: izomaltitol (E953)). Bolniki z redko dedno intoleranco za fruktozo ne smejo jemati tega zdravila. Uporaba benzidamina ni priporočljiva za bolnike s preobčutljivostjo za salicilno kislino ali druga nesteroidna protivnetna zdravila. Pri bolnikih, ki imajo ali so imeli bronhialno astmo, lahko pride do bronhospazma. Pri takih bolnikih je potrebna previdnost.

Medsebojno delovanje z drugimi zdravili in druge oblike interakcij
Pri ljudeh raziskav o interakcijah niso opravljali.

Nosečnost in dojenje
Tantum Verde z okusom mentola 3 mg pastile se med nosečnostjo in dojenjem ne smejo uporabljati.

Vpliv na sposobnost vožnje in upravljanja s stroji
Uporaba benzidamina lokalno v priporočenem odmerku ne vpliva na sposobnost vožnje in upravljanja s stroji.

Neželeni učinki
Bolezni prebavil Redki: pekoč občutek v ustih, suha usta.
Bolezni imunskega sistema Redki: preobčutljivostna reakcija.
Bolezni dihal, prsnega koša in mediastinalnega prostora Zelo redki: laringospazem.
Bolezni kože in podkožja Občasni: fotosenzitivnost. Zelo redki: angioedem.

Rok uporabnosti
4 leta. Zdravila ne smete uporabljati po datumu izteka roka uporabnosti, ki je naveden na ovojnini. Posebna navodila za shranjevanje Za shranjevanje pastil niso potrebna posebna navodila. Plastenko z raztopino shranjujte v zunanji ovojnini za zagotovitev zaščite pred svetlobo. Shranjujte pri temperaturi do 25°C. Shranjujte v originalni ovojnini in nedosegljivo otrokom.

Erbitux 5 mg/ml raztopina za infundiranje
Skrajšan povzetek glavnih značilnosti zdravila

Sestava: En ml raztopine za infundiranje vsebuje 5 mg cetuksimaba in pomožne snovi. Cetuksimab je himerno monoklonsko IgG$_1$ protitelo. **Terapevtske indikacije:** Zdravilo Erbitux je indicirano za zdravljenje bolnikov z metastatskim kolorektalnim rakom z ekspresijo receptorjev EGFR in nemutiranim tipom RAS v kombinaciji s kemoterapijo na osnovi irinotekana, kot primarno zdravljenje v kombinaciji s FOLFOX in kot samostojno zdravilo pri bolnikih, pri katerih zdravljenje z oksaliplatinom in zdravljenje na osnovi irinotekana ni bilo uspešno in pri bolnikih, ki ne prenašajo irinotekana. Zdravilo Erbitux je indicirano za zdravljenje bolnikov z rakom skvamoznih celic glave in vratu v kombinaciji z radioterapijo za lokalno napredovalo bolezen in v kombinaciji s kemoterapijo na osnovi platine za ponavljajočo se in/ali metastatsko bolezen. **Odmerjanje in način uporabe:** Zdravilo Erbitux pri vseh indikacijah infundirajte enkrat na teden. Pred prvo infuzijo mora bolnik prejeti premedikacijo z antihistaminikom in kortikosteroidom najmanj 1 uro pred uporabo cetuksimaba. Začetni odmerek je 400 mg cetuksimaba na m² telesne površine. Vsi naslednji tedenski odmerki so vsak po 250 mg/m². **Kontraindikacije:** Zdravilo Erbitux je kontraindicirano pri bolnikih z znano hudo preobčutljivostno reakcijo (3. ali 4. stopnje) na cetuksimab. Kombinacija zdravila Erbitux s kemoterapijo, ki vsebuje oksaliplatin, je kontraindicirana pri bolnikih z metastatskim kolorektalnim rakom z mutiranim tipom RAS ali kadar status RAS ni znan. **Posebna opozorila in previdnostni ukrepi:** Pojav hude reakcije, povezane z infundiranjem, zahteva takojšnjo in stalno ukinitev terapije s cetuksimabom. Če pri bolniku nastopi blaga ali zmerna reakcija, povezana z infundiranjem, lahko zmanjšate hitrost infundiranja. Priporočljivo je, da ostane hitrost infundiranja na nižji vrednosti tudi pri vseh naslednjih infuzijah. Če se pri bolniku pojavi kožna reakcija, ki je ne more prenašati, ali huda kožna reakcija (≥ 3. stopnje po kriterijih CTCAE), morate prekiniti terapijo s cetuksimabom. Z zdravljenjem smete nadaljevati le, če se je reakcija izboljšala do 2. stopnje. Če ugotovite intersticijsko bolezen pljuč, morate zdravljenje s cetuksimabom prekiniti, in bolnika ustrezno zdraviti. Zaradi možnosti pojava znižanja nivoja elektrolitov v serumu se pred in periodično med zdravljenjem s cetuksimabom priporoča določanje koncentracije elektrolitov v serumu. Pri bolnikih, ki prejemajo cetuksimab v kombinaciji s kemoterapijo na osnovi platine, obstaja večje tveganje za pojav hude nevtropenije. Takšne bolnike je potrebno skrbno nadzorovati. Pri predpisovanju cetuksimaba je treba upoštevati kardiovaskularno stanje in indeks zmogljivosti bolnika in sočasno dajanje kardiotoksičnih učinkovin kot so fluoropirimidini. Če je diagnoza ulcerativnega keratitisa potrjena, je treba zdravljenje s cetuksimabom prekiniti ali ukiniti. Cetuksimab je treba uporabljati previdno pri bolnikih z anamnezo keratitisa, ulcerativnega keratitisa ali zelo suhih oči. Cetuksimaba ne uporabljajte za zdravljenje bolnikov s kolorektalnim rakom, če imajo tumorje z mutacijo RAS ali pri katerih je tumorski status RAS neznan. **Interakcije:** Pri kombinaciji s fluoropirimidini se je v primerjavi z uporabo fluoropirimidinov, kot monoterapije, povečala pogostnost srčne ishemije, vključno z miokardnim infarktom in kongestivno srčno odpovedjo ter pogostnost sindroma dlani in stopal. V kombinaciji s kemoterapijo na osnovi platine se lahko poveča pogostnost hude levkopenije ali hude nevtropenije. V kombinaciji s kapecitabinom in oksaliplatinom (XELOX) se lahko poveča pogostnost hude driske. **Neželeni učinki:** Zelo pogosti (≥ 1/10): hipomagneziemija, povečanje ravni jetrnih encimov, kožne reakcije, blage ali zmerne reakcije povezane z infundiranjem, mukozitis, v nekaterih primerih resen. Pogosti (≥ 1/100 do < 1/10): dehidracija, hipokalciemija, anoreksija, glavobol, konjunktivitis, driska, navzeja, bruhanje, hude reakcije povezane z infundiranjem, utrujenost. **Posebna navodila za shranjevanje:** Shranjujte v hladilniku (2 °C - 8 °C). **Pakiranje:** 1 viala z 20 ml ali 100 ml raztopine. **Način in režim izdaje:** Izdaja zdravila je le na recept-H. **Imetnik dovoljenja za promet:** Merck KGaA, 64271 Darmstadt, Nemčija.

Datum zadnje revizije besedila: junij 2014.

Pred predpisovanjem zdravila natančno preberite celoten Povzetek glavnih značilnosti zdravila.

Samo za strokovno javnost.

Podrobnejše informacije so na voljo pri predstavniku imetnika dovoljenja za promet z zdravilom: Merck d.o.o., Ameriška ulica 8, 1000 Ljubljana, tel.: 01 560 3810, faks: 01 560 3830, el. pošta: info@merck.si
www.merckserono.net
www.Erbitux–international.com

Skrajšan povzetek glavnih značilnosti zdravila ZELBORAF®

Ime zdravila: Zelboraf 240 mg filmsko obložene tablete
Kakovostna in količinska sestava: Ena tableta vsebuje 240 mg vemurafeniba (v obliki precipitata vemurafeniba in hipromeloze acetat sukcinata).
Terapevtske indikacije: Vemurafenib je indiciran za samostojno zdravljenje odraslih bolnikov z neresektabilnim ali metastatskim melanomom, s pozitivno mutacijo BRAF V600.
Odmerjanje in način uporabe: Zdravljenje z vemurafenibom mora uvesti in nadzorovati usposobljen zdravnik, ki ima izkušnje z uporabo zdravil za zdravljenje raka. Odmerjanje: Priporočeni odmerek vemurafeniba je 960 mg (4 tablete po 240 mg) dvakrat na dan (to ustreza celotnemu dnevnemu odmerku 1920 mg). Vemurafenib lahko vzamemo s hrano ali brez nje, izogibati pa se moramo stalnemu jemanju obeh dnevnih odmerkov na prazen želodec. Zdravljenje z vemurafenibom moramo nadaljevati do napredovanja bolezni ali pojava nesprejemljive toksičnosti. Če bolnik izpusti odmerek, ga lahko vzame do 4 ure pred naslednjim odmerkom za ohranitev sheme dvakrat na dan. Obeh odmerkov pa se ne sme vzeti hkrati. Če bolnik po zaužitju vemurafeniba bruha, ne sme vzeti dodatnega odmerka zdravila, ampak mora z zdravljenjem normalno nadaljevati. Prilagoditve odmerjanja: Za obvladovanje neželenih učinkov ali ob podaljšanju intervala QTc je potrebno zmanjšanje odmerka, začasna prekinitev in/ali dokončno prenehanje zdravljenja (za podrobnosti o prilagoditvi odmerka, prosimo glejte SmPC zdravila). Zmanjšanje odmerka pod 480 mg dvakrat na dan ni priporočljivo. Če se pri bolniku pojavi ploščatocelični karcinom kože, priporočamo nadaljevanje zdravljenja brez zmanjšanja odmerka vemurafeniba. Posebne populacije: Za bolnike, starejše od 65 let, prilagajanje odmerka ni potrebno. O bolnikih z okvaro ledvic ali jeter je na voljo malo podatkov. Bolnike s hudo okvaro ledvic ali z zmerno do hudo okvaro jeter je treba pozorno spremljati. Varnost in učinkovitost vemurafeniba pri otrocih in mladostnikih, mlajših od 18 let, še nista bili dokazani. Podatkov ni na voljo. Način uporabe: Tablete vemurafeniba je treba zaužiti cele, z vodo. Ne sme se jih žvečiti ali zdrobiti.
Kontraindikacije: Preobčutljivost na zdravilno učinkovino ali katerokoli pomožno snov.
Posebna opozorila in previdnostni ukrepi: Pred uporabo vemurafeniba je treba z validirano preiskavo potrditi, da ima bolnik tumor s pozitivno mutacijo BRAF V600. Dokazi o učinkovitosti in varnosti vemurafeniba pri bolnikih s tumorji z izraženo redko BRAF V600 mutacijo, ki ni V600E ali V600K, niso prepričljivi. Vemurafeniba se ne sme uporabljati pri bolnikih z malignim melanomom, ki ima divji tip BRAF. Preobčutljivostne reakcije: V povezavi z vemurafenibom so bile opisane resne preobčutljivostne reakcije, vključno z anafilaksijo. Hude preobčutljivostne reakcije lahko vključujejo Stevens-Johnsonov sindrom, generaliziran izpuščaj, eritem ali hipotenzijo. Pri bolnikih, pri katerih se pojavijo resne preobčutljivostne reakcije, je treba zdravljenje z vemurafenibom dokončno opustiti. Kožne reakcije: Pri bolnikih, ki so prejemali vemurafenib, so v ključnem kliničnem preskušanju poročali o hudih kožnih reakcijah, vključno z redkim Stevens-Johnsonovim sindromom in toksično epidermalno nekrolizo. Po prihodu vemurafeniba na trg so v povezavi z njim poročali o reakciji na zdravila z eozinofilijo in sistemskimi simptomi (DRESS, *Drug Reaction with Eosinophilia and Systemic Symptoms*). Pri bolnikih, pri katerih se pojavi huda kožna reakcija, je treba zdravljenje z vemurafenibom dokončno opustiti. Podaljšanje intervala QT: V nekontrolirani, odprti študiji faze II pri predhodno zdravljenih bolnikih z metastatskim melanomom, so opazili podaljšanje intervala QT, odvisnega od izpostavljenosti vemurafenibu. Podaljšanje intervala QT lahko poveča tveganje za ventrikularne aritmije, vključno s t. i. *Torsade de Pointes*. Z vemurafenibom ni priporočljivo zdraviti bolnikov z elektrolitskimi motnjami (vključno z magnezijem), ki jih ni mogoče odpraviti, bolnikov s sindromom dolgega intervala QT in bolnikov, zdravljenih z zdravili, ki podaljšajo interval QT. Pred zdravljenjem z vemurafenibom, en mesec po zdravljenju in po spremembi odmerka je treba pri vseh bolnikih posneti elektrokardiogram (EKG) in kontrolirati elektrolite (vključno z magnezijem). Nadaljnje kontrole so priporočljive predvsem pri bolnikih z zmerno do hudo jetrno okvaro, in sicer mesečno prve 3 mesece zdravljenja, potem pa na 3 mesece oziroma pogosteje, če je to klinično indicirano. Zdravljenja z vemurafenibom ni priporočljivo uvesti pri bolnikih, ki imajo interval QTc > 500 milisekund (ms). Bolezni oči: Poročali so o resnih neželenih učinkih na očeh, vključno z uveitisom, iritisom in zaporo mrežnične vene. Bolnikom je treba oči redno kontrolirati glede morebitnih neželenih učinkov na očeh. Ploščatocelični karcinom kože: Pri bolnikih, zdravljenih z vemurafenibom, so bili opisani primeri ploščateceličnega karcinoma kože, vključno s ploščateceličnim karcinomom, opredeljenim kot keratoakantom ali mešani keratoakantom. Priporočljivo je, da vsi bolniki pred uvedbo zdravljenja opravijo dermatološki pregled in da so med zdravljenjem deležni rednih kontrol. Vsako sumljivo spremembo je treba izrezati, poslati na histopatološko oceno in jo zdraviti v skladu z lokalnimi smernicami. Med zdravljenjem in do šest mesecev po zdravljenju ploščateceličnega karcinoma mora zdravnik enkrat mesečno pregledati bolnika. Pri bolnikih, ki se jim pojavi ploščatocelični karcinom kože, je priporočljivo nadaljevati zdravljenje brez zmanjšanja odmerka. Nadzor se mora nadaljevati še 6 mesecev po prenehanju zdravljenja z vemurafenibom ali do uvedbe drugega antineoplastičnega zdravljenja. Bolnikom je treba naročiti, naj svojega zdravnika obvestijo o pojavu kakršnih koli sprememb na koži. Ploščatocelični karcinom, ki se ne nahaja na koži: Pri bolnikih, ki so prejemali vemurafenib v kliničnih preskušanjih, so poročali o primerih ploščateceličnega karcinoma, ki se ne nahaja na koži. Bolnikom je treba pred uvedbo zdravljenja in na 3 mesece med zdravljenjem pregledati glavo in vrat (pregled mora obsegati vsaj ogled ustne sluznice in palpacijo bezgavk). Poleg tega morajo bolniki pred zdravljenjem in na 6 mesecev med zdravljenjem opraviti računalniško tomografijo (CT) prsnega koša. Pred in po končanem zdravljenju ali kadar je klinično indicirano, je priporočljivo opraviti pregled zadnjika in ginekološki pregled (pri ženskah). Po prenehanju zdravljenja z vemurafenibom se mora zadnje pregled ploščateceličnega karcinoma, ki se ne nahaja na koži, nadaljevati še 6 mesecev ali do uvedbe antineoplastičnega zdravljenja. Nenormalne spremembe je treba obravnavati v skladu s klinično prakso. Novi primarni melanom: V kliničnih preskušanjih so poročali o novih primarnih melanomih. Bolnike s takšnimi primeri so zdravili z ekscizijo, bolniki pa so nadaljevali z zdravljenjem brez prilagoditve odmerka. Nadzor nad pojavom lezij je treba izvajati, kot je navedeno zgoraj pri ploščateceličnem karcinomu kože. Druge malignosti: Glede na mehanizem delovanja lahko vemurafenib povzroči napredovanje rakov, povezanih z mutacijo RAS. Pred dajanjem vemurafeniba bolnikom, ki so imeli ali imajo raka, povezanega z mutacijo RAS, skrbno razmislite o koristih in tveganjih. Pankreatitis: Pri bolnikih, zdravljenih z zdravilom Zelboraf, so poročali o pankreatitisu. Nepojasnjeno bolečino v trebuhu je treba nemudoma preiskati. Bolnike je treba skrbno spremljati, ko po epizodi pankreatitisa ponovno uvedemo vemurafenib. Poškodbe jeter: Med uporabo vemurafeniba so poročali o poškodbah jeter, vključno s primeri hudih poškodb. Pred uvedbo zdravljenja in mesečno med zdravljenjem oz. kot je

klinično indicirano, je treba kontrolirati jetrne encime (transaminaze in alkalno fosfatazo) ter bilirubin. Laboratorijske nepravilnosti je treba obvladati z zmanjšanjem odmerka, prekinitvijo zdravljenja ali prenehanjem zdravljenja (za podrobnosti o prilagoditvi odmerka, prosimo glejte SmPC zdravila). Jetrna okvara: Bolnikom z jetrno okvaro začetnih odmerkov ni treba prilagajati. Bolnike, ki imajo zaradi metastaz v jetrih blago jetrno okvaro in nimajo hiperbilirubinemije, se lahko nadzoruje v skladu s splošnimi priporočili. Podatkov o bolnikih z zmerno do hudo jetrno okvaro je le malo; pri takih bolnikih je izpostavljenost lahko večja. Tako je posebej po prvih tednih zdravljenja potreben skrben nadzor, saj lahko po daljšem obdobju (več tednih) pride do kopičenja. Ledvična okvara: Bolnikom z blago ali zmerno ledvično okvaro začetnih odmerkov ni treba prilagajati. Pri bolnikih s hudo ledvično okvaro je treba vemurafenib uporabljati previdno ter jih pozorno spremljati. Fotosenzibilnost: Pri bolnikih, ki so v kliničnih študijah prejemali vemurafenib, je bila opisana blaga do huda fotosenzibilnost. Vsem bolnikom je treba naročiti, naj se med jemanjem vemurafeniba ne izpostavljajo soncu. V primeru fotosenzibilnosti stopnje 2 (neprenosljivo) ali več so priporočljive prilagoditve odmerka. Ženske v rodni dobi morajo med zdravljenjem in vsaj še 6 mesecev po zdravljenju uporabljati učinkovito kontracepcijsko zaščito. Vemurafenib lahko zmanjša učinkovitost hormonskih kontraceptivov. Sočasno dajanje ipilimumaba: pri sočasni uporabi ipilimumaba in vemurafeniba so v preskušanju faze I poročali o asimptomatskih zvišanjih transaminaz in bilirubina stopnje 3. Glede na te preliminarne podatke sočasna uporaba ipilimumaba in vemurafeniba ni priporočljiva.
Medsebojno delovanje z drugimi zdravili in druge oblike interakcij: *Vplivi vemurafeniba na substrate CYP* Vemurafenib lahko poveča izpostavljenost v plazmi tistih snovi, ki se presnavljajo pretežno s CYP1A2; v takem primeru je treba razmisliti o prilagoditvi odmerka. Vemurafenib lahko zmanjša plazemsko izpostavljenost zdravilom, ki se presnavljajo pretežno s CYP3A4. Tako je lahko učinkovitost kontracepcijskih tablet, ki se presnavljajo s CYP3A4 in se uporabljajo sočasno z vemurafenibom, zmanjšana. Pri substratih CYP3A4, ki imajo ozko terapevtsko okno, je treba razmisliti o prilagoditvi odmerka. Zaenkrat še ni znano ali lahko vemurafenib pri 100 µM koncentraciji v plazmi, ki je bila opažena pri bolnikih v stanju dinamičnega ravnovesja (približno 50 µg/ml), zmanjša plazemske koncentracije sočasno dajanih substratov CYP2B6, kot je bupropion. Kadar se vemurafenib pri bolnikih z melanomom uporabi hkrati z varfarinom (CYP2C9), je potrebna previdnost. Tveganja za klinično pomemben učinek na sočasno uporabljene učinkovine, ki so substrati CYP2C8, pa ni mogoče izključiti. Zaradi dolge razpolovne dobe vemurafeniba je mogoče, da popolnega inhibitornega učinka vemurafeniba na sočasno dajano zdravilo ne opazimo, dokler ne mine 8 dni zdravljenja z vemurafenibom. Po koncem zdravljenja z vemurafenibom bo morda potreben 8-dnevni premor, da se izognemo interakcijam z nadaljnjim zdravljenjem. *Vpliv vemurafeniba na transportne sisteme zdravil* Možnosti, da vemurafenib morda poveča izpostavljenost drugih zdravil, ki se prenašajo s P-gp, ni mogoče izključiti. Možen vpliv vemurafeniba na druge prenašalce trenutno ni znan. *Vplivi sočasno uporabljenih zdravil na vemurafenib* Študije *in vitro* kažejo, da sta presnova s CYP3A4 in glukuronidacija odgovorni za presnovo vemurafeniba. Zdi se, da je tudi izločanje z žolčem pomembna pot izločanja. Vemurafenib je treba uporabljati previdno v kombinaciji z močnimi inhibitorji CYP3A4, glukuronidacije in/ali prenašalnih beljakovin (npr. ritonavirjem, sakvinavirjem, telitromicinom, ketokonazolom, itrakonazolom, vorikonazolom, posakonazolom, nefazodonom, atazanavirjem). Sočasna uporaba močnih induktorjev P-gp, glukuronidacije, in/ali CYP3A4 (npr. rifampicina, rifabutina, karbamazepina, fenitoina ali šentjanžrevke [Hypericum perforatum]) lahko vodi v suboptimalno izpostavljenost vemurafenibu in se ji je treba izogibati. Študije *in vitro* so pokazale, da je vemurafenib substrat sekretornih prenašalcev, P-gp in BCRP. Vplivi induktorjev in inhibitorjev P-gp in BCRP na izpostavljenost vemurafenibu niso znani. Ne moremo pa izključiti možnosti, da imajo lahko zdravila, ki vplivajo na P-gp (npr. verapamil, ciklosporin, ritonavir, kinidin, itrakonazol) ali BCRP (npr. ciklosporin, gefitinib), vpliv na farmakokinetiko vemurafeniba. Za zdaj ni znano, ali je vemurafenib substrat tudi za druge beljakovinske prenašalce.
Neželeni učinki: Med najpogostejšimi neželenimi učinki (> 30 %), o katerih so poročali v zvezi z vemurafenibom, so artralgija, utrujenost, kožni izpuščaj, fotosenzibilnostna reakcija, navzea, alopecija in srbenje. Zelo pogosto je bil opisan ploščatocelični karcinom kože. Najpogostejši neželeni učinki, ki so se pojavili pri bolnikih, zdravljenih z vemurafenibom v študiji faze II in III in dogodki iz varnostnih poročil vseh preskušanj in obdobja po prihodu zdravila na trg. Zelo pogosti: ploščatocelični karcinom kože, seboroična keratoza, kožni papilom, zmanjšanje teka, glavobol, disgevzija, kašelj, driska, bruhanje, slabost, zaprtost, fotosenzibilna reakcija, aktinična keratoza, kožni izpuščaj, makulo-papulozen izpuščaj, papulozen izpuščaj, srbenje, hiperkeratoza, eritem, alopecija, suha koža, sončne opekline, artralgija, mialgija, bolečina v okončini, mišično-skeletne bolečine, bolečine v hrbtu, utrujenost, pireksija, periferni edem, astenija, zvišanje GGT. Pogosti: folikulitis, bazalocelični karcinom, novi primarni melanom, ohromelost sedmega živca, omotica, uveitis, sindrom palmarno-plantarne eritrodisestezije, panikulitis (vključno z nodoznim eritemom), pilarna keratoza, artritis, zvišanje ALT, alkalne fosfataze, bilirubina in izguba telesne mase, podaljšanje QT. Posebne populacije: Pri starejših bolnikih (≥ 65 let) je možna večja verjetnost neželenih učinkov, vključno s ploščateceličnim karcinomom kože, zmanjšanjem teka in motnjami srčnega ritma. Med neželene učinke stopnje 3, ki so bili med kliničnimi preskušanji vemurafeniba pri ženskah opisani pogosteje kot pri moških, spadajo kožni izpuščaj, artralgija in fotosenzibilnost. Poročanje o domnevnih neželenih učinkih: Poročanje o domnevnih neželenih učinkih zdravila po izdaji dovoljenja za promet je pomembno. Omogoča namreč stalno spremljanje razmerja med koristmi in tveganji zdravila. Od zdravstvenih delavcev se zahteva, da poročajo o katerem koli domnevnem neželenem učinku zdravila na: Univerzitetni klinični center Ljubljana, Interna klinika, Center za zastrupitve, Zaloška cesta 2, SI-1000 Ljubljana, Faks: + 386 (0)1 434 76 46, e-pošta: farmakovigilanca@kclj.si.
Režim izdaje zdravila: Rp/Spec
Imetnik dovoljenja za promet: Roche Registration Limited, 6 Falcon Way, Shire Park, Welwyn Garden City, AL7 1TW, Velika Britanija
Verzija: 2.0/15
Informacija pripravljena: junij 2015
Samo za strokovno javnost.

DODATNE INFORMACIJE SO NA VOLJO PRI:
Roche farmacevtska družba d.o.o., Vodovodna cesta 109, 1000 Ljubljana

Roche

Fotografija je simbolična.

Zelboraf®

- **Zaviralec BRAF kinaze**
- **Indiciran za zdravljenje bolnikov z neoperabilnim ali metastaskim melanomom s pozitivno mutacijo BRAF V600**
- **Dokazano daljše preživetje v primerjavi z dakarbazinom**
- **Izkušnje pri zdravljenju več tisoč bolnikov**

▼ Za to zdravilo se izvaja dodatno spremljanje varnosti. Tako bodo hitreje na voljo nove informacije o njegovi varnosti. Zdravstvene delavce naprošamo, da poročajo o katerem koli domnevnem neželenem učinku zdravila.

Referenca: Povzetek glavnih značilnosti zdravila Zelboraf, dostopano 17. 6. 2015 na http://www.ema.europa.eu/docs/sl_SI/document_library/EPAR_-_Product_Information/human/002409/WC500124317.pdf

Zelboraf®

vemurafenib

Učinkovitost. Dokazi. Izkušnje.

Instructions for authors

The editorial policy

Radiology and Oncology is a multidisciplinary journal devoted to the publishing original and high quality scientific papers and review articles, pertinent to diagnostic and interventional radiology, computerized tomography, magnetic resonance, ultrasound, nuclear medicine, radiotherapy, clinical and experimental oncology, radiobiology, radiophysics and radiation protection. Therefore, the scope of the journal is to cover beside radiology the diagnostic and therapeutic aspects in oncology, which distinguishes it from other journals in the field.

The Editorial Board requires that the paper has not been published or submitted for publication elsewhere; the authors are responsible for all statements in their papers. Accepted articles become the property of the journal and, therefore cannot be published elsewhere without the written permission of the editors.

Submission of the manuscript

The manuscript written in English should be submitted to the journal via online submission system Editorial Manager available for this journal at: **www.radioloncol.com**.

In case of problems, please contact Sašo Trupej at saso.trupej@computing.si or the Editor of this journal at gsersa@onko-i.si

All articles are subjected to the editorial review and when the articles are appropriated they are reviewed by independent referees. In the cover letter, which must accompany the article, the authors are requested to suggest 3-4 researchers, competent to review their manuscript. However, please note that this will be treated only as a suggestion; the final selection of reviewers is exclusively the Editor's decision. The authors' names are revealed to the referees, but not vice versa.

Manuscripts which do not comply with the technical requirements stated herein will be returned to the authors for the correction before peer-review. The editorial board reserves the right to ask authors to make appropriate changes of the contents as well as grammatical and stylistic corrections when necessary. Page charges will be charged for manuscripts exceeding the recommended length, as well as additional editorial work and requests for printed reprints.

Articles are published printed and on-line as the open access (**www.degruyter.com/view/j/raon**).

All articles are subject to 700 EUR + VAT publication fee. Exceptionally, waiver of payment may be negotiated with editorial office, upon lack of funds.

Manuscripts submitted under multiple authorship are reviewed on the assumption that all listed authors concur in the submission and are responsible for its content; they must have agreed to its publication and have given the corresponding author the authority to act on their behalf in all matters pertaining to publication. The corresponding author is responsible for informing the coauthors of the manuscript status throughout the submission, review, and production process.

Preparation of manuscripts

Radiology and Oncology will consider manuscripts prepared according to the Uniform Requirements for Manuscripts Submitted to Biomedical Journals by International Committee of Medical Journal Editors (www.icmje.org). The manuscript should be written in grammatically and stylistically correct language. Abbreviations should be avoided. If their use is necessary, they should be explained at the first time mentioned. The technical data should conform to the SI system. The manuscript, excluding the references, tables, figures and figure legends, must not exceed 5000 words, and the number of figures and tables is limited to 8. Organize the text so that it includes: Introduction, Materials and methods, Results and Discussion. Exceptionally, the results and discussion can be combined in a single section. Start each section on a new page, and number each page consecutively with Arabic numerals.

The Title page should include a concise and informative title, followed by the full name(s) of the author(s); the institutional affiliation of each author; the name and address of the corresponding author (including telephone, fax and E-mail), and an abbreviated title (not exceeding 60 characters). This should be followed by the abstract page, summarizing in less than 250 words the reasons for the study, experimental approach, the major findings (with specific data if possible), and the principal conclusions, and providing 3-6 key words for indexing purposes. Structured abstracts are required. Slovene authors are requested to provide title and the abstract in Slovene language in a separate file. The text of the research article should then proceed as follows:

Introduction should summarize the rationale for the study or observation, citing only the essential references and stating the aim of the study.

Materials and methods should provide enough information to enable experiments to be repeated. New methods should be described in details.

Results should be presented clearly and concisely without repeating the data in the figures and tables. Emphasis should be on clear and precise presentation of results and their significance in relation to the aim of the investigation.

Discussion should explain the results rather than simply repeating them and interpret their significance and draw conclusions. It should discuss the results of the study in the light of previously published work.

Charts, Illustrations, Images and Tables

Charts, Illustrations, Images and Tables must be numbered and referred to in the text, with the appropriate location indicated. Charts, Illustrations and Images, provided electronically, should be of appropriate quality for good reproduction. Illustrations and charts must be vector image, created in CMYK color space, preferred font "Century Gothic", and saved as .AI, .EPS or .PDF format. Color charts, illustrations and Images are encouraged, and are published without additional charge. Image size must be 2.000 pixels on the longer side and saved as .JPG (maximum quality) format. In Images, mask the identities of the patients. Tables should be typed double-spaced, with a descriptive title and, if appropriate, units of numerical measurements included in the column heading. The files with the figures and tables can be uploaded as separate files.

References

References must be numbered in the order in which they appear in the text and their corresponding numbers quoted in the text. Authors are responsible for the accuracy of their references. References to the Abstracts and Letters to the Editor must be identified as such. Citation of papers in preparation or submitted for publication, unpublished observations, and personal communications should not be included in the reference list. If essential, such material may be incorporated in the appropriate place in the text. References follow the style of Index Medicus. All authors should be listed when their number does not exceed six; when there are seven or more authors, the first six listed are followed by "et al.". The following are some examples of references from articles, books and book chapters:

Dent RAG, Cole P. In vitro maturation of monocytes in squamous carcinoma of the lung. *Br J Cancer* 1981; **43:** 486-95.

Chapman S, Nakielny R. *A guide to radiological procedures*. London: Bailliere Tindall; 1986.

Evans R, Alexander P. Mechanisms of extracellular killing of nucleated mammalian cells by
macrophages. In: Nelson DS, editor. *Immunobiology of macrophage.* New York: Academic Press; 1976. p. 45-74.

Authorization for the use of human subjects or experimental animals

When reporting experiments on human subjects, authors should state whether the procedures followed the Helsinki Declaration. Patients have the right to privacy; therefore the identifying information (patient's names, hospital unit numbers) should not be published unless it is essential. In such cases the patient's informed consent for publication is needed, and should appear as an appropriate statement in the article. Institutional approval and Clinical Trial registration number is required.

The research using animal subjects should be conducted according to the EU Directive 2010/63/EU and following the Guidelines for the welfare and use of animals in cancer research (Br J Cancer 2010; 102: 1555 – 77). Authors must state the committee approving the experiments, and must confirm that all experiments were performed in accordance with relevant regulations.

These statements should appear in the Materials and methods section (or for contributions without this section, within the main text or in the captions of relevant figures or tables).

Transfer of copyright agreement

For the publication of accepted articles, authors are required to send the License to Publish to the publisher on the address of the editorial office. A properly completed License to Publish, signed by the Corresponding Author on behalf of all the authors, must be provided for each submitted manuscript.

The non-commercial use of each article will be governed by the Creative Commons Attribution-NonCommercial-NoDerivs license.

Conflict of interest

When the manuscript is submitted for publication, the authors are expected to disclose any relationship that might pose real, apparent or potential conflict of interest with respect to the results reported in that manuscript. Potential conflicts of interest include not only financial relationships but also other, non-financial relationships. In the Acknowledgement section the source of funding support should be mentioned. The Editors will make effort to ensure that conflicts of interest will not compromise the evaluation process of the submitted manuscripts; potential editors and reviewers will exempt themselves from review process when such conflict of interest exists. The statement of disclosure must be in the Cover letter accompanying the manuscript or submitted on the form available on **www.icmje.org/coi_disclosure.pdf**

Page proofs

Page proofs will be sent by E-mail to the corresponding author. It is their responsibility to check the proofs carefully and return a list of essential corrections to the editorial office within three days of receipt. Only grammatical corrections are acceptable at that time.

Open access

Papers are published electronically as open access on **www.degruyter.com/view/j/raon**, also papers accepted for publication as E-ahead of print.

Za zdravljenje odraslih bolnikov s predhodno zdravljenim, napredovalim nedrobnoceličnim pljučnim rakom, ki je ALK* pozitiven.

Drugačen gen
Drugačna terapija

XALKORI®
KRIZOTINIB

*anaplastična limfomska kinaza

BISTVENI PODATKI IZ POVZETKA GLAVNIH ZNAČILNOSTI ZDRAVILA

XALKORI 200 mg, 250 mg trde kapsule

▼ Za to zdravilo se izvaja dodatno spremljanje varnosti. Tako bodo hitreje na voljo nove informacije o njegovi varnosti. Zdravstvene delavce naprošamo, da poročajo o kateremkoli domnevnem neželenem učinku zdravila. Glejte poglavje 4.8 povzetka glavnih značilnosti zdravila, kako poročati o neželenih učinkih. **Sestava in oblika zdravila:** Ena kapsula vsebuje 200 mg ali 250 mg krizotiniba. **Indikacije:** Zdravljenje odraslih bolnikov s predhodno zdravljenim, napredovalim nedrobnoceličnim pljučnim rakom (NSCLC - *non-small cell lung cancer*), ki je ALK (anaplastična limfomska kinaza) pozitiven. **Odmerjanje in način uporabe:** Zdravljenje mora uvesti in nadzorovati zdravnik z izkušnjami z uporabo zdravil za zdravljenje rakavih bolezni. *Preverjanje prisotnosti ALK:* Pri izbiri bolnikov za zdravljenje z zdravilom XALKORI je treba opraviti točno in validirano preverjanje prisotnosti ALK. *Odmerjanje:* Priporočeni odmerek je 250 mg dvakrat na dan (500 mg na dan), bolniki pa morajo zdravilo jemati brez prekinitev. Če bolnik pozabi vzeti odmerek, ga mora vzeti takoj, ko se spomni, razen če do naslednjega odmerka manjka manj kot 6 ur. V tem primeru bolnik pozabljenega odmerka na sme vzeti. *Prilagajanja odmerkov:* Glede na varnost uporabe zdravila pri posameznem bolniku in kako bolnik zdravljenje prenaša, utegne biti potrebna prekinitev in/ali zmanjšanje odmerka zdravila na 200 mg dvakrat na dan; če je potrebno še nadaljnje zmanjšanje, pa znaša odmerek 250 mg enkrat na dan. Prilagajanje odmerkov pri *hematološki in nehematološki* (povečanje vrednosti AST, ALT, bilirubina; ILD/pnevmonitis; podaljšanje intervala QTc, bradikardija) *toksičnosti:* glejte preglednici 1 in 2 v povzetku glavnih značilnosti zdravila. *Okvara jeter:* Pri blagi in zmerni okvari je zdravljenje treba izvajati previdno, pri hudi okvari se zdravila ne sme uporabljati. *Okvara ledvic:* Pri blagi in zmerni okvari prilagajanje začetnega odmerka ni priporočeno. Pri hudi okvari ledvic (ki ne zahteva peritonealne dialize ali hemodialize) je odmerek 250 mg peroralno enkrat na dan; po vsaj 4 tednih zdravljenja se lahko poveča na 200 mg dvakrat na dan. *Starejši bolniki (≥ 65 let):* V primerjavi z mlajšimi bolniki niso opazili nobenih splošnih razlik v varnosti ali učinkovitosti. *Pediatrična populacija:* Varnost in učinkovitost nista bili dokazani. *Način uporabe:* Kapsule je treba pogoltniti cele, z nekaj vode, s hrano ali brez nje. Ne sme se jih zdrobiti, raztopiti ali odpreti. Izogibati se je treba uživanju grenivk, grenivkinega soka ter uporabi šentjanževke. **Kontraindikacije:** Preobčutljivost na krizotinib ali katerokoli pomožno snov. Huda okvara jeter. **Posebna opozorila in previdnostni ukrepi:** *Določanje statusa ALK:* Pomembno je izbrati dobro validirano in robustno metodologijo, da se izognemo lažno negativnim ali lažno pozitivnim rezultatom. *Hepatotoksičnost:* Zaradi jemanja zdravila je prišlo do hepatotoksičnosti s smrtnim izidom. Delovanje jeter, vključno z ALT, AST in skupnim bilirubinom, je treba preveriti enkrat na teden v prvih 2 mesecih zdravljenja, nato pa enkrat na mesec in kot je klinično indicirano. Ponovitve preverjanj morajo biti pogostejše pri povečanih vrednostih stopnje 2, 3 ali 4. *Intersticijska bolezen pljuč/pnevmonitis:* Lahko se pojavi huda, življenjsko nevarna in/ali smrtna intersticijska bolezen pljuč (ILD - *interstitial lung disease*)/pnevmonitis. Bolnike s simptomi, ki nakazujejo na ILD/pnevmonitis, je treba spremljati, zdravljenje pa prekiniti ob sumu na ILD/pnevmonitis. *Podaljšanje intervala QT:* Opažali so podaljšanje intervala QTc. Pri bolnikih z obstoječo bradikardijo, podaljšanjem intervala QTc v anamnezi ali predispozicijo zanj, pri bolnikih, ki jemljejo antiaritmike ali druga zdravila, ki podaljšujejo interval QT, ter pri bolnikih s pomembno obstoječo srčno boleznijo in/ali motnjami elektrolitov je treba zdravilo uporabljati previdno; potrebno je redno spremljanje EKG, elektrolitov in delovanja ledvic; preiskavi EKG in elektrolitov je treba opraviti čimbližje uporabi prvega odmerka, potem se priporoča redno spremljanje. *Bradikardija:* Lahko se pojavi simptomatska bradikardija (lahko se razvije več tednov po začetku zdravljenja); izogibati se je treba uporabi krizotiniba v kombinaciji z drugimi zdravili, ki povzročajo bradikardijo; pri simptomatski bradikardiji je treba prilagoditi odmerek. *Nevtropenija in levkopenija:* V kliničnih preskušanjih so poročali o nevtropeniji, levkopeniji in febrilni nevtropeniji (pri manj kot 1 % bolnikov); spremljati je treba popolno krvno sliko (pogostejše preiskave, če se opazijo abnormalnosti stopnje 3 ali 4 ali če se pojavi povišana telesna temperatura ali okužba). *Perforacija v prebavilih:* V kliničnih študijah so poročali o perforacijah v prebavilih, v obdobju trženja pa o smrtnih primerih perforacij v prebavilih. Krizotinib je treba pri bolnikih s tveganjem za nastanek perforacije v prebavilih uporabljati previdno; bolniki, pri katerih se razvije perforacija v prebavilih, se morajo prenehati zdraviti s krizotinibom; bolnike je treba poučiti o prvih znakih perforacije in jim svetovati, naj se nemudoma posvetujejo z zdravnikom. *Vplivi na vid:* Opažali so motnje vida; če so trdovratne ali se poslabšajo, je treba razmisliti o oftalmološkem pregledu. *Histološka preiskava, ki ne nakazuje adenokarcinoma:* Na voljo so le omejeni podatki pri NSCLC, ki je ALK pozitiven in ima histološke značilnosti, ki ne nakazujejo adenokarcinoma. **Medsebojno delovanje z drugimi zdravili in druge oblike interakcij:** Zdravila, ki lahko povečajo koncentracije krizotiniba v plazmi (atazanavir, indinavir, nelfinavir, ritonavir, sakvinavir, itrakonazol, ketokonazol, vorikonazol, klaritromicin, telitromicin, troleandomicin), tudi grenivke in grenivkin sok. Zdravila, ki lahko zmanjšajo koncentracije krizotiniba v plazmi (karbamazepin, fenobarbital, fenitoin, rifabutin, rifampicin, šentjanževka). Zdravila, katerih koncentracije v plazmi lahko krizotinib spremeni (midazolam, alfentanil, cisaprid, ciklosporin, derivati ergot alkaloidov, fentanil, pimozid, kinidin, sirolimus, takrolimus, bupropion, efavirenz, peroralni kontraceptivi, raltegravir, irinotekan, morfin, nalokson, digoksin, dabigatran, kolhicin, pravastatin, metformin, prokainamid). Zdravila, ki podaljšujejo interval QT ali ki lahko povzročijo Torsades de pointes (kinidin, dizopiramid, amiodaron, sotalol, dofetilid, ibutilid, metadon, cisaprid, moksifloksacin, antipsihotiki). Zdravila, ki povzročajo bradikardijo (verapamil, diltiazem, antagonisti adrenergičnih receptorjev beta, klonidin, guanfacin, digoksin, meflokin, antiholinesteraze, pilokarpin). **Plodnost, nosečnost in dojenje:** Ženske v rodni dobi se morajo izogibati zanositvi. Med zdravljenjem in najmanj 90 dni po njem je treba uporabljati ustrezno kontracepcijo (velja tudi za moške). Zdravilo lahko škoduje plodu in se ga med nosečnostjo ne sme uporabljati, razen če klinično stanje matere ne zahteva takega zdravljenja. Matere naj se med jemanjem zdravila dojenju izogibajo. Zdravilo lahko zmanjša plodnost moških in žensk. **Vpliv na sposobnost vožnje in upravljanja s stroji:** Lahko se pojavijo simptomatska bradikardija (npr. sinkopa, omotica, hipotenzija), motnje vida ali utrujenost; potrebna je previdnost. **Neželeni učinki:** Najresnejši neželeni učinki so hepatotoksičnost, ILD/pnevmonitis, nevtropenija in podaljšanje intervala QT. Najpogostejši neželeni učinki (≥ 25 %) so motnje vida, navzea, driska, bruhanje, zaprtje, edem, povečane vrednosti transaminaz in utrujenost. Ostali zelo pogosti (≥ 1/10 bolnikov) neželeni učinki so: nevtropenija, anemija, pomanjkanje apetita, nevropatija, disgevzija, omotica. **Način in režim izdaje:** Predpisovanje in izdaja zdravila je le na recept, zdravilo pa se uporablja samo v bolnišnicah. Izjemoma se lahko uporablja pri nadaljevanju zdravljenja na domu ob odpustu iz bolnišnice in nadaljnjem zdravljenju. **Imetnik dovoljenja za promet:** Pfizer Limited, Ramsgate Road, Sandwich, Kent, CT13 9NJ, Velika Britanija. **Datum zadnje revizije besedila:** 23.04.2015
Pred predpisovanjem se seznanite s celotnim povzetkom glavnih značilnosti zdravila.

XAR-02-15

Pfizer

Pfizer Luxembourg SARL, GRAND DUCHY OF LUXEMBOURG, 51, Avenue J.F. Kennedy, L – 1855, Pfizer, podružnica Ljubljana, Letališka cesta 3c, 1000 Ljubljana

SAMO ZA STROKOVNO JAVNOST